Beneficiation of sugarcane bagasse for production of GreenCoal

ANE Laubscher

orcid.org/0000-0003-4013-8410

Dissertation accepted in fulfilment of the requirements for the degree *Master of Engineering in Chemical Engineering* at the North-West University

Supervisor:	Prof S Marx
Co-supervisor:	Prof JR Bunt
Assistant-supervisor:	Dr RJ Venter

Graduation:	July 2020
Student number:	22160086

ACKNOWLEDGEMENTS

Glory and honour to YHWH.

I would like to thank the following individuals and institutions:

- The Sugar Mill Research Institute (SMRI) as the financial sponsor for this project
- My Supervisor, Prof. Sanette Marx, for her guidance and expertise.
- My Co-supervisor, Prof. John R. Bunt, for his guidance and expertise.
- Dr. Roelf Venter for his guidance and expertise.
- My wife, Mrs. Simoné Laubscher, for her moral support and patience.
- Julius Von Wellicht, who worked alongside me on the pilot plant.
- Mr Adrian Brock and Mr. Jan Kroeze for their technical expertise and Mr. Alias for his assistance.
- SMRI's representative, Brian Barker, for his assistance to retrieve samples.
- ARC Irene Analytical Services, Bureau Veritas, Dr. Innocence Shuro, Dr. Anine Jordaan, and Mrs. Belinda Venter for conducting analyses.
- My peers: Karina van der Merve, Nontembiso Piyo, Maans Marais, and LC Muller.
- My father and mother for their financial and moral support.
- My family and friends for their support.

ABSTRACT

The sugarcane mills in South Africa are to some extent self-sustaining by using sugarcane bagasse and coal to generate heat and power; however, due to the inferior physicochemical properties of sugarcane bagasse, there is potential to add maximum value to the entire crop by investing in a bio-refinery concept. Hydrothermal liquefaction has the potential to add value to the sugarcane crop by converting sugarcane bagasse to hydrochar and using it to produce heat and power.

This study aimed to evaluate GreenCoal pellets, prepared from coal and hydrochar, for combustion and gasification applications. The objectives of this study were to characterise the sugarcane bagasse, hydrochar, GreenCoals and coal, and to evaluate the effect the hydrochar fraction had on the pellet properties and behaviour during thermochemical processing.

In this study, a continuous HTL pilot plant upgraded sugarcane bagasse with the main reactor operating at 270°C under a system pressure of 70 bar and a flow rate of 120 L/hr. The feed was a slurry containing 4% biomass. The solid yield was 20.47%. The samples were characterised according to the chemical and structural characteristics. Chemical and structural analyses included proximate analysis, elemental analysis, higher heating value (HHV), Fourier-transform Infrared Spectroscopy (FTIR), Scanning Electron Microscopy (SEM), X-ray powder diffraction (XRD) and X-ray fluorescence. Additional analysis conducted on the sugarcane bagasse and hydrochar included fibre analysis (NDF, ADF, and ADL). Following HTL of sugarcane bagasse, all samples were pelletised and evaluated for the strength, as well as the combustion -, and CO_2-gasification behaviour.

The results showed that GreenCoal pellets had superior properties. The energy density of hydrochar and GreenCoal pellets (31.61 GJ/m^3 – 33.28 GJ/m^3) was significantly higher than the sugarcane bagasse pellets (21.24 GJ/m^3), whereas both the mass and energy density of hydrochar and GreenCoal pellets were higher than that of coal pellets, following a linear relationship with the hydrochar/coal ratio. The mechanical strength and durability of GreenCoal pellets improved with higher hydrochar/coal ratios, showcasing the natural binding effect of hydrochar. Furthermore, all GreenCoal pellets and hydrochar pellets showcased excellent hydrophobic properties, with the pellets remaining intact after submerging the pellets for two hours in water and showing negligible amounts of water absorbed. In contrast, sugarcane bagasse and coal pellets dissolved within five minutes.

FTIR analysis and SEM images suggested that the hydrochar consisted out an aromatic hydrochar with a high degree of aromatisation. The thermal degradation of hydrochar under inert conditions revealed two phases: the secondary- and primary hydrochar. The hydrochar demonstrated improved combustion behaviour opposing the sugarcane bagasse pellets with prolonged combustion at higher temperatures and lower reactivity. The ignition and peak temperatures increased with 78°C ─ 117°C and 137°C ─ 168°C, respectively. The results showed that hydrochar had higher ignition and peak temperatures than that of coal; however, the GreenCoal pellets demonstrated synergetic behaviour with lower ignition and peak temperatures. Both the ignition index and comprehensive combustion index of GreenCoal pellets were favourable against the pure hydrochar and pure coal pellets and showed that GreenCoal 1:1 demonstrated the best combustion behaviour.

The hydrochar pellets showed favourable, lower reactivity of the chars in opposition to the sugarcane bagasse pellets. At a conversion of 50%, the reactivity ($R_{50\%}$) of sugarcane bagasse and hydrochar pellets was 107.9 min^{-1} and 28.2 min^{-1}, respectively. Coal demonstrated the lowest reactivity, with $R_{50\%}$ of 17.7 min^{-1}. The benefit of producing GreenCoal blends was observed, with GreenCoal pellets showing synergistic behaviour. Overall, the effect of the hydrochar/coal blend was less apparent at higher gasification temperatures.

Keywords: Continuous hydrothermal liquefaction, sugarcane bagasse, hydrochar, hydrochar/coal blend, GreenCoal, pyrolysis, combustion, CO_2-gasification, pellets.

TABLE OF CONTENTS

ACKNOWLEDGEMENTS ..... **I**

ABSTRACT ..... **II**

CHAPTER 1 - INTRODUCTION **1**

1.1 Background **1**

1.2 Problem statement **6**

1.3 Aim and objectives **6**

1.4 Project scope **7**

CHAPTER 2 - LITERATURE STUDY **10**

2.1 Introduction **10**

2.2 The chemical and physical properties of sugarcane bagasse **10**

2.2.1 Proximate and elemental composition 11

2.2.2 Van Krevelen diagram 13

2.2.3 The energy content of lignocellulosic biomass 14

2.2.4 Mass and energy density 15

2.2.5 Grindability 16

2.3 Hydrothermal carbonisation and hydrothermal liquefaction: upgrading lignocellulosic biomass to hydrochar **16**

2.4 The effect of hydrothermal parameters on physicochemical properties of hydrochar **17**

2.4.1 Temperature 17

2.4.2 Residence time 20

2.4.3 Biomass-to-water ratio 21

2.5 HTL via continuous reactors 22

2.6 Densification 24

2.6.1 Strength and durability 24

2.7 Combustion behaviour 26

2.7.1 Combustion behaviour of lignocellulosic biomass against coal 26

2.7.2 Co-combustion of lignocellulosic biomass and coal 29

2.7.3 Combustion behaviour of hydrochar and hydrochar-coal blends against lignocellulosic biomass and coal 31

2.8 Gasification 34

2.8.1 Reactivity of Char-CO_2-gasification 35

2.8.2 The effect of pyrolytic conditions on char reactivity during CO_2 gasification 36

2.8.3 Reactivity and synergy of lignocellulosic biomass and coal during co-pyrolysis 37

2.8.4 Reactivity of lignocellulosic biochar and biochar-coal blends compared to coal during CO_2-gasification 38

2.8.4.1 Synergy during lignocellulosic biomass and coal co-gasification 41

2.8.5 Reactivity of hydrochar and hydrochar-coal char blends against lignocellulosic biomass and coal during CO_2 gasification 44

CHAPTER 3: EXPERIMENTAL SETUP 47

3.1 Introduction 47

3.2 Materials, origin and characterisation 47

3.2.1 Proximate and ultimate analysis 48

3.2.2 XRD and XRF analysis 49

3.2.3 Fibre analysis 50

3.2.4 Analysis of heating value 50

3.2.5 Fourier-transform Infrared Spectroscopy (FTIR) 50

3.2.6 Scanning electron microscopy (SEM) 51

3.3 Beneficiation of sugarcane bagasse via continuous hydrothermal liquefaction 51

3.4 Pelletizing 52

3.4.1 Mass and energy density 54

3.4.2 Equilibrium moisture content 54

3.4.3 Compression strength 54

3.4.4 Drop test: durability and impact resistance 55

3.4.5 Water-resistance capacity 55

3.5 Combustion behaviour of sugarcane bagasse, hydrochar and GreenCoal against coal 56

3.6 CO_2-gasification of sugarcane bagasse, hydrochar, GreenCoal, and coal 59

CHAPTER 4 RESULTS AND DISCUSSION 61

4.1 Introduction 61

4.2 Characterisation of sugarcane bagasse, GreenCoals, hydrochar, and coal 61

4.2.1 Proximate and ultimate analysis 61

4.2.2 FTIR results for sugarcane bagasse and hydrochar 65

4.2.3 SEM analysis of sugarcane bagasse, hydrochar, and coal 68

4.2.4 Mineralogy of sugarcane bagasse, hydrochar and coal 71

4.3 Densification: improving the logistics of renewable fuels 75

4.3.1 Mass and energy density 75

4.3.2 Hydrophobicity 77

4.3.3 Strength and durability 78

4.4 Pyrolysis of sugarcane bagasse, hydrochar, coal and GreenCoal pellets 82

4.5 Combustion behaviour of sugarcane bagasse-, hydrochar-, GreenCoal- and coal pellets 85

4.5.1 Combustion behaviour of sugarcane bagasse and coal 88

4.5.2 Combustion behaviour of hydrochar against sugarcane bagasse and coal..... 90

4.5.3 Combustion behaviour of GreenCoal against hydrochar and coal..... 92

4.5.4 Combustion calculations..... 99

4.6 CO_2 gasification behaviour of sugarcane bagasse, hydrochar, coal and GreenCoal pellets..... 101

4.6.1 Conversion and reactivity 101

4.6.2 Synergy 108

CHAPTER CONCLUSION AND RECOMMENDATIONS..... 113

5.1 Introduction 113

5.2 Conclusion..... 113

5.3 Recommendations..... 115

REFERENCES..... 117

ANNEXURES..... 138

Appendix A – Raw data..... 138

A.1. Proximate analysis and analysis of the heating value..... 138

A.2. Fibre analysis..... 140

A.3. EDS analysis of hydrochar 141

A.4. Pellet properties 141

A.5. Pyrolysis 149

A.6. Combustion 151

A.7. CO_2 gasification 160

Appendix B – Confidence interval and experimental error 161

Appendix C - Coal combustion mass balance and pollutant emissions 162

C.1. The air required for combustion and composition of flue gas 162

C.2. Ash burden 165

C.3. SOx and NOx 165

LIST OF TABLES

Table 2-1: Fibre analysis of sugarcane bagasse reported by previous authors 10

Table 2-2: Proximate composition (ad) of sugarcane bagasse and South African coal 11

Table 2-3: Ultimate composition (daf) of sugarcane bagasse and South African coal ... 13

Table 2-4: Mass -, bulk -, and energy density of various materials 15

Table 2-5: Ultimate composition (daf), higher heating value (HHV), and H/C-O/C atomic ratios of various biomasses and hydrochars 19

Table 2-6: The ignition -, peak -, burnout temperature, and maximum combustion rate of various lignocellulosic biomasses..... 27

Table 2-7: The ignition -, peak -, burnout temperature and maximum combustion rate of various lignocellulosic biomasses..... 29

Table 3-2: Compositional analysis performed by ARC-Irene Analytical Services Pty (Ltd) 50

Table 4-1: Proximate composition (ad), ultimate composition (daf) and higher heating value (HHV) of sugarcane bagasse (SB), hydrochar (HC), GreenCoal (GC3:1, GC1:1 and GC1:3) blends and Coal 63

Table 4-2: FTIR absorbance bands adapted from indicated authors 65

Table 4-3: XRD results: mineral content of sugarcane bagasse- (SB), hydrochar- (HC) and coal samples..... 71

Table 4-4: XRF results: elemental composition of sugarcane bagasse (SB), hydrochar (HC) and coal 72

Table 4-5: Mass- and energy density of sugarcane bagasse- (SB), hydrochar- (HC), GreenCoal- (GC3:1, GC1:1 and GC 1:3) and coal pellets 76

Table 4-6: Equilibrium moisture content (EMC) and water resistance capacity (WRC) of sugarcane bagasse- (SB), hydrochar- (HC), GreenCoal- (GC3:1, GC1:1 and GC 1:3) and coal pellets 77

Table 4-7: Impact resistance index (IRI) of sugarcane bagasse-, hydrochar-, GreenCoal-, and Coal pellets 80

Table 4-8: Pyrolysis characteristic parameters for samples heated at 10 °C/min 84

Table 4-9: Combustion characteristic parameter for samples..... 88

Table 4-10: The calculated amount of flue gas (mole and volume) and dust burden produced during combustion of sugarcane bagasse (SB), hydrochar (HC), GreenCoals (GC3:1, GC1:1 and GC1:3) and coal 100

Table 4-11: SO_2 and NO_x emissions of sugarcane bagasse (SB), hydrochar (HC), GreenCoals (GC3:1, GC1:1 and GC1:3) and coal..... 100

Table 4-12: Fixed carbon content and an ash content of charred pellets..... 105

Table 4-13: Compositional analysis of sugarcane bagasse-, hydrochar-, and coal ash, and calculated alkali index..... 112

Table A-1: Proximate composition for sugarcane bagasse,- hydrochar-, GreenCoal- (GC3:1, GC1:1 and GC1:3) and coal samples 138

Table A-2: Fibre analysis..... 140

Table A-3: Surface composition of hydrochar according to EDS analysis..... 141

Table A-4: Diameter, height, volume and mass density of sugarcane bagasse-, hydrochar-, GreenCoal- (GC3:1, GC1:1 and GC1:3), and coal pellets 141

Table A-5: Compression strength, durability and impact resistance index of sugarcane bagasse-, hydrochar-, GreenCoal- (GC3:1, GC1:1 and GC1:3), and coal pellets 144

Table A-6: Hydrophobicity: equilibrium moisture content (EMC) and water resistance capacity (WRC) of sugarcane bagasse-, hydrochar-, GreenCoal- (GC3:1, GC1:1 and GC1:3), and coal pellets 146

Table A-7: Conversion times and reactivities for CO_2 gasification of charred samples at 950°C, 1000°C, and 1050°C 160

Table B-1: Critical value for a 95% t-interval 161

LIST OF FIGURES

Figure 1-1: Project scope 9

Figure 2-1: Van Krevelen diagram based on data from Table 2-3 for South African coal (◆) and Sugarcane bagasse (●) 14

Figure 3-1: Experimental flow chart 47

Figure 3-2: PFD of the continuous HTL plant 52

Figure 3-3: Specac's Atlas Series Manual Hydraulic Press 53

Figure 3-4: Parts and assembly of 13 mm die 53

Figure 3-5: Thermogravimetric analyser setup 56

Figure 3-6: Approximation of ignition – and burnout temperature (example: TG curve of HC, dT/dt = 10 °C/min) 57

Figure 3-7: Thermogravimetric analyser setup 59

Figure 4-1: Van Krevelen diagram: Sugarcane bagasse, hydrochar and coal (Kambo & Dutta, 2014) 65

Figure 4-2: FTIR of sugarcane bagasse (—), hydrochar (—) 66

Figure 4-3: SEM images of (a) sugarcane bagasse, (b) hydrochar and (c) coal at 600 magnification 68

Figure 4-4: SEM images of a sugarcane bagasse particle at (a) 4000 magnification and (b) 20000 magnification 69

Figure 4-5: SEM images of a sugarcane bagasse particle at (a) 5000 magnification and (b) 20000 magnification 69

Figure 4-6: SEM images of a hydrochar particle at (a) 5000 magnification and (b) 20000 magnification 70

Figure 4-7: SEM images of a hydrochar particle at (a) 4000 magnification and (b) 20000 magnificationXRD and XRF analysis 71

Figure 4-8: Mass percentage retained by hydrochar- (100%), GC3:1- (75%), GC1:1- (50%), GC1:3- (25%) and Coal pellets (0%) after four drops 79

Figure 4-9: Compression strength of hydrochar- (100%), GC3:1- (75%), GC1:1- (50%), GC1:3- (25%) and coal pellets (0%) pellets in a horizontal orientation 80

Figure 4-10: TG (──) and DTG (**- - -**) curves of SB (■), HC (■), and coal (■) under inert conditions and a heating rate of 10 °C/min 82

Figure 4-11: TG curves of HC (──), GC3:1 (── ──), GC3:1 (─ ─ ─), GC3:1 (- - -), and coal (──) under inert conditions and a heating rate of 10 °C/min 82

Figure 4-12: DTG curves of HC (──), GC3:1 (── ──), GC3:1 (─ ─ ─), GC3:1 (- - -), and coal (──) under inert conditions and a heating rate of 10 °C/min 83

Figure 4-13: TG (■) and DTG (■) curves of sugarcane bagasse at a heating rate of 5 °C/min (─ ─), 7.5 °C/min (- - -), and 10 °C/min (──) 85

Figure 4-14: TG (■) and DTG (■) curves of hydrochar at a heating rate of 5 °C/min (─ ─), 7.5 °C/min (- - -), and 10 °C/min (──) 86

Figure 4-15: TG (■) and DTG (■) curves of GreenCoal 3:1 at a heating rate of 5 °C/min (─ ─), 7.5 °C/min (- - -), and 10 °C/min (──) 86

Figure 4-16: TG (■) and DTG (■) curves of GreenCoal 1:1 at a heating rate of 5 °C/min (─ ─), 7.5 °C/min (- - -), and 10 °C/min (──) 86

Figure 4-17: TG (■) and DTG (■) curves of GreenCoal 1:3 at a heating rate of 5 °C/min (─ ─), 7.5 °C/min (- - -), and 10 °C/min (──) 87

Figure 4-18: TG (■) and DTG (■) curves of coal at a heating rate of 5 °C/min (— —), 7.5 °C/min (- - -), and 10 °C/min (——)..... 87

Figure 4-19: The (a) ignition – and (b) burnout temperature as a function of the fraction hydrochar and the three heating rate: 5 °C/min (▲), 7.5 °C/min (♦) and 10 °C/min (■)..... 93

Figure 4-20: The ignition temperature as a function of the secondary hydrochar (example: TG curve of HC, dT/dt = 10 °C/min)..... 94

Figure 4-21: The ignition temperature as a function of the fraction hydrochar and the three heating rate: 5 °C/min (▲), 7.5 °C/min (♦) and 10 °C/min (■)..... 95

Figure 4-22: The (a) peak temperature and (b) maximum combustion rate as a function of the fraction hydrochar and the three heating rates: 5 °C/min (▲), 7.5 °C/min (♦) and 10 °C/min (■)..... 98

Figure 4-23: The (a) ignition index (C) and (b) comprehensive combustion index (S) as a function of the fraction hydrochar and the three heating rate: 5 °C/min (▲), 7.5 °C/min (♦) and 10 °C/min (■)..... 99

Figure 4-24: Conversion (X) of SB (——), HC (——), GC3:1 (—— ——), GC3:1 (— — —), GC3:1 (- - -), and coal (——) charred pellets at an isothermal temperature of 950°C..... 101

Figure 4-25: Reactivity (R) of SB (——), HC (——), GC3:1 (—— ——), GC3:1 (— — —), GC3:1 (- - -), and coal (——) charred pellets at an isothermal temperature of 950°C..... 102

Figure 4-26: Conversion (X) of SB (——), HC (——), GC3:1 (—— ——), GC3:1 (— — —), GC3:1 (- - -), and coal (——) charred pellets at an isothermal temperature of 1000°C..... 102

Figure 4-27: Reactivity (R) of SB (——), HC (——), GC3:1 (—— ——), GC3:1 (— — —), GC3:1 (- - -), and coal (——) charred pellets at an isothermal temperature of 1000°C..... 102

Figure 4-28: Conversion (X) of SB (──), HC (──), GC3:1 (── ──), GC3:1 (─ ─ ─), GC3:1 (- - -), and coal (──) charred pellets at an isothermal temperature of 1050°C 103

Figure 4-29: Reactivity (R) of SB (──), HC (──), GC3:1 (── ──), GC3:1 (─ ─ ─), GC3:1 (- - -), and coal (──) charred pellets at an isothermal temperature of 1050°C 103

Figure 4-30: The (a) conversion time ($t_{X=10\%}$) and (b) reactivity ($R_{X=10\%}$) at X=10% as a function of the fraction hydrochar and gasification temperature: 950°C (■), 1000°C (■), and 1050°C (■) 105

Figure 4-31: The (a) conversion time ($t_{X=50\%}$) and (b) reactivity ($R_{X=50\%}$) at X=50% as a function of the fraction hydrochar and gasification temperature: 950°C (■), 1000°C (■), and 1050°C (■) 106

Figure 4-32: The (a) conversion time ($t_{X=90\%}$) and (b) reactivity ($R_{X=90\%}$) at X=90% as a function of the fraction hydrochar and gasification temperature: 950°C (■), 1000°C (■), and 1050°C (■) 107

Figure 4-33: The experimental (■) and calculated (■) conversion curves of GC3:1 (── ──), GC3:1 (─ ─ ─), GC3:1 (- - -) chars at a gasification temperature of 950°C 108

Figure 4-34: The experimental (■) and calculated (■) conversion curves of GC3:1 (── ──), GC3:1 (─ ─ ─), GC3:1 (- - -) chars at a gasification temperature of 1000°C 109

Figure 4-35: The experimental (■) and calculated (■) conversion curves of GC3:1 (── ──), GC3:1 (─ ─ ─), GC3:1 (- - -) chars at a gasification temperature of 1050°C 109

Figure 4-36: The synergy index ($SI_{X=10\%}$) as a function of hydrochar's fraction and gasification temperature: 950°C (■), 1000°C (■), and 1050°C (■) 110

Figure 4-37: The synergy index ($SI_{X=50\%}$) as a function of hydrochar's fraction and gasification temperature: 950°C (■), 1000°C (■), and 1050°C (■) 110

Figure 4-38: The synergy index ($SI_{X=90\%}$) as a function of hydrochar's fraction and gasification temperature: 950°C (■), 1000°C (■), and 1050°C (■) 111

Figure A-1: EDS measurement of hydrochar surface..... 141

Figure A-2: The mass loss and mass loss rate of sugarcane bagasse during pyrolysis at a heating rate of 10 °C/min..... 149

Figure A-2: The mass loss and mass loss rate of hydrochar during pyrolysis at a heating rate of 10 °C/min 149

Figure A-2: The mass loss and mass loss rate of GreenCoal 3:1 during pyrolysis at a heating rate of 10 °C/min 150

Figure A-2: The mass loss and mass loss rate of GreenCoal 1:1 during pyrolysis at a heating rate of 10 °C/min 150

Figure A-2: The mass loss and mass loss rate of GreenCoal 1:3 during pyrolysis at a heating rate of 10 °C/min 151

Figure A-2: The mass loss and mass loss rate of coal during pyrolysis at a heating rate of 10 °C/min..... 151

Figure A-2: The mass loss and mass loss rate of sugarcane bagasse at 5 °C/min: (a) run 1 and (b) run 2..... 152

Figure A-3: The mass loss and rate of mass loss of hydrochar at 5 °C/min 152

Figure A-4: The mass loss and rate of mass loss of GreenCoal 3:1 at 5 °C/min..... 153

Figure A-5: The mass loss and rate of mass loss of GreenCoal 1:1 at 5 °C/min..... 153

Figure A-6: The mass loss and rate of mass loss of GreenCoal 1:3 at 5 °C/min..... 153

Figure A-7: The mass loss and rate of mass loss of coal at 5 °C/min: (a) run 1 and (b) run 2 154

Figure A-8: The mass loss and rate of mass loss of sugarcane bagasse at 7.5 °C/min: (a) run 1 and (b) run 2..... 154

Figure A-9: The mass loss and rate of mass loss of hydrochar at 7.5 °C/min: (a) run 1 and (b) run 2 155

Figure A-10: The mass loss and rate of mass loss of GreenCoal 3:1 at 7.5 °C/min 155

Figure A-11: The mass loss and rate of mass loss of GreenCoal 1:1 at 7.5 °C/min 155

Figure A-12: The mass loss and rate of mass loss of GreenCoal 1:3 at 7.5 °C/min 156

Figure A-13: The mass loss and rate of mass loss of Coal at 7.5 °C/min..... 156

Figure A-14: The mass loss and rate of mass loss of sugarcane bagasse at 10 °C/min: (a) run 1 and (b) run 2..... 157

Figure A-15: The mass loss and rate of mass loss of hydrochar at 10 °C/min: (a) run 1 and (b) run 2 158

Figure A-16: The mass loss and rate of mass loss of GreenCoal 3:1 at 10 °C/min 158

Figure A-17: The mass loss and rate of mass loss of GreenCoal 1:1 at 10 °C/min: (a) run 1 and (b) run 2 158

Figure A-18: The mass loss and rate of mass loss of GreenCoal 1:3 at 10 °C/min: (a) run 1 and (b) run 2 159

Figure A-19: The mass loss and rate of mass loss of coal at 10 °C/min: (a) run 1 and (b) run 2 159

CHAPTER 1 - INTRODUCTION

1.1 Background

The South African sugar industry is under financial pressure due to the ripple effect of the Health Promotion Levy (HPL), approved by Parliament under the Rates and Monetary Amounts and Revenue Laws Amendment Bill on the 5th of December 2017 and implemented on the 1st of April 2018, as well as neighbouring countries flooding the South African market with sugar (i.e. Swaziland) (SARS, 2017; SARS, 2018; SASA, 2019a). The latter causes the demand for locally produced sugar to decrease, forcing the South African sugar industry to sell to an already saturated international market at low prices. The sugarcane industry aims to create a plan towards sustainable development and diversification by exploring a bio-refinery concept, adding value to the entire sugarcane crop. The bio-refinery concept eludes to the integrated process that converts, fractionates/prepares, and separate, sugarcane to produce bio-chemicals, bio-materials, energy products, as well as the optimisation of existing processes, such as power generation (SMRI, 2019).

In South Africa, there are 14 sugar mills owned by six companies, namely Illovo Sugar Limited, Tongaat Sugar Ltd, RCL Foods, Sugar and Milling (Pty) Ltd, UCL Company Ltd, Gledhow Sugar Company (Pty) Ltd, and Umfolozi Sugar Mill (Pty) Ltd (SASA, 2019b). Operations associated with a sugar production of the first four companies mentioned above are to some extent, self-sufficient. The Illovo group's operations and the RCL sugar mills are, with regards to electricity consumption, 90% and 87% self-sustainable by using bagasse for co-generation, whereas Tongaat Sugar produces 52 MW via co-generation (Illovo Sugar, 2019a; RCL Foods, 2018; Tongaat Hulett Sugar, 2019). UCL uses wattle waste, i.e. spent bark, and bagasse to generate electricity for the wattle extraction and sugar factories (UCL, 2019). Concerning bio-based value-added products, the Illovo group is the only South African based company which produces a range of products, e.g. various sugars, molasses, lactulose, furfural and furfural derivatives, agricultural products, flavourings (i.e. diacetyl, 2,3-pentanedione and methanol) and alcohols (i.e. potable, anhydrous, rectified and industrial alcohol) (Illovo Sugar, 2019b). Subsequently, the South African sugar industry could benefit significantly from the bio-refinery concept and in doing so assist the South African Government achieving their goals set out in the National Development Plan (NDP) 2010 to 2030, as well as the government's commitments made towards the United

Nations Framework Convention on Climate Change (UNFCCC) as a voluntary signatory of the both the Kyoto Protocol and the Paris Agreement.

South Africa ratified the Kyoto Protocol and Paris Agreement in 2002 and 2016, respectively (Department of Energy, 2019; Department of Environmental Affairs, 2016). The Kyoto Protocol placed more emphasis on developed countries and their actions towards mitigation of climate change. Still, with the Paris Agreement, all parties ratifying the agreement were obligated to prepare an Intended Nationally Determined Contribution (INDC) to mitigate the effects of climate change in the context of sustainable development and elimination of poverty (UN, 2019). The main goal of the Paris Agreement is to keep the global average temperature increase to a maximum of 2°C above pre-industrial levels and pursuing efforts to limit the temperature increase to 1.5°C (UN, 2015). South Africa's environmental right set out in section 24 of the constitution, and the NDP was the foundation on which the INDC was built, emphasising the countries priority towards the elimination of poverty and reducing inequality, but also addressing the short-term challenges to transition to a low-carbon economy due to historical coal-based economy (CSIR, 2015; DEA South Africa, 2015). Nevertheless, with regards to GHG emissions, South Africa committed to a peak, plateau and decline (PPD) trajectory, of which the first will occur between 2021 to 2025, hereafter GHG emissions will plateau for a decade and then decline (DEA South Africa, 2015). These commitments are achievable via the 2011 National Climate Change Response Policy (DEA South Africa, 2011a), the National Strategy for Sustainable Development and Action Plan (NSSDAP) (DEA South Africa, 2011b), the Integrated Energy Plan (IEP) (DoE South Africa, 2015) and the Integrated Resource Plan (IRP) (DoE South Africa, 2018).

The Renewable Energy Independent Power Producer Procurement Programme (REIPPPP) was developed to meet the objectives set out by the NDP and IRP via private renewable energy projects (IPP Office, 2019). To date, 112 IPP's procured through seven Bid Windows have produced more than 6422 MW (IPP Office, 2019). Solar photovoltaic and onshore wind technology were the two main technologies that were procured during Bid Windows 1 to 4 on a mega-watt basis (IPP Office, 2019). Other technologies included and procured in the Bid Windows included concentrated solar power, small hydro, landfill gas, biomass and biogas (DoE South Africa, 2015; IPP Office, 2019). With one of the world's highest solar radiation areas found in South Africa and coastal and mountainous areas suitable for wind generation, the large investment into these technologies are logical (DoE South Africa, 2015); however, other renewable energy resources such as biomass remains largely untapped with only 52 MW procured during Bid Windows 3 and 4 and the first of the smaller Bid Windows (IPP Office, 2019).

Put into perspective, Tongaat has the potential to increase their current power production from 52 MW to 320 MW ─ 360 MW; however, concerning the bio-refinery concept, power generation is only one of many potential applications to valorise an entire crop.

Biomass is, by definition, any biological material that originates from living or recently living plants. Biomass is a source of carbon and is convertible to bioenergy (heat and power), biofuels, bio-chemical and materials via various thermochemical or biological processes, including, combustion-, gasification-, pyrolysis, hydrothermal treatment (carbonisation, liquefaction and gasification) and biological conversion (Xu *et al.*, 2018). These conversion technologies each have challenges with commercialisation; however, there are common barriers to overcome, such as a constant supply chain, logistics, costly transportation and storage. The supply chain relates to the type of biomass sourced and its availability, the geographical location of the supplier and consumer, and the infrastructure, which will also affect the cost of transportation (Mashoko *et al.*, 2013; Visser *et al.*, 2019). Transportation and storage are also largely affected by the inherent chemical-, and physical properties of the sourced biomass, e.g. agricultural waste has a very high moisture content, which would harm the economics of transportation by reducing the value of the feedstock (lower energy density) and increasing the fuel cost (higher bulk density) (Akhtari *et al.*, 2018; Baxter, 2005).

Pretreatment of biomass, i.e. drying and densification, solve certain issues associated with transportation, handling, and storage (i.e. briquetting); however, these methods have certain disadvantages or temporary solutions (Jackson *et al.*, 2016). Solar drying is a very cost-effective method to dry biomass but may be very time consuming depending on the geographical location and solar irradiation in the area. Conventional drying methods are more effective but are costly and energy-intensive (Kumar *et al.*, 2016). Alternatively, densification adds value to biomass per volume units by increasing the energy density and subsequently improves the economics of transportation; yet, the same difficulties arises over long storage periods, i.e. biodegradation. Furthermore, the strength and integrity of a briquette is a function of the moisture content, for example, the former corresponds to different optimum moisture content values for various biomasses, whereas the latter may result in the briquettes swelling if the moisture content is too high (Mostafa *et al.*, 2019; Zawiślak *et al.*, 2019). Therefore, densification improves certain qualities of biomass and add value, but may still require drying to a certain degree, which would impose additional processing costs.

Concerning heat and power generation, large-scale direct combustion of biomass relates to difficulties associated with the supply chain, storage capacity, handling, process efficiency (severe fouling, slagging and corrosion) and the overall economy of all operations (Malmgren & Riley, 2018). These problems are mainly associated with the inherent properties and chemical composition of biomass, e.g. the high moisture content, low fixed carbon content, high fraction volatile matter, ash composition (i.e. alkali and alkaline earth metals) and low energy density (Malmgren & Riley, 2018). Nevertheless, woody biomass has been used for decades to generate heat and power on a small-scale. Apart from woody biomass, the utilisation of other biomass sources has remained untouched due to unfavourable properties, i.e. a high moisture content that limits the co-firing fraction (Agbor *et al.*, 2014; Al-mansour & Zuwala, 2010).

Biomass gasification is an attractive alternative to direct combustion since it is possible to process biomass with a higher fraction moisture content. Various technology associative challenges oppose commercialization of biomass gasification for heat and power generation, e.g. process efficiency (boiler operation), inconsistent producer gas composition due to heterogeneous feedstock, impurities in the producer gas and expensive gas cleaning technologies (gas engines and gas turbines) (Sansaniwal *et al.*, 2017).

Pyrolysis of biomass is widely researched and entails the thermal degradation of biomass in the absence of oxygen (Hu & Gholizadeh, 2019). The main products produced via this process are char (solid), condensable gases (bio-oil) and non-condensable gases (Roddy & Manson-Whitton, 2012). Depending on the original feedstock and process conditions, i.e. temperature and heating rate, the product distribution and properties will vary. The biochar can be used as a co-firing agent and shows improved physical properties, chemical properties, and combustion behaviour in comparison with the raw feedstock (Li *et al.*, 2018; Xue *et al.*, 2018). The bio-oil can be used directly for diesel engines with other fuels, i.e. ethanol, or valorised to other transportation fuels and various chemicals (Choung *et al.*, 2018; Koike *et al.*, 2016; Prajitno *et al.*, 2016). The non-condensable gas is upgradable via a catalytic conversion process or utilised to produce power and heat (Görling *et al.*, 2013). Though pyrolysis demonstrates potential, it is best suited for dry biomass, since the processing of wet biomass is more energy-intensive (Shemfe *et al.*, 2015).

The treatment of biomass (carbon-based material) in hot compressed water, known as hydrothermal treatment, has gained more attention as a pretreatment method of wet biomass since it eliminates the need for a pre-drying step. Moreover, in comparison to pyrolysis, it produces higher quality products at lower temperatures (Nakason *et al.*, 2018). Classification of

hydrothermal treatment as hydrothermal carbonisation, hydrothermal liquefaction, and hydrothermal gasification, is done according to the operating conditions (temperature), inherent reactions, and product distribution. The hydrothermal treatment of biomass produces four products, i.e. hydrochar, bio-oil, non-condensable gas (containing H_2, CO and CO_2), and an aqueous phase. The yield distribution is primarily a function of the temperature, but also the biomass-to-water ratio and residence time (Nakason *et al.*, 2018).

Hydrothermal processing at low temperatures produces predominantly a solid product referred to as hydrochar (Volpe *et al.*, 2018; Zhang *et al.*, 2018). The aqueous phase contains the second largest fraction of the carbon and the gas phase the least. The former contains various organic molecules, such as formic acid, acetic acid, levulinic acid, furfural, and 5-hydroxymethyl furfural. These molecules are platform molecules for other high-value chemicals, e.g. formic acid is a preservative and antibacterial agent for live feedstock, whereas levulinic acid, furfural, and 5-hydroxymethyl furfural are reagents for renewable diesel or jet fuel via catalytic conversion routes (Ma *et al.*, 2019). Alternatively, the aqueous phase can be utilised as a feed for microalgae and potentially create a closed-loop microalgae system or recycled to create a carbon-rich feed for the HTL reactor (Leng *et al.*, 2018). With regards to the feedstock, the hydrochar has a higher carbon density, energy density and superior physical qualities, i.e. improved grindability and more hydrophobic nature (Volpe *et al.*, 2018; Zhang *et al.*, 2018). The hydrochar also demonstrated improved combustion properties and higher reactivity during combustion and CO_2-gasification, making it an attractive supplement or substitute for fossil fuels (Ul *et al.*, 2018; Yang *et al.*, 2016).

Currently, most of the sugar mills are to some extent self-sustaining, using the sugarcane bagasse waste as fuel to generate heat and power.

Upgrading lignocellulosic biomass to hydrochar as a fuel substitute or co-combustion agent, would increase the process efficiency and mitigate the CO_2 emissions and other GHG emissions (i.e. SO_2). A patent on GreenCoal® (Waanders *et al.*, 2018) has shown the potential of using waste biomass with a high lignin content to produce biochar and discarded coal briquettes. This application could exploit large reserves of discarded coal and potentially reduce the cost by eliminating the need for binders and wax layers since hydrochar is a natural binder and has hydrophobic properties.

1.2 Problem statement

In light of current challenges such as a saturated national and international market, the tax on sugary beverages a result of the Health Promotion Levy (National Treasury, 2018), and climate change, the sugar industry is under pressure to add value to the entire crop via the bio-refinery concept. Sugar mills in South Africa are to some extent self-sufficient by utilising sugarcane bagasse directly as a co-firing agent with coal to generate heat and power. Direct combustion of bagasse gives rise to low efficiencies and various technical challenges associated with the chemical and physical properties of sugarcane bagasse, i.e. corrosion and fouling due to high concentrations of alkali and alkaline earth metals (AAEM). Alternatively, hydrothermal liquefaction of wet sugarcane bagasse produces hydrochar and a carbon-rich aqueous phase of which the former has improved properties, i.e. lower AAEM and higher energy density. Hydrohcar could potentially be used as a fuel for co-firing or co-gasification due to improved properties.

1.3 Aim and objectives

The project aims to determine the efficiency of GreenCoal pellets, prepared from coal and hydrochar derived from sugarcane bagasse for combustion and gasification applications. The following objectives were defined:

- Evaluate continuous hydrothermal liquefaction of sugarcane bagasse as a pre-treatment method by comparing the chemical and physical properties of hydrochar with sugarcane bagasse and coal.
- Compare the stability and strength of GreenCoal pellets with sugarcane bagasse, hydrochar and coal pellets.
- Compare the combustion properties of GreenCoal pellets for heat and power generation with hydrochar, sugarcane bagasse or coal pellets.
- Compare the gasification reactivity and synergy of GreenCoal pellets during CO_2-gasification.
- Determine any reduction in particulate matter, sulphur and nitrogen emissions as a result of using GreenCoal pellets to replace coal or sugarcane bagasse pellets as an energy source on sugar mills.

1.4 Project scope

Figure 1-1 demonstrates the basic project scope of this investigation. This report includes five chapters, including this one, that consists of the following content, to achieve the objectives as mentioned above:

Chapter 1 is the introduction that gives a brief background on the current coal-derived economy of South Africa, motivating why research and investment into a renewable resource to supplement or substitute coal are essential and how this is interlinked to research into beneficiation of renewable energy resources via continuous hydrothermal treatment. Chapter 2 is a summary of

the literature study completed about related topics that aided the researcher to lay the foundation of this study. Lignocellulosic biomass as a fuel to generate heat and power, including obstacles hindering commercial. A brief overview of potential pretreatment methods is discussed, motivating why this study uses hydrothermal liquefaction above other methods. Research completed on continuous hydrothermal liquefaction is scarce, which is why the research will be based on batch processes. Nevertheless, a discussion will be given on continuous processes. Chapter 3 presents the experimental setup used to achieve the objectives, including the materials and characterisation, experimental setup and analytical methods. The results and discussion thereof will be conferred in Chapter 4. Lastly, the main conclusions, outlook and recommendations towards future research are presented in Chapter 5.

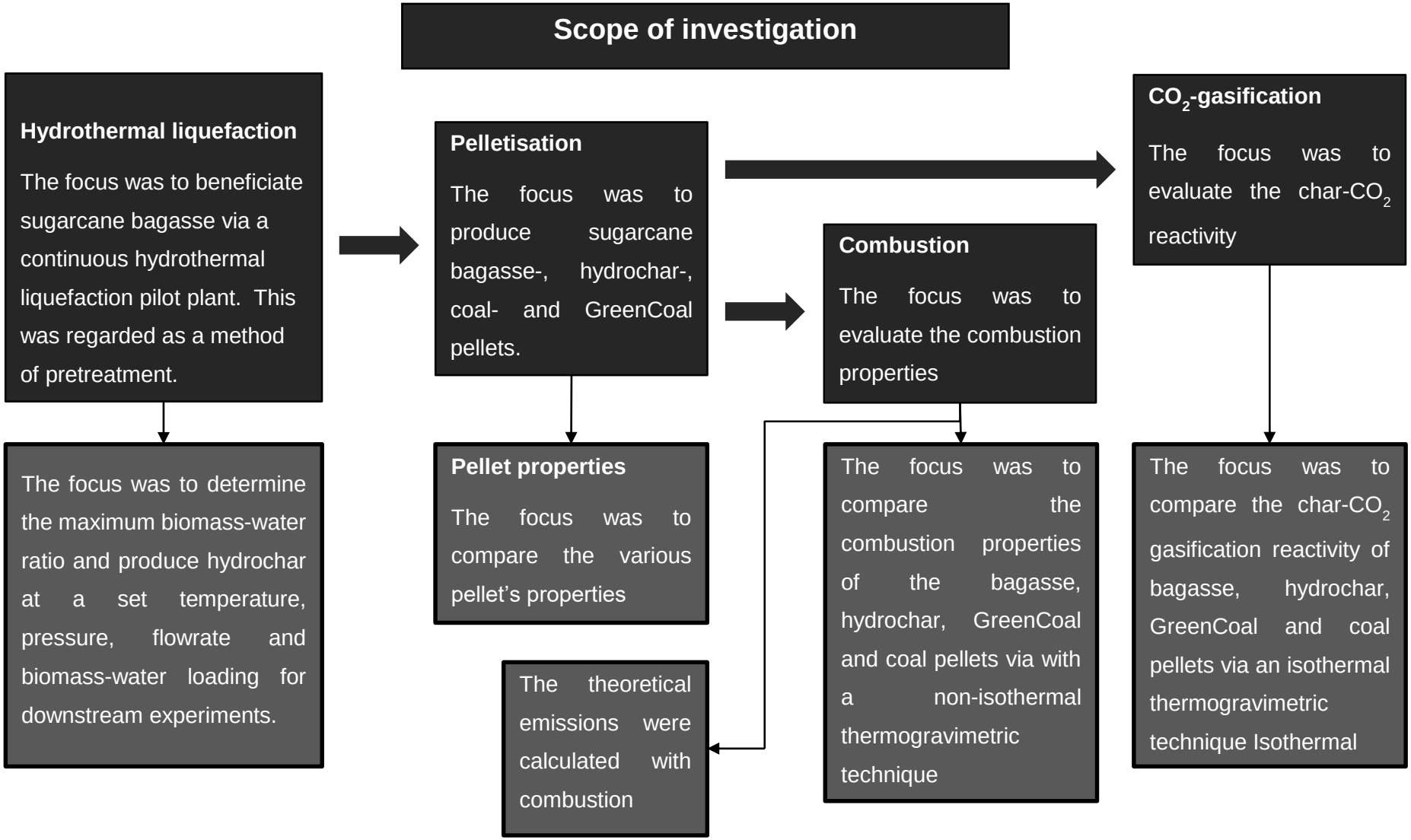
Scope of investigation
Hydrothermal liquefaction
The focus was to beneficiate sugarcane bagasse via a continuous hydrothermal liquefaction pilot plant. This was regarded as a method of pretreatment.
The focus was to determine the maximum biomass-water ratio and produce hydrochar at a set temperature, pressure, flowrate and biomass-water loading for downstream experiments.
Pelletisation
The focus was to produce sugarcane bagasse-, hydrochar-, coal- and GreenCoal pellets.
Pellet properties
The focus was to compare the various pellet's properties
The theoretical emissions were calculated with combustion
Combustion
The focus was to evaluate the combustion properties
The focus was to compare the combustion properties of the bagasse, hydrochar, GreenCoal and coal pellets via with a non-isothermal thermogravimetric technique
CO2-gasification
The focus was to evaluate the char-CO2 reactivity
The focus was to compare the char-CO2 gasification reactivity of bagasse, hydrochar, GreenCoal and coal pellets via an isothermal thermogravimetric technique Isothermal

Figure 1-1: Project scope

CHAPTER 2 - LITERATURE STUDY

2.1 Introduction

This chapter contains a summary of relevant literature, terminologies and data that was used to lay the foundation of this investigation. This chapter contains five main subsections representing the main topics of this dissertation.

Section 2.2 focuses on sugarcane bagasse as a renewable energy resource and discusses the benefits and drawbacks associated with the physical and chemical properties by comparing it with various South African coal sources. Section 2.3, 2.4 and 2.5 focus on the application of hydrothermal liquefaction to upgrade lignocellulosic biomass, the effect of the main process parameters on the yield, properties of hydrochar, as well as progress made with regards to continuous operation. Section 2.6 discusses densification (i.e. pellets or briquettes) and the benefits associated with it. Finally, Section 2.7 and 2.8 discuss combustion and CO_2-char gasification.

2.2 The chemical and physical properties of sugarcane bagasse

The main components of the structure of lignocellulosic biomass are cellulose, hemicellulose and lignin (Marriott *et al.*, 2016). Cellulose and hemicellulose are complex carbohydrate polymers composed out of sugar monomers (mainly glucose and xylose), whereas lignin is composed of aromatic polymers (Sekar *et al.*, 2016). Table 2-1 reports the fibrous content of sugarcane bagasse as reported by indicated authors. Based on the reported data of these authors, cellulose is the main constituent of sugarcane bagasse (42.2% ─ 47.4%) while hemicellulose and lignin have similar compositional values, ranging from 16.3% ─ 27.1% and 20.9% ─ 27.1%, respectively.

Table 2-1: Fibre analysis of sugarcane bagasse reported by previous authors

Cellulose	Hemicellulose	Lignin	Reference
46.9	16.3	27.1	(Moretti *et al.*, 2014)
47.4	25.1	23.4	(Miléo *et al.*, 2016)
46.6	26.5	21.7	(Camargo *et al.*, 2016)

Table 2-1: Fibre analysis of sugarcane bagasse reported by previous authors

Cellulose	Hemicellulose	Lignin	Reference
44.3	27.1	20.9	(Gonçalves *et al.*, 2014)
42.2	26.7	22.6	(Rocha *et al.*, 2015)[a]

2.2.1 Proximate and elemental composition

In general, the fractional distribution of dried biomass in descending order is the volatile matter, fixed carbon and ash (Vassilev *et al.*, 2015).

Table 2-2 reports the proximate analysis of sugarcane bagasse samples originating from different geographical sites, including South Africa (Carrier *et al.*, 2012), Sudan (Edreis *et al.*, 2014), and Iran (Lu & Chen, 2015). The moisture, volatile matter, fixed carbon and ash content ranged from 2.8% ─ 8.1%, 73.7% ─ 76.9%, 10.9% ─ 12.1%, and 4.3% ─ 11.4%, respectively.

Table 2-2: Proximate composition (ad) of sugarcane bagasse and South African coal

Material	Inherent moisture (%)	VM (%)	FC (%)	Ash (%)	Reference
Sugarcane bagasse					
South Africa	8.1	75.8	10.9	5.1	(Carrier *et al.*, 2012)
Sudan	7.3	76.9	11.3	4.3	(Edreis *et al.*, 2014)
Taiwan	2.8	73.7	12.1	11.4	(Lu & Chen, 2015)
South African coal					
Highveld No. 5 Seam		32.0		19.0	(Jeffrey, 2005)
Limpopo (Tuli, washed)		35.5 ─ 36.5		10.0 ─ 12.0	(Jeffrey, 2005)
Molteno-Indwe (washed)	7.0 ─ 11.0	7.0 ─ 12.0		26.0 ─ 27.0	(Jeffrey, 2005)
Fine coal discard	4.0	24.4	42.2	29.4	(Bunt *et al.*, 2015)
Bituminous coal	-	24.9	52.5	22.6	(Leeuw *et al.*, 2016)
Highveld coalfields	4.0	21.5	48.6	25.9	(Okolo *et al.*, 2015)

Table 2-2: Proximate composition (ad) of sugarcane bagasse and South African coal

Material	Inherent moisture (%)	VM (%)	FC (%)	Ash (%)	Reference
Highfield coalfields	2.7	22.4	50.4	24.5	(Okolo *et al.*, 2015)
Witbank	3.3	26.6	48.1	22.0	(Okolo *et al.*, 2015)
Tshipise-Pafuri	0.7	22.0	60.5	16.8	(Okolo *et al.*, 2015)

Volatile matter in biomass is associated with cellular structures and include radical groups such as ─OH, ─CH_2, ─CH_3 and ═CH. Moreover, the main constituents of biomass, i.e. cellulose, hemicellulose and lignin, has a low degree of order (Wang *et al.*, 2016). The fixed carbon content of biomass has a high correlation to the lignin content, as demonstrated by Demirbas (2003a). In comparison with South African coal, sugarcane bagasse has a higher fraction of volatile matter and lower fixed carbon content. In comparison sugarcane bagasse has a lower ash fraction than the cited coal samples, which is considered an advantage since ash reduces the higher heating value; however, biomass amplifies other problems due to the composition (Imran & Khan, 2018). Imran & Khan (2018) and Rodríguez-díaz *et al.* (2015) reported the composition of various bagasse ash samples using a scanning electron microscope (SEM) and X-ray diffraction (XRD). The main oxide in bagasse ash was SiO_2, but also contained CaO, Al_2O_3, Fe_2O_3, Fe_3O_4 and K_2O (Imran & Khan, 2018; Rodríguez-díaz *et al.*, 2015). SEM analysis of bagasse ash samples showed that composition is a function of time. Elements present in these samples after one hour of thermal treatment at 1100°C in descending order were Si, K, O, Fe, P, C, Cl, S, Al, Mg and Na (Imran & Khan, 2018).

In general, biomass has a high carbon and oxygen content, fair amounts of hydrogen and nitrogen, and very low sulphur content. Saidur *et al.* (2011:2262–2289) reported the elemental content of various biomass sources from previous authors with ranges of 40% ─ 60%, 30% ─ 50%, 3% ─ 10% for carbon, oxygen and hydrogen, respectively. Vassilev *et al.* (2015:330–350) reported ranges between 42.2% ─ 60.5%, 20.8% ─ 49.0%, 3.2% ─ 10.2%, 0.1% ─ 12.3% and 0.01% ─ 1.69% for carbon, oxygen, hydrogen, nitrogen and sulphur, respectively. Table 2-3 reports the ultimate analysis (or elemental analysis) of five sugarcane bagasse samples. The carbon, hydrogen, oxygen, nitrogen and sulphur content of the cited sugarcane bagasse samples ranged from 41.2% ─ 58.1%, 5.5% ─ 6.5%, 34.6% ─ 52.9%, 0.1% ─ 1.0%, and 0% ─ 0.2%, respectively (Carrier *et al.*, 2012; Chen *et al.*, 2012; Edreis *et al.*, 2014; Tavasoli *et al.*, 2015; Varma & Mondal, 2016). The elemental composition is related to the

main organic components of bagasse, i.e. cellulose, hemicellulose and lignin, which are hydrocarbons with various oxygen functional groups, i.e. hydroxyl, carboxyl, ether and ketone functional groups.

Table 2-3: Ultimate composition (daf) of sugarcane bagasse and South African coal

Location	C (%)	H (%)	N (%)	O (%)	S (%)	HHV (MJ/kg)	Reference
Sugarcane							
South Africa	51.9	6.9	0.4	40.5	0.5	16.6	(Aboyade *et al.*, 2013)
Taiwan	41.2	5.5	0.4	52.9	0.0	17.1	(Chen *et al.*, 2012)
Iran	58.1	6.5	0.7	34.6	0.2	-	(Tavasoli *et al.*, 2015)
Sudan	47.0	6.1	0.1	46.8	0.1	17.8[a]	(Edreis *et al.*, 2014)
India	44.9	5.9	0.2	49.0	0.1	18.0	(Varma & Mondal, 2016)
South African coal							
Highveld	77.1	4.2	2.1	15.3	1.3	28.7[a]	(Leeuw *et al.*, 2016)
Highveld Seam 4	85.6	3.6	1.7	7.9	1.2	20.2	(Bunt *et al.*, 2015)
Highveld	78.7	4.4	2.2	13.0	1.7	-	(Okolo *et al.*, 2015)
Witbank	78.5	4.9	2.0	13.2	1.4	-	(Okolo *et al.*, 2015)
Tshipise-Pafuri	86.9	5.1	2.1	4.8	1.0	-	(Okolo *et al.*, 2015)

[a] Calculated with HHV correlation (Channiwala & Parikh, 2002)

2.2.2 Van Krevelen diagram

The carbon, hydrogen and oxygen elemental fractions, as determined with the ultimate analysis and calculated on a dry-ash-free basis, is used to create a visual presentation known as the Van Krevelen diagram. The Van Krevelen diagram plots the O/C and H/C atomic ratios to generate a visual comparison between carbonaceous fuels (Kambo & Dutta, 2014; Liu *et al.*, 2013). The O/C and H/C atomic ratios are calculated with

$$O/C = 0.75 \times \frac{O_{daf}}{C_{daf}} \qquad \text{(Eqn. 2-1)}$$

and

$$H/C = 12 \times \frac{H_{daf}}{C_{daf}}, \qquad \text{(Eqn. 2-2)}$$

respectively (Van Krevelen, 1950).

Figure 2-1 is a Van Krevelen diagram based on the data reported in Table 2-3. Fuel with a low O/C-H/C atomic ratio is typically associated with a decrease in smoke, water vapour and energy losses during combustion; hence, coal (see Figure 2-1) is considered favourable in comparison with sugarcane bagasse (Kambo & Dutta, 2014). The high H/C and O/C atomic ratios of sugarcane bagasse (and biomass in general) were associated with the hydrocarbon nature of biomass and high density oxygenated functional groups. High H/C atomic ratios are also common for biomass due to the low energy H─C bonds and inherent moisture content (Liu *et al.*, 2013).

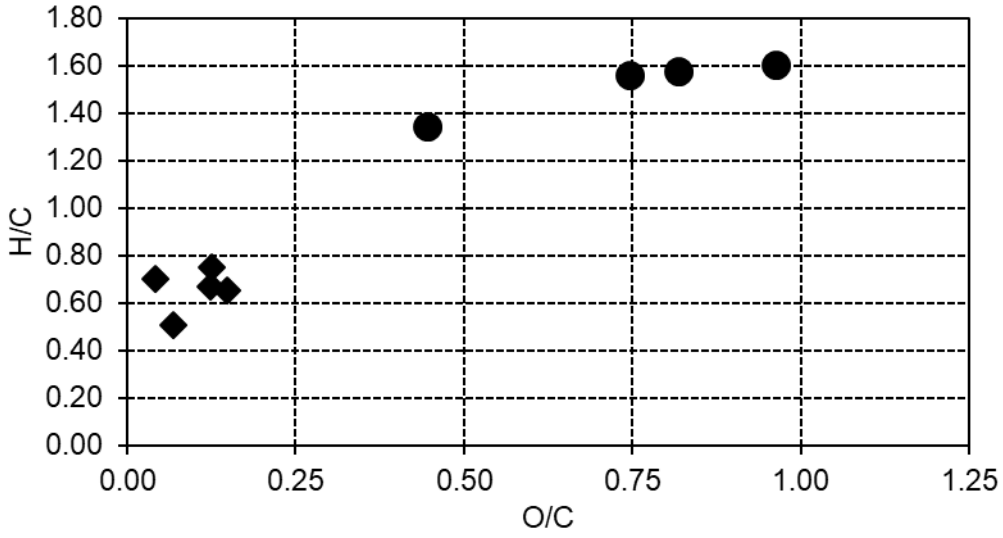

Figure 2-1: Van Krevelen diagram based on data from Table 2-3 for South African coal (◆) and Sugarcane bagasse (●)

2.2.3 The energy content of lignocellulosic biomass

The higher heating value (HHV) or calorific value represents the energy content of a given substance and is a function of composition as seen by the various correlations found in the literature (Channiwala & Parikh, 2002; Demirbas, 2001; Friedl *et al.*, 2005; Tan *et al.*, 2015). Sugarcane bagasse sourced in South Africa (Aboyade *et al.*, 2013), Taiwan (Chen *et al.*, 2012), Sudan (Edreis *et al.*, 2014) and India (Varma & Mondal, 2016) had HHV of 16.6 MJ/kg, 17.1 MJ/kg, 17.8 MJ/kg, and 18.0 MJ/kg, respectively (see Table 2-3). As for South African coal, the HHV varies depending on the origin and may range from 18 MJ/kg ─ 27 MJ/kg (Jeffrey, 2005).

The Highveld coals in Table 2-3 had an HHV of 20.2 MJ/kg (Bunt *et al.*, 2015) and 28.7 MJ/kg (Leeuw *et al.*, 2016). The main chemical properties of materials that had a negative influence on the HHV were low carbon-, high oxygen-, high ash-, and high moisture content. Carbon in coal is mainly associated with high energy carbon-carbon bonds, whereas biomass is associated with weak C─H and C─O bonds with smaller energy potential.

2.2.4 Mass and energy density

The mass density relates to a single particle and bulk density to the mass of particles occupying a volume, including the voids between particles. The bulk density is important when taking the economics of transportation and storage of solid fuel into account (Kambo & Dutta, 2014). Table 2-4 reports the mass- (or bulk-) and energy density of various lignocellulosic biomass sources and a coal sample as reported by the indicated authors. The calculated energy densities were the product of the mass/bulk density and the HHV. One major drawback of lignocellulosic biomass is the low bulk density, and consequently, a low energy density. Bach & Skreiberg (2016) reported the mass density of biomass within the range of 250 kg/m^3 ─ 954 kg/m^3. As seen in Table 2-4, lignocellulosic biomass is considerably less dense than coal and together with the low HHV, these two characteristic properties result in a very low energy density. The two sugarcane bagasse samples used by Munir *et al.* (2009) had an energy density 13 times smaller than the coal sample reported by Demirbas (2003).

Table 2-4: Mass -, bulk -, and energy density of various materials

Material	Mass density (kg/m^3)	Energy density (GJ/m^3)	Reference
Palm kernel cake	623.0[a]	11.6	(Razuan *et al.*, 2011)
Miscanthus	321.1[b]	5.9	(Kambo & Dutta, 2014)
Cotton stalk	310.0[c]	5.4	(Munir *et al.*, 2009)
Sugarcane bagasse	140[c]	2.5	(Munir *et al.*, 2009)
Sugarcane bagasse	160[c]	2.5	(Munir *et al.*, 2009)
Shea meal	490[c]	9.7	(Munir *et al.*, 2009)
Coal	1300[a]	32.5	(Demirbas, 2003b)

a – bulk density, b – dried, c – as received.

2.2.5 Grindability

The particle size distribution in thermal systems, i.e. pulverised fuel boilers and gasifiers, play a significant role regarding process parameters, i.e. combustion efficiency, carbon conversion, NO_x reduction and syngas composition. Producing a homogeneous feed with a normalised particle size distribution is important and is dependent on factors such as the grindability (Gil *et al.*, 2015; Wang, Barta-rajnai, *et al.*, 2018).

Since different lignocellulosic biomass has a varying chemical composition, it would require pretreatment methods such as shredding, grinding and milling to produce a homogeneous mixture; however, the polymeric fibrous nature of lignocellulosic biomass reduces the grindability thereof and makes it an energy-intensive process (Gil *et al.*, 2015; Wang, Barta-rajnai, *et al.*, 2018).

2.3 Hydrothermal carbonisation and hydrothermal liquefaction: upgrading lignocellulosic biomass to hydrochar

Hydrothermal carbonisation and hydrothermal liquefaction are conversion processes which take place in hot compressed water. Depending on the temperature, different reactions occur during hydrothermal treatment, influencing the product distribution and are classified accordingly. Hydrothermal carbonisation occurs at temperatures below 250°C and is in general associated with higher hydrochar yield and smaller quantities of bio-oil and syngas (Cha *et al.*, 2016; Elliott *et al.*, 2015; Román *et al.*, 2012; Xiao *et al.*, 2012). At higher temperatures, the solvolytic breakdown of biomass is promoted and shifts the carbon distribution to the aqueous phase and bio-oil (Jena & Das, 2011). Previous authors reported liquefaction temperatures between 250°C – 400°C and high pressures ranging from 5 MPa – 20 MPa, depending on the solvent used (Cha *et al.*, 2016; Chan *et al.*, 2014; Elliott *et al.*, 2015; Jena & Das, 2011). Further increase in temperature (>400°C) will result in hydrothermal gasification of biomass, producing syngas (CO, CO_2 CH_4, and H_2) as the main product (Cha *et al.*, 2016; Elliott *et al.*, 2015; Kruse, 2009).

During hydrothermal treatment, water acts as an acid/base catalyst precursor due to increased ionic product formation. The degree of ionisation is a function of the temperature since dissociation of water into H_3O^+ and OH^- is an endothermic process. Properties of water such as the ionic products and dielectric constant, both a function of temperature and pressure, influence the reaction rates of chemical reactions and it is possible to control the nature of products by

manipulating the properties of water during hydrothermal treatment. The relative dielectric constant of hot compressed water under critical conditions improves the solubility of organic components (Holzapfel, 1969; Kruse & Dinjus, 2007; Marshall & Franck, 1983).

The high ionisation constant of hot compressed water also facilitates hydrolysis reactions and fragmentation of lignocellulosic biomass resulting in deoxygenation and densification of the feed. During hydrothermal carbonisation, the formation of organic acids lowers the pH of the water phase, which then further catalyse reactions like hydrolysis and the decomposition of oligomers and monomers to smaller fragments (Jain *et al.*, 2016). Depending on the process conditions during hydrothermal carbonisation, a variety of products and yields are possible. Hydrothermal carbonisation at low temperatures (160°C ─ 250°C) is a proven process to produce hydrochar: a solid product with improved fuel characteristics in comparison with raw biomass (Kambo & Dutta, 2014; Liu *et al.*, 2013).

2.4 The effect of hydrothermal parameters on physicochemical properties of hydrochar

The three main hydrothermal variables that affect the physicochemical properties of hydrochar and product distribution are temperature, residence time and biomass-to-water ratio.

2.4.1 Temperature

Hydrochar yield is greatly affected by the hydrothermal temperature and demonstrates a rapid decrease in solid yield with increasing temperature, which transitions to less intense effect under hydrothermal liquefaction conditions (Liu *et al.*, 2013). Liu *et al.* (2013) investigated the hydrochar yield during hydrothermal carbonisation of coconut fibre and eucalyptus leaves, as a function of temperature, for constant residence time and biomass/water ratio (30 min and 10% respectively). The solid yield decreased sharply with ±47% between 150°C ─ 250°C and transitioned to a gradual decrease of 9% ─ 14% between 250°C ─ 360°C. Hydrothermal carbonisation of a mixed wood feedstock demonstrated similar results to Liu *et al.* (2013), a rapid reduction of 18.8% in solid yield from 215°C ─ 255°C with a negligible decrease at higher temperatures of 255°C ─ 295°C (Kent Hoekman, S.; Broch, A.; Robbins, 2011). Hydrothermal treatment of eucalyptus bark at 220°C for two hours had a solid yield of 46.4%, which decreased gradually to 40.0% at 300°C.

The rapid mass loss rate at low temperatures coincides with the effect of hydrothermal treatment on the volatile content. Hydrothermal treatment of eucalyptus bark (Gao, Zhou, *et al.*, 2016), coconut husk (Nakason *et al.*, 2018), rice husk (Nakason *et al.*, 2018), and paper mill sludge (Sermyagina *et al.*, 2015) at corresponding temperature ranges of 220°C ─ 300°C, 140°C ─ 200°C, 140°C ─ 200°C, and 180°C ─ 250°C, showed a decrease in volatile content of 9.4% ─ 20.5%, 2.0% ─ 7.8%, 4.1% ─ 12.0%, and 9.7% ─ 37.4%, respectively. Furthermore, the volatile fraction of biomass corresponds with the hemicellulose and cellulose content (Acharjee *et al.*, 2011; Gao, Zhou, *et al.*, 2016; Liu *et al.*, 2013; Nakason *et al.*, 2018). Acharjee *et al.* (2011) showed that most of the hemicellulose was removed from the hydrochar produced from loblolly pine at 200°C and completely removed at 230°C. Similarly, nearly all of the hemicellulose and cellulose in hydrochar produced from coconut fibre and eucalyptus leaves was decomposed at 250°C (Liu *et al.*, 2013). Thermal degradation at low temperatures is associated with the dehydration and decarboxylation reactions and was confirmed with diminishing hydroxyl and carboxyl groups as demonstrated with FTIR (Gao, Zhou, *et al.*, 2016)

Gao, Zhou, *et al.* (2016) linked the increased fixed carbon content to the removal of volatile matter. The fixed carbon content increased, which is highly favourable since carbon contributes to the energy density. The fixed carbon content of the hydrochar derived from the biomass feedstock mentioned above increased with 10.3% ─ 18.2%,4.8% ─ 10.9%, 2.4% ─ 8.6%, and 17.0% ─ 43.0%. The general observation with regards to the moisture and ash content of the hydrochar is that both these fractions are smaller compared to the raw samples; however, the ash fraction may decrease or increase as a function of temperature (Gao, Zhou, *et al.*, 2016; Nakason *et al.*, 2018; Sermyagina *et al.*, 2015). The decrease may relate to a portion of the ash content that dissolved in the aqueous phase (Gao, Zhou, *et al.*, 2016; Nakason *et al.*, 2018). The increase may be due to: (i) an overall fractional increase since cellular structure decomposed, (ii) or the precipitation/reabsorption of mineral content (Gao, Zhou, *et al.*, 2016; Nakason *et al.*, 2018).

Table 2-5: Ultimate composition (daf), higher heating value (HHV), and H/C-O/C atomic ratios of various biomasses and hydrochars

Sample	T range (°C)	C (%)	H (%)	O (%)	N (%)	S (%)	HHV (MJ/kg)	H/C	O/C	Reference
Miscanthus	-	47.6	6.1	46.1	0.2	0.0	18.5	1.54	0.73	(Kambo & Dutta, 2014)
Hydrochar	190 ─ 260	48.9 ─ 62.1	6.0 ─ 5.4	32.1 ─ 44.8	0.2 ─ 0.4	0.0	20.2 ─ 25.9	1.04 ─ 1.48	0.39 ─ 0.69	
Eucalyptus bark	-	45.2	6.4	48.4	-	-	18.5	1.69	0.80	(Gao, Zhou, *et al.*, 2016)
Hydrochar	220 ─ 300	49.5 ─ 72.7	5.6 ─ 5.1	22.2 ─ 44.9	-	-	20.2 ─ 29.2	0.83 ─ 1.36	0.23 ─ 0.68	
Coconut fibre	-	47.8	5.6	45.5	0.9	0.2	18.4	1.41	0.71	(Liu *et al.*, 2013)
Hydrochar	200 ─ 300	62.5 ─ 73.2	5.1 ─ 5.3	20.2 ─ 31.1	0.9 ─ 1.1	0.3 ─ 0.4	24.7 ─ 29.4	0.83 ─ 1.01	0.21 ─ 0.37	
Eucalyptus leaves	-	47.0	6.2	44.8	1.2	0.8	18.9	1.59	0.72	(Liu *et al.*, 2013)
Hydrochar	200 ─ 300	61.1 ─ 68.9	6.0 ─ 6.1	22.8 ─ 30.7	1.4 ─ 1.6	0.4 ─ 0.7	25.3 ─ 28.7	1.05 ─ 1.20	0.25 ─ 0.38	
Coconut husk	-	50.1	5.8	43.6	0.4	0.1	19.1	1.39	0.65	(Nakason *et al.*, 2018)
Hydrochar	140 ─ 200	51.6 ─ 59.5	5.7 ─ 6.0	34.2 ─ 41.8	0.5	0.1	20.7 ─ 23.9	1.15 ─ 1.41	0.43 ─ 0.61	
Rise husk	-	47.3	6.7	45.1	0.7	0.1	15.6	1.70	0.72	(Nakason *et al.*, 2018)
Hydrochar	140 ─ 200	48.1 ─ 56.8	6.4 ─ 6.8	35.8 ─ 44.8	0.6 ─ 0.8	0.1	16.1 ─ 18.2	1.38 ─ 1.61	0.47 ─ 0.70	

Regarding the elemental composition of raw biomass material, the carbon and nitrogen content of hydrochar increased, whereas the oxygen and hydrogen content decreased with increasing temperature. Sulphur content is, in most cases, negligible (Gao, Zhou, *et al.*, 2016; Kambo & Dutta, 2014; Liu *et al.*, 2013). The degree to which the composition of each element changes depends strongly on the type of biomass material and temperature. The carbon, hydrogen and oxygen content of miscanthus (Kambo & Dutta, 2014), eucalyptus bark (Gao, Zhou, *et al.*, 2016), coconut fibre, and eucalyptus leaves (Liu *et al.*, 2013), coconut husk, and rice husk (Nakason *et al.*, 2018) are shown in Table 2-5. As an example, the carbon content increased with 1.8%—63.6%, whereas the oxygen content decreased with 19.0%—31.6% after hydrothermal treatment. The main differences difference between the experiments conducted were the biomass samples, the temperature range, and the holding/retention time.

Dehydration and decarboxylation reactions, the two main reactions that take place during hydrothermal carbonisation, leads to the chemical composition as discussed above (Donar *et al.*, 2016; Gao, Zhou, *et al.*, 2016; Nakason *et al.*, 2018). Hydrothermal treatment of biomass is beneficial, since it decreases the oxygen content and increases the carbon content, which explains the lower H/C and O/C atomic ratios. The H/C atomic ratio was influenced by dehydration reactions, removing hydrogen from the solid product. Table 2-5 reports the H/C and O/C atomic ratios based on the work of indicated authors.

2.4.2 Residence time

Most of the work completed by previous authors, investigating the effect of residence time on the product yield and physicochemical properties, was done using a batch reactor. These investigations show that the effect of residence time is small in batch processes, and some cases insignificant when compared to other variables such as temperature. For example, Donar *et al.* (2016) showed that residence time (two to six hours) had no significant effect on the elemental composition of hydrochars produced from hazelnut shell and olive residue through hydrothermal treatment. Donar *et al.* (2016) suggested that at the specific temperature, longer a residence time did not contribute to the final product. At these conditions, hemicellulose degrades easily; yet, cellulose and lignin were more resistant.

Gao *et al.* (2016) reported a marginal effect of residence time on the physicochemical properties of hydrothermally treated eucalyptus bark. The fixed carbon content increased slightly due to loss of volatile matter, and the HHV values for all hydrochar were in the range

of 27.0 MJ/kg ─ 28.2 MJ/kg. FTIR spectra demonstrated only marginal differences with regards to the functional groups present on the hydrochars (Gao, Zhou, *et al.*, 2016).

A study on coconut husk and rice husk showed that the retention time had a slight effect on the solid yield. Increasing the retention time from one to four hours caused a decrease in solid yield from 70.9% ─ 67.8% and 70.1% ─ 69.0%, respectively (Nakason *et al.*, 2018). Similar to Gao *et al.* (2016), the VM content decreased from 55.2% ─ 54.0% and 51.1% ─ 48.3%, respectively, whereas the FC content increased from 44.2% ─ 45.7% and 28.0% ─ 30.1%, respectively. Subsequently, the relationship between the FC and VM content of the hydrochars and the retention time translated to an improved fuel ratio (FC/VM) (Nakason *et al.*, 2018). Nakason *et al.* (2018b) also reported that longer hydrothermal treatment times increased the HHV from 22.6 MJ/kg ─ 23.9 MJ/kg and 17.5 MJ/kg ─ 18.2 MJ/kg, respectively.

Mäkelä *et al.* (2015) concluded that the retention time affected hydrochar ash content, solid yield, carbon content, O/C atomic ratio, energy densification and energy yield. Compared to temperature, the effect of retention time was three to seven times lower.

Sermyagina *et al.* (2015) reported that longer holding time resulted in higher mass loss and a slight increase in the heating value of hydrochar. The mass loss was largely related to loss in the volatile matter, for example, doubling the holding time to six hours (at different temperatures ranging between 180°C ─ 250°C) the volatile content decreased with 4% ─ 9%. Low temperatures (180°C and 200°C) demonstrated a greater effect on energy content. At higher temperature, the HHV increased with less than 1 MJ/kg.

2.4.3 Biomass-to-water ratio

Mäkelä *et al.* (2015) used a recycled paper mill sludge residue from a Swedish pulp and paper mill and showed that biomass-to-water ratio was statistically insignificant within the original design range and did not have an effect on the hydrochar properties (Mäkelä *et al.*, 2015).

Sermyagina *et al.* (2015) showed an increase in the mass yield, fixed carbon content and energy content with an increase in the biomass-to-water ratio. The lower solid yield at higher water loadings was attributed to increased decomposition reactions (hydrolysis) (Sermyagina *et al.*, 2015). Similarly, Volpe and Fiori (2017b) found that high biomass-to-water ratios favour secondary hydrochar formation, which translates to higher solid yield and hydrochar with

higher energy content. For example, increasing the biomass-to-water ratio from 7% ─ 25%, increased the solid yield with 9.6% (olive trimmings) and 7.7% (olive pulp). For the same values and order, the heating value increased with 1.2 MJ/kg and 1.8 MJ/kg. Likewise, the fixed carbon content increased with 6.3% and 4.5% respectively. Secondary char microspheres on the surface of hydrochar had a C/O atomic ratio four and two times greater than primary char found in the hydrochar derived from the olive trimmings and olive pulp, respectively.

2.5 HTL via continuous reactors

Research in continuous hydrothermal liquefaction is limited in literature, but have been used to some extent for the production of bio-oil from algae.

Ocfemia *et al.* (2006) developed and tested a small-scale continuous hydrothermal process for treating swine manure for the production of bio-oil. The test was successful and produced oil yields ranging from 62.0% ─ 70.4% with heating values ranging from 25.2 MJ/kg ─ 31.1 MJ.kg.

(Patel & Hellgardt, 2015) investigated the effect temperature and residence time had on the product distribution and chemical properties of the product, derived from microalgae via a continuous hydrothermal liquefaction process. HTL at 380°C and 30 seconds produced the highest bio-oil yield. The bio-oil had favourable low oxygen content and high carbon content and explained the high HHV; yet, low O/C atomic ratios suggest more oxidative stability due to a smaller amount of C─O functional groups. An increase in stable C─H bond was observed, which was supported by higher hydrogen and carbon (H/C atomic ratio) content.

Makishima *et al.* (2009) used a semi-pilot scale continuous flow type hydrothermal reactor to recover hemicellulose from corncob. A recovery of 82.2% of xylan was achieved as a mixture of xylose, xylooligosaccharides and higher-xylooligosaccharide.

Prapaiwatcharapan *et al.* (2015) evaluated two types of semi-continuous systems, a two-step sequential hydrothermal liquefaction system and a single-step hydrothermal liquefaction system. The two-step system produced a higher oil yield, less solid residue and bio-oil with reduced nitrogen content.

Jazrawi *et al.* (2013a) investigated the effect of temperature, pressure and solid loading on bio-oil production via continuous hydrothermal liquefaction processing of two microalgae strains. Higher bio-oil yields were achieved with higher temperatures, higher pressures and longer residence times. More severe conditions favoured deoxygenation and bio-oil derived from protein content, which resulted in higher nitrogen content. Jazrawi *et al.*[1] (2013a) noted that higher yields were possible with continuous processing of algae, but it might come down to a trade-off between yield and properties. The maximum bio-oil yield was 47.7% at a solid loading of 10%, a temperature of 350°C and a residence time of 3 min.

Mariusz *et al.* (2018) evaluated a continuous hydrothermal liquefaction process and the effect of process parameters, e.g. temperature and residence time, on the bio-oil production by using microalgae as feedstock. The carbon content of bio-oil and bio-oil yield increased with higher temperatures, while the oxygen content decreased. The carbon content of the bio-oil produced at the lower bound (250°C, 7 min.) and upper bound (350°C, 30 min.) conditions was 66.1 % and 72.5 %, respectively. The corresponding oxygen content decreased by 7.9 %. Both the hydrogen and nitrogen content increased slightly. The resulting energy content, due to lower oxygen content and higher carbon content, increased with 3.8 MJ/kg. Higher nitrogen levels contribute towards better lubricity of bio-oil but are undesirable due to increased NO_x emissions. It was proposed that bio-oil with tailored properties could be produced by manipulating the parameters; however, secondary reactions must be considered.

Elliott *et al.* (2013) performed hydrothermal liquefaction of four algae feedstock at subcritical liquid water conditions (350°C, 20 MPa). The solid loadings ranged from 17% ─ 34% and produced bio-oil yields from 38% ─ 64%, with carbon conversions from 77% ─ 79%. In comparison with bio-oil derived from lignocellulosic biomass, the algae bio-oil had a lower density, contained less dissolved water and had a lower acid content. However, it was more viscous and had a higher sulphur and nitrogen content, which is unfavourable due to associated NO_x and SO_x emissions. The analysis showed that the bio-oil consisted mainly of alkane products and derived heterocyclic hydrocarbons. Later, hydrothermal liquefaction of macroalgal was investigated by Elliott *et al.* (2014), using the bench-scale continuous flow reactor to produce bio-oil at the same subcritical liquid water conditions (350°C, 20 MPa). Overall the bio-oil yield increased with increasing solid loading. At a dry solid loading of 21.7%,

7.6% of the carbon was converted to bio-oil, which consisted mainly of heterocyclic hydrocarbons. The bio-oil was easily separated from the aqueous phase by gravity separation and did not require a solvent to be recovered.

2.6 Densification

Densification is the production of regular shaped pellets, briquettes or cubes that improves physical properties such as the mass and energy density and subsequently, the logistics of biomass (Kaliyan & Vance Morey, 2009). Kambo & Dutta (2014) pelletised miscanthus in their study and reported an increased mass- and energy density, ranging between 321.1 kg/m^3 ─ 834.1 kg/m^3 and 5.9 kg/m^3 ─ 15.7 MJ/m^3, respectively. Pelletised loblolly pine's mass density increased 36% from 813.0 kg/m^3 ─ 1102.4 kg/m^3 and the energy density from 15.9 MJ/m^3 ─ 22.8 MJ/m^3 (Reza *et al.*, 2012). Other less dense raw biomass sources also showed good improvement. The densities of wheat straw, corn stover, big bluestem, and sorghum stalk, ranging from 46 kg/m^3 ─ 60 kg/m^3, increased and ranged from 360 kg/m^3 ─ 500 kg/m^3 (Theerarattananoon *et al.*, 2011). In general, the highest density of lignocellulosic pellets is associated with optimum moisture content. Huang *et al.* (2017) produced denser pellets by increasing the pelletising temperature and pressure.

Biomass pellets must have a certain quality based on properties that are associated with forces and conditions, to which pellets are exposed, within the supply chain. Generally, the main measure of a pellet's quality is the strength and durability that relates to the inter-particle bonds formed during the densification process (Kaliyan & Vance Morey, 2009).

2.6.1 Strength and durability

In their review, Kaliyan and Vance Morey (2009) cited four key characteristics used as a measure of strength and durability. These included compression resistance, impact resistance, durability and water resistance. Compression resistance is a measure of the force a pellet can withstand before shattering, commonly characterised by compression strength. Impact resistance may be reported with various indexes; for example, the impact resistance index (IRI). Durability relates to mechanical or pneumatic handling and can be measured with an impact resistance test such as the drop test. Water-resistance addresses the ability of pellets to stay intact after short term exposure to moisture (real-world conditions are exposed to rain or high humidity) (Kaliyan & Vance Morey, 2009).

Some investigators have compared and analysed the quality of pellets produced from various biomasses (Carroll & Finnan, 2012; Castellano *et al.*, 2015; Gil, Oulego, *et al.*, 2010; Liu, Mi, *et al.*, 2016). The effect of properties such as moisture (Castellano *et al.*, 2015; Huang *et al.*, 2017; Kaliyan & Vance Morey, 2010; Razuan *et al.*, 2011; Theerarattananoon *et al.*, 2011), pelletising temperature (Castellano *et al.*, 2015; Huang *et al.*, 2017; Kaliyan & Vance Morey, 2010; Razuan *et al.*, 2011), pelletising pressure (Huang *et al.*, 2017; Razuan *et al.*, 2011), and the particle size of the feed (Castellano *et al.*, 2015; Theerarattananoon *et al.*, 2011) have also been investigated. The moisture content acts as a lubricant and a bonding agent (Kaliyan & Vance Morey, 2009). The maximum strength of a pellet corresponds to optimum moisture content, and similar to mass density, a deviation from this value results in weaker pellets (Huang *et al.*, 2017). The optimum moisture content of birch, spruce and reed canary grass corresponding to a maximum density and strength (density/strength), was 6.1%, 5.2%/8.5%, and 5.1%/8.3% respectively. Similarly, by manipulating the pelletising temperature, a stronger and more durable pellet is produced. This phenomenon is connected to the amorphous portion of semi-crystalline solids, such as lignin. At a certain temperature, known as the glass transition temperature, lignin changes from a rigid, 'glass' state to a pliable, liquid state, forming solid bridges between particles once it is cooled (Reza *et al.*, 2012). Similar to the moisture content, an optimum temperature, coinciding with the glass transition temperature of lignin in a specific material, is observed and exceeding this temperature during pelletisation, may produce a hard, brittle pellet (Reza *et al.*, 2012).

When biomass pellets are exposed to wetting or high humidity conditions, water is absorbed, causing the pellet to swell and become fragile (Bergström *et al.*, 2008; Theerarattananoon *et al.*, 2011),. The absorbed moisture content of lignocellulosic biomass is categorised as free-water, non-freezing bounded water and freezing bounded water. The latter two relates to hydrogen-bonded hydroxyl groups of the cell wall. Free-water is present in the micro and macroporous capillaries and is a function of the polymeric composition and relative humidity (Kambo & Dutta, 2014). Of the three main constituents of biomass, hemicellulose is the most hydrophilic, while lignin is more hydrophobic in nature (Acharjee *et al.*, 2011).

In general, lignocellulosic biomass pellets have a fair to good quality based on compression resistance, impact resistance, and durability tests. This is related to the natural binders in biomass, such as protein, fat, lignin and starch; activated under high pelletising pressure and in the range of the glass transition temperature. The natural binders in biomass are utilised by using mixtures of various biomasses to generate stronger pellets (Kaliyan & Vance Morey, 2010).

2.7 Combustion behaviour

Lignocellulosic biomass is an attractive renewable resource that can be used as a co-firing agent or a substitute for fossil fuels on a commercial scale; however, existing reactors (e.g. boilers or gasifiers) were designed based on the properties and kinetic parameters of a specific fuel and may relate to operational problems. When considering a different fuel or designing new reactors, the thermochemical behaviour and kinetic parameters must be determined. Non-isothermal thermogravimetric (TG) analysis is a technique commonly employed to study combustion characteristics. In the case of non-isothermal technique, the mass loss is determined as a function of a temperature profile and heating rate. The thermogravimetric (TG) curve and derivative thermogravimetric (DTG) curve (or burning profile), generated from non-isothermal TG data, is used to obtain experimental values for thermochemical properties and kinetic parameters.

2.7.1 Combustion behaviour of lignocellulosic biomass against coal

Lignocellulosic biomass typically exhibits several characteristic peaks with regions that tend to overlap. The three main regions associated with mass loss, in sequential order, are identified as evaporation of moisture, oxidative degradation and char combustion (Munir *et al.*, 2009). Mass loss below 105°C is linked to the inherent moisture content of biomass. Oxidative degradation, or oxidative pyrolysis, is described as the degradation of cellulosic components and subsequent ignitions (Gani & Naruce, 2007), or ignition of volatile content (Haykiri-Açma, 2003). After oxidative pyrolysis, char combustion occurs, which is associated with the combustion of the fixed carbon content of biomass and generally overlaps with the preceding region (Munir *et al.*, 2009). The intensity and extent of these regions are linked to the proximate composition of the lignocellulosic biomass sample.

In their study, Munir *et al.* (2009) investigated the thermal degradation of four biomass samples under an inert and oxidative atmosphere. The behaviour of cotton stalk, two sugarcane bagasse, and shea meal under oxidative atmosphere could be explained from their respective chemical composition. All the samples demonstrated rapid, intense mass loss during oxidative pyrolysis and slower, damped mass loss during char combustion. Oxidative pyrolysis occurs within the range of 226°C ─ 357°C. It has also been shown that depending on the chemical nature of the biomass material, that is: if the biomass has a fibrous or woody nature or combination of the two, it may demonstrate different char combustion behaviour. Shea meal

exhibited two char combustion regions that were linked to the woody and fibrous nature, whereas the other samples (fibrous in nature) had only one region of char combustion. The char combustion region ranged from 352°C ─ 500°C.

The burning profile is also used to obtain experimental values for characteristic temperatures, including ignition, peak and burnout temperature. The ignition temperature is defined as the temperature at which a substance ignites spontaneously without an external source of ignition and relates to safety considerations during storage and handling when it is utilised in industrial processes (Lu & Chen, 2015). The peak temperature and burnout temperature is associated with the maximum combustion rate and the end of char combustion, respectively. The peak temperature is obtained by examining the DTG-plot to determine the maximum combustion rate. In certain studies, two peak temperatures are reported: the one associated with oxidative pyrolysis and the other with char combustion. Finally, the burnout temperature is obtained by either an intersection method of two tangent lines or calculating the temperature at which the thermal conversion of a sample reaches 99% (Lu & Chen, 2015).

Table 2-6 shows the ignition, peak and burnout temperature as well as the maximum combustion rate of various lignocellulosic biomasses as reported by indicated authors. The data reported in Table 2-6 was determined with the so-called intersection method and non-isothermal TG data at one of two heating rates (10 °C/min or 20 °C/min). Except for tobacco stalk, subjected to a heating rate of 20 °C/min, the ignition, peak and burnout temperatures ranged from 226°C ─ 354°C, 283°C ─ 511°C and 443°C ─ 578°C, respectively. The low ignition temperature of biomass relates to the low degree of order associated with hemicellulose, cellulose and lignin. The cellular structure has high concentrations of ─OH, ─CH_2, ─CH_3, and ─C─H radical groups. The high reactivity and maximum combustion rate at low temperatures are associated with the high concentration of volatile organic components and low fixed carbon content (Wang *et al.*, 2016).

Table 2-6: The ignition -, peak -, burnout temperature, and maximum combustion rate of various lignocellulosic biomasses

Biomass	$T_{ignition}$ (°C)	T_{peak} (°C)	$T_{burnout}$ (°C)	$[dm/dt]_{max}$ (%/min)	Reference
10 °C/min					
Olive kernel	295	378	522	11.7	(Kastanaki & Vamvuka, 2006)
Forest residue	354	511	554	13.3	(Kastanaki & Vamvuka, 2006)
Cotton residue	282	412	517	8.6	(Kastanaki & Vamvuka, 2006)
Wood	350	509	578	12.3	(Kastanaki & Vamvuka, 2006)

Table 2-6: The ignition -, peak -, burnout temperature, and maximum combustion rate of various lignocellulosic biomasses

Biomass	$T_{ignition}$ (°C)	T_{peak} (°C)	$T_{burnout}$ (°C)	$[dm/dt]_{max}$ (%/min)	Reference
			10 °C/min		
Sawdust	243	417	449	10.4	(Sahu *et al.*, 2010)
Rice husk	252	323	483	7.6	(Sahu *et al.*, 2010)
Rice husk	242	319	455	9.6	(Wang *et al.*, 2016)
Pine sawdust	260	322	462	12.1	(Wang *et al.*, 2016)
Tabacco stalk	254	284	568	9.3	(Cong *et al.*, 2019)
			15 °C/min		
Coconut fibre	247	307	458	7.1	(Liu *et al.*, 2012)
Eucalyptus leaves	261	313	417	8.4	(Liu *et al.*, 2012)
			20 °C/min		
Cotton stalk	228	283	443	16.8	(Munir *et al.*, 2009)
Sugarcane bagasse	226	304	480	11.4	(Munir *et al.*, 2009)
Sugarcane bagasse	247	312	487	15.6	(Munir *et al.*, 2009)
Shea meal	232	287	500	12.6	(Munir *et al.*, 2009)
Cornstalk	261	308	535	13.5	(Wang *et al.*, 2012)
Rice straw	257	313	564	11.6	(Wang *et al.*, 2012)
Rice hull	276	322	568	9.5	(Wang *et al.*, 2012)
Sawdust	293	357	578	14.9	(Wang *et al.*, 2012)
Empty fruit bunch	220	-	662	29.1	(Parshetti *et al.*, 2014)
Bamboo	254	302	492	7.0	(Lu & Chen, 2015)
Sugarcane bagasse	302	338	494	16.7	(Lu & Chen, 2015)
Tobacco stalk	288	329	737	14.8	(Cong *et al.*, 2019)

Shenhua bituminous coal (Wang *et al.*, 2016), hard coal (Kastanaki & Vamvuka, 2006), Yunnan low-rank coal (Cong *et al.*, 2019), bituminous coal and anthracite (Wang, Wang, *et al.*, 2018) all had one main peak concentrated in 360°C ─ 500°C, 400°C ─ 700°C, 410°C ─ 765°C, 380°C ─ 545°C and 510°C ─ 625°C, respectively, while the Greek pre-dried lignite (Kastanaki & Vamvuka, 2006) had two peaks separated by a small dip, both peaks ranging from 316°C ─ 600°C. It is clear that in most cases the oxidative pyrolysis and char combustion zone of coal overlaps and that the ignition and burnout of coal occur at much higher temperatures. In contrast to lignocellulosic biomass, coal has a much higher degree of order, with lower volatile matter and higher fixed carbon. Based on the atomic ratios, the H/C and O/C atomic ratios are very low and characterised by a higher concentration C═C functional groups (Kastanaki & Vamvuka, 2006; Wang *et al.*, 2016). Considering the above

properties of coal with a higher peak temperature and lower maximum combustion rate of coal, it is clear that coal has a lower reactivity.

Table 2-7: The ignition -, peak -, burnout temperature and maximum combustion rate of various lignocellulosic biomasses

Coal	$T_{ignition}$ (°C)	T_{peak} (°C)	$T_{burnout}$ (°C)	$[dm/dt]_{max}$ (%/min)	Reference
			10°C/min		
Shenhua bituminous coal	361	465	504	14.8	(Wang *et al.*, 2016)
Greek pre-dried lignite	316	434	600	7.7	(Kastanaki & Vamvuka, 2006)
Hard coal	402	592	710	7.1	(Kastanaki & Vamvuka, 2006)
Bituminous coal	378	-	546	13.0	(Wang, Wang, *et al.*, 2018)
Anthracite	512	-	625	14.0	(Wang, Wang, *et al.*, 2018)
	388	-	640		
	291	-	608		
			20°C/min		
Indonesian lignite	368	514	708	3.6	(Liu *et al.*, 2012)
Low rank Indonesian coal	340	-	438	24.2	(Parshetti *et al.*, 2014)

2.7.2 Co-combustion of lignocellulosic biomass and coal

Co-combustion of biomass and coal was investigated by (Gil, Casal, *et al.*, 2010),

Wang *et al.* (2016), and Zhou *et al.* (2014). Blends of biomass with coal were rice husk and pine sawdust with Shenhua bituminous coal, and peanut shell and wheat straw with coal gangue,

In all three studies, the blends demonstrated a combined burning profile according to the characteristics of the individual biomass and coal samples' burning curve. For example, increasing the fraction lignocellulosic biomass reduces the mass loss rate associated with the main combustion zone of coal, while a peak develops and increases at the lower temperature region as the fraction lignocellulosic biomass increases (Gil, Casal, *et al.*, 2010; Wang *et al.*, 2016; Zhou *et al.*, 2014). For pine sawdust and bituminous coal blends, the mass gain rate at 198°C ─ 365°C increased from1.0 %/min ─ 15.2 %/min, and the mass loss rate at 343°C ─ 617°C decreased from 13.2 %/min ─ 2.6 %/min (Gil *et al.*, 2010). For peanut shell/wheat straw and gangue coal blends, the mass gain rate at 183°C ─ 365°C and

189°C ─ 420°C increased from 0.094 %/°C ─ 0.427 %/°C and 0.066 %/°C ─ 0.342 %/°C, and the mass loss rate at 356°C ─ 687°C and 342°C ─ 750°C decreased from 0.322 %/°C ─ 0.193 %/°C and 0.342 %/°C ─ 0.239 %/°C, respectively (Zhou *et al.*, 2014). The corresponding increase and decrease at lower and higher temperatures is related to the fractional increase and fractional decrease volatile matter and fixed carbon content (Gil, Casal, *et al.*, 2010; Zhou *et al.*, 2014).

Concerning the coal sample, both the ignition and burnout temperature decreases with an increase in lignocellulosic biomass, which was linked to the volatile nature of organic content in lignocellulosic biomass, the alkali and alkaline earth metals, and the biomass char (Gil, Casal, *et al.*, 2010; Wang *et al.*, 2016; Zhou *et al.*, 2014). This translated to improved ignition properties, but a decrease for the comprehensive combustion characteristic, since blends with larger fraction biomass has a more prolonged, less intense combustion profile as appose to the individual samples (Wang *et al.*, 2016). As an example, for rice husk/pine sawdust and Shenhua bituminous coal blends, the ignition, peak and burnout temperature decreased with 42°C ─ 50°C, 140°C, and 19°C ─ 23°C, respectively (Wang *et al.*, 2016). Gil, Casal, *et al.* (2010) and Zhou *et al.* (2014) had similar results.

A comparison between calculated and experimental conversion data as a function of the conversion of individual samples and respective fractions indicated a synergy effect at a higher temperature. The devolatilisation and ignition were hindered by poor heat transfer, due to different particles and particle sizes. Synergy at higher temperatures was attributed to char from biomass, with better ignition property, which generates heat, as well as the catalytic effect of alkali and alkaline earth metals (Wang *et al.*, 2016). Zhou *et al.* (2014) and Gil, Casal, *et al.* (2010) demonstrated similar results in their study. Wang, Zhang, *et al.* (2016) observed a correlation between the reactivity and the concentration of SiO_2 and Al_2O_3, indicating that these species have a negative impact on the reactivity.

Co-firing of lignocellulosic biomass has certain advantages such as improved ignition coefficient, synergetic behaviour at higher temperatures, less ash, and less nitrogen and sulphur related emissions; yet, the comprehensive combustion coefficient decreases and the fuel ratio increases. As discussed in Section 2.3, most of the disadvantages associated with lignocellulosic biomass are mitigated through hydrothermal treatment. The combustion behaviour of hydrochar and hydrochar-coal blends against coal is discussed in the following section.

2.7.3 Combustion behaviour of hydrochar and hydrochar-coal blends against lignocellulosic biomass and coal

The burning profile of lignocellulosic biomass and hydrochar can be divided into two main regions. The first region relates to the release and combustion of volatile matter. As discussed in Section 2.2.1, the volatile matter of lignocellulosic biomass is associated with the volatile organic components, such as hemicellulose and cellulose. Lignin is thermally stable under hydrothermal carbonisation temperatures and forms part of the fixed carbon content. The first peak disappears with higher temperature and longer holding times, due to the extent of decomposition for hemicellulose and cellulose. In contrast, the hydrothermal treatment produces a thermally stable solid product which causes the burning profile to shift to a higher temperature region and is characterised by higher ignition, peak, and burnout temperatures, as well as a lower rate of combustion (maximum combustion rate) (Liu *et al.*, 2013). The ignition temperature of coconut fibre and eucalyptus leaves increased from 247°C and 261°C with 68°C ─ 111°C after hydrothermal treatment at 250°C for a holding time of 20 minutes and from 273°C (Liu *et al.*, 2012) and 253°C with 22°C ─ 177°C after hydrothermal treatment at 210 ─ 280°C for 30 min, 60 min, and 90 min (Liu *et al.*, 2013). For pine sawdust, rice husk, coconut fibre, and coconut shell, an increase from 290°C, 269°C, 251°C, and 267°C with 1°C, 8°C, 30°C, and 102°C were observed after hydrothermal treatment at 250°C for 20 minutes (Liu *et al.*, 2014). Also, the ignition temperature of sweet potato waste increased from 317°C with up to 71°C after hydrothermal treatment at 180°C ─ 300°C for 60 minutes (Chen *et al.*, 2018). Chen *et al.* (2018) also demonstrated the ignition temperature as a function of holding time. The ignition temperature increased with 3°C ─ 51°C after hydrothermal treatment at 240°C for 0 min ─ 120 min.

In the same order, the burnout temperature of coconut fibre and eucalyptus leaves demonstrated separate behaviour, the former an increase from 326°C with 146°C ─ 152°C and the latter a decrease from 456°C with 7°C ─ 11°C (Liu *et al.*, 2013). The pine sawdust, rice husk, coconut fibre and coconut shell increased from 464°C, 345°C, 466°C, and 340°C with 236°C, 316°C, 177°C, and 276°C (Liu *et al.*, 2014). The sweet potato waste increased from 529°C with 1°C ─ 25°C after hydrothermal treatment at 180°C ─ 300°C for 60 minutes. Hydrothermal treatment at 240°C for holding times of 0 ─ 120 minutes, increased the burnout temperature from 5°C ─ 21°C (Chen *et al.*, 2018).

As stated in Section 2.7.1, an increase in peak temperature and a decrease in the maximum combustion rate is characteristic of lower reactivity. Hydrothermal treatment of biomass produces a hydrochar with a lower reactivity. The peak temperature of coconut fibre and eucalyptus leaves increased from 295°C and 312°C with 141°C ─ 163°C and 102°C ─ 111°C, respectively. The maximum combustion rate of hydrochar derived from coconut fibre was lower (47.8 %/min against 32.8 %/min ─ 34.2 %/min) (Liu *et al.*, 2013). For pine sawdust, rice husk, coconut fibre, coconut shell, an increase from 333°C, 297°C, 275°C, and 290°C with 139°C, 205°C, 206°C, 218°C was achieved. The maximum combustion rate decreased from 42.0 %/min, 70.8 %/min, 62.4 %/min, and 98.4 %/min to 6.0 %/min, 4.8 %/min, 7.8 %/min, and 8.4 %/min (Liu *et al.*, 2014). The peak temperature of sweet potato waste first decreased after hydrothermal treatment at 180°C ─ 220°C for a holding time of 60 minutes, but concerning the biomass, the peak temperature increased with 117°C ─ 128°C after hydrothermal treatment at 240°C ─ 300°C for the same holding time. The maximum combustion rate decreased from 18.9 %/min with 0.1 %/min ─ 8.2 %/min after hydrothermal treatment at 180°C ─ 240°C but increased to 11.2 %/min ─ 14.1 %/min for hydrochar produced under hydrothermal temperatures ranging from 260°C ─ 300°C. A hydrochar with a higher peak temperature and lower maximum combustion rate was only observed for holding time exceeding 60 minutes (Chen *et al.*, 2018).

Several benefits of hydrochar-coal blends trump biomass-coal blends for commercial application. The overlapping of combustion regions and similar ignition temperatures, suggests that hydrochar-coal blends can be used in existing furnaces. Also, lower volatile matter and improved thermal stability mitigate the fire hazard associated with biomass-coal blends.

Since coal, in general, is thermally more stable than hydrochar, blends with hydrochar have a lower ignition temperature, but compared to lignocellulosic biomass and coal blends, the effect is less. The hydrochar-coal blends made with coconut fibre/eucalyptus leave's hydrochar and Indonesian lignite had very high ignition temperatures and approached that of the sourced lignite. The blends' ignition temperatures ranged between 342°C ─ 355°C (Liu *et al.*, 2012). Gao *et al.* (2019) demonstrated similar results and demonstrated that the ignition temperature decreased by increasing the fraction hydrochar. The ignition temperature of blends made with either the hydrochar of olive mill waste or the hydrochar of Opuntia ficus indica cladodes and Illinoisan bituminous coal decreased from 348°C ─ 199°C (T_{HT}=220°C) and 295°C ─ 158°C (T_{HT}=250°C) for an increase from 10% ─ 50% hydrochar blends. Similar results were reported by Liu *et al.* (2016). However, as shown by Liu *et al.* (2016) and Parshetti *et al.* (2014), blends

with very high fractions hydrochar, may ignite at temperatures exceeding the raw coal's ignition temperature. For example, the ignition temperature of equivalent mass hydrochar/Indonesian coal blends and a pure coal sample, was 345°C ─ 360°C and 340°C, respectively, suggesting synergistic interaction (Parshetti *et al.*, 2014).

The high burnout temperature of hydrochar and coal translates to high burnout temperatures of blends. The same hydrochar/Indonesian coal blends studied by Parshetti *et al.* (2014) had burnout temperature of 640°C and 672°C, which was far greater than the coal sample's burnout temperature of 438°C and a slight improvement compared to the empty fruit bunch and coal blend (T_B = 610°C). In some cases, the blends show combined behaviour and fell within the range set by the upper and lower bound of the two individual samples; for example, the hydrochar made from coconut fibre and eucalyptus leaves and Illinoisan coal had a corresponding burnout temperature of 558°C, 556°C, and 708°C. The burnout temperature of the blends was within this range and increased with lower fractions hydrochar (Gao *et al.*, 2019). Combining Indonesian coal with hydrochar made from either coconut fibre or coconut shell, exhibited different behaviour. The latter showed synergistic behaviour, with burnout temperatures below the individual samples of coal and hydrochar, whereas that of the former was higher. In both cases, the burnout temperature of the blends increased with higher fractions hydrochar (Liu *et al.*, 2016).

Hydrochar/coal blends have similar combustion behaviour, and in some cases, as with the Indonesian lignite, it is improved. The peak temperature of hydrochar/lignite blends increased with higher fractions hydrochar. The corresponding peak temperature of the lignite, and blends with 25%, 50%, and 75% hydrochar (coconut fibre/coconut shell) were 385°C, 413°C/406°C, 478°C/437°C, and 481°C/503°C (Liu *et al.*, 2016). The two hydrochars (T_{HT} = 150°C and 250°C) made from empty fruit bunch and their respective blends, had a higher peak temperature than the sourced coal (345°C ─ 360°C against 340°C), but also a higher maximum combustion rate than the raw biomass (35.1 %/min ─ 46.3 %/min against 29.1 %/min). Nevertheless, the blends had a prolonged and intense combustion profile, whereas the coal's combustion profile stretched from 340°C ─ 438°C with lower intensity (Parshetti *et al.*, 2014). This eludes to the benefit of supplementing low ranked coals with hydrochar. In support of this statement, the reactivity (based on the peak temperature) of hydrochar/coal blends investigated by Liu *et al.* (2012), was similar and fell within the upper and lower bound set by the individual samples. Also, the maximum combustion rate showed combined behaviour, and the combustion time of blends (18.0 min ─ 22.7 min) versus lignite's (22.3 min) was similar (Liu *et al.*, 2012).

2.8 Gasification

Gasification is a process used to convert carbon-based fuels to syngas that can be used to produce electricity, various chemical and liquid fuels. Sasol, a South African based company, is the most successful commercial applications of a coal-to-liquid (CTL) process, which is based on the indirect coal liquefaction (ICL) approach known as Fischer-Tropsch (FT) synthesis.

At the core of Sasol's CTL process is the Sasol® fixed bed dry bottom (Sasol® FBDB™) gasifier that produces the two reactant gases, i.e., hydrogen and carbon monoxide (also known as syngas), required by the FT synthesis (Höök & Aleklett, 2010). The thermochemical process within a Sasol® FBDB™ gasifier are complex but can be divided into sequential zones from top to bottom according to the inherent reactions, namely drying, pyrolysis, reduction, and combustion region (Bunt & Waanders, 2008).

Pyrolysis is the heating of coal in the absence of oxygen and is represented with (Higman & Van der Burgt, 2008:1):

$$\text{Coal} \rightarrow \text{Coke(s)} + \text{volatiles(g)}. \quad \text{(R.2-1)}$$

The main gasification reactions associated with the reduction zone, includes the Boudouard, steam gasification, and methanation (Bunt & Waanders, 2008; Higman & Van der Brugt, 2008:12-13). In the same order as above, the reaction equations are

$$C(s) + CO2(g) \rightarrow 2CO(g), \quad \text{(R.2-2)}$$

$$C(s) + H2O(g) \rightarrow CO(g) + H2(g), \quad \text{(R.2-3)}$$

and

$$C(s) + 2H2(g) \leftrightarrow CH4(g). \quad \text{(R.2-4)}$$

respectively.

The gasification region is associated with char gasification and is the controlling step owing to the low gasification rate. Furthermore, CO_2 gasification is considered the rate-determining step since the reaction rate is slower than steam gasification (Wang *et al.*, 2015).

Several authors have developed reaction mechanisms to describe the Boudouard reaction of which the two-step model, developed by Ergun, is the most famous model. Ergun proposed a two-step reaction mechanism described with

$$C() + CO_2 \rightarrow C(O) + CO \qquad \text{(R.2-5)}$$

and

$$C(O) \rightarrow CO + C(). \qquad \text{(R.2-6)}$$

The first step entails the reduction of carbon dioxide to carbon monoxide at an active carbon site on the char surface. The oxygen atom forms an oxidised surface complex with the active site and can occur at low temperatures of 600°C. Step two is the rate-limiting step and involves the desorption of the carbon-oxygen complex and formation of a new carbon active site (Higman & Van der Burgt, 2008:36).

2.8.1 Reactivity of Char-CO_2-gasification

The two-step reaction mechanism of the Boudouard reaction described above is reduced to a single global reaction (Reaction R.2-7) for kinetic analysis (Guizani *et al.*, 2016).

$$C_{char} + CO_2 \rightarrow 2CO \qquad \text{R.2-7}$$

Di Blasi (2009) calculated the specific reaction rate, also known as the reactivity (R), with:

$$R = -\frac{1}{m_t}\frac{dm_t}{dt} = \frac{1}{1-X}\frac{dX}{dt}. \qquad \text{(Eqn. 2-3)}$$

as a function of char conversion, where m_t denoted the instantaneous mass of the carbon on a dry-ash-free basis at time t, dX/dt the conversion rate, and X the degree of conversion. Di Blasi (2009) calculated the degree of conversion with:

$$X = \frac{m_0 - m_t}{m_0 - m_f}. \qquad \text{(Eqn. 2-4)}$$

The mass quantities in (Eqn. 2-4, m_0, m_t, and m_f refers to the initial mass of the char, the mass of the charred sample at time t, and the final mass of the ash after CO_2 gasification was completed, respectively. The conversion of char is based on an ash-free basis.

2.8.2 The effect of pyrolytic conditions on char reactivity during CO_2 gasification

The reactivity of char during CO_2 gasification is related to the morphological structure, which is strongly related to the pyrolysis condition under which char is formed, and the inorganic matter, such as the alkali and alkaline earth metals (AAEM). The main pyrolytic conditions that influences reactivity is the heating rate, peak temperature, residence time and pressure. This section will only focus on the heating rate and final pyrolytic temperature.

Char production via pyrolysis at a high heating rate, yields a reactive char during CO_2 gasification (Cetin *et al.*, 2005; Guizani *et al.*, 2013). Guizani *et al.* (2013) compared the reactivity of beech wood chip charred at a high (100 K/s) and low heating rate (5 °C/min). The reactivity of the so-called higher-heating-rate chars in 20% CO_2 atmosphere, were 4.3 times higher than the lower-heating-rate chars. Similarly, Cetin *et al.* (2005) evaluated the effect of heating rates (20 °C/min and 500 °C/min) on char morphology and how it translates to the reactivity of the char. The radiate pine char's reactivity increased after pyrolysis under more severe conditions (higher heating rates). This increase in reactivity was attributed to the increased surface area. Pyrolysis of hardwoods under more severe conditions increased the extent of pore development due to higher rates of devolatilisation. The increase in surface area may be attributed to the development of new pores, the opening of previously closed pores, widening of existing pores and coalescence of neighbouring pores (Rocca *et al.*, 1999). The number of active sites of chars is also closely related to the heating rate. Lower heating rates produce chars with a higher-order structure and is associated with lower oxygen content. Chars produced under higher heating rates have a less ordered structure with more carbon-oxygen complexes that decrease the number of the active site.

In general, the study of reactivity, synergy, and kinetics during CO_2-gasification is based on the carbon conversion; therefore, CO_2-gasification is done on the pyrolysis product char. Pyrolysis is done under an inert atmosphere, such as nitrogen, at a temperature in the region of 1000°C. The final temperature and heating rate during pyrolysis influences the reactivity.

2.8.3 Reactivity and synergy of lignocellulosic biomass and coal during co-pyrolysis

Rapid co-pyrolysis of bituminous coal and rice straw was investigated by Yuan *et al.* (2012a). The higher degree of decomposition of rice straw in comparison with coal and the direct relationship between the degree of decomposition and the biomass-coal is related to the main components of biomass, namely cellulose, hemicellulose and lignin. The thermally unstable nature of these components was credited to the weak ether bonds, or overall it may be described as having a lower degree of order (Krerkkaiwan *et al.*, 2013; Yuan *et al.*, 2012). Similar results were reported during separate co-pyrolysis experiments of an Indonesian sub-bituminous coal with rice straw and leucaena leucocepha wood (Krerkkaiwan *et al.*, 2013), bituminous coal with various biomass sources (Chinese Redwood, soybean stalk, orange peel, and peanut shells), and orange peel with three coals varying in coal rank and ash content (a bituminous coal, low ash lignite, and high ash lignite) (Zhang *et al.*, 2016). In the study by Yuan *et al.* (2012a), as the final pyrolysis temperature increased, the char yield decreased, whereas the tar yield decreased, and gas yield increased. Similar results were reported by Krerkkaiwan *et al.* (2013).

Synergy during co-pyrolysis may be related to the inherent high H/C and O/C atomic ratios of lignocellulosic biomass, which leads to the formation of higher amounts of H and OH radicals. These species act as hydrogen donors and promotes the cracking of aromatic compounds in coal (Zhang *et al.*, 2007). Since lignocellulosic biomass has higher H/C and O/C atomic ratio than coal, increasing the biomass/coal ratio may have a positive effect towards the reactivity, as observed by Zhang *et al.* (2007). Yet, Krerkkaiwan *et al.* (2013) and Yuan *et al.* (2012a) reported less or no synergy with higher biomass-coal ratios during co-pyrolysis, which was likely due to excess volatile and lower heat transfer properties, respectively.

The synergetic effect during co-pyrolysis is commonly linked to the alkali and alkaline earth metal content of lignocellulosic biomass (Krerkkaiwan *et al.*, 2013; Yuan *et al.*, 2012; Zhang *et al.*, 2007). Calcium, potassium, sodium, and magnesium are reported to have a catalytic effect during co-pyrolysis, while silicon and aluminium act as inhibitors (Krerkkaiwan *et al.*,

2013; Yuan *et al.*, 2012). The rice straw and wood sample sourced by Krerkkaiwan *et al.* (2013) had a potassium content of 15.0 and 6.5 times greater than the bituminous coal sample; therefore, the synergetic effect was linked to the potassium content and more specifically the fraction that is evaporated and deposited on the surface of the coal char. This volatile potassium promotes the decomposition of secondary char (Krerkkaiwan *et al.*, 2013). However, Krerkkaiwan *et al.* (2013) observed that even though rice straw had a higher amount of potassium, a large portion was retained in the ash in the form of a silicon compound. Subsequently, the potassium mass balance showed that similar amounts of potassium were released as volatile potassium. Krerkkaiwan *et al.* (2013) suggested that the lower yield during co-pyrolysis with rice straw was linked to the combined effect of volatile potassium and higher amounts of pyrolytic steam; hence, the decomposition and gasification of secondary char.

Silicon and aluminium has a high affinity towards active AAEMs and may have a notable effect on synergy if high concentrations are present during pyrolysis. This effect was demonstrated by the amount of potassium retained in the ash as K_2SiO_3 after co-pyrolysis with rice straw (Krerkkaiwan *et al.*, 2013).

2.8.4 Reactivity of lignocellulosic biochar and biochar-coal blends compared to coal during CO_2-gasification

In general, biochar has a higher reactivity during CO_2 gasification. It is relatable to one of several properties, such as elemental composition, intrinsic chemical structure and mineral content, as well as morphology. Jeong *et al.* (2014) compared the reactivity of pine sawdust with Shinhwa coal and observed a higher reactivity which was attributed to the alkali content of pine sawdust. The potassium content of pine sawdust and coal was 6.91 % and 1.90 %, respectively. In a study by Yuan *et al.* (2012a), the biochar derived from rice straw had a very high reactivity in comparison with the sourced coal, which was attributed to the lower degree of order and higher specific surface area. In their study, the degree of order was quantified by the ratio crystal stacking height (L_c) to the crystal plane distance (d_{002}), which can be calculated with The Bragg formulation (Bragg, 1913), and Scherrer formula (Patterson, 1939). A higher degree of order is associated with a decreased in the crystal plane height and an increase in the crystal stacking height; subsequently, a higher ratio (L_c/d_{002}) signifies a higher degree of order. The corresponding value of the specified ratio for rice straw and coal, rounded off to the first decimal, was 4.7 and 1.7.

Wei, Guo, Gong, *et al.* (2017) calculated the reactivity index ($RI_{X=50\%}$) at a conversion of 50% with

$$RI_{X=50\%} = \frac{0.5}{t_{X=50\%}} \quad \text{(Eqn. 2-5)}$$

to make a quantitative comparison during gasification. Based on this reactivity index, rice straw had a reactivity 30.8 times greater than the petroleum coke at a gasification temperature of 950°C. At 1000°C, the factorial increased was 59.8, clearly showing how temperature has a positive influence on the reactivity.

Although there are many other differences between rice straw and petroleum coke which would contribute to the overall reactivity, for example, the chemical composition, crystallinity and morphology, Wei *et al.* (2017) referred to the high active potassium content of rice straw and the very low ash content of petroleum coke.

Wei *et al.* (2019) calculated the reactivity index ($RI_{X=90\%}$) at a conversion of 90% with

$$RI_{X=90\%} = \frac{0.9}{t_{X=90\%}} \quad \text{(Eqn. 2-6)}$$

to make a quantitative comparison between the reactivity of anthracite, bituminous coal and rice straw. The reactivity of biochar was 1.73 and 52.0 times greater than the reactivity of bituminous coal char and anthracite char, respectively.

In general, a higher specific surface area, a lower degree of carbon order and active AAEM will contribute to higher reactivity, e.g. anthracite had the lowest specific surface area, the highest degree of crystallinity, and lowest AAEM content, which explained the low reactivity of anthracite. In contrast, rice straw char had the largest specific surface area, the lowest degree of order and the highest AAEM content with the highest reactivity.

Mafu *et al.* (2018) highlighted the higher reactivity of biomass by comparing it with bituminous coal, but also explored the difference between the various biomasses with regards to behaviour during CO_2 gasification. For example, the reactivity of all three biomass samples increased with conversion, but the reactivity of sorghum bagasse started to decrease at conversions exceeding 50%. The bituminous coal's reactivity decreased over the entire

conversion profile. Mafu *et al.* (2018) were able to link the observed reactivity during gasification with the mineral content. The hardwood and softwood char had high reactivity beyond conversions of 80%, which was likely due to the high potassium content and low silicon and aluminium content. Even though sorghum bagasse had the highest potassium content, it had ample amounts of silicon, aluminium, and phosphorous, which explained the decreasing reactivity at mid-to-late gasification stages. Similarly, the coal's low potassium-, high silicon-, and high aluminium concentrations explained the low reactivity, which decreased as the conversion progressed.

Mafu *et al.* (2018) were able to draw correlations between the reactivity of any feedstock and the feedstock's inherent H/C atomic ratio and alkali index ((Eqn. 2-7). Mafu *et al.* (2018) calculated the alkali index with:

$$AI = \frac{K_2O}{SiO_2 + Al_2O_3 + P_2O_5}. \qquad \text{(Eqn. 2-7)}$$

Also, a relationship between the reactivity and the crystalline size, crystalline size/interlayer spacing ratio, and the micropore surface area of the biomass feedstock was observed.

In most cases, biomass-coal blends would exhibit a combined reactivity, according to the mass fraction of individual samples used (Jeong *et al.*, 2014; Mafu *et al.*, 2018; Wei *et al.*, 2019; Wei, Guo, Gong, *et al.*, 2017; Yuan *et al.*, 2012). Co-gasification of hardwood-coal and softwood-coal blends in comparison with coal had a higher reactivity at conversions below 40%; afterwards, the reactivity decreased and converged to a conversion profile similar to that of coal. This was linked with the biomass portion reacting more readily since no synergy was observed. The reactivity of sorghum-bagasse-coal blends showed improved reactivity over the entire conversion profile and was linked with the high ash content and ash composition of the biomass. The increase in reactivity with higher biomass-to-coal ratios was attributed to the higher AAEM concentrations of biomass (Mafu *et al.*, 2018). Similar observations were made by Jeong *et al.* (2014), referring specifically to potassium's ability to form intercalation compounds with carbon.

Based on the reactivity index ($R_{X=50\%}$), rice straw and petroleum coke blends showed improved reactivity with larger fractions of rice straw. The reactivity index increased with a factor of 1.3, 1.8 and 3.5 with higher fractions of hydrochar at a gasification temperature of 950°C (Wei, Guo, Gong, *et al.*, 2017). At a gasification temperature of 1000°C, the factorial increase was

2.3, 3.5 and 4.5, respectively. Wei *et al.* (2017) linked the increased reactivity to the effect of active AAEM on the petroleum cokes reactivity. Wei *et al.* (2017) calculated the relative transformation ratio (P) with:

$$P_{i,X}=1-\frac{W_{i,X,exp}}{W_{i,X,cal}}, \quad \text{(Eqn. 2-8)}$$

showing that potassium underwent an inhibiting effect during co-gasification, which eluded to the volatile potassium in rice straw evaporating and depositing onto the surface of the petroleum char.

In the study by Wei *et al.* (2019), the reactivity of blends (anthracite-rice-straw and bituminous-coal-rice-straw blend) against the anthracite and bituminous coal, increased with a factor of 3.0 and 1.5, respectively, at a gasification temperature of 900°C (Wei *et al.*, 2019).

Zhang *et al.* (2016) investigated the effect of different biomass (orange peel, Chinese redwood and soybean stalk) on the reactivity of biomass-coal blends during CO_2 co-gasification. A comparison between experimental and calculated conversion data showed improved reactivity (synergy) and achieved 95% conversion in $7\ \text{min} - 18\ \text{min}$, whereas the calculated conversion time for all four cases was 21 minutes.

Xu *et al.* (2016) investigated the gasification reactivity of four biomasses and linked the reactivity of the biochars to the ash composition. Xu *et al.* (2016) calculated the catalytic index (A) with

$$A=ASH\times\frac{Fe_2O_3+CaO+MgO+Na_2O+K_2O}{SiO_2+Al_2O_3}, \quad \text{(Eqn. 2-9)}$$

using the index to draw a comparison between the biochars.

2.8.4.1 Synergy during lignocellulosic biomass and coal co-gasification

Synergy/inhibition is determined by comparing the experimental reactivity as a function of time, with the calculated reactivity based on the mass fraction. Previous authors calculated a synergy factor/index (SI_X) with

$$SI_X = \frac{t_{X,cal}}{t_{X,exp}}, \quad \text{(Eqn. 2-10)}$$

quantifying the synergistic/inhibiting behaviour as a function of time (Wei *et al.*, 2019; Wei, Guo, Gong, *et al.*, 2017; Zhang *et al.*, 2016). A synergy index greater than 1 suggested synergistic behaviour and a synergy index less than one an inhibiting behaviour.

Zhang *et al.* (2016) evaluated synergy at a conversion of 95 %. According to the synergy index, the blends with the highest synergy corresponded with blends made up of biomass with the highest potassium content, which were orange peel and soybean stalk. Active AAEM, such as potassium, migrates to other particles during gasification at high temperatures. According to Huang *et al.* (2009), alkali metals are inclined to form intercalation compounds with carbon, which weakens the carbon-carbon bonds by increasing the interlayer distance and causing volume expansion. On the other hand, there is a difference between active and non-active AAEM, which could be highlighted by comparing the synergy index of blends with peanut shell and Chinese Redwood. Higher concentrations potassium was measured on the surface of coal's semi-char during co-gasification of peanut shell-coal blends; however, this was non-catalytic potassium likely originating from volatile potassium bound to cellulosic fragments during co-pyrolysis. A synergetic effect during co-gasification of peanut shell-coal blends was observed after complete ash generation occurred; therefore, it was suggested by Zhang *et al.* (2016) that the potassium in the ash is catalytic.

Jeong *et al.* (2014) reported synergy for all pine sawdust-coal blends. It was observed that synergy increased with larger fractions pine sawdust and elevated temperatures. Contrary to the relationship between synergy and the biomass fraction, Yuan *et al.* (2012a) observed synergy for only low biomass-coal ratios and was credited to the lower degree of order of the blend versus the theoretical value. The calculated and experimental value for the L_c/d_{002} ratio was 4.2 and 3.5 (rounded to the first decimal), respectively. The specific surface area of the co-pyrolysis char was smaller than the calculated value; therefore, it was concluded that the degree of order, along with the active AAEM, was the main contributors towards the observed synergy. The one-to-one biomass-coal ratio exhibited a lower reactivity and was attributed to the lower specific surface area and higher degree of order with respect to the calculated values. Even though higher biomass-coal ratios had increased specific surface area and a lower degree of order, no synergy was observed, which was likely due to the packing density having a negative effect on the diffusion rates. These results shows that synergy or inhibition may be the results of a combined effect of several factors.

Wei *et al.* (2019) used the synergy index (Eqn. 2-10) to quantify the synergetic effect during the co-gasification of biomass and coal samples. The synergy factor at a conversion of 90% was used to describe the overall synergetic effect. As per this definition, the overall synergy behaviour during co-gasification of rice straw and bituminous coal was classified as a synergetic effect. However, opposing the results reported by Jeong *et al.* (2014) with regards to the relationship between synergy and temperature, the synergetic effect was weakened with higher temperatures. Regarding the entire conversion profile, the initial behaviour was inhibition, but as the gasification process progresses, the behaviour changed to a synergetic effect, which was enhanced with higher conversion.

Similar to the rice straw and bituminous coal blends, the overall synergy behaviour for co-gasification of rice straw and anthracite, was reported as a synergetic effect. However, the degree of synergy was weakened with higher gasification temperatures. A comparison between the two coals showed that the anthracite had a higher overall synergy (at a conversion of 90%). Furthermore, the rice straw and bituminous coal blends initially exhibited decreasing inhibition, which transitioned to a synergetic effect at conversions below 30%. A rapid increase in synergy, as quantified by the synergy factor, was observed and reached a maximum at a conversion of 50%, after which a gradual decrease in the synergy factor was observed.

Wei *et al.* (2019) used the relative transformation ratios to clarify active AAEM transformation characteristics and to explain reactivity and synergy during co-gasification. The rice straw char had ample amount of potassium in comparison with bituminous coal, with lesser amounts of calcium. The calcium content of bituminous coal char was greater than that of the rice straw char. The rice straw and bituminous coal blends initially demonstrated a decreasing promoting effect for potassium, transitioning to an inhibition effect at a conversion of 50%, which was strongly inhibited between conversions of 50% and 90%. Calcium exhibited a gradual increasing promotional effect over the entire conversion profile. The promoting effect observed for calcium was linked to the high silicon content in the rice straw, which promote calcium in bituminous coal via deactivation reactions and the formation of acid-soluble and residual calcium. The initial promoting effect of potassium was linked to the increased residence time of potassium in dense cluster biochar-coal-char blend. The potassium was promoted via deactivation reactions with mineral matter such as SiO_2. As the biochar is converted and ash formation of biochar is completed, more SiO_2 is exposed. At the same time, coal char is converted, which exposes more calcium and creates a more porous structure as quantified by specific surface area. Since SiO_2 has a higher affinity towards calcium and

potassium is easily absorbed on the surface of the porous carbon structure, potassium is inhibited, and calcium is promoted as higher conversions are reached. The adsorption of K was supported by a K/Si ratio from 0.35 ─ 1.80 (Wei *et al.*, 2019).

With regards to the biomass-anthracite blends, active potassium was the main active AAEM in the char blends. Initially, a promoting effect was observed, which changed to an increasing inhibition effect up to a conversion of 50%. Between 50% and 90%, a decreasing inhibition effect was observed. Inhibition at low temperatures was linked to the adsorption of potassium on the increased surface area of anthracite char during co-gasification, which was supported with the high K/Si ratio for semi-chars. The decreasing inhibition effect of potassium was connected to the decreasing specific surface area at higher conversion, a characteristic of anthracite char as the conversion progresses, and the deactivation reaction with SiO_2 and Al_2O_3 after complete formation of anthracite ash (Wei *et al.*, 2019).

2.8.5 Reactivity of hydrochar and hydrochar-coal char blends against lignocellulosic biomass and coal during CO_2 gasification

The reactivity and synergy of hydrochar-petroleum coke (Wei *et al.*, 2017b) and hydrochar-bituminous coal blends (Wei *et al.*, 2017b) were investigated as a function of the fraction of hydrochar and temperature during co-gasification. It was found that the gasification time required to achieve equivalent conversion decreased with higher temperature and larger hydrochar/coal ratios (Wei, Guo, Ding, *et al.*, 2017; Wei, Guo, He, *et al.*, 2017a). In both studies, the reactivity index ((Eqn. 2-6) was used to compare the blends and hydrochar against the petroleum coke quantitatively. A higher RI value is indicative of higher reactivity.

For all samples, the RI value increased with higher hydrochar fractions and increasing temperature, yet the effect of hydrochar was smaller at higher gasification temperatures. As an example, at a constant gasification temperature (1000°C) the sample blends with increasing mass fraction hydrochar (0.25, 0.50, 0.75, and 1) had a RI value of 3.6, 9.6, 7.7, and 234.7 greater than that of the petroleum coke RI value, but at 1150°C the RI value was 2.7, 6.1, 10.8, and 60.4 times greater (Wei, Guo, Ding, *et al.*, 2017). Similar observations were made by (Wei, Guo, He, *et al.*, 2017a) and elude to the narrowing gap between the reactivity of hydrochar and coal.

Comparing calculated and experimental conversion curves, early stages of co-gasification exhibited an inhibition effect but transforms to a synergistic effect at mid-late stages (Wei, Guo, Ding, *et al.*, 2017; Wei, Guo, He, *et al.*, 2017a). A synergy factor defined as

$$A_{X,T}=\frac{t_{X,T,cal}}{t_{X,T,exp}} \qquad \text{(Eqn. 2-11)}$$

quantified the synergistic effect of blends (Wei, Guo, Ding, *et al.*, 2017; Wei, Guo, He, *et al.*, 2017a). Based on the synergy factor, all hydrochar-coke/coal blends had a synergistic effect during co-gasification and higher overall synergistic effect occurred at lower temperatures and higher fractions of hydrochar (Wei, Guo, Ding, *et al.*, 2017; Wei, Guo, He, *et al.*, 2017a). For hydrochar-petroleum blends, the synergy increased with conversion; however, after reaching a maximum value during mid-late stages of conversion, it decreased, which correlated with the active AAEM content. The active AAEM content decreased at higher conversions due to volatilisation and deactivation. Based on the relative transformation ratio of active AAEM, early stages characterised with continuously enhanced synergy during co-gasification was linked to continuous increasing inhibition effect of potassium and calcium and decreasing promotion effect of sodium. During mid-late stages of conversion, the decreasing synergy was linked to the decreasing inhibition effect and increasing promotion effect as mentioned before. Overall, it was concluded that higher fractions hydrochar and higher temperatures would be beneficial for longer-lasting and enhanced the synergistic effect (Wei, Guo, Ding, *et al.*, 2017).

(Wei, Guo, He, *et al.*, 2017a) investigated co-gasification synergy and reactivity of hydrochar-bituminous coal blends as a function of temperature and hydrochar fraction. The results agreed with (Wei, Guo, Ding, *et al.*, 2017). High synergy, as quantified by the synergy factor, was observed at lower temperatures (800°C ─ 850°C), but decreased when co-gasification was executed at higher temperatures. This behaviour was attributed to calcium, which was one of the main active AAEM species in the blends. The relative transformation ratio of the active calcium, as determined by

$$P=1-\frac{W_{active\ i\text{-}exp}}{W_{active\ i\text{-}cal}}, \qquad \text{(Eqn. 2-12)}$$

was positive and gradually increased with higher co-gasification temperatures, which alludes to the promotion of active calcium transformation. The concentration of sodium was lower but had similar behaviour as to calcium.

Active potassium transformation was increasingly inhibited over the entire temperature range that was tested. This inhibition was likely due to preferential reaction with calcium/sodium and inert matter. A strong connection between the promotion of active AAEM transformation and the mineral content of the ash of the bituminous coal was observed. SEM analysis indicated the migration and deposition of active AAEM species on the semi-char surface of bituminous coal. Therefore, the increased synergy of blends with higher fractions hydrochar is related to a decline in deactivation reactions since the blends contained a smaller amount of ash derived from the bituminous coal (Wei, Guo, He, *et al.*, 2017a).

CHAPTER 3: EXPERIMENTAL SETUP

3.1 Introduction

The experimental methods, materials, analytical methods, and equipment used in this study are discussed in Chapter 3. Figure 3-1 illustrates the process flowchart for the experimental plan. In short, hydrochar was produced from sugarcane bagasse via continuous hydrothermal liquefaction. The properties of pellets produced from sugarcane bagasse, hydrochar, GreenCoal (GC3:1, GC1:1 and GC1:3) and coal were evaluated, and the pellets thermal characteristics were compared under combustion and gasification conditions.

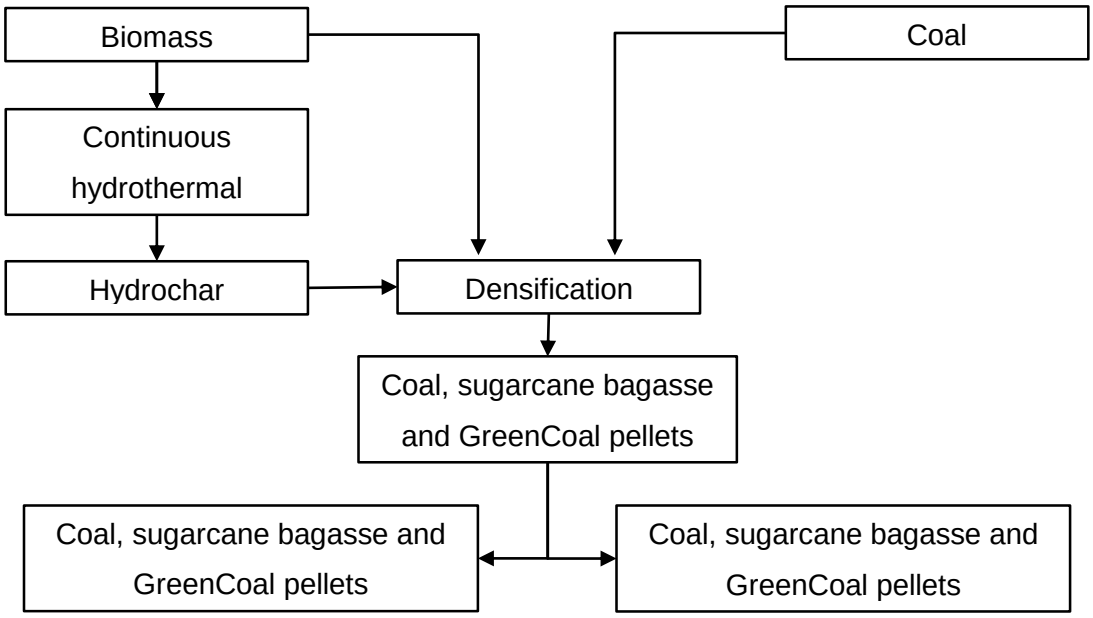

Figure 3-1: Experimental flow chart

3.2 Materials, origin and characterisation

The Sugar Milling Research Institute (SMRI) sourced and supplied sugarcane bagasse (SB) and coal (C) samples from a sugar mill based in Kwazulu-Natal (South Africa). Upon delivery, the sugarcane bagasse had a very high extraneous moisture content and was relatively clean. The bagasse was air-dried in an enclosed area for three weeks to prevent

moulding/biodegradation and screened to remove fine particulates. A hammer mill with a 0.8 mm aperture strainer was used to mill the sugarcane bagasse, and a sieve with 1 mm apertures retained the oversized sugarcane bagasse. The oversized product originated from sugarcane bagasse bypassing the strainer and was circulated back into the hammer mill feed until it passed the 1 mm sieve size. A cone and quartering procedure was employed to divide the large sample into representative samples, which was stored in vacuum-sealed bags.

The coal sample consisted of large lumps with varying sizes. The coal was crushed with a jaw crusher into smaller pieces and screened with a sieve having 3 mm apertures. Oversized product was circulated back into the feed of the jaw crusher. Afterwards, the crushed coal was dried in ambient conditions for 24 hours and then pulverised with an in-house built ball mill. Oversized particles (>710 µm) circulated back into the ball mill. Afterwards, a rotary sample splitter separated the coal sample into six representative samples, which was stored in zip lock sealed bags.

3.2.1 Proximate and ultimate analysis

Samples were placed in an environment-controlled room for 24 hours to ensure that the moisture content of samples was at equilibrium. The environment-controlled room was kept at a temperature and humidity of 22°C and 40%, respectively. Proximate analysis was conducted on sugarcane bagasse-, hydrochar-, GreenCoal 3:1-, GreenCoal 1:1-, GreenCoal 1:3- and coal samples. A sample of one-gram was used for analysis.

The mass of all samples was recorded with an analytical balance (Mettler Toledo AB204-s) to the nearest $1x10^{-4}$ g and a Lenton muffle furnace with a TOHO 300 Series Ramp Micro-Processor Temperature Controller was used for Step 3 and 4. The vacuum oven was built in-house and was kept at 50 kPa vacuum. The inherent moisture-, volatile matter- (VM), ash- (ASH), and fixed carbon content (FC) was calculated with

$$\text{Inherent moisture (\%)} = \frac{m_i - m_D}{m_i} \times 100\%, \qquad \text{(Eqn. 3-1)}$$

$$\text{VM (\%)} = \frac{m_D - m_{VM}}{m_i} \times 100\%, \qquad \text{(Eqn. 3-2)}$$

$$\text{ASH (\%)} = \frac{m_{ash}}{m_i} \times 100\%, \qquad \text{(Eqn. 3-3)}$$

and

FC (%) = 100%-inherent moisture-VM-ASH, (Eqn. 3-4)

respectively.

Representative sugarcane bagasse, hydrochar, GreenCoal (GC3:1, GC1:1 and GC1:3) and coal sample was submitted to Bureau Veritas Analytical Services Pty. (Ltd.) for ultimate analysis and total sulphur analysis. The ultimate and total sulphur analysis was carried out according to ISO 29541: 2010 and ISO 19579: 2006, respectively. The oxygen content was calculated by difference.

3.2.2 XRD and XRF analysis

The mineralogy and the composition of sugarcane bagasse, hydrochar and coal samples were determined with XRD and XRF analysis and were submitted to the XRD and XRF laboratory at the Centre for Water Science and Management, North-West University (NWU) Potchefstroom Campus.

A black loading preparation method was used for XRD analysis. A PANalytical X'Pert Pro diffractometer with X'Celerator detector and fixed slits with Fe-filtered Co-Kα radiation was used for XRD analysis. The crystalline mineral phases were identified using PANalytical Highscore^{+}program, ICDD PDF 4+ and PAN ICSD database, while the relative phase amounts (weight %) were estimated using the Rietveld method.

For the XRF analysis, the samples were first dried at 105°C for 3 hours to determine the loss of moisture. The loss on ignition was determined by high-temperature ashing (HTA) of samples in the air with an oven at 1000°C. This was followed by a 15-minute borate fusion (0.3 g sample +6 g flux) using Claisse® 66:33 LiT:LiM (Lithium Tetraborate:Lithium Metaborate) flux with a LiI (Lithium Iodide) releasing agent in a platinum crucible. A PANalytical (Axios Max) WD-XRF spectrometer, equipped with a 50 kV Rh-anode X-ray tube, six filters, a P10 gas purge facility and a high-resolution silicon drift detector was used. The PANalytical (Axios Max) WD-XRF spectrometer was calibrated with international and national certified reference materials (CRMs). For XRF data quantification, the intensity of the

characteristic lines of the elements was measured, and the concentrations of the elements in the sample were calculated from the measured intensities.

3.2.3 Fibre analysis

A sugarcane bagasse and hydrochar sample was submitted to ARC-Irene Analytical Services PTY (Ltd) for fibre composition analysis and were carried out according to ASM methods, which are declared in Table 3-1. Fibre analysis was determined according to the Van Soest method, which determines the neutral detergent fibre (NDF), acid detergent fibre (ADF) and acid detergent lignin (ADL).

Table 3-1: Compositional analysis performed by ARC-Irene Analytical Services Pty (Ltd)

Analysis	Method number
Neutral detergent fibre	ASM 060
Acid detergent fibre	Not SANAS accredited
Acid detergent liquids	Not SANAS accredited

3.2.4 Analysis of heating value

The higher heating value (HHV) was determined in-house for sugarcane bagasse, hydrochar, GreenCoal (GC3:1, GC1:1 and GC1:3) and coal with an IKA C 2000 calorimeter system (ISO 1928:2009). Prior to analysis, the samples were placed in an environment-controlled room for 24 hours to ensure the moisture content was at equilibrium. One-gram sample was used for analysis.

3.2.5 Fourier-transform Infrared Spectroscopy (FTIR)

Diffuse reflectance spectra were recorded on a Shimadzu IRAffinity-1 FTIR spectrometer fitted with a PIKE Technologies EasiDiff accessory. Samples of sugarcane bagasse, hydrochar and coal were analysed in a KBr matrix. Spectra were recorded between 4000 cm^{-1}–400 cm^{-1}, at 4 cm^{-1} resolutions with 45 scans.

3.2.6 Scanning electron microscopy (SEM)

A FEI Quanta 250 Field Emission Gun (FEG) Scanning Electron Microscope (Environment Scanning Electron Microscope) on high vacuum was used to analyse the morphology of the sugarcane bagasse, hydrochar and coal. Powder samples were mounted on an aluminium stud using double-sided carbon tape, which increases conductivity. The mounted sample was coated with carbon to enhanced conductivity and prevent charge build-up in the SEM.

Secondary electron images of the samples were obtained in an FEI Quanta FEG 250 Scanning electron microscope (SEM) operating at an accelerating voltage of 15 kV. For compositional analysis, an Oxford Energy Dispersive Spectrometer (EDS) working on Inca software was used.

3.3 Beneficiation of sugarcane bagasse via continuous hydrothermal liquefaction

A continuous hydrothermal liquefaction pilot plant was used for hydrothermal liquefaction of sugarcane bagasse. Mass and Heat Transfer Pty. (Ltd) designed and fabricated the pilot plant for North-West University. The process consists of a feed system, preheater, reactor, cooler, four product tanks, as well as a hot oil plant (see Figure 3-2). The feed system is a series of four interconnected tanks and a special design slurry pump. Flow-through the reactor was controlled with a pressure difference between the feed side and product side by continuously pressurising the feed tanks and relieving the pressure on the product side.

A sugarcane bagasse slurry was prepared a day in advance to allow the biomass to absorb water and swell completely. A biomass to water mass ratio of 1 to 25 was used. The biomass-water slurry prepared contained 100 kg of water. The biomass-water mixture was loaded into the feed tanks, and the tanks were sealed. The circulating pump was activated to keep the biomass-water mixture in suspension. The system was pressurized with nitrogen to 70 bar while the hot oil plant was systematically ramped to the desired temperature to heat the reactor section. The hot-oil plant's outlet temperature was set to 270°C. Once the temperature inside the reactor had stabilized, valves upstream and downstream to the preheater were opened to heat the preheater. After the temperature of the hot oil plant, reactor and preheater stabilized, a constant pressure difference between the feed and product tanks was induced to initiate flow. A flow rate of 120 L/hr (the maximum flow rate of the reactor) was chosen. The resulting residence time inside the reactor was 10 minutes. A water cooler cooled the product exiting

the reactor before entering the product tanks. The plant was operated for approximately one hour to allow all the feed to pass through the plant at the chosen flow rate. Once all the feed passed through the reactor, the system was cooled to ambient temperature, and the products tanks were depressurised and drained.

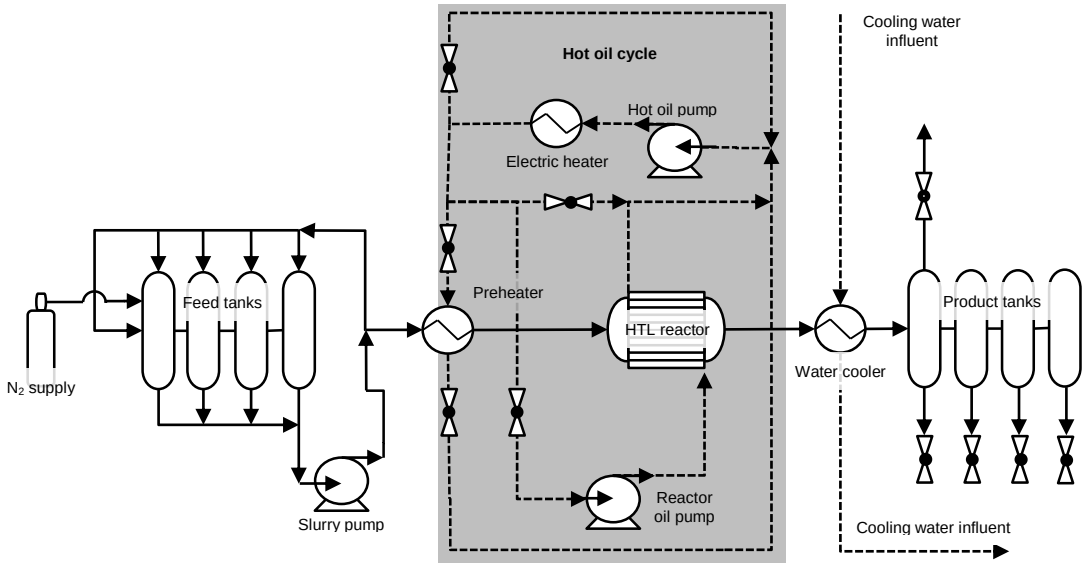

Figure 3-2: PFD of the continuous HTL plant

The hydrochar was separated from the aqueous phase with Büchner funnel with a particle retention size of 2.5 µm. The hydrochar collected on the filter paper was washed with demineralised water until the filtrate was clear. The hydrochar was dried at 105°C for 24 hours and stored in zip lock bags.

3.4 Pelletizing

Pelletisation was performed using a similar method employed by Kambo & Dutta (2014). All three samples, namely raw sugarcane bagasse, hydrochar and coal, were milled to a particle size range less than 710µm (Kambo & Dutta, 2014). The sugarcane bagasse and coal were milled with an in-house built ball mill. The hydrochar was milled with a mortar and pestle. The materials were stored in a climate control room (22°C and 40% humidity) for 24 hours to ensure the moisture content of the different sample was at equilibrium under the same conditions. A Specac's Atlas Series Manual Hydraulic Press (GS25011 Manual 25-ton

Hydraulic Press) with a 13 mm cylindrical die, made of hardened stainless steel, was used (see Figure 3-3 and Figure 3-4) for pelletising. One gram of sample was used to produce pellets.

Sugarcane bagasse, hydrochar, coal and three types of GreenCoal pellets were produced. The GreenCoal pellets were made with blends of hydrochar and coal with a hydrochar/coal ratio of 3:1, 1:1 and 1:3 and the labels used were GC3:1, GC1:1 and GC1:3, respectively. Small batches of hydrochar and coal mixtures were prepared in advance. The inner surface of the die was lubricated with demineralised water, using a 5 mL pipette, to facilitate the removal of the pellet from the die and to prevent it from breaking. Excess water was removed by absorbance onto a hand towel. The die was assembled, and the sample was loaded into the die, as shown in Figure 3-4, and compressed to 8.6 MPa. The sample was kept under pressure for 30 seconds. A custom-built manual lever press was used to remove the pellet from the die. After exposing the pellets to a controlled environment for 48 hours, it was stored in sealable containers.

Figure 3-3: Specac's Atlas Series Manual Hydraulic Press

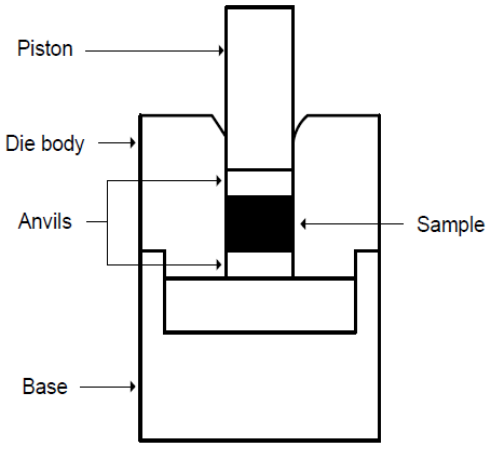

Figure 3-4: Parts and assembly of 13 mm die

3.4.1 Mass and energy density

A stereometric method was used to calculate the mass density of each pellet. Each pellet was weighed with an analytical balance (Mettler Toledo AB204-s) to the nearest $1x10^{-4}$ g. The volume of each cylindrical pellet was calculated by measuring the dimensions (diameter and length) of each pellet with a calliper to the nearest 0.02 mm. The equation to calculate the energy density, by multiplying the mass density of the pellet with the HHV of the pellet (Kambo & Dutta, 2014), was

$$\text{Energy density } (GJ/m^3) = \rho_{pellet}\ (kg/m^3) \times HHV\ (MJ/kg). \qquad \text{(Eqn. 3-5)}$$

3.4.2 Equilibrium moisture content

The equilibrium moisture content (EMC) of the different pellets was used as an indicator of hydrophobicity. After exposing the pellets to a controlled environment for 24 hours, the mass of the pellets was recorded with an analytical balance (Mettler Toledo AB204-s) to the nearest $1x10^{-4}$ g, and dried in a vacuum oven at 105°C for 24 hours. The EMC was the difference between the mass of the pellets before and after drying, calculated with (Kambo & Dutta, 2014)

$$EMC\ (\%) = \frac{m_{pellet,i} - m_{pellet,f}}{m_{pellet,i}} \times 100\%, \qquad \text{(Eqn. 3-6)}$$

where m is the mass of the pellet, i is the conditions before drying, and f is the conditions after drying.

3.4.3 Compression strength

In this study, an MTS Landmark Servohydraulic Test System was used to test the compression strength. The compression strength of sugarcane bagasse, hydrochar, GreenCoal (GC3:1, GC1:1 and GC1:3) and coal pellets were determined with a method similar to the one developed by Nielsen *et al.* (2009:3211–3216), which was also replicated by other authors (Kambo & Dutta, 2014). A pellet was placed on its side (the weaker orientation) between two

horizontal plates and was compressed at a rate of 0.01 mm/s. The compression strength was quantified as the maximum force (N) a pellet can withstand before the pellet fractured.

3.4.4 Drop test: durability and impact resistance

During the manufacturing and transportation of pellets, the pellets are exposed to different physical forces that can be simulated in the laboratory. The unloading from tipper trucks or feeding on chutes into bins at pellet manufacturing plants, can be simulated by measuring the impact resistance, drop resistance or the shattering resistance (Kambo & Dutta, 2014). A drop test, similar to Kambo & Dutta (2014), was used to evaluate the drop resistance of sugarcane bagasse, hydrochar, GreenCoal (GC3:1, GC1:1 and GC1:3) and coal pellets. Pellets were weighed to the nearest $1x10^{-4}$ grams and were dropped four times on a steel plate from a two-meter height. The drop resistance was quantified as percentage mass loss after the pellet was dropped four times (Kambo & Dutta, 2014). In cases where the pellet broke into two large particles, the largest particle was used to complete the drop resistance test.

The impact resistance of sugarcane bagasse, hydrochar, GreenCoal (GC3:1, GC1:1 and GC1:3) and coal pellets were quantified by the impact resistance index (IRI) (Division, 1990). Five pellets from each sample were weighed individually to the near $1x10^{-4}$ g and were dropped from a two-meter height on a concrete floor. After each drop test, the unbroken pellets were dropped again. The drop test was repeated five times for unbroken pellets. The number of drops and pieces for each pellet was recorded, calculating the IRI with

$$\text{Impact resistance index (IRI)} = \frac{\text{average number of drops}}{\text{average number of pieces}} \times 100. \qquad \text{(Eqn. 3-7)}$$

For laboratory work, an IRI of 50 is the lowest acceptable index for fuel briquettes that are developed for industrial or domestic application.

3.4.5 Water-resistance capacity

The short term exposure to high humidity conditions or rain during storage or transportation may affect the quality of the pellet; therefore, it is important to investigate the strength of the pellets when exposed to wet conditions. The water resistance capacity (WRC) of pellets was determined with a method developed by previous authors (Pimchuai *et al.*, 2010) and was

used as an indicator of hydrophobicity. Sugarcane bagasse-, hydrochar-, GreenCoal- (GC3:1, GC1:1 and GC1:3) and coal pellets were weighed to the nearest $1x10^{-4}$ gram and submerged in water for two hours. Pellets were placed on a hand towel to absorb excess water and exposed to a controlled environment for four hours. Afterwards, the mass of the pellets was measured. The water resistance capacity was calculated with

$$\text{WRC (\%)} = \frac{\text{Initial mass of pellet (g) - final mass of pellet/material (g)}}{\text{Initial mass of pellet (g)}} \times 100\%. \quad \textbf{(Eqn. 3-8)}$$

3.5 Combustion behaviour of sugarcane bagasse, hydrochar and GreenCoal against coal

A non-isothermal thermogravimetric (TG) and derivative thermogravimetric (DTG) technique were employed to investigate the combustion behaviour of sugarcane bagasse, hydrochar, GreenCoal (GC3:1, GC1:1 and GC1:3) and coal pellets. Figure 3-5 demonstrates the setup used, which had the following components: An Elite Thermal System with a vertical tube furnace mounted on a rig and a temperature controller, an analytical balance (Radwag PS 750.R1) connected to a computer that records the mass every two seconds, and Econo-Trak Model C50 mass flow controller. For the combustion experiments, thermogravimetric analysis was executed under an oxidative atmosphere which was induced by dry air with a volumetric flow rate of two sLpm (standard litres per minute). The temperature range was room temperature to 1000°C.

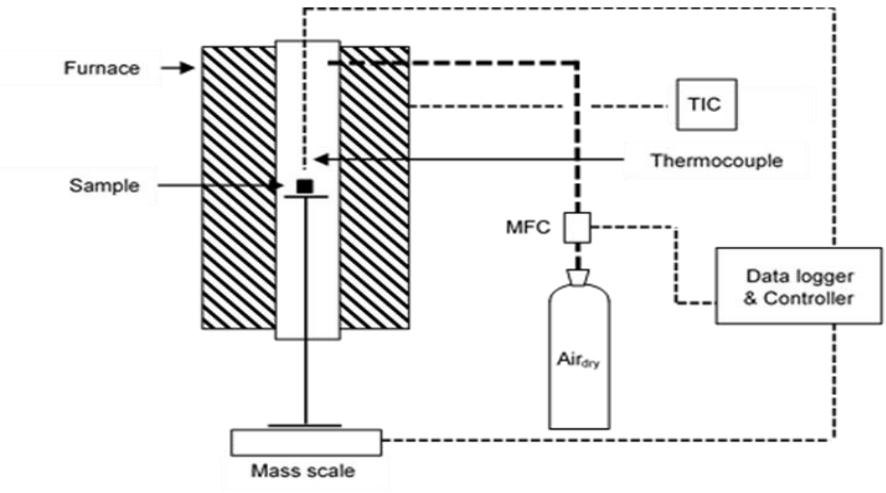

Figure 3-5: Thermogravimetric analyser setup

One gram pellets with a 13 mm diameter were used for thermogravimetric analysis. The effect of three heating rates (5 °C/min, 7.5 °C/min and 10 °C/min) was investigated. The mass of the pellet and the temperature, measured five millimetres above the pellet, was recorded every two seconds.

The mass-time-temperature data generated, was used to determine the combustion properties of each sample, including the ignition temperature (T_i), peak temperature (T_p), burnout temperature (T_f), maximum combustion rate ($[dm/dt]_{max}$) and mean combustion rate ($[dm/dt]_{mean}$).

Figure 3-6 shows by what method the ignition and peak temperature was determined. An intersection method (Lu & Chen, 2015) was used to determine the ignition temperature and was determined at the intersection point of two lines tangential to the mass curve (TG curve). The first line was tangential to the curve at the start of the thermogravimetric analysis, and the second line was tangential to the point on the mass curve corresponding to the maximum combustion rate.

The mass-time-temperature data was used to construct a DTG-curve, i.e. the mass loss rate over temperature. The DTG-curve was used to determine the peak temperature and the maximum combustion rate. The peak temperature (coincides with the maximum mass loss rate ($[dm/dt]_{max}$) as shown in Figure 3-6 (Demirbas, 2004).

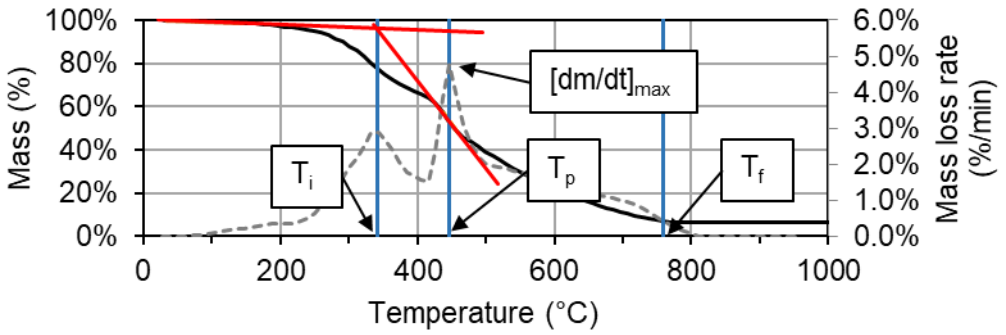

Figure 3-6: Approximation of ignition – and burnout temperature (example: TG curve of HC, dT/dt = 10 °C/min)

The burnout temperature was the point at which 99% conversion (ash-free basis) was achieved (Lu & Chen, 2015). The mass percentage at a conversion of 99% was calculated with

$$\text{Mass (\%)}|_{@\ X=99\%} = \frac{0.99\times(m_i-m_f)}{m_i}\times 100\%. \qquad \text{(Eqn. 3-9)}$$

The burnout temperature was determined with the aid of the thermograph, as demonstrated in Figure 3-6.

The mean combustion rate was calculated with

$$[dm/dt]_{mean} = \frac{\sum_{i=1}^{n}[dm/dt]_i}{N}, \qquad \text{(Eqn. 3-10)}$$

and taking the mean mass loss rate over a temperature range starting at the ignition temperature and ending at the burnout temperature. The subscript i denotes the mass loss rate of data point i in a collection of data points with N components. For i = 1 and i = n, the mass-loss rate corresponds to the mass loss rate measured at the ignition temperature and burnout temperature, respectively.

The equations used to calculate the ignition index (C) and comprehensive combustion index (S) were

$$C = \frac{[dm/dt]_{max}}{T_i^2} \qquad \text{(Eqn. 3-11)}$$

and

$$S = \frac{[dm/dt]_{max}[dm/dt]_{mean}}{T_i^2 T_f}, \qquad \text{(Eqn. 3-12)}$$

respectively (Wang *et al.*, 2016).

3.6 CO_2-gasification of sugarcane bagasse, hydrochar, GreenCoal, and coal

An isothermal thermogravimetric technique was employed to investigate the reactivity of sugarcane bagasse, hydrochar, GreenCoal (GC3:1, GC1:1 and GC1:3) and coal pellets. Figure 3-7 demonstrates the setup used, which had the following components: an Elite tube furnace mounted on a rig, Econo-Trak Model C50 mass flow controllers, an analytical scale (Radwag PS 750.R1), a temperature controller and a data logger. The main gas feed line to the TGA was connected to nitrogen and a carbon dioxide gas line. Small manual ball valves (not shown in Figure 3-7) was connected downstream from the mass flow controllers to switch between nitrogen and carbon dioxide. Nitrogen (Baseline 5.0) and Technical Carbon Dioxide was supplied by Afrox and were used as inert and reactant gas, respectively.

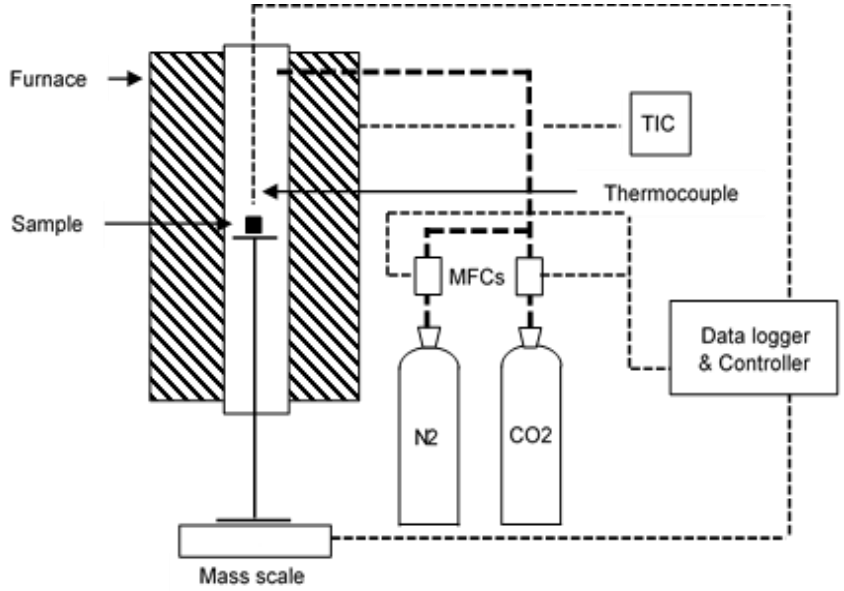

Figure 3-7: Thermogravimetric analyser setup

The technique entailed a three-step procedure, which included a drying, pyrolysis, and gasification step. Drying was completed in an inert atmosphere (N_2) with a volumetric flow rate of four-sLpm and a heating rate of 5 °C/min from room temperature to 105°C. The sample was kept at 105°C for 20 minutes. Pyrolysis was executed in an inert atmosphere (N_2) with a volumetric flow rate of four-sLpm and a heating rate of 10 °C/min from 105°C to the desired final temperature. Once the final temperature was reached, the system was allowed 15 minutes to reach thermal equilibrium, and the gas feed was switched to CO_2. A CO_2 volumetric

flow rate of five-sLpm was used. The experiment was stopped after the mass loss stabilised (dm/dt≈0).

The pellets used for isothermal thermogravimetric analysis had a mass of 500 mg and a diameter of 10 mm. The three temperatures investigated during CO_2 gasification was 950°C, 1000°C and 1050°C. The mass of the pellet and the temperature, 5 mm above the pellet, was recorded every two seconds.

The normalised mass, temperature and time data was used to calculate the conversion (X) as a function of time with

$$X_{(t)} = \frac{m_0 - m_t}{m_0 - m_f}, \qquad \textbf{(}\text{Eqn. 3-13}\textbf{)}$$

where m_0 denotes the initial mass of the sample, m_t the mass of the sample at time t and m_f the final mass of the sample after CO_2 gasification is completed. The equation used to calculate the reactivity $R_{(t)}$ was

$$R_{(t)} = \frac{1}{(1-X_{(t)})} \times \frac{dX_{(t)}}{dt}. \qquad \textbf{(}\text{Eqn. 3-14}\textbf{)}$$

CHAPTER 4 RESULTS AND DISCUSSION

4.1 Introduction

Chapter 4 provides a discussion of the results obtained for the experiments and analyses completed according to the experimental setup presented in Chapter 3. All the raw data used is provided in Appendix A.

Section 4.1 compares the hydrochar and GreenCoal pellets with the raw sugarcane bagasse and coal sample using physical properties and chemical composition. The physical and chemical properties included the proximate-, ultimate composition, higher heating value, organic structure via FTIR analysis, morphology via SEM analysis, mineral composition via XRD and XRF analysis, organic components via fibre analysis and other derived parameters, i.e. O/C and H/C atomic ratios.

Section 4.2 discussed the pellet properties of sugarcane bagasse-, hydrochar-, GreenCoal-, and coal pellets. This discussion extends to the physical properties of the various pellets, i.e. the mass and energy density, the hydrophobic nature of the pellets, as well as the strength and durability.

In Section 4.4, the thermal decomposition of the various pellets under inert conditions (Section 4.4) and oxidising conditions (Section 4.5) discussed. Finally, in Section 4.6, the char-CO_2 gasification results were discussed.

4.2 Characterisation of sugarcane bagasse, GreenCoals, hydrochar, and coal

This section reports the results obtained from analysis completed for characterisation of sugarcane bagasse-, hydrochar-, GreenCoal- and coal samples.

4.2.1 Proximate and ultimate analysis

Table 4-1 shows the proximate composition, elemental composition (dry-ash-free basis), higher heating value (HHV) and the calculated O/C- and H/C atomic ratio for the sugarcane bagasse-, hydrochar-, GreenCoal 3:1-, GreenCoal 1:1-, GreenCoal 1:3-, and coal samples.

The sugarcane bagasse's fibre analysis (cellulose, hemicellulose, and lignin) was determined. Table 4-1 shows the confidence interval for the proximate composition and the HHV.

Table 4-1 shows that the sugarcane bagasse had low moisture-, high volatile matter-, and low fixed carbon content. The proximate composition of the sourced sugarcane bagasse was similar to other sources (Carrier *et al.*, 2012; Edreis *et al.*, 2014; Lu & Chen, 2015). Table 4-1 shows that ≈73% of the sugarcane bagasse was neutral detergent fibre (cellulose, hemicellulose, and lignin), which was linked to high volatile content (Zhao *et al.*, 2017). The main source of fixed carbon content was sugarcane bagasse's lignin content (Zhao *et al.*, 2017).

Comparing the proximate analysis of the hydrochar and the sugarcane bagasse, the inherent moisture-, volatile matter-, and ash content of hydrochar was lower, whereas the fixed carbon content increased. The moisture-, volatile matter- and ash content decreased with 1.2%, 24.8%, and 4.9%, respectively. Most noteworthy was the sharp increase in the fixed carbon content of the hydrochar with a factor of 3.4. Considering the hydrothermal liquefaction (HTL) conditions used to upgrade sugarcane bagasse to hydrochar (270°C), the observed chemical nature, i.e. lower volatile matter content and higher fixed carbon content were attributed to the decomposition of cellulose, hemicellulose, and lignin content, the formation of primary hydrochar, and the formation and re-deposition of secondary hydrochar (Lucian *et al.*, 2018). Previous work has shown that both cellulose and hemicellulose degradation products were precursors to secondary char formation, forming microspheres that were re-deposited on the surface of the hydrochar (Kang *et al.*, 2012; Sevilla & Fuertes, 2009; Sheng *et al.*, 2019). Previously, other authors showed that microspheres formed via polymerisation of glucose, which was a hydrothermal product of cellulose (Kang *et al.*, 2012; Sevilla & Fuertes, 2009; Sheng *et al.*, 2019). The proximate analysis revealed the difference between coal and sugarcane bagasse, and that HTL was an effective treatment process of sugarcane bagasse by producing a hydrochar with improved volatile matter- and fixed carbon content. The coal sample had a low volatile content (25.1%), high fixed carbon content (60.6%) and a low ash content of 14.0%.

Table 4-1: Proximate composition (ad), ultimate composition (daf) and higher heating value (HHV) of sugarcane bagasse (SB), hydrochar (HC), GreenCoal (GC3:1, GC1:1 and GC1:3) blends and Coal

Sample	SB	HC	GC3:1	GC1:1	GC1:3	Coal
Inherent moisture (%)	6.3± 0.1	5.1 ± 1.1	4.1 ± 0.3	2.6 ± 0.2	1.4 ± 0.1	0.3 ± 0.3
VM (%)	69.7 ± 0.7	44.9 ± 1.2	41.9 ± 0.7	34.7 ± 0.5	30.3 ± 0.6	25.1 ± 0.4
FC (%)	13.1 ± 0.8	44.1 ± 0.3	46.7 ± 0.4	53.6 ± 0.2	57.0 ± 0.4	60.6 ± 0.2
Ash (%)	10.9 ± 0.1	6.0 ± 0.1	7.3 ± 0.8	9.1 ± 0.7	11.3 ± 0.6	14.0 ± 0.2
C (%)	49.79	65.60	67.97	72.90	75.58	78.90
H (%)	6.92	5.60	5.40	5.24	5.12	4.97
N (%)	0.42	0.69	1.07	1.38	1.70	2.10
O (%)	42.78	27.55	24.93	19.75	16.80	13.17
S (%)	0.08	0.56	0.63	0.73	0.80	0.85
HHV (MJ/kg)	15.8 ± 0.1	27.3 ± 0.0	27.2 ± 0.1	27.1 ± 0.0	27.0 ± 0.0	26.8 ± 0.2
O/C	0.64	0.31	0.28	0.20	0.17	0.13
H/C	1.67	1.02	0.95	0.86	0.81	0.76
NDF (%)	72.8	-	-	-	-	-
ADF (%)	37.6	-	-	-	-	-
ADL (%)	7.7	-	-	-	-	-
Hemicellulose (%)	35.2	-	-	-	-	-
Cellulose (%)	29.9	-	-	-	-	-
Lignin (%)	7.7	-	-	-	-	-

Table 4-1 shows that the sugarcane bagasse had a total carbon-, oxygen-, and hydrogen content of 49.79%, 42.78%, and 6.92%, respectively. The nitrogen- and sulphur content of the sugarcane bagasse was negligible (<1%). Comparing the elemental composition of the sugarcane bagasse and hydrochar, it was clear that HTL carbonised the sugarcane bagasse and produced a hydrochar with a significantly higher carbon fraction. The total carbon content increased by ≈24% and the hydrogen content with 0.6%, whereas the oxygen content decreased by ≈24%. The higher total carbon content and lower oxygen content was mainly associated with the deoxygenation reactions, i.e. decarboxylation- and dehydration reactions (Kang *et al.*, 2012). Both the nitrogen- and sulphur fractions increased slightly. The coal sample had a very high total carbon- (78.90%), low oxygen- (13.17%), and hydrogen content (4.97%). Among the samples, coal had the highest nitrogen- (2.10%) and sulphur content (0.85%). The respective nitrogen- and sulphur content of coal was 5 and 10 times higher than that found in the sugarcane bagasse. A comparison with hydrochar shows that the nitrogen- and sulphur content of the coal was 3 times and 1.5 times higher, respectively. Table 4-1 shows that the GreenCoals had a proximate-, ultimate composition and HHV equivalent to the sum of the hydrochar- and coal fraction used to produce the various pellets.

Figure 4-1 is a general Van Krevelen diagram which includes zones indicating values for O/C- H/C atomic ratios associated with biomass, lignite, coal (i.e. sub-bituminous and bituminous coal) and anthracite. The O/C and H/C atomic ratio for the sugarcane bagasse, hydrochar, GreenCoals, and coal are shown in the Van Krevelen diagram. In general, very high O/C- and H/C values of biomass was characterised by high volumes of smoke and water vapour during thermal processing, and an indicator of low combustion efficiency (Kambo & Dutta, 2014). HTL of sugarcane bagasse produced a hydrochar with improved O/C- and H/C atomic ratios, similar to lignite (a young coal rank). The lower O/C- and H/C atomic ratios suggested that dehydration was the main reaction taking place during HTL (Lucian *et al.*, 2018). The coal sourced via SMRI is similar to other South African coal samples used in previous work (Bunt *et al.*, 2015; Leeuw *et al.*, 2016; Okolo *et al.*, 2015). GreenCoal 3:1 was located within the lignite region, while GreenCoal 1:1 and GreenCoal 1:3 approach the coal value as the fraction of coal increased. Both the GreenCoal 1:1 and GreenCoal 1:3 was similar to value typically associated with coal.

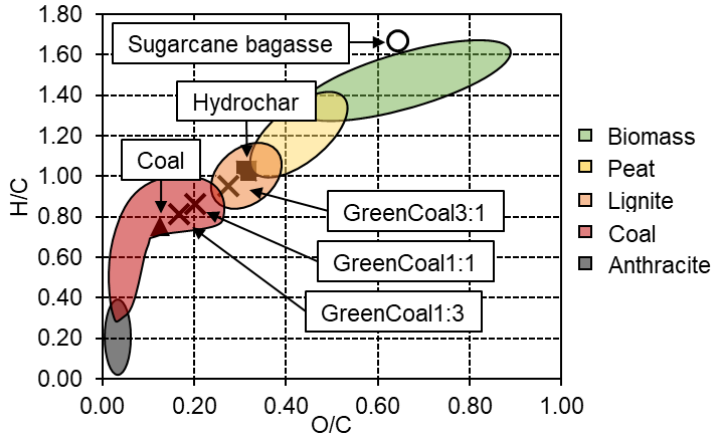

Figure 4-1: Van Krevelen diagram: Sugarcane bagasse, hydrochar and coal (Kambo & Dutta, 2014)

The HHV of the hydrochar showed a very good improvement, increasing from 16.2 MJ/kg to 27.9 MJ/kg, and was attributed to the increased carbon-, decreased oxygen-, lower moisture-, and lower ash content (Channiwala & Parikh, 2002; Demirbas, 2001; Friedl *et al.*, 2005; Sabio *et al.*, 2016; Tan *et al.*, 2015). The HHV of the hydrochar and the GreenCoals was on par with that of the coal sample, ranging between 27.0 MJ/kg─27.3 MJ/kg.

4.2.2 FTIR results for sugarcane bagasse and hydrochar

FTIR analysis used to analyse sugarcane bagasse and hydrochar with a wavelength between 4000 cm^{-1} ─ 400 cm^{-1}. Table 4-2 shows the absorbance bands previously identified for functional groups by the indicated authors. The FTIR spectra were interpreted based on these absorbance bands.

Table 4-2: FTIR absorbance bands adapted from indicated authors

Wavelength	Description	Reference
3400 ─ 3200 cm^{-1}	─OH stretching	(Boeriu *et al.*, 2004; de Miranda & Mothé, 2009; Fang *et al.*, 2002; Qua *et al.*, 2011)
3350	OH···O (hydrogen bond)	(Qua *et al.*, 2011)
3000 ─ 2800 cm^{-1}	C─H stretching	(Fuertes *et al.*, 2011; Gao *et al.*, 2013; Kang *et al.*, 2012)
1250 cm^{-1}	C─O─C	(de Miranda & Mothé, 2009)

Table 4-2: FTIR absorbance bands adapted from indicated authors

Wavelength	Description	Reference
1160-1050 cm^{-1}	C─O linkage (ether bond) CO─CH_3 group	(de Miranda & Mothé, 2009; Kang *et al.*, 2012)

The FTIR spectrums of the functional groups for sugarcane bagasse and hydrochar showed considerable change after HTL due to the effect of hot compressed water on the fibre content. The operating conditions of the HTL pilot plant, 270°C and a residence time of 10 minutes, was sufficient to promote the degradation of cellulose, hemicellulose, and lignin.

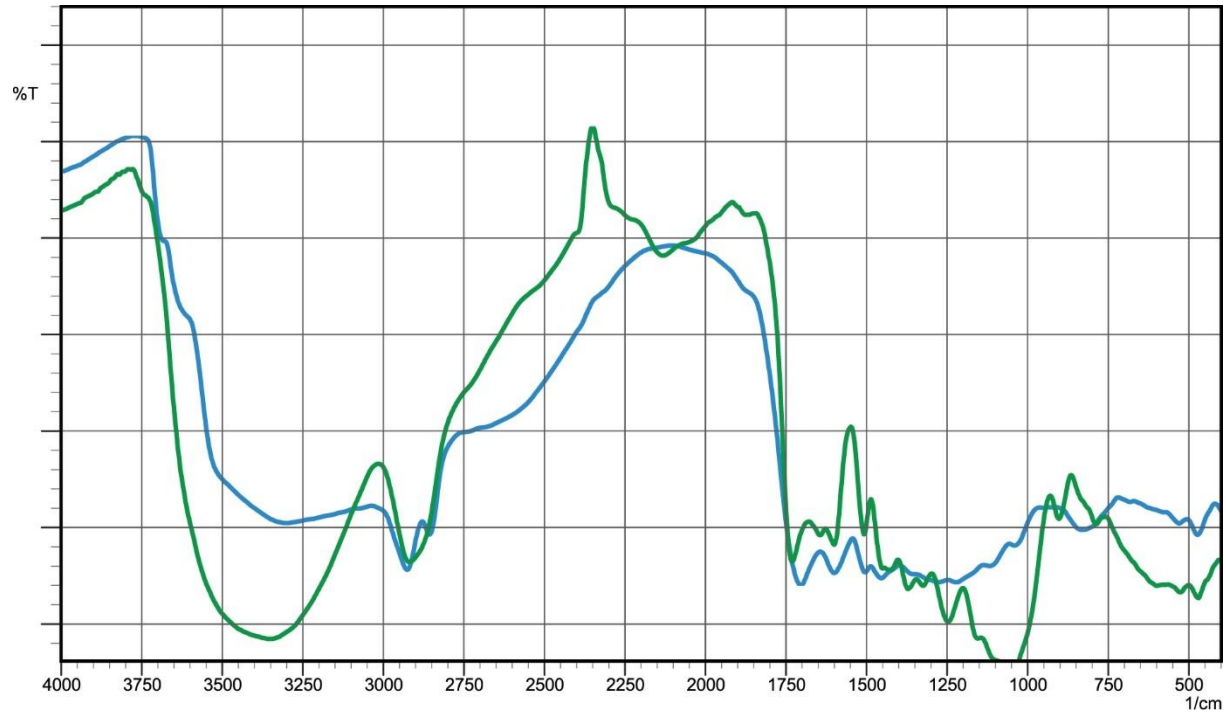

Figure 4-2: FTIR of sugarcane bagasse (—), hydrochar (—)

Figure 4-2 shows the FTIR spectra for the sugarcane bagasse and hydrochar samples. The spectrum showed a large peak for sugarcane bagasse between 3700 cm^{-1} ─ 3050 cm^{-1}. The region between 3400 cm^{-1} ─ 3200 cm^{-1} was associated with the ─OH stretching and indicated the presence of alcohols, phenols and hydrogen bonds (OH···O), which was previously accredited to the phenolic and aliphatic structures of lignin, hydroxyl groups in hemicellulose and cellulose, and the hydrogen bonds that were associated with the crystalline structure of cellulose (Boeriu *et al.*, 2004; de Miranda & Mothé, 2009; Fang *et al.*, 2002; Qua *et al.*, 2011). For the sugarcane bagasse sample, the broad band peaked at 3350 cm^{-1}.

Figure 4-2 shows that the peak between the 3400 cm^{-1} ─ 3200 cm^{-1} band for the hydrochar disappeared and indicated complete removal of cellulose, as well as the alcoholic and phenolic functional groups. The removal of hydroxyl groups was linked to dehydration reactions and supported by the lower O/C- and lower H/C atomic ratios since lower O/C-, and lower H/C atomic ratios were indicative of dehydration reaction as the main reaction (Gao, Zhou, *et al.*, 2016; Lucian *et al.*, 2018).

Both the sugarcane bagasse and the hydrochar sample demonstrated a broad peak between 3000 cm^{-1} ─ 2800 cm^{-1}. Sugarcane bagasse had one peak with a maximum absorbance at 2900 cm^{-1} and linked to the stretching of the C─H in aliphatic and aromatic compounds (Boeriu *et al.*, 2004; de Miranda & Mothé, 2009; Fang *et al.*, 2002; Kang *et al.*, 2012; Qua *et al.*, 2011). In contrast, the hydrochar had two peaks within the 3000 cm^{-1} ─ 2800 cm^{-1} band, assigned to symmetric and asymmetric C─H stretching. The peak with the highest intensity had a maximum at 2940 cm^{-1} and the second peak a maximum at 2850 cm^{-1}. The higher C─H bonds observed for hydrochar were due to the deoxygenation reactions, also reflected by the notable decreased elemental oxygen content and negligible change in the hydrogen content.

The aromatic C═C bending in sugarcane bagasse was assigned to the absorbance peaks observed between 1700 cm^{-1} ─ 1500 cm^{-1} (Fuertes *et al.*, 2011; Gao, Yu, *et al.*, 2016; Hu *et al.*, 2014). The vibration of aromatic structures of lignin in sugarcane bagasse corresponded to the spectral peaks between 1650 cm^{-1} ─ 1400 cm^{-1} with maximum absorbance peaks at 1600 cm^{-1}, 1500 cm^{-1}, and 1450 cm^{-1} (Kang *et al.*, 2012). The absorbance associated with these peaks increased, indicating a higher concentration of aromatic groups on the surface of the hydrochar after HTL. Also, a strong, broad peak appeared between 900 cm^{-1} ─ 750 cm^{-1}, which was associated with the C─H bending of aromatics (Fuertes *et al.*, 2011). The strong peak in the fingerprint region, reaching a maximum absorbance at 800 cm^{-1} was associated with the condensed aromatic compounds originating from the lignin in the sugarcane bagasse.

Figure 4-2 shows that the sugarcane bagasse sample had maximum absorbance peaks at 1250 cm^{-1}, 1160 $cm^{-}1$, and 1050 cm^{-1}. The peak at 1250 cm^{-1} was associated with the C─O─C group in cellulose; whereas, the peaks at 1160 cm^{-1} and 1050 cm^{-1} with the C─O linkage. The latter was previously considered representative of ether bonds in cellulose and hemicellulose, as well as ether bonds and CO─CH_3 (methoxy groups) in lignin. The ether bonds and methoxy groups were easy to break during subcritical HTL conditions (de Miranda & Mothé, 2009; Kang *et al.*, 2012). The hydrochar sample did not show any absorbance at these spectrums, which

suggests complete decomposition of cellulose and hemicellulose. The work of previous authors supported the complete degradation of cellulose and hemicellulose under these HTL conditions (Acharjee *et al.*, 2011; Gao, Zhou, *et al.*, 2016; Liu *et al.*, 2013).

The FTIR results showed that the surface functional groups of hydrochar were mainly associated with aromatic structures, originating from the decomposition of cellulose and hemicellulose and the condensation and re-polymerisation of the resulting HTL products (Kang *et al.*, 2012). Alternatively, cleavage of ether bonds produced monomeric fragments (Belkheiri *et al.*, 2018; Roberts *et al.*, 2011). These depolymerised lignin monolignol fragments could be a precursor for the aromatic structure of hydrochar via condensation and re-polymerisation.

4.2.3 SEM analysis of sugarcane bagasse, hydrochar, and coal

SEM analysis was used to investigate the effect HTL had on the surface morphology by comparing SEM images of sugarcane bagasse and hydrochar. Figure 4-3 shows the SEM images of sugarcane bagasse and hydrochar at a 600-time magnification. It was evident that hydrothermal liquefaction affected the morphology. The sugarcane bagasse sample had a varying particle size distribution with different shapes. The majority of the particles had a flake-like appearance with sharp edges.

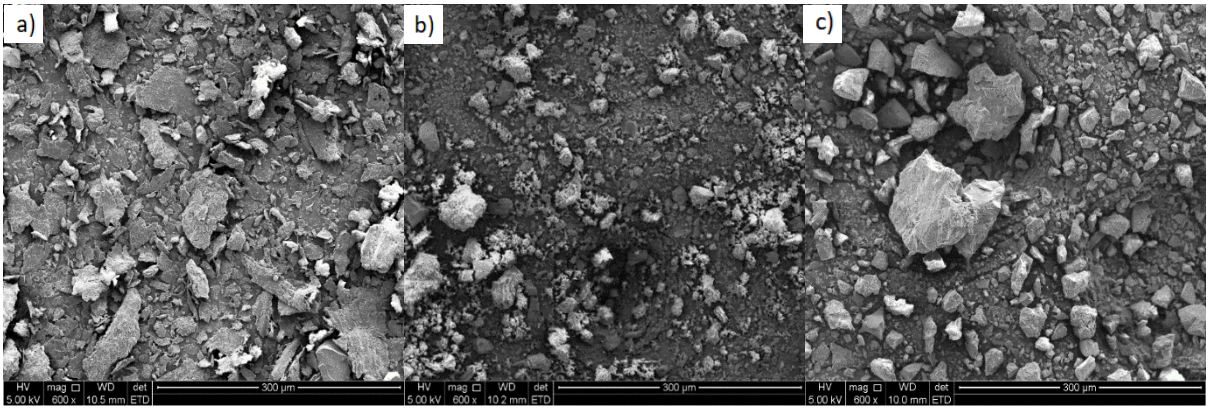

Figure 4-3: SEM images of (a) sugarcane bagasse, (b) hydrochar and (c) coal at 600 magnification

Figure 4-4 shows a sugarcane bagasse particle at a 4000-time and a 20000-time magnification and Figure 4-5 shows a different sugarcane bagasse particle 5000-time and 20000-time magnification. It was clear to see that the particles consisted of randomly stacked layers and

fibres. The fibres of the sugarcane bagasse were measured to be in the range of 100 nm. The morphology of sugarcane bagasse originated from the cellulose, hemicellulose and lignin content.

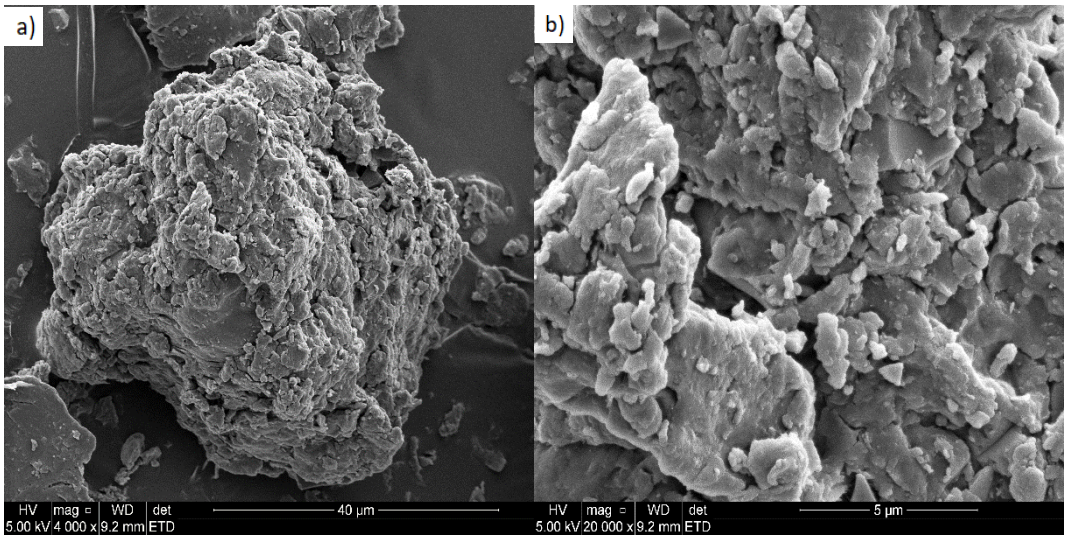

Figure 4-4: SEM images of a sugarcane bagasse particle at (a) 4000 magnification and (b) 20000 magnification

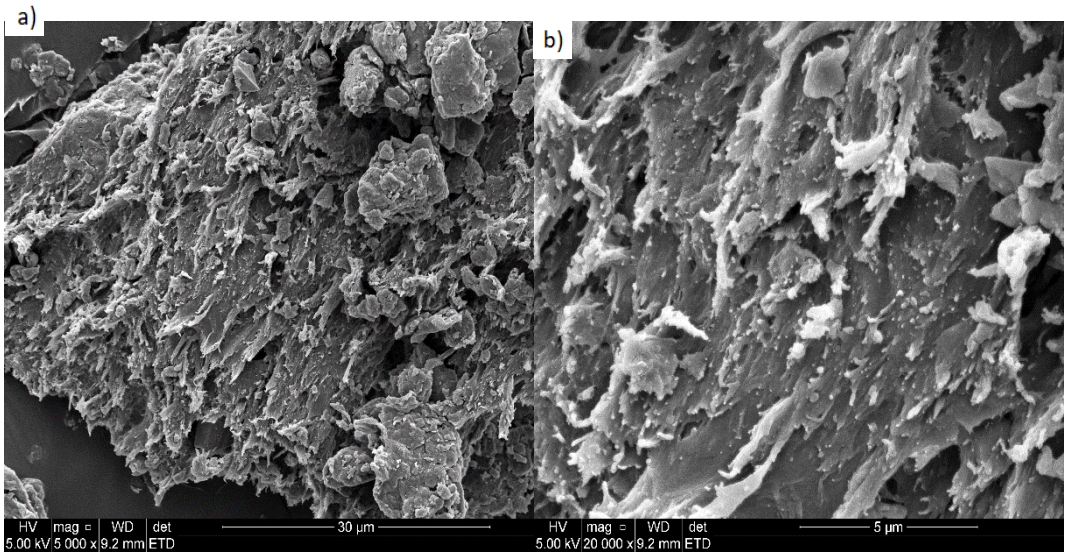

Figure 4-5: SEM images of a sugarcane bagasse particle at (a) 5000 magnification and (b) 20000 magnification

Figure 4-6 shows a hydrochar particle at a 5000-time and 20000-time magnification, which appeared to have an amorphous structure with scattered microsphere particles and characteristic pores on the surface. The pore formation on the surface was most likely due to the release of

volatile matter content from the organic structure, i.e. cellulose and hemicellulose degrade at hydrothermal temperatures below 250°C. The cellulose and hemicellulose content in sugarcane bagasse degraded easily during HTL since a temperature of 270°C was used (Liu *et al.*, 2013).

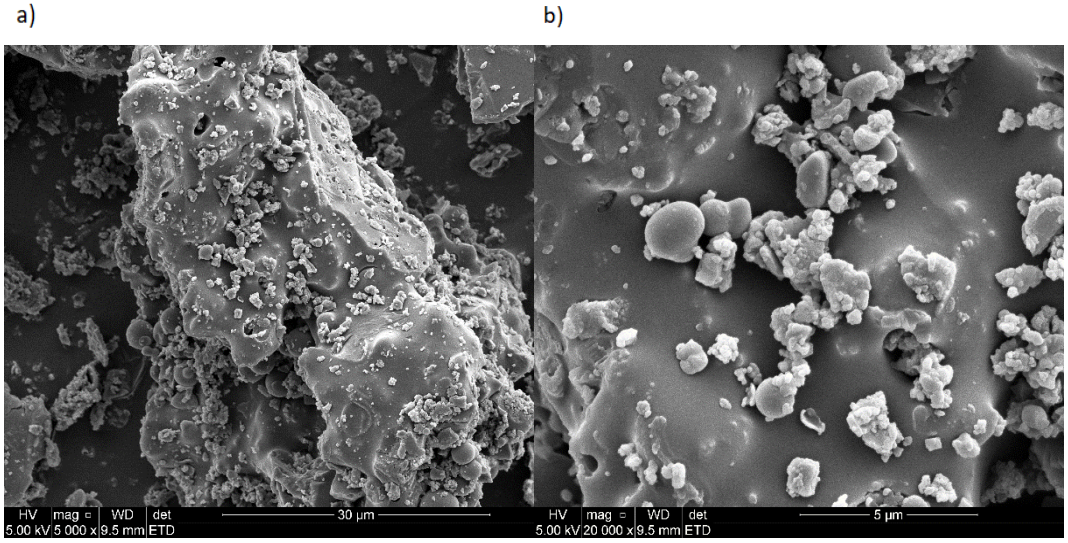

Figure 4-6: SEM images of a hydrochar particle at (a) 5000 magnification and (b) 20000 magnification

Figure 4-7 shows the SEM images of hydrochar with characteristic nanoparticles or microspheres of varying sizes. FTIR analysis indicated that cellulose, hemicellulose, and lignin decomposed and that the hydrochar consisted out of aromatic components; subsequently, the amorphous surface and microspherical particles observed were most likely associated with the condensed aromatics. The oligosaccharide or monosaccharides, originating from the decomposition of cellulose and hemicellulose via dehydration and condensation reactions, formed the condensed aromatic hydrochar (Fuertes *et al.*, 2011; Gao *et al.*, 2013; Karayıldırım *et al.*, 2008; Kruse *et al.*, 2013; Lucian *et al.*, 2018; Sevilla & Fuertes, 2009; Titirici *et al.*, 2008; Volpe & Fiori, 2017). The SEM images and FTIR spectrum of hydrochar suggested that monolignol fragments, produced via cleavage of lignin ether bonds, formed condensed aromatic polymers that contributed to the amorphous surface and microspheres (Belkheiri *et al.*, 2018; Roberts *et al.*, 2011).

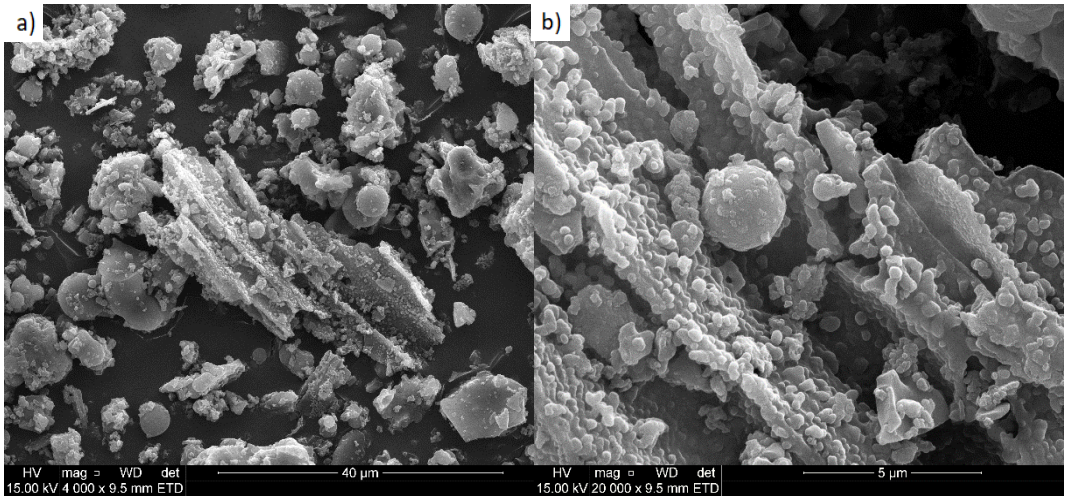

Figure 4-7: SEM images of a hydrochar particle at (a) 4000 magnification and (b) 20000 magnificationXRD and XRF analysis

4.2.4 Mineralogy of sugarcane bagasse, hydrochar and coal

Table 4-3 and Table 4-4 shows the XRD and XRF results, respectively, for the sugarcane bagasse, hydrochar and coal. Table 4-3 includes the normalised data by excluding the amorphous content of each sample.

Table 4-3: XRD results: mineral content of sugarcane bagasse- (SB), hydrochar- (HC) and coal samples

Compound	SB (%)	$SB_{Norm.}$ (%)	Compound	HC (%)	$HC_{Norm.}$ (%)	Compound	Coal (%)	$Coal_{Norm.}$ (%)
Quartz	6.4	85.3	Quartz	4.3	36.4	Quartz	2.2	8.3
Graphite	0.6	8.0	Pyrrhotite	0.1	0.8	Kaolinite	14.8	55.8
Cristobalite beta	0.5	6.7	Anatase	0.2	1.7	Calcite	0.6	2.3
Amorphous	92.5	-	Graphite	0.1	0.8	Dolomite	0.9	3.4
			Muscovite	0.4	3.4	Anorthite	4.1	15.5
			Gypsum	0.8	6.8	Illite	1.3	4.9
			Anhydrite	0.2	1.7	Microcline	0.2	0.8
			Hematite	0.1	0.8	Pyrite	0.4	1.5
			Anorthite	4.8	40.7	Anatase	0.3	1.1
			Cristobalite low	0.3	2.5	Graphite	0.1	0.4
			Mullite	0.2	1.7	Muscovite	1.0	3.8

Table 4-3: XRD results: mineral content of sugarcane bagasse- (SB), hydrochar- (HC) and coal samples

Compound	SB (%)	$SB_{Norm.}$ (%)	Compound	HC (%)	$HC_{Norm.}$ (%)	Compound	Coal (%)	$Coal_{Norm.}$ (%)
			Sillimanite	0.3	2.5	Gypsum	0.2	0.8
			Amorphous	88.2	-	Carbonate-fluorapatite	0.3	1.1
						Bassanite	0.1	0.4
						Amorphous	73.3	-

Table 4-3 shows that sugarcane bagasse had the highest amorphous content, followed by hydrochar and coal. Based on the XRD analysis, the sugarcane bagasse consisted primarily of amorphous content and quartz. After hydrothermal liquefaction, it was possible to observe a range of crystalline material in the hydrochar, of which the main components were quartz and anorthite.

Table 4-3 shows that the coal sample contained a large fraction of kaolinite. Previous authors showed that kaolinite mitigated challenges associated with biomass combustion, i.e. low ash fusion temperature (Boström *et al.*, 2009; Davidsson *et al.*, 2008; Kalen *et al.*, 2008; Niu *et al.*, 2016). Subsequently, producing biomass/coal or hydrochar/coal blends with coal containing kaolinite could prove beneficial.

Table 4-4 shows that the mineral content of sugarcane bagasse primarily consisted of SiO_2, Al_2O_3 and Fe_2O_3, adding up to 93.9%. Excluding the latter oxides, only K_2O and CaO had fractions larger than 1%.

Table 4-4: XRF results: elemental composition of sugarcane bagasse (SB), hydrochar (HC) and coal

	SB (%)	HC (%)	Coal (%)	Inorganic yield (%)
SiO_2	75.0	78.1	48.2	21.2
Fe_2O_3	12.0	2.8	6.8	4.7
Al_2O_3	6.8	12.1	30.6	36.5
K_2O	1.7	0.8	1.0	9.7
CaO	1.3	1.1	6.4	18.5
MgO	0.8	0.1	1.6	3.1
TiO_2	0.7	1.8	1.4	50.2
P_2O_5	0.6	1.7	0.3	63.5
Cr_2O_3	0.4	0.5	0.0	23.8

Table 4-4: XRF results: elemental composition of sugarcane bagasse (SB), hydrochar (HC) and coal

	SB (%)	HC (%)	Coal (%)	Inorganic yield (%)
Na_2O	0.2	0.0	0.4	2.8
Mn_3O_4	0.1	0.0	0.0	3.8
NiO	0.1	0.1	0.0	18.1
SO_3	0.1	0.2	2.5	63.0
ZrO_2	0.1	0.1	0.1	34.3
PbO	0.0	0.0	0.0	20.2
SrO	0.0	0.0	0.2	26.7
CuO	0.0	0.1	0.0	-
BaO	0.0	0.3	0.5	-

The SiO_2 in sugarcane bagasse was within the ranges that were previously published (Edreis *et al.*, 2014; Rodríguez-díaz *et al.*, 2015; Teixeira *et al.*, 2008). High silicate content may result in bed agglomeration at lower temperatures due to the formation of low-melting silicates that formed from volatile alkaline metals (i.e. KCl) and non-volatile, water-soluble alkaline metals reacting with silicate (SiO_2) (Brus *et al.*, 2005; Mu *et al.*, 2012; Niu *et al.*, 2016). The volatile alkaline metals also act as a bonding agent between fly ash particles and fly ash particles and heating surfaces; therefore, high SiO_2 and high K_2O content pose challenges associated with slagging and fouling.

The sugarcane bagasse had a high fraction of Al_2O_3 content, with lower fractions of CaO and MgO. The Al_2O_3 falls within the ranges reported by previous authors; however, CaO and MgO were slightly lower (Edreis *et al.*, 2014; Rodríguez-díaz *et al.*, 2015; Teixeira *et al.*, 2008). Aluminium, calcium and silicate in the form of alkali aluminium silicates, alkali calcium/magnesium silicates and insoluble alkali silicates were considered to be high-melting silicates and have shown to mitigate challenges such as fouling and slagging (Boström *et al.*, 2009; Davidsson *et al.*, 2008; Kalen *et al.*, 2008; Niu *et al.*, 2016). As an example, kaolin and calcite were both used as additives and demonstrated reduced slagging at low temperatures by capturing K and Si and forming high-temperature melting silicates (Boström *et al.*, 2009; Davidsson *et al.*, 2008; Kalen *et al.*, 2008; Niu *et al.*, 2016).

The sugarcane bagasse's Fe_2O_3 content was higher in comparison with literature (Edreis *et al.*, 2014; Rodríguez-díaz *et al.*, 2015; Teixeira *et al.*, 2008). The high iron content might improve combustion characteristics. Vamvuka *et al.* (2014) evaluated various oxides as a catalyst for lignite/biomass blends and showed that Fe_2O_3 had the second-highest relative activity; however, these oxides had no clear catalytic effect during biomass combustion.

In comparison with other sources, the sugarcane bagasse also had a smaller fraction CaO, which could be considered unfavourable (Edreis *et al.*, 2014; Rodríguez-díaz *et al.*, 2015; Teixeira *et al.*, 2008). Similar to the Fe_2O_3, CaO also has the potential to increase the relative activity of biomass/coal blends (Vamvuka *et al.*, 2014). Wang *et al.* (2018) showed the benefit of higher CaO and P_2O_5 quantities in char briquettes during combustion. Phosphorous containing additives forms potassium sulphates that were melt-resistant, and calcium silicates and calcium phosphates improved the ash fusion properties (Wang, Han, *et al.*, 2018).

Based on the XRF results, the hydrochar sample consisted mainly out of SiO_2 and Al_2O_3, which added up to 90.2% of the total mineral content. Other oxides with a mass fraction larger than 1%, accounted for 7.5% and included Fe_2O_3, CaO, TiO_2 and P_2O_5. Table 4-4 shows the inorganic yield of the oxides. From the calculated inorganic yields, it single-stage that the majority of the inorganic species retained less than 50% in the hydrochar, resulted from mineral species transferring to the aqueous phase during hydrothermal liquefaction (Nakason *et al.*, 2018).

The inorganic yield was expressed as the inorganic mass fraction in the hydrochar to the inorganic mass fraction in the raw sugarcane bagasse, multiplied by the mass yield (SY=20.4%) after hydrothermal liquefaction. Overall, the inorganic yield varied between the individual species, ranging between ≈3%─64%. Removing ash components during HTL would have a positive effect on several aspects associated with heat and power production, i.e. lower ash content would improve the energy density and the combustion efficiency and reduce scaling and fouling of heat transfer surfaces generally linked to AAEM.

Table 4-4 shows that the inorganic yield of Al_2O_3 and SiO_2 in hydrochar was 21.2% and 36.5%, respectively. Although the yield was low, the mass fraction of Al_2O_3 and SiO_2 in hydrochar increased. The higher Al_2O_3 and SiO_2 mass fraction found in hydrochar, along with the higher P_2O_5/K_2O and CaO/K_2O ratios, would likely demonstrate improved combustion behaviour, i.e. high ash fusion temperatures (Boström *et al.*, 2009; Davidsson *et al.*, 2008; Kalen *et al.*, 2008; Niu *et al.*, 2016; Vamvuka *et al.*, 2014; Wang, Han, *et al.*, 2018). Apposing sugarcane bagasse, this would likely translate to lower bed agglomeration and fouling/slagging of heating surfaces.

The hydrochar had a very low Fe_2O_3 content with an inorganic yield of 4.7%. As previously, discussed, iron oxides had a positive influence on the combustion behaviour of certain coals; therefore, it was likely that lower Fe_2O_3 fractions might contribute to lower combustion reactivity (Vamvuka *et al.*, 2014).

The ash of the hydrochar had lower potassium (K_2O) and calcium (CaO) mass fraction compared to the sugarcane bagasse. With regards to combustion, K_2O and CaO species contribute to bed agglomeration, as well as fouling and slagging; therefore, the lower potassium and calcium species was beneficial (Garcia-maraver *et al.*, 2017). However, the removal of these species may be less desirable for the gasification application due to the observed catalytic effect associated with these species (Mafu *et al.*, 2018; Wei *et al.*, 2017).

Table 4-4 shows that 92.0% of the coal ash consisted mainly of SiO_2 (48.2%) and Al_2O_3 (30.7%), as well as smaller quantities of Fe_2O_3 (6.8%) and CaO (6.4%). Other inorganic species with a mass fraction greater than 1% were MgO, TiO_2 and SO_3, adding up to 5.4%.

Substantiated from the discussion above, blends with hydrochar may elude to a GreenCoal with greater reactivity during combustion, due to the high Fe_2O_3 content in coal (Vamvuka *et al.*, 2014), as well as improved combustion behaviour, i.e. higher ash fusion temperatures due to the presence of ample Al_2O_3, as well as high CaO/K_2O and P_2O_5/K_2O ratios (Boström *et al.*, 2009; Davidsson *et al.*, 2008; Kalen *et al.*, 2008; Niu *et al.*, 2016; Vamvuka *et al.*, 2014; Wang, Han, *et al.*, 2018).

Sulphur capturing during coal combustion is generally associated with the Ca content, i.e. $CaCO_3$ (Sheng *et al.*, 2000). As seen with the XRD analysis, the coal sample contained dolomite and calcite that was likely associated with the high sulphur content in the ash. Using the proximate-, ultimate- and XRF compositions, the sulphur yield calculated by the mass sulphur retained in the coal ash and dividing it by the mass of sulphur in the coal, showed retention of 27.0% of the sulphur content.

4.3 Densification: improving the logistics of renewable fuels

4.3.1 Mass and energy density

Table 4-5 shows the mass and energy density of the sugarcane bagasse, hydrochar, GreenCoals and coal pellets with the respective confidence intervals.

Table 4-5: Mass- and energy density of sugarcane bagasse- (SB), hydrochar- (HC), GreenCoal- (GC3:1, GC1:1 and GC 1:3) and coal pellets

Sample	Mass density (kg/m^3)	ρ_{exp}/ρ_{cal}	Energy density (GJ/m^3)
SB	1344.7 ± 7.6	-	21.3
HC	1220.5 ± 4.2	-	33.3
GC3:1	1200.8 ± 6.0	1.00	32.7
GC1:1	1176.1 ± 2.6	0.99	31.9
GC1:3	1170.0 ± 5.5	1.00	31.6
Coal	1150.6 ± 7.4	-	30.9

Densification was an effective method to improve the economics of transportation, handling, and storage of a material, or to produce a larger pellet or briquettes as required by a process (Bunt *et al.*, 2015; Kambo & Dutta, 2014). The average mass density of the sugarcane bagasse, hydrochar and coal pellets were 1344.7 kg/m^3, 1220.5 kg/m^3, and 1150.6 kg/m^3, respectively. The higher density associated with sugarcane bagasse pellets against the hydrochar and coal pellets was likely due to the combined effect of its compressibility (Adapa *et al.*, 2009; Harun & Afzal, 2016) and varying particle size distribution leading to more effective filling of interparticle voids (Harun & Afzal, 2016).

The milling of lignocellulosic biomass is time-consuming and energy-intensive due to the poor grindability of lignocellulosic biomass (Adapa *et al.*, 2009; Arias *et al.*, 2008; Commandré & Leboeuf, 2015). Although there were no parameters measured during the milling process, there was a clear difference observed between sugarcane bagasse and hydrochar concerning the milling time. The milling of sugarcane bagasse was time-consuming, whereas the milling of hydrochar was rapid. The decomposition of the plant polymers during HTL improved grindability as was confirmed by FTIR and SEM analysis. (Figure 4-3, Figure 4-6 and Figure 4-7).

The mass density of the GreenCoal pellets increased with higher hydrochar fractions and showed a linear relationship between the hydrochar fraction and the mass density. Since the mass density of the GreenCoal pellets increased in proportion to the fraction of hydrochar, no other effect contributed to the mass density of the GreenCoal pellet, i.e. filling effect. In this study, $\rho_{exp}/\rho_{cal} \approx 1$ indicating no filling effect, even though SEM images showed a clear difference between the hydrochar and coal particles (Yuan *et al.*, 2012).

Table 4-5 shows that even though the sugarcane bagasse pellets had the highest mass density, the low HHV translated to a low energy density. The sugarcane bagasse pellets had an energy

density of 21.3 GJ/m^3, an improvement with regards to the raw sugarcane bagasse; yet, the hydrochar, different GreenCoals and coal pellets had an energy density ranging between 31.1 GJ/m^3–33.3 GJ/m^3. The hydrochar and coal sample had more or less the same HHV; therefore, the varying energy density originated from the different mass densities.

In agreement with other authors, the combined effect of the higher mass density and HHV of hydrochar and GreenCoal pellets translated to a solid fuel with improved economic value due to lower transportation cost (Kambo & Dutta, 2014; Zhu *et al.*, 2019).

4.3.2 Hydrophobicity

The equilibrium moisture content (EMC) and water resistance capacity (WRC) of sugarcane bagasse-, hydrochar-, GreenCoals-, and coal pellets in this study, were used as a measure of hydrophobicity for the different samples. The effect of the hydrochar fraction on the EMC and water resistance capacity of GreenCoal pellets were investigated and compared with the hydrochar- and coal pellets. Table 4-6 reported the EMC and the water-resistance of the sugarcane bagasse-, hydrochar-, GreenCoal-, and coal pellets, as well as the confidence level.

Table 4-6: Equilibrium moisture content (EMC) and water resistance capacity (WRC) of sugarcane bagasse- (SB), hydrochar- (HC), GreenCoal- (GC3:1, GC1:1 and GC 1:3) and coal pellets

Sample	EMC (%)	WRC (%)
SB	10.1 ± 0.1	-
HC	7.2 ± 0.1	1.0 ± 0.2
GC3:1	6.2 ± 0.3	2.5 ± 0.2
GC1:1	4.8 ± 0.1	2.9 ± 0.3
GC1:3	2.8 ± 0.1	3.1 ± 0.6
Coal	2.1 ± 0.2	-

Table 4-6 shows that the equilibrium moisture content of the sugarcane bagasse pellet was the highest, whereas the coal pellet had the lowest EMC. The respective EMC's for sugarcane bagasse and coal pellets were 10.1% and 2.1%. The hydrochar pellet had a lower EMC of 7.2%. As observed in Table 4-6, the EMC of the GreenCoal pellets increased proportionally to the fraction hydrochar used. A high moisture content relates to high transportation costs, lowers the combustion efficiency, and concerning biomass, may lead to fungal growth that results in

biodegradation (Kambo & Dutta, 2014). Therefore, the hydrochar and GreenCoal pellets with lower moisture content and improved resistance to biodegradation would be beneficial.

Sugarcane bagasse- and coal pellets proved to have no resistance against water, and the integrity of the pellets was lost within one to five minutes, which was consistent with the literature (Kambo & Dutta, 2014; Khan *et al.*, 2015). The hydrochar and all the GreenCoal pellets demonstrated strong water resistance capacity, showing no observable change (swelling or disintegrating). After the pellets were submerged for two hours and exposed to a controlled environment for 24 hours, the EMC's was determined for the hydrochar, GreenCoal 3:1, GreenCoal 1:1 and GreenCoal 1:3 to evaluate any change in the moisture content. The moisture content of the corresponding pellets increased by 1.0%, 2.5%, 2.9%, and 3.1%, respectively. The EMC and the hydrochar's fraction demonstrated a linear trend, decreasing as hydrochar's fraction increased; however, the amount of water absorbed was almost negligible, which demonstrated the improved hydrophobicity of GreenCoal pellets.

The observed hydrophobic nature of the GreenCoal pellets was a very favourable property when producing hydrochar and coal blends. Previous authors reported that beneficiation of biomass via hydrothermal treatment produced a more hydrophobic solid product and linked it to the dehydration reactions reducing the absorbance capability by reducing the hydroxyl groups (Acharjee *et al.*, 2011; Bach & Skreiberg, 2016; Kambo & Dutta, 2014; Liu *et al.*, 2013). As with the current case, a lower O/C- and lower H/C atomic ratio was suggestive of dehydration being the main reaction taking place during HTL (Lucian *et al.*, 2018).

Furthermore, the depolymerisation of lignin into monolignols, followed by deoxygenation reactions (i.e. dehydration) and condensation reactions produced a hydrochar with a higher degree of aromatisation and a lower concentration of oxygen functional groups, contributing to the increased hydrophobic nature of the hydrochar (He *et al.*, 2013; Zhang & Yang, 2012). In this study, FTIR analysis of the hydrochar supported a higher degree of aromatisation.

4.3.3 Strength and durability

Handling and storage require a strong, durable pellet that can withstand impact forces, e.g. feeding through chutes and dropping into bins during the manufacturing of pellets, the unloading process, as well as the weight of the bulk mass during storage (Kambo & Dutta, 2014). The durability test was a good tool to evaluate the strength and quality of a pellet by measuring the

mass retained after executing the drop test. Figure 4-8 presents the mass retained after four drops. Calculating the impact resistance index (IRI) was done with data collected from a separate drop test. Table 4-7 reports the average number of drops before the pellets broke, the number of pieces and the calculated IRI values.

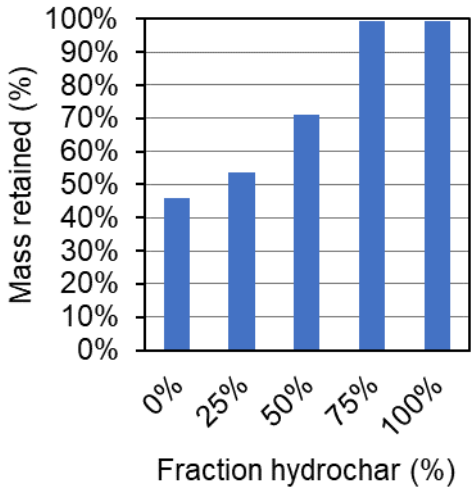

Figure 4-8: Mass percentage retained by hydrochar- (100%), GC3:1- (75%), GC1:1- (50%), GC1:3- (25%) and Coal pellets (0%) after four drops

Sugarcane bagasse pellets performed well, retaining +99% of the pellet mass after four drops and had an IRI of 400. As reported by previous authors, the durability and strength of raw biomass pellets was a function of various factors, including the type of biomass, the pelletising conditions (pressure and temperature), and the moisture- and lignin content (Kambo & Dutta, 2014; Razuan *et al.*, 2011; Reza *et al.*, 2012).

The hydrochar- and GreenCoal 3:1 pellets lost negligible mass (+99% retained) demonstrating excellent resistance to the drop test; however, as the fraction of hydrochar decreased, i.e. GreenCoal 1:1 (50%), GreenCoal 3:1 (25%) and coal (0%), the mass retained decreased to 70.9%, 53.7%, and 46.1% respectively.

The Impact Resistance Index (IRI) calculated with the average number of drops a pellet withstood before it broke, and the average number of pieces the pellet broke into was used to calculate the IRI. In general, the lowest IRI value accepted in the laboratory when producing briquettes for commercial and industrial processes is an IRI value of 50 (Division, 1990). Table 4-7 shows that all the pellets had an IRI above 50. The sugarcane bagasse, hydrochar and GreenCoal 3:1 pellets

performed the best, with the pellets remaining intact after four drops. In this study, the relationship between the IRI and the fraction of hydrochar was positive, i.e. as the fraction of hydrochar increased, the IRI of the pellets increased.

Table 4-7: Impact resistance index (IRI) of sugarcane bagasse-, hydrochar-, GreenCoal-, and Coal pellets

Sample	Drops[a]	Pieces[a]	IRI
Sugarcane bagasse	4	1	400
Hydrochar	4	1	400
GreenCoal 3:1	4	1	400
GreenCoal 1:1	3.8	1.8	211
GreenCoal 1:3	2.4	2.4	100
Coal	2.2	2.4	92

In this study, the maximum peak load under which the pellet fractured while being compressed on its weakest orientation, was a measure of the compression strength. Figure 4-9 depicts the average compression strength each sample withstood. Sugarcane bagasse pellets proved to be the strongest, fracturing under a load of 646.4 N. Hydrochar and coal fractured under a load of 174.6 N and 42.4 N respectively. Similar to the drop test results and Impact Resistance Index, the compression test demonstrated similar results: an exponential relationship between the hydrochar content and the mechanical strength. The force the GreenCoal pellets could withstand decreased as the fraction of hydrochar decreased.

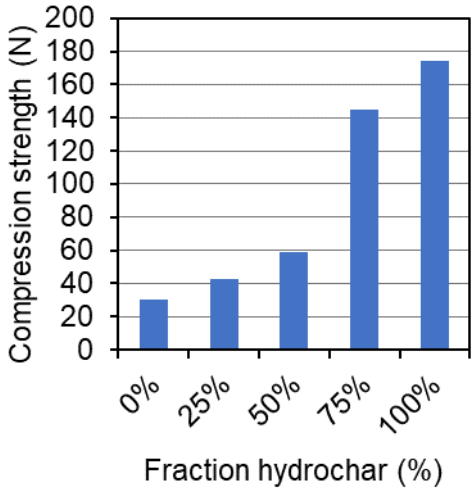

Figure 4-9: Compression strength of hydrochar- (100%), GC3:1- (75%), GC1:1- (50%), GC1:3- (25%) and coal pellets (0%) pellets in a horizontal orientation

Overall, the results for the strength and durability of hydrochar- and GreenCoal pellets had the same trend: the strength and durability increased with higher hydrochar fractions. This positive relationship supports the narrative of hydrochar acting as a natural binder.

In Section 4.3.1, the observation made was that the mass density increased with higher fractions of hydrochar. The observation made for the mechanical strength followed the same trend: the mechanical strength increased with higher fractions of hydrochar; therefore, the mass density and mechanical strength of the pellets had a positive relationship. In previous work, the higher mass density of hydrochar pellets was linked to the friability, resulting in smaller particles when the material is milled with higher contact surface area in the particle (Liu *et al.*, 2014; Zhu *et al.*, 2019). The higher contact surface area would increase the strength of the attractive forces, e.g. hydrogen bonds and van der Waals forces, within the pellet, contributing to the strength of the pellet (Liu *et al.*, 2014; Zhu *et al.*, 2019). The SEM images (see Figure 4-3) supported this narrative. The large fibrous particles observed for sugarcane bagasse in the SEM images showed that sugarcane bagasse was less fragile than the hydrochar- and coal samples.

The hydrochar (excluding sugarcane bagasse) had the highest moisture content; subsequently, the moisture content of the GreenCoal pellets increased with higher fractions of hydrochar (see Table 4-1). In this study, the relationship between the mechanical strength and the moisture content was positive, the former increasing as the moisture content increased with higher fractions of hydrochar. The work of previous authors suggested that moisture acted as a lubricant and binding agent by creating liquid bridges between adjacent particles (Huang *et al.*, 2017; Kaliyan & Vance Morey, 2009).

Furthermore, as discussed in Section 4.2.2, the FTIR spectrum and a lower O/C atomic ratio suggested condensed lignin with a high degree of aromatisation. Similar to the moisture content, high molecular organic compounds deposited on the surface of the hydrochar could contribute to the strength and durability of hydrochar pellets by forming liquid bridges during pelletisation (Liu *et al.*, 2014). The O/C atomic ratio suggested that the oxygen functional group were still present (Donar *et al.*, 2016). The oxygenated functional groups facilitate hydrogen bonding, improving the mechanical strength of pellets (Liu *et al.*, 2014; Liu, Guo, *et al.*, 2016).

4.4 Pyrolysis of sugarcane bagasse, hydrochar, coal and GreenCoal pellets

Thermogravimetric analysis under inert conditions evaluated the thermal degradation of sugarcane bagasse- (SB), hydrochar- (HC), GreenCoal- (GC3:1, GC1:1 and GC1:3) and coal pellets. The samples were heated to 1050°C at 10 °C/min under an inert atmosphere. Using the TG data, TG-DTG curves were constructed (see Appendix A.5. and used to determine thermal degradation characteristics. Table 4-8 shows the determined characteristic temperatures (initiation-, peak-, and termination temperature), the maximum rate of decomposition ($[dm/dT]_{max}$) and the final mass (m_f).

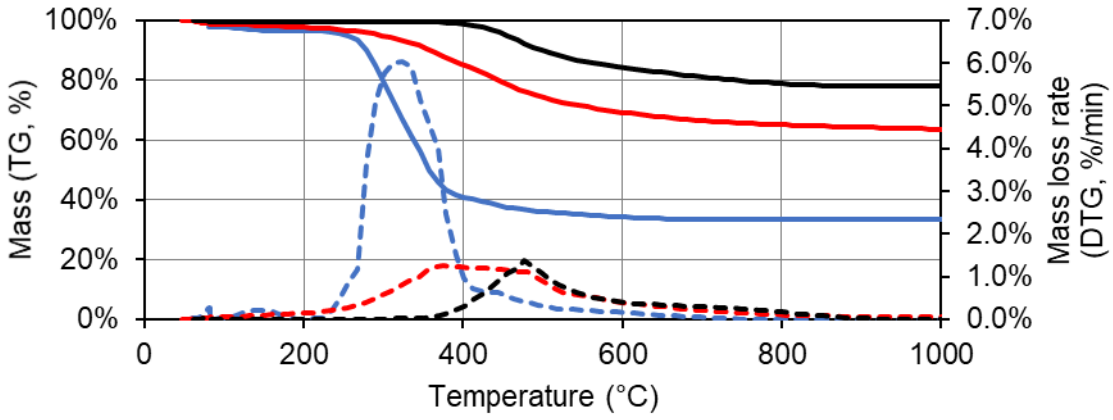

Figure 4-10: TG (——) and DTG (- - -) curves of SB (■), HC (■), and coal (■) under inert conditions and a heating rate of 10 °C/min

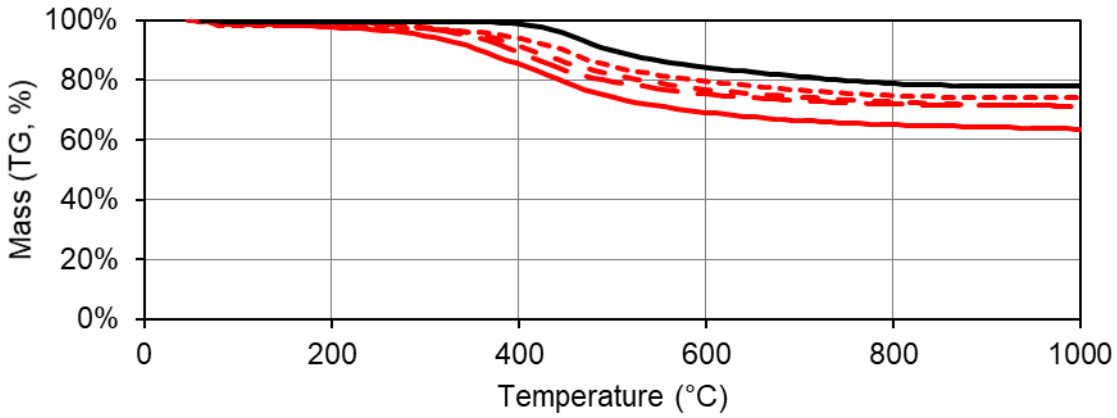

Figure 4-11: TG curves of HC (——), GC3:1 (— —), GC3:1 (— — —), GC3:1 (- - -), and coal (——) under inert conditions and a heating rate of 10 °C/min

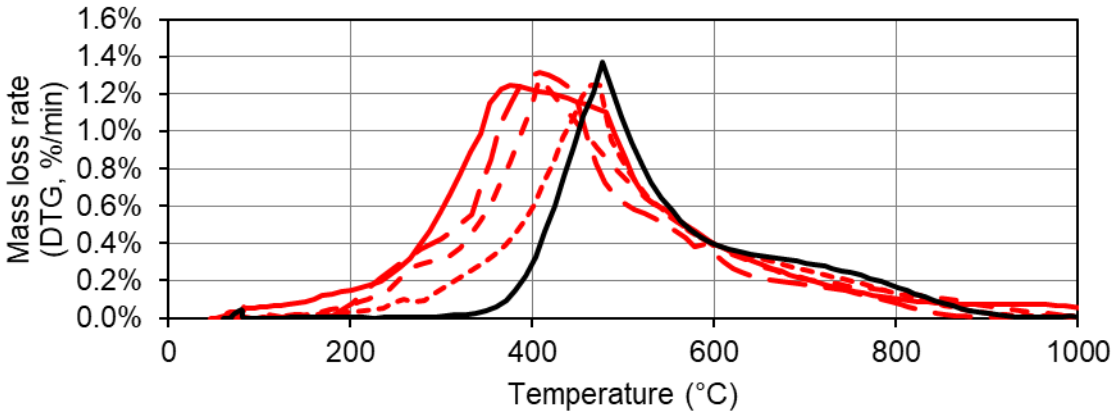

Figure 4-12: DTG curves of HC (—), GC3:1 (— —), GC3:1 (– – –), GC3:1 (- - -), and coal (—) under inert conditions and a heating rate of 10 °C/min

The TG and DTG curves are shown in Figure 4-10 and Figure 4-11, respectively, demonstrated the different thermal degradation behaviour of sugarcane bagasse, hydrochar and coal pellets. The sugarcane bagasse pellet had one large peak; yet, it was possible to distinguish three zones. The first zone had a small peak between 100°C – 200°C and was associated with moisture content and light volatiles. The second zone included a large peak between ≈250°C – 400°C and had a very high mass-loss rate. The large peak was linked to the rapid degradation of organic structures in sugarcane bagasse, i.e. cellulose, hemicellulose, and lignin content (Dewangan *et al.*, 2016; Hu & Gholizadeh, 2019). Organic structures are unstable under thermal conditions due to the high concentration of the ether bonds and oxygen functional groups (Krerkkaiwan *et al.*, 2013; Yuan *et al.*, 2012). As seen in Table 4-8, the initiation temperature of the main decomposition zone was measured at 270.7°C and reached a maximum decomposition rate of 6.0 %/min at 324.3°C. Following the large peak, the zone between 400°C – 500°C showed a low mass loss that gradually decreased, commonly linked to the fixed carbon content. In this study, the sugarcane bagasse had very low fixed carbon content (Dewangan *et al.*, 2016; Hu & Gholizadeh, 2019).

Comparing the decomposition profiles of sugarcane bagasse and hydrochar under inert conditions, it is clear that the thermal decomposition of hydrochar occurred at higher temperatures, which demonstrates the less reactive nature of hydrochar. The less reactive nature of hydrochar can be quantified by the characteristic temperatures during thermal decomposition. Table 4-8 shows that with respect to the sugarcane bagasse, the initiation temperature of hydrochar was 20.1°C higher, the peak temperature was 51.6°C higher, and the termination

temperature was 262.8°C. The characterisation of the hydrochar supported the less reactive nature, i.e. a higher degree of carbonisation (lower O/C and H/C atomic ratios), lower volatile content, and higher fixed carbon content (Volpe & Fiori, 2017). Furthermore, the FTIR analysis and SEM images showed the complete decomposition of organic components, producing primary and secondary hydrochar.

As shown in Table 4-8, the coal pellet had an initiation-, peak-, and termination temperature of 407.9°C, 477.3°C, and 1025.4°C, respectively, which was the highest of all the samples. Comparing the thermal stability of sugarcane bagasse and coal under inert condition exhibits the difference between the two fuels. As discussed above, the thermally unstable nature of sugarcane bagasse was related to the volatile content, fixed carbon content and low degree of order associated with biomass. In previous work, the volatile cellular structure of sugarcane bagasse was characterised by hydroxyl, methylene, methyl and ═C─H radical groups, whereas bituminous coal was by alkene functional groups (Wang *et al.*, 2016). The DTG curves for hydrochar and coal supported the narrative of upgrading sugarcane bagasse via HTL to produce hydrochar with a higher degree of carbonisation.

Overall, the GreenCoal pellets demonstrated behaviour that appeared to be the combined behaviour of hydrochar and coal according to the hydrochar/coal ratio. The initiation- and peak temperature increased with higher hydrochar/coal ratios, whereas the termination temperature was above 900°C for all three GreenCoal pellets. Overall, the maximum rate of decomposition ($[dm/dT]_{max}$) for sugarcane bagasse was 4 ─ 5 times greater than all other samples, emphasising the improved thermal stability of hydrochar and GreenCoal.

Table 4-8: Pyrolysis characteristic parameters for samples heated at 10 °C/min

Sample	T_i (°C)	T_p (°C)	T_f (°C)	$[dm/dT]_{max}$ (°C/min)	m_f (%)
SB	270.7	324.3	748.0	6.0%	32.2%
HC	297.8	375.9	1010.8	1.2%	63.4%
GC3:1	307.1	408.1	968.7	1.3%	71.0%
GC1:1	323.0	409.0	900.9	1.3%	71.2%
GC1:3	369.0	464.9	927.4	1.2%	73.6%
C	407.9	477.3	1025.4	1.4%	77.3%

4.5 Combustion behaviour of sugarcane bagasse-, hydrochar-, GreenCoal- and coal pellets

Thermogravimetric analysis was used to investigate the combustion behaviour of sugarcane bagasse (SB), hydrochar (HC), GreenCoals (GC3:1, GC1:1 and GC1:3) and coal pellets for three heating rates (5 °C/min, 7.5 °C/min, and 10 °C/min). Appendix A.5 includes all the required combustion data and TG-DG curves.

Figure 4-13 to Figure 4-18 shows the mass loss (%) and mass loss rate (%/min) of the various samples. Overall, the mass-loss rate curves shifted to higher temperature regions as the heating rate increased. Wang *et al.* (2016) and Mureddu *et al.* (2018) demonstrated similar results for various biomass samples and coal samples of different rank, attributing this shift to high-temperature regions to two possible reasons: (i) higher heating rates resulted in the temperature increasing faster and inadequate time for the completion of reactions; therefore, overlapping with adjacent regions at higher temperatures, or (ii) the increased temperature gradient over the cross-sectional area of the sample at higher heating rates (Mureddu *et al.*, 2018; Wang *et al.*, 2016).

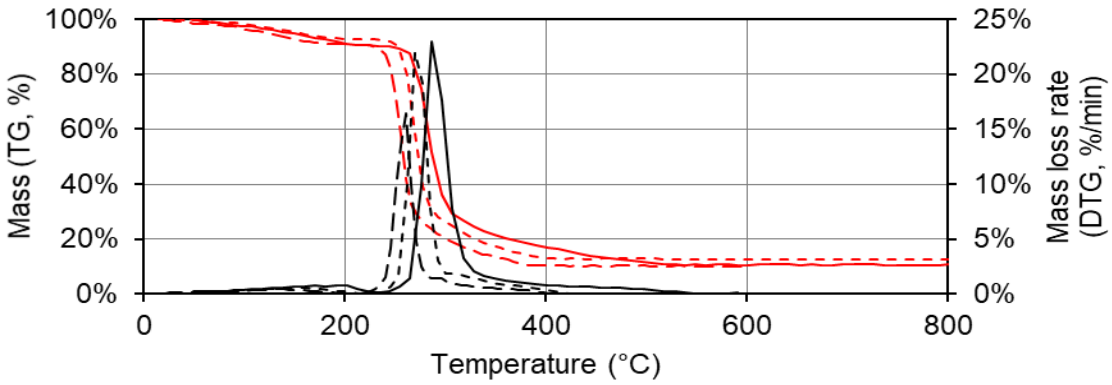

Figure 4-13: TG (■) and DTG (■) curves of sugarcane bagasse at a heating rate of 5 °C/min (— —), 7.5 °C/min (- - -), and 10 °C/min (——)

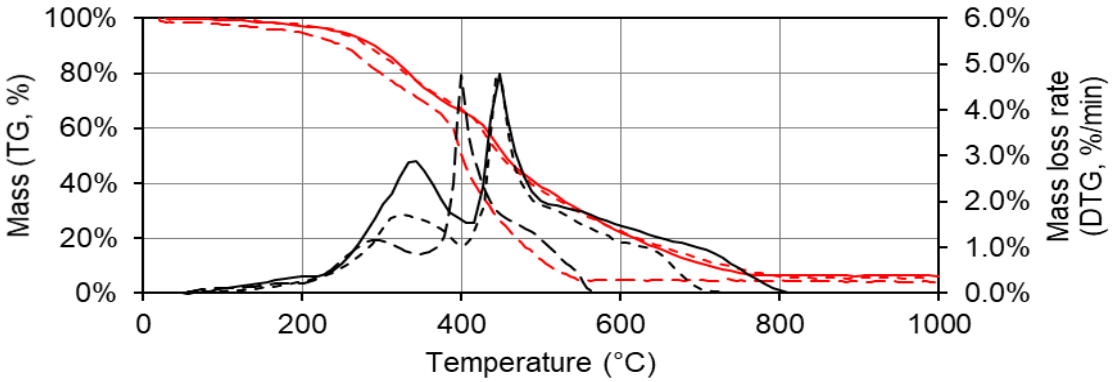

Figure 4-14: TG (■) and DTG (■) curves of hydrochar at a heating rate of 5 °C/min (— —), 7.5 °C/min (- - -), and 10 °C/min (——)

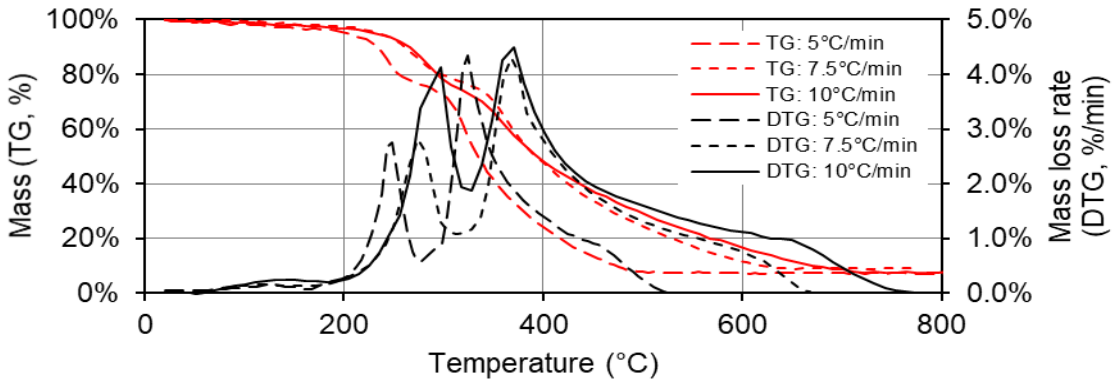

Figure 4-15: TG (■) and DTG (■) curves of GreenCoal 3:1 at a heating rate of 5 °C/min (— —), 7.5 °C/min (- - -), and 10 °C/min (——)

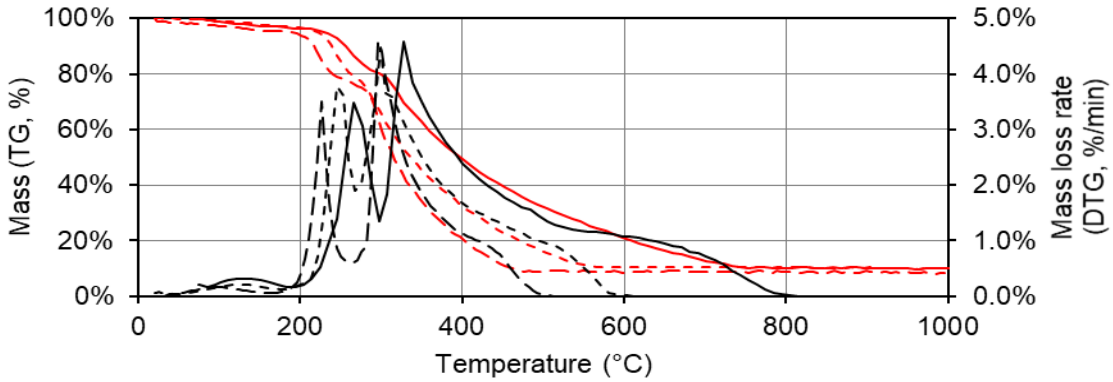

Figure 4-16: TG (■) and DTG (■) curves of GreenCoal 1:1 at a heating rate of 5 °C/min (— —), 7.5 °C/min (- - -), and 10 °C/min (——)

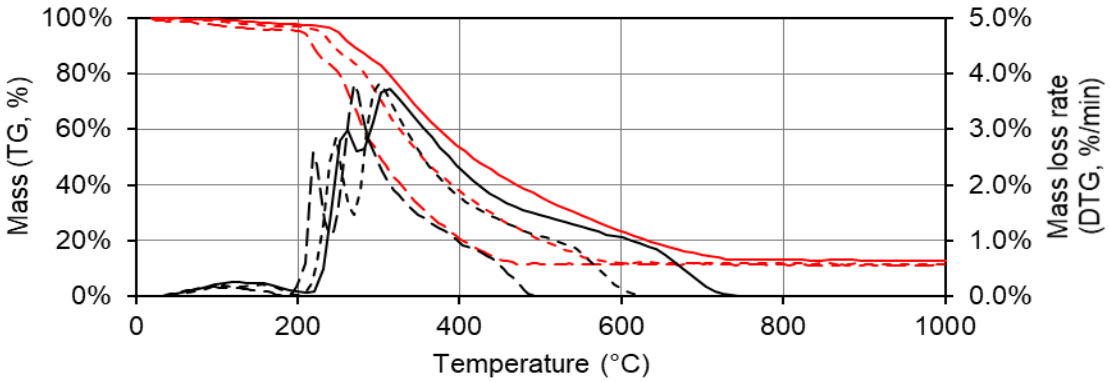

Figure 4-17: TG (■) and DTG (■) curves of GreenCoal 1:3 at a heating rate of 5 °C/min (— —), 7.5 °C/min (- - -), and 10 °C/min (——)

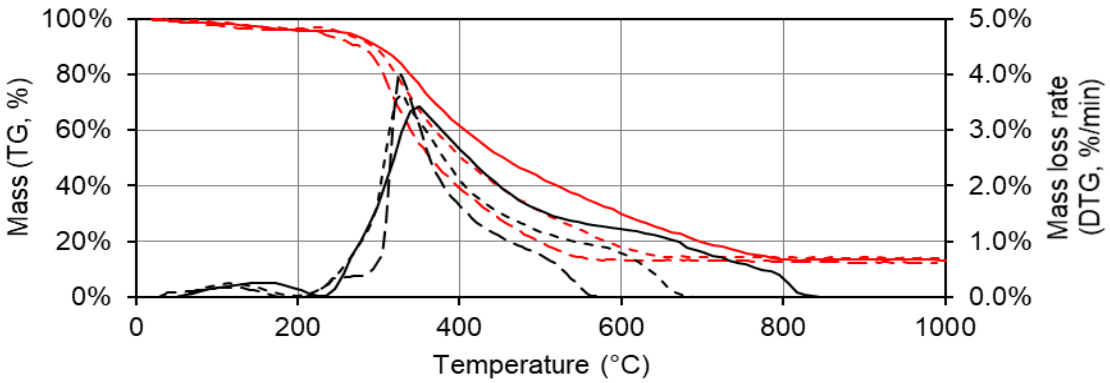

Figure 4-18: TG (■) and DTG (■) curves of coal at a heating rate of 5 °C/min (— —), 7.5 °C/min (- - -), and 10 °C/min (——)

Table 4-9 summarises the derived characteristic parameters for combustion including the ignition- (T_i), peak- (T_p), burnout temperature (T_f), maximum combustion rate ($[dm/dt]_{max}$), mean combustion rate ($[dm/dt]_{mean}$), as well as the calculated ignition index (C) and comprehensive combustion index (S).

Table 4-9: Combustion characteristic parameter for samples

dT/dt	Sample	T_i (°C)	T_p (°C)	T_f (°C)	$[dm/dt]_{max}$ (%/min)	$[dm/dt]_{mean}$ (%/min)	C	S
5°C/min	SB	245	262	374	16.6%	3.0%	10.4	79.4
	HC	347	399	542	4.7%	1.4%	2.0	6.0
	GC3:1	278	324	491	4.3%	1.6%	2.4	8.3
	GC1:1	262	296	467	4.6%	1.6%	2.7	9.7
	GC1:3	230	269	460	3.8%	1.6%	2.5	9.2
	Coal	294	319	542	3.7%	1.3%	1.9	6.5
7.5°C/min	SB	260	276	423	20.4%	3.6%	12.0	103.3
	HC	377	444	670	4.7%	1.4%	1.8	4.7
	GC3:1	298	368	621	4.3%	1.7%	2.2	7.0
	GC1:1	237	299	551	4.5%	1.9%	2.9	11.2
	GC1:3	247	301	576	3.8%	1.8%	2.4	8.3
	Coal	288	329	636	3.7%	1.6%	1.9	6.6
10°C/min	SB	267	286	522	21.5%	3.1%	12.3	79.5
	HC	345	451	758	4.6%	1.8%	2.0	6.0
	GC3:1	270	370	702	4.5%	1.9%	2.5	8.3
	GC1:1	243	331	670	4.4%	2.0%	2.6	9.3
	GC1:3	263	323	720	3.7%	1.8%	2.2	6.7
	Coal	290	349	786	3.5%	1.6%	1.9	5.0

4.5.1 Combustion behaviour of sugarcane bagasse and coal

The sugarcane bagasse pellets underwent combustion at lower temperatures, which distinguished it from the other pellets. The DTG curves for sugarcane bagasse, shown in

Figure 4-13, demonstrate one small peak between 25°C – 230°C which was likely due to the loss of moisture, light volatiles and adsorbed gases (Demirbas, 2004; Munir *et al.*, 2009). For all three heating rates, sugarcane bagasse had a single-stage combustion profile with a maximum combustion rate of 16.6 %/min – 21.5 %/min. The single peak indicates that the oxidative pyrolysis region overlapped with the main char combustion region. Following the main peak, combustion continued but was negligible due to the very low rate.

As seen in Figure 4-18, the coal pellets were also characterised with small peaks at low temperatures, generally associated with moisture content and possibly light volatiles. The small peaks were followed by a single combustion stage initiated by the release and combustion of

volatiles. After coal reached a maximum combustion rate of 3.5 %/min ─ 3.7 %/min, the DTG curve decreased sharply at first, but then transitioned to a medium combustion rate, as char combustion continued at elevated temperatures.

Table 4-9 shows that the ignition temperature for sugarcane bagasse was between 245°C ─ 267°C. The peak temperature was measured at the maximum combustion rate and regarded as a measure of reactivity. The peak temperature for sugarcane bagasse ranged between 262°C ─ 286°C. The burnout temperature for the sugarcane bagasse ranged between 374°C ─ 522°C. Table 4-9 shows that the coal pellets ignited between 294°C ─ 290°C, reached a maximum combustion rate at 319°C ─ 349°C and was burned out at 542°C ─ 786°C.

As seen from the results, the sugarcane bagasse pellets ignited at low temperatures, had low peak temperatures, rapid combustion rates (very high reactivity) and low burnout temperatures. The volatile matter- and fixed carbon content of sugarcane bagasse- and coal pellets could explain the different combustion behaviour between the two samples (Munir *et al.*, 2009; Mureddu *et al.*, 2018). The high volatile matter of sugarcane bagasse (≈70%) could easily explain the rapid-combustion at lower temperatures which are followed by lower combustion activity that is linked to the low fixed carbon content (≈13%). In contrast to the combustion behaviour of sugarcane bagasse pellets, coal pellets initially demonstrated small peaks between 200°C ─ 300°C due to lower combustion activity linked to the lower volatile content of the coal samples (≈25%). As the volatile matter was liberated from the coal's structure and ignited, more energy was released and heated the surrounding particles. The heat generated could explain the rapid increase in combustion activity and the overlapping of the two combustion zones to form one zone. Subsequently, as the volatile matter decreased, the burning profile reached a maximum and transitioned to a lower and decreasing combustion rate. The broad and relatively high char combustion region is associated with the high fixed carbon content of the coal (≈61%) Wang *et al.*, 2016).

As seen in Table A-2, the cellulose, hemicellulose and lignin content of sugarcane bagasse accounted for ≈73% and accounts for the high volatile content of sugarcane bagasse. The hemicellulose, cellulose and lignin, have volatile ─OH, ─CH_2, ─CH_3, and ─C─H radical groups that easily degraded at low temperatures and ignited. (Mureddu *et al.*, 2018; Wang *et al.*, 2016). (Haykiri-Açma, 2003; Wang *et al.*, 2016). In this study, the fibre analysis supported the observed low ignition temperature of sugarcane bagasse. As shown by previous authors, oxidising conditions at low temperatures (200°C ─ 220°C) initiated the decomposition of hemicellulose and

lignin. The work of previous authors showed that lignin degraded slowly over a wide temperature range (200°C ─ 500°C), whereas hemicellulose degraded rapidly and completely converted at 350°C (Dorez *et al.*, 2014). The higher burnout temperature was accredited to the cellulose- and lignin content, which has a higher ignition temperature than hemicellulose and lignin (Dorez *et al.*, 2014). The very low mass-loss rate following the main peak was likely due to the decomposition of lignin residue (Dorez *et al.*, 2014).

Sugarcane bagasse pellets had a maximum combustion rate of 4.5 ─ 6.1 times greater than the coal, indicative of fast degradation of the organic material and rapid release and combustion of volatiles. The high hemicellulose and cellulose content of sugarcane bagasse supported the rapid combustion due to a high concentration of thermally unstable components (Munir *et al.*, 2009; Mureddu *et al.*, 2018).

Table 4-1 shows that the sugarcane bagasse had an O/C and H/C atomic ratio, approximately, two times and five times greater than the coal sample, respectively. The FT-IR analysis showed that the sugarcane bagasse had a high concentration carbon-hydrogen and carbon-oxygen bonds, which supported the high O/C and H/C atomic ratios. In contrast, the coal sample had lower O/C and H/C atomic ratios, due to the higher total carbon content, which implies stronger carbon-carbon bonds that have greater bonding energies and would result in greater thermal stability with a combustion profile at higher temperatures (Munir *et al.*, 2009; Mureddu *et al.*, 2018). Consequently, the lower ignition temperature of sugarcane bagasse in comparison with the coal samples for the three heating rates, as well as the higher reactivity, could be linked to the organic structure with characteristic weaker carbon-oxygen and carbon-hydrogen bonds, which are with respect to the carbon-carbon bonds, easier to combust at lower temperatures.

4.5.2 Combustion behaviour of hydrochar against sugarcane bagasse and coal

Figure 4-14 showed that the burning profile of hydrochar pellets had two distinct combustion zones. The first peak was associated with the secondary hydrochar, formed from organic HTL products via condensation reactions, polymerisation, and re-deposited on the surface of the primary hydrochar. The second peak was associated with the primary hydrochar, which is the product of solid-solid conversion, i.e. the condensed lignin of sugarcane bagasse with a higher degree of carbonisation (Lucian *et al.*, 2018; Volpe & Fiori, 2017). The FTIR analysis and the SEM images showed that HTL converted the organic content of sugarcane bagasse, and the hydrochar consisted out of primary-and secondary hydrochar. The two-stage combustion profile

resembling the combustion of primary- and secondary hydrochar supported the results obtained from the FTIR analysis and SEM images.

In comparison with sugarcane bagasse, the hydrochar's ignition temperature was higher for all three heating rates and ranged between 345°C ─ 377°C. Comparing the ignition temperatures of the hydrochar pellets with the sugarcane bagasse pellets showed an increase of 78°C ─ 117°C. The higher ignition temperatures showed that the secondary hydrochar produced under the HTL conditions had higher thermal stability than the sugarcane bagasse. The FTIR analysis supported the improved thermal stability, showing that the surface had a higher degree of aromatisation.

The peak temperatures of the hydrochar pellets were higher than the coal for all three heating rates. In contrast, the burnout temperatures of the hydrochar- and the coal pellets were within the same region with no repetitive trend observed for the three heating rates. The peak- and the burnout temperatures ranged between 399°C ─ 451°C and 542°C ─ 758°C, respectively. Figure 4-14 explained the high peak temperatures observed for hydrochar. The second peak was the combustion of the fixed carbon content, which in the case of the hydrochar, was the primary hydrochar. The combustion of the primary hydrochar accounted for 55% ─ 60% of the hydrochar's mass, which occurred at higher temperatures over a wide temperature range, and had the highest maximum combustion rate.

In contrast, coal pellets had one main peak with a maximum combustion rate at lower temperatures; yet, the coal pellets demonstrated prolonged combustion over a wide temperature range at a relatively high combustion rate. The observed combustion behaviour of hydrochar was favourable. One of the disadvantages associated with the combustion of biomass-coal blends are the different burning profiles, i.e. biomass combust at lower temperatures, while coal combusts at higher temperatures. Co-firing biomass and coal have shown to improve the ignition property of coal, but at the cost of comprehensive combustion, characteristic decreased due to a prolonged, less intense combustion profile (Gil, Casal, *et al.*, 2010; Wang *et al.*, 2016; Zhou *et al.*, 2014). However, from the discussion above, it was clear that hydrochar had improved combustion behaviour over the sugarcane bagasse with higher ignition-, peak- and burnout temperatures. In addition, the hydrochar- and coal pellets demonstrated similar combustion behaviour within the same temperature regions. This would include favourable combustion properties during co-firing.

The elemental composition supported the improved combustion behaviour of hydrochar. The low H/C and O/C atomic ratios suggested that the hydrochar contained less carbon-hydrogen and

carbon-oxygen bonds and more carbon-carbon bonds with higher bonding energy (Munir *et al.*, 2009), supporting the lower rate of decomposition during oxidative pyrolysis (4.1% ─ 4.6% versus 16.6% ─ 21.5%) and higher peak temperatures (400°C ─ 451°C versus 319°C ─ 349°C).

4.5.3 Combustion behaviour of GreenCoal against hydrochar and coal

The burning profiles of the GreenCoal pellets (see Figure 4-15, Figure 4-16 and Figure 4-17) demonstrated the combined combustion behaviour of hydrochar- and coal pellets, transforming to a burning profile similar to the hydrochar pellet's burning profile as the fraction of hydrochar increased. Qualitatively, GreenCoal pellets had two-stage combustion profiles. As the fraction hydrochar increased, the first peak became more intense and the second peak shifted to a higher temperature range, showing a more distinct separation of the oxidative pyrolysis and char combustion zones as the hydrochar fraction increased.

The first peak intensified as the hydrochar/coal ratio was increased due to the secondary hydrochar. In contrast, the second peak shifted to a higher temperature range owing to an increased fraction of primary hydrochar. Figure 4-19 (a) and Figure 4-19 (b) shows the ignition- (T_i) and burnout temperature (T_f) of hydrochar, respectively, as a function of the hydrochar/coal ratio and the three heating rates. Overall, the ignition temperature as a function of the heating rate did not indicate a repetitive trend for the different pellets; however, the burnout temperature increased by increasing a higher heating rate. As stated at the beginning of Section 4.5, the possible reasons for the shift were: (i) inadequate time for reactions to complete, or (ii) higher temperature gradient over the cross-sectional area of the pellet (Mureddu *et al.*, 2018; Wang *et al.*, 2016).

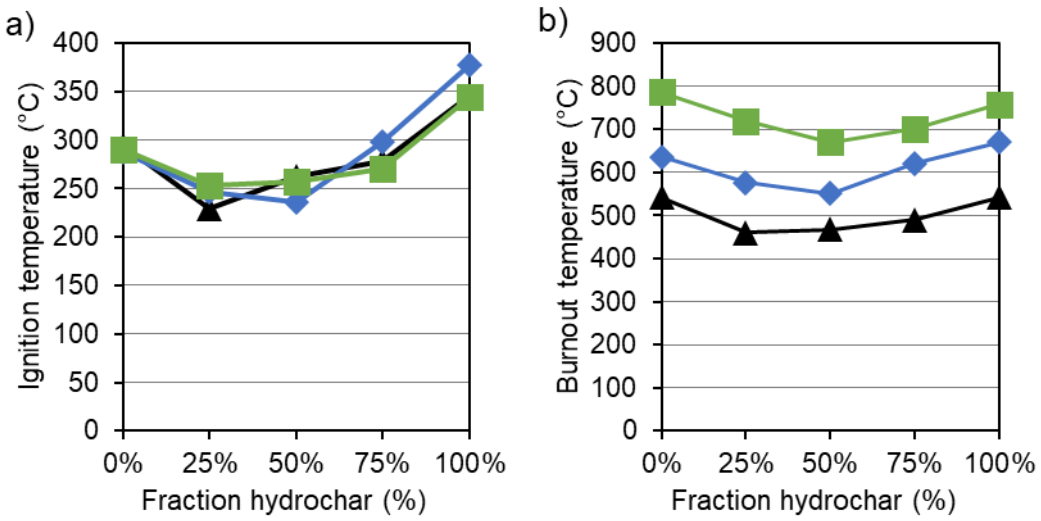

Figure 4-19: The (a) ignition – and (b) burnout temperature as a function of the fraction hydrochar and the three heating rate: 5 °C/min (▲), 7.5 °C/min (♦) and 10 °C/min (■)

As seen in Figure 4-19 (a), GreenCoal 1:3 pellets had a lower ignition temperature in comparison with the coal pellets, decreasing between 27°C ─ 64°C. The lower ignition temperature of GreenCoal 1:3 was likely due to the secondary hydrochar that was more volatile and ignited at lower temperatures. Excluding the coal sample, the ignition temperature showed a positive-, exponential relationship with the hydrochar/coal ratio. The exponential relationship was likely due to the two-stage combustion profiles observed for the GreenCoal- and the hydrochar pellets and the method used to determine the ignition temperature. This statement is explained with reference to Figure 4-20 and the method to determine the ignition temperature described in Section 3.5 as follow.

Suppose a burning profile has two peaks with the second peak associated with the maximum combustion rate. The ignition temperature is determined at the point where two lines, tangent to the TG-curve, intersect. The first line is tangential to the curve at the start of the thermogravimetric analysis, and the second line is tangential to the point on the mass curve corresponding to the maximum combustion rate. The maximum combustion rate was associated with the combustion zone of primary hydrochar, which shifted into higher temperature regions as the hydrochar/coal ratio increased, which in turn translated to higher ignition temperatures. Subsequently, the ignition temperature was indirectly a function of the hydrochar/coal blend, proven by the observed trend for the peak temperature shown in Figure 4-22. Consequently, the high ignition temperature

at higher hydrochar/coal ratios suggested that the main combustion zone shifted to higher temperature regions, suggesting improved heat production.

As discussed above, the hydrochar and GreenCoal pellets all demonstrated two main peaks. The first small peak was the combustion of the secondary hydrochar, and the second peak was the combustion of the primary hydrochar. The method used to determine the ignition temperature was a function of the maximum combustion rate associated with the primary hydrochar; therefore, the method used did not take the ignition of the secondary hydrochar (or the volatile matter content) into account. The ignition of secondary hydrochar at lower temperatures should be taken into consideration since it might pose a fire risk if ignited. The method used to determine the ignition temperature of the secondary hydrochar was similar to the one used to determine the ignition temperature of each pellet with one difference. As seen in Figure 4-20, the maximum combustion rate of the zone associated with the combustion of secondary hydrochar was used instead of the overall maximum combustion rate.

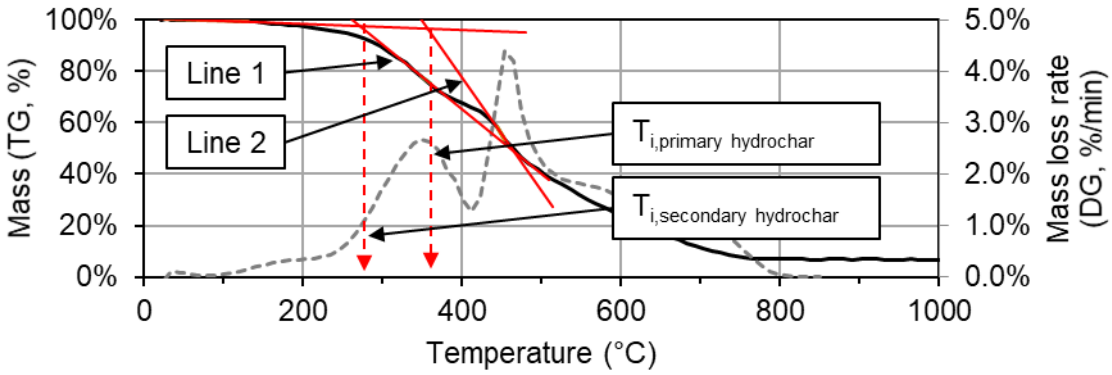

Figure 4-20: The ignition temperature as a function of the secondary hydrochar (example: TG curve of HC, dT/dt = 10 °C/min)

Figure 4-21 shows the ignition temperature for the hydrochar- and GreenCoal pellets, taking the secondary hydrochar into account and comparing it with the coal pellets. The plot of the ignition temperature was a function of the hydrochar/coal ratio, and the heating rate. Excluding the coal pellets, the ignition temperature and the heating rate had a repetitive relationship for all the pellets. The ignition temperatures of the hydrochar- and GreenCoal pellets increased with higher heating rates and indicated a linear relationship.

For all three heating rates, the hydrochar- and the three GreenCoal's pellets had, in comparison with the coal pellets, lower ignition temperatures which might be linked to the secondary hydrochar ($T_{i,\ secondary\ hydrochar}$) hydrochar. In contrast to the exponential relationship observed for the ignition temperature of the main combustion zone as a function of the hydrochar/coal ratio, the observed relationship between the ignition of the secondary hydrochar were linear and increased with higher heating rates. Concerning the ignition temperature of the coal pellets, GreenCoal 1:3 had an ignition temperature 19°C – 66°C lower, clearly illustrating the reactive nature of the secondary hydrochar; however, as the hydrochar/coal ratio increased, the ignition temperature of the GreenCoal pellets increased linearly and converged to the ignition temperature of the hydrochar pellets. As previously discussed, the mass density of GreenCoal pellets increased with higher hydrochar/coal ratios. The void volume and the total surface area of a dense pellet would likely be lower; thereby, result in mass and heat transfer limitations and, subsequently, explain the linear relationship between the ignition temperature and the hydrochar/coal ratio.

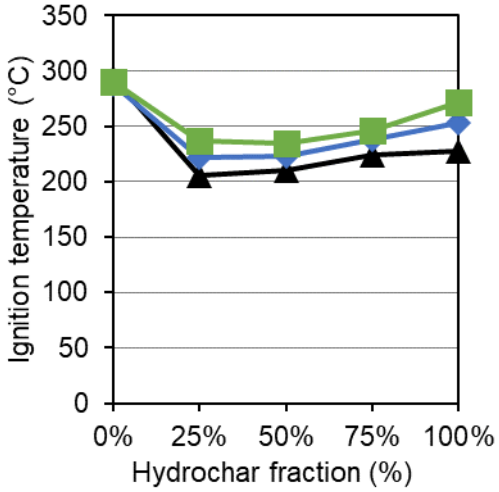

Figure 4-21: The ignition temperature as a function of the fraction hydrochar and the three heating rate: 5 °C/min (▲), 7.5 °C/min (♦) and 10 °C/min (■)

The hydrochar and coal pellet had similar burnout temperatures; which was likely due to the higher fixed carbon content (i.e. the primary hydrochar) of hydrochar and the higher bonding energies associated with a higher degree of aromatisation as indicated by the FTIR analysis and the low O/C and H/C atomic ratios. At low hydrochar/coal ratios (GreenCoal 1:3 and GreenCoal 1:1) the burnout temperature decreased with higher hydrochar/coal ratios, indicating a reverse

relationship; though, as the hydrochar/coal ratio was further increased the burnout temperature increased and showcased a linear relationship.

The following interpretation of the combustion profiles at a heating rate of 10 °C/min was an attempt to try and explain the observed trend of the burnout temperature. The coal pellet demonstrated one broad peak with a peak temperature at 349°C. The high burnout temperature was related to the high fixed carbon content with stronger C═C bonds, supported by the low O/C and H/C atomic ratios. In comparison, the GreenCoal 1:3 demonstrated a small peak before the main combustion peak, which was associated with the secondary hydrochar. The heat produced by the ignition of secondary hydrochar might explain the shift of the main combustion peak to lower temperatures. The extra heat generated from the combustion of secondary hydrochar might heat the primary char, which in turn shift the main combustion region to lower temperature and result in a lower peak temperature. Concerning the coal pellet, the burnout temperature of GreenCoal 1:3 decreased with 66°C. The lower burnout temperature might be related to the heat generated at a lower temperature, excelling the main combustion region and reducing the burnout temperature.

The GreenCoal 1:1 pellets demonstrated a similar burning profile to the GreenCoal 1:3. With regards to the GreenCoal 1:3 pellet, the main difference was the increased intensity of the first- and second peak and the burnout temperature decreasing with 50°C. Similar to GreenCoal 1:3, the lower burnout temperature might be related to the increased combustion intensity at lower temperatures. Both the GreenCoal 1:3- and GreenCoal 1:1 pellet, had only one main peak following the first peak associated with the combustion of volatile matter. The latter indicated that the combustion of the coal's volatile matter and the combustion of the primary char of the hydrochar, overlapped, which would contribute to higher combustion intensity at lower temperatures.

Again, the GreenCoal 3:1 pellet demonstrated a burning profile similar to the GreenCoal 1:3- and GreenCoal 1:1 pellet; however, both peaks shifted to a slightly higher temperature, demonstrated a small increase in the combustion intensity, and had a higher burnout temperature, which increased with 32°C concerning GreenCoal 1:1. The main combustion zone, shifting into a higher temperature zone, might account for the higher burnout temperature. As previously discussed, the hydrochar pellet showed two distinct combustion peaks with the combustion of the primary hydrochar taking place at higher temperatures (higher peak temperature), which again might explain the higher burnout temperature. Based on this discussion, it is suggested that the burnout

temperature was related to the peak temperature, following a similar trend as the burnout temperature.

Figure 4-22 (b) shows the maximum combustion rate as a function of the fraction hydrochar. For all three heating rates, the maximum combustion rate of coal, GreenCoal 1:3- and GreenCoal 1:1 pellets increased for the given order; however, GreenCoal 1:1, GreenCoal 3:1, and hydrochar had similar maximum combustion rates, indicating that at higher hydrochar/coal ratios, the effect of the fraction of hydrochar was less apparent. The maximum combustion rate for GreenCoal 1:1-, GreenCoal 1:3-, and hydrochar pellets ranged between 4.3 %/min ─ 4.7 %/min. The maximum combustion rate plateauing at higher hydrochar/coal ratio was likely due to mass and heat transfer limitations associated with denser pellets.

Figure 4-22 (a) shows that the peak temperature increased with higher heating rates. The peak temperatures increasing with higher heating rates were due to the combustion profile shifting into higher temperature regions. As discussed in Section 4.5, two reasons could explain the shift, which was inadequate time for reactions to complete due to the higher heating rate, or a higher temperature gradient over the pellet.

Figure 4-22 (a) shows that the peak temperatures of GreenCoal 1:3 pellets were lower than the peak temperatures of the coal pellets, but as the hydrochar/coal ratio increased, the peak temperature increased and converged to the peak temperature measured for the hydrochar. The trend observed for the peak temperature was similar to the trend observed for the ignition temperature. GreenCoal pellets with a low hydrochar/coal ratio showed a lower peak temperature in comparison with the coal pellets, but as the hydrochar/coal ratio increased, the peak temperature of GreenCoal pellets increased. This was previously observed by (Liu, Guo, *et al.*, 2016) and suggested that combining hydrochar with low-rank coal, i.e. lignite, might produce a blend with superior combustion properties such as high peak temperature. By observing the respective TG-DTG profile of hydrochar and coal, the trend observed for the peak temperature as the hydrochar/coal ratio increased might be explained by these burning profiles. The coal had a low peak temperature which might be attributed to the rapid release and combustion of the coal's volatile matter, whereas the coal's fixed carbon content combusted at a medium rate (see Figure A-25). In contrast, the hydrochar had a high peak temperature since the maximum combustion rate was linked to the primary hydrochar. The secondary hydrochar was represented by a smaller peak at lower temperatures (see Figure A-21). considering the two burning profiles of coal and hydrochar (Figure A-25 and Figure A-21), it is clear that the second peak of GreenCoal

pellets was associated with the combustion of primary hydrochar, which explains the increase in peak temperature as the hydrochar/coal ratio increased for GreenCoal.

As seen in Figure 4-22 (a), the peak temperature first decreased with respect to the coal's peak temperature. This might suggest that the combined combustion of the secondary hydrochar and coal's volatile matter catalysed the combustion of the primary hydrochar, but as the hydrochar's fraction increased, this effect was lower.

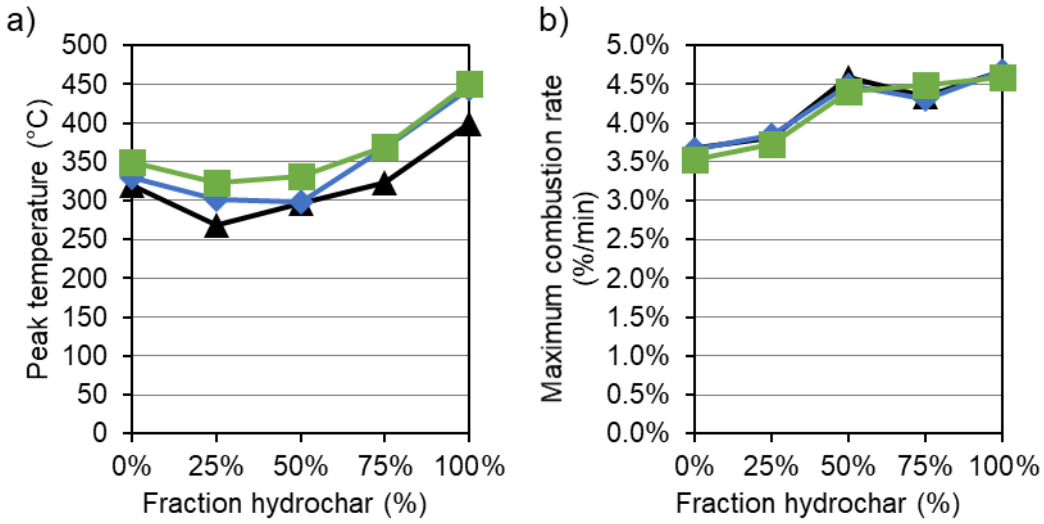

Figure 4-22: The (a) peak temperature and (b) maximum combustion rate as a function of the fraction hydrochar and the three heating rates: 5 °C/min (▲), 7.5 °C/min (♦) and 10 °C/min (■)

Figure 4-23 (a) and Figure 4-23 (b) shows the ignition index (C) and comprehensive combustion index (S), respectively. The ignition index represents the ignition performance of the fuel, i.e. a higher ignition index indicates an improved ignition performance, whereas a lower ignition index indicates reduced ignition performance. Figure 4-23 (a) shows that the hydrochar- and coal pellets had similar ignition performances and in comparison with the GreenCoal, the hydrochar- and coal pellets had the lowest ignition indices. All GreenCoals demonstrated improved ignition performances with GreenCoal 1:1 showing the best ignition performance. Using GreenCoal 1:1 as a reference point, the ignition index of GreenCoal decreased as the hydrochar/coal ratio increased or decreased. The ignition index indicated that GreenCoal had an advantage over pure hydrochar- and coal pellets as fuel based on the improved ignition performances of the GreenCoals.

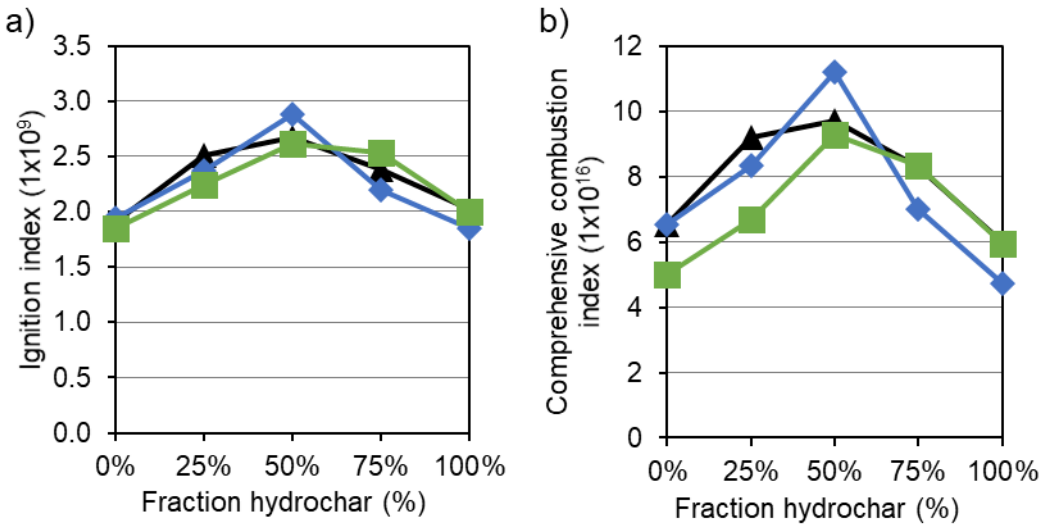

Figure 4-23: The (a) ignition index (C) and (b) comprehensive combustion index (S) as a function of the fraction hydrochar and the three heating rate: 5 °C/min (▲), 7.5 °C/min (♦) and 10 °C/min (■)

Figure 4-23 (b) shows the comprehensive combustion index, demonstrating a similar trend to the ignition index. The comprehensive combustion index indicates combustion activity. Higher comprehensive combustion indices point to higher combustion activity and vice versa. Figure 4-23 (b) shows that the hydrochar- and coal pellets had the lowest combustion activity, whereas GreenCoal pellets showed improved combustion activity with GreenCoal 1:1 having the highest combustion activity among the three GreenCoals. The combustion activity of the GreenCoal pellets improved due to the lower ignition- and burnout temperatures, as well as the higher maximum combustion rates.

Overall, the comprehensive combustion index indicated that GreenCoal pellets had an advantage over pure hydrochar- and coal pellets as fuel based on the improved combustion activity of the GreenCoals. However, the lower ignition temperature for GreenCoal with a low hydrochar/coal ratio (GreenCoal 1:3) might pose problems for certain combustion systems. Nevertheless, the ignition temperature increased for higher hydrochar/coal ratios.

4.5.4 Combustion calculations

Table 4-10 shows the calculated flue gas mole quantities, the volume of the flue gas, and the dust burden generated for a basis of 100 kg daf sample during combustion in 20% excess air.

Table 4-10: The calculated amount of flue gas (mole and volume) and dust burden produced during combustion of sugarcane bagasse (SB), hydrochar (HC), GreenCoals (GC3:1, GC1:1 and GC1:3) and coal

	SB	HC	GC3:1	GC1:1	GC1:3	Coal
$n_{flue\ gas}$ (kmole gas)	41.7	42.6	42.7	43.1	43.3	43.5
V (m^3 gas)	9.3	9.5	9.6	9.7	9.7	9.8
m_{fly_ash} (kg ash/m^3 gas)	1.4	0.7	1.0	1.2	1.4	1.7

Concerning the other samples, the sugarcane bagasse and coal samples generated large quantities of fly ash, releasing 1.4 kg and 1.7 kg of fly ash per volume flue gas. Due to the lower ash content, it was clear that hydrochar would release the least amount of fly ash. The GreenCoal demonstrated an increasing fly ash content with increasing coal content. The hydrochar, GreenCoal 3:1, GreenCoal 1:1 and GreenCoal 1:3 had an ash burden smaller than the coal, whereas hydrochar, GreenCoal 3:1 and GreenCoal 1:1 had an ash burden smaller than sugarcane bagasse. GreenCoal 1:3 had an ash burden equivalent to the sugarcane bagasse. Subsequently, upgrading sugarcane bagasse to a hydrochar and using the hydrochar to produce GreenCoal, would be beneficial with regards to the ash burden.

Table 4-11 shows the calculated amount of SO_2 and NO_x released as emissions during combustion by assuming 90% of the sulphur- and 25% of the nitrogen content combusted to form SO_2 and NO_x, respectively. Table 4-11 shows that the sugarcane bagasse had the lowest emissions, with hydrochar and coal, respectively, releasing approximately seven and ten times more. The SO_2 emissions of GreenCoal showed an inverse relationship with the hydrochar fraction, decreasing as the hydrochar fraction increased.

Table 4-11: SO_2 and NO_x emissions of sugarcane bagasse (SB), hydrochar (HC), GreenCoals (GC3:1, GC1:1 and GC1:3) and coal

	SB	HC	GC3:1	GC1:1	GC1:3	Coal
SO_x (ppm)	59.9	411.2	459.2	515.2	561.2	610.0
SO_x (mg/Nm^3)	171.2	1175.0	1311.9	1472.1	1603.4	1742.8
NO_x (ppm)	179.8	289.5	444.7	572.2	706.3	861.1
NO_x (mg/Nm^3)	369.1	594.6	913.2	1175.0	1450.5	1768.4

4.6 CO_2 gasification behaviour of sugarcane bagasse, hydrochar, coal and GreenCoal pellets

Thermogravimetric (TG) analysis on sugarcane bagasse- (SB), hydrochar- (HC), GreenCoals- (GC3:1, GC1:1 and GC1:3) and coal char during CO_2 gasification at three isothermal gasification temperatures, generated isothermal conversion (X) data. The char used for CO_2 gasification was the product of pyrolysis discussed in Section 4.4. In this section, the sample labels refer to the charred pellets.

4.6.1 Conversion and reactivity

Figure 4-24, Figure 4-26, and Figure 4-28 show the isothermal conversion of chars as a function of time and at 950°C, 1000°C, and 1050°C, respectively. Figure 4-25, Figure 4-27, and Figure 4-29 show the reactivity (R) of the chars at 950°C, 1000°C, and 1050°C, respectively, calculated from the isothermal conversion data.

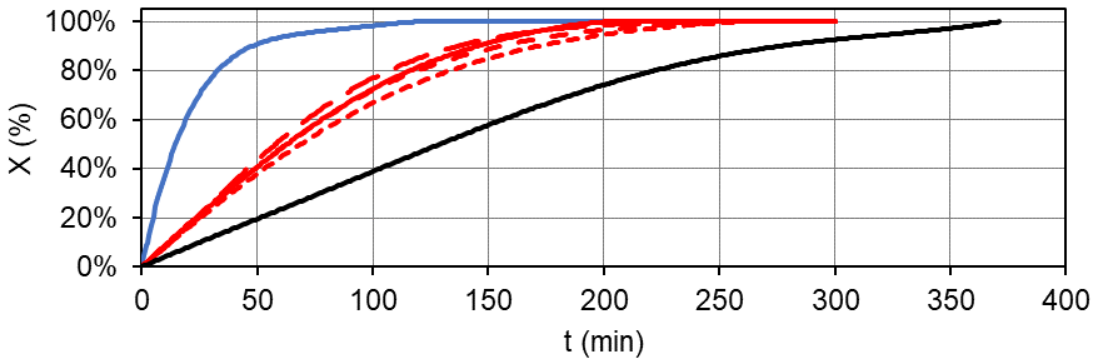

Figure 4-24: Conversion (X) of SB (—), HC (—), GC3:1 (— —), GC3:1 (– – –), GC3:1 (- - -), and coal (——) charred pellets at an isothermal temperature of 950°C

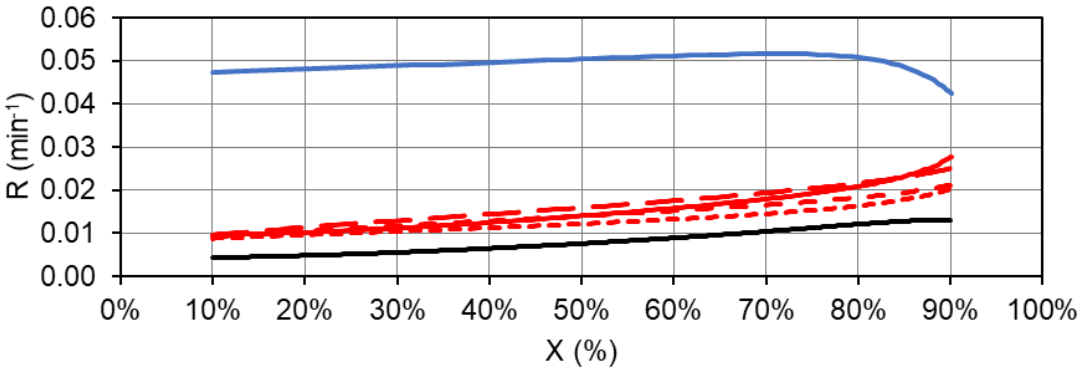

Figure 4-25: Reactivity (R) of SB (—), HC (—), GC3:1 (— —), GC3:1 (– – –), GC3:1 (- - -), and coal (——) charred pellets at an isothermal temperature of 950°C

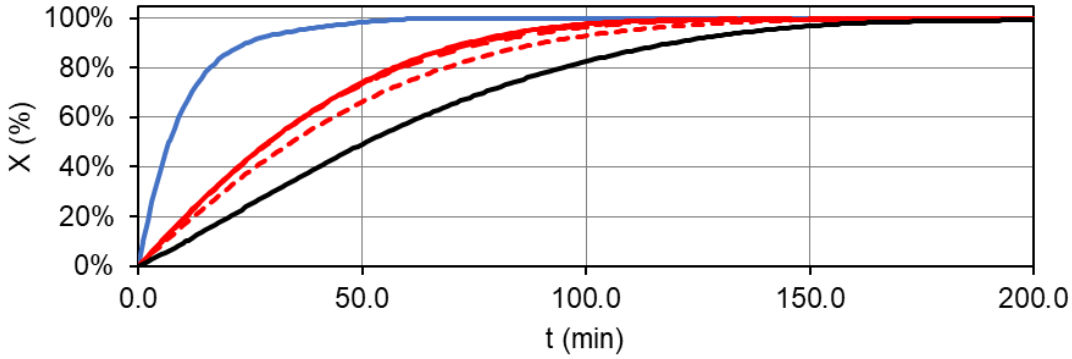

Figure 4-26: Conversion (X) of SB (—), HC (—), GC3:1 (— —), GC3:1 (– – –), GC3:1 (- - -), and coal (——) charred pellets at an isothermal temperature of 1000°C

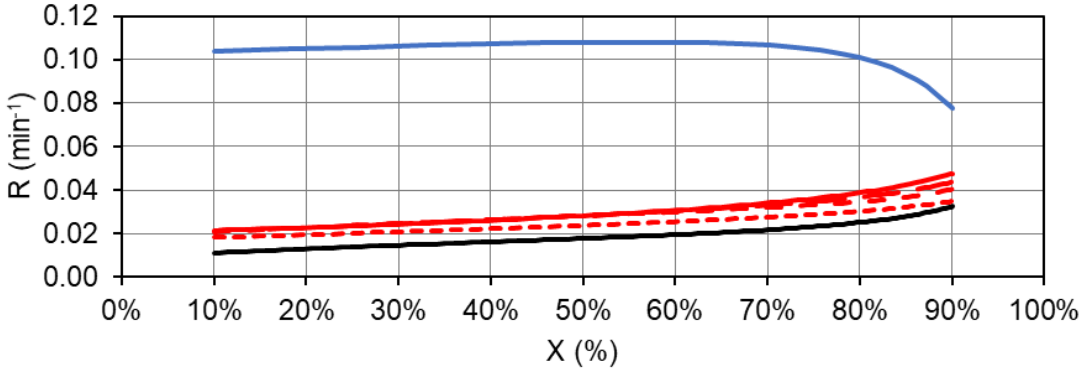

Figure 4-27: Reactivity (R) of SB (—), HC (—), GC3:1 (— —), GC3:1 (– – –), GC3:1 (- - -), and coal (——) charred pellets at an isothermal temperature of 1000°C

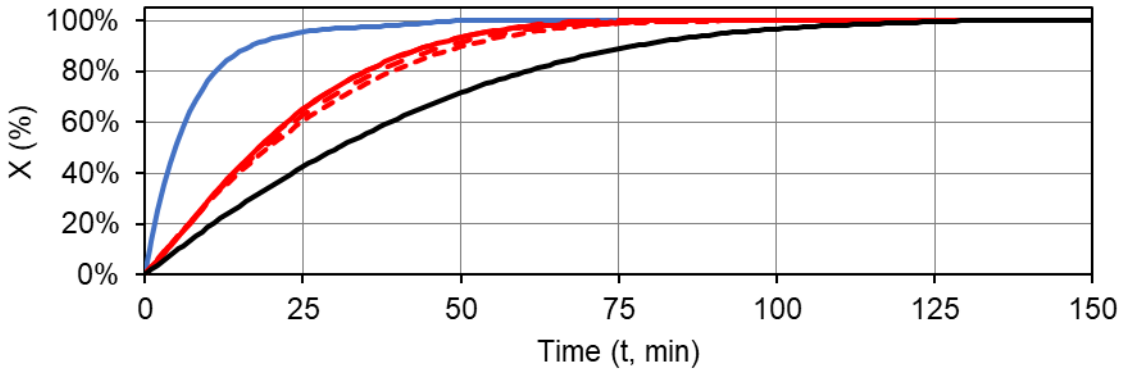

Figure 4-28: Conversion (X) of SB (—), HC (—), GC3:1 (— —), GC3:1 (– – –), GC3:1 (- - -), and coal (——) charred pellets at an isothermal temperature of 1050°C

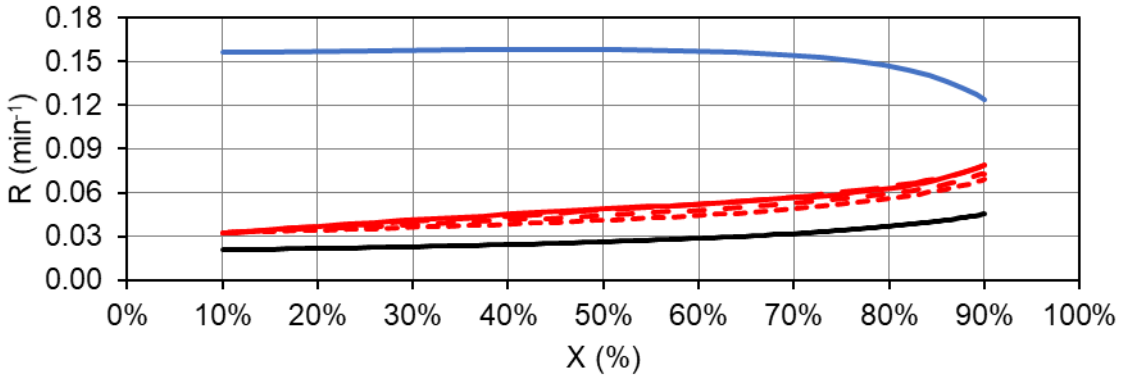

Figure 4-29: Reactivity (R) of SB (—), HC (—), GC3:1 (— —), GC3:1 (– – –), GC3:1 (- - -), and coal (——) charred pellets at an isothermal temperature of 1050°C

A comparison between these curves showed that hydrothermal liquefaction yielded a hydrochar that had improved thermal stability and was less reactive than the sugarcane bagasse during CO_2 gasification. As expected, the coal was the least reactive of all the samples. The conversion trends for the sugarcane bagasse, hydrochar, and coal samples were consistent with those reported by previous authors (Wei, Guo, Gong, *et al.*, 2017; Wei, Guo, He, *et al.*, 2017b; Zhang *et al.*, 2016). For all three isothermal gasification temperatures, the hydrochar- and GreenCoal 3:1 samples had very similar conversion profiles, whereas the GreenCoal- 1:1 and GreenCoal 1:3 samples demonstrated a slower conversion rate with lower hydrochar/coal ratios. The conversion times (t_X) and reactivity (R_X) for X=10%, 50%, and 90%, are reported in Table A-7.

As seen in Figure 4-25 for gasification at 950°C, sugarcane bagasse had a high reactivity throughout gasification, with $R_{X=10\%}$=47.4 min^{-1}, $R_{X=50\%}$=50.4 min^{-1}, and $R_{X=90\%}$=42.6 min^{-1}. In contrast, the reactivity of the hydrochar- and the coal samples was initially slow, but increased as gasification progressed. The reactivity of hydrochar was higher than the coal's with $R_{X=10\%}$=9.5 min^{-1}, $R_{X=50\%}$=14.0 min^{-1}, and $R_{X=90\%}$=27.6 min^{-1}, whereas the coal was $R_{X=10\%}$=4.3 min^{-1}, $R_{X=50\%}$=7.6 min^{-1}, and $R_{X=90\%}$=13.0 min^{-1}. The reactivity of the sugarcane bagasse-, hydrochar-, and coal samples explained the very fast conversion of sugarcane bagasse, followed by the hydrochar and then the coal with a conversion time at X=90% of 47.9 min, 145.5 min, and 276.8 min.

As shown in Figure 4-25, Figure 4-27, and Figure 4-29 the $R_{X=10\%}$, $R_{X=50\%}$, and $R_{X=90\%}$ of the sugarcane bagasse, hydrochar, and coal at higher gasification temperatures, showed similar trends as discussed above, i.e. the reactivity of the sugarcane bagasse initially increased as gasification progressed, but at higher conversions, the reactivity decreased. Nevertheless, the reactivity of sugarcane bagasse was very high throughout gasification. The reactivity of hydrochar and coal increased with higher conversions, and the hydrochar had a higher reactivity than the coal.

For all three gasification temperatures, the respective conversion times at X=90% for the hydrochar and coal were 2.7—3.0 times and 4.6—5.8 times greater than the sugarcane bagasse's conversion time at X=90%. The calculated fixed carbon content of the chars (normalised proximate composition by excluding the inherent moisture content and volatile matter) and the conversion time (at X=90%) showed a correlation and could, to some extent, explained the overall conversion times of the sugarcane bagasse, hydrochar and coal. Table 4-12 shows the approximated composition of the charred pellets. The second- and the third column indicates the fixed carbon- and ash's fraction of a charred sample (free of moisture and volatile matter). The third-, fourth- and fifth column indicates the mass percentage, the percentage fixed carbon content, and the percentage ash content that remained after charring. Overall, using the conversion time ($t_{X=90\%}$), the order of the charred samples from high to low was coal>HC>SB. The total carbon content from high to low followed the same trend, i.e. coal>HC>SB. The respective fixed carbon content of the charred hydrochar- and the charred coal pellets was 3.2 and 3.6 greater than the sugarcane bagasse.

Previous authors reported that the mineralogy and morphology of charred samples, as well as the charring conditions, played a pivotal role during CO_2 gasification; however, these analyses were outside the scope of this study.

Table 4-12: Fixed carbon content and an ash content of charred pellets

Sample	FC[a] (%)	ASH[a] (%)	$m_{charred}$ (%)	FC (%)	ASH (%)
SB	54.5	45.5	32.2	17.5	14.7
HC	88.1	11.9	63.4	55.9	7.5
Coal	81.3	18.7	77.3	62.8	14.5

a – Inherent moisture and volatile matter free

Figure 4-30, Figure 4-31, and Figure 4-32 shows t_X (X=10%, 50%, and 90%) and R_X (X=10%, 50%, and 90%) as a function of the hydrochar's fraction and the three gasification temperatures. Figure 4-30 (b), Figure 4-31 (b), and Figure 4-32 (b) compared the $R_{X=10\%}$, $R_{X=50\%}$, and $R_{X=90\%}$, respectively, of the hydrochar, GreenCoal, and coal as a function of the hydrochar's fraction and the gasification temperature. Reactivity at low ($R_{X=10\%}$), mid ($R_{X=50\%}$), and high ($R_{X=90\%}$) conversions were a function of the gasification temperature, increasing as the temperature increased, e.g. taking $R_{X=50\%}$ (see Figure 4-31 (b)) of all samples at 950°C as a point of reference, $R_{X=50\%}$ of all the samples increased with a factor of 1.8—2.3 and 3.0—3.5 for gasification at 1000°C and 1050°C, respectively. The reactivity at low ($R_{X=10\%}$) and high ($R_{X=90\%}$) conversions showed similar trends.

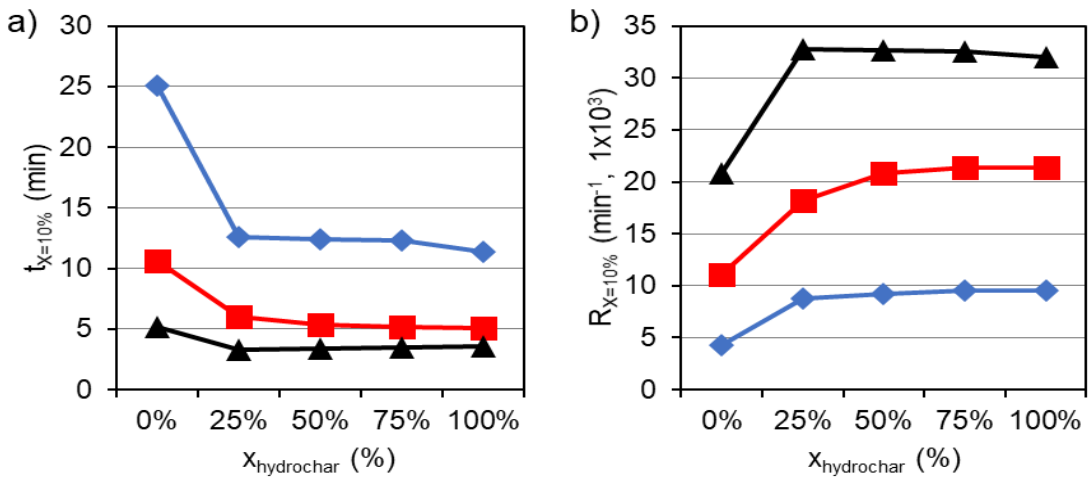

Figure 4-30: The (a) conversion time ($t_{X=10\%}$) and (b) reactivity ($R_{X=10\%}$) at X=10% as a function of the fraction hydrochar and gasification temperature: 950°C (■), 1000°C (■), and 1050°C (■)

As seen in Figure 4-30 (b), the $R_{X=10\%}$ of GreenCoals and hydrochar were alike, irrespective of the hydrochar's fraction. The $R_{X=10\%}$ of hydrochar, GreenCoal 3:1, GreenCoal 1:1, and GreenCoal 1:3 ranged between $8.8x10^{-3}$ min^{-1} to $9.6x10^{-3}$ min^{-1}, $18.2x10^{-3}$ min^{-1} to $21.4x10^{-3}$ min^{-1} and $32.0x10^{-3}$ min^{-1} to $36.1x10^{-3}$ min^{-1} for the respective temperatures (950°C, 1000°C and 1050°C). The small difference in $R_{X=10\%}$ between hydrochar- and GreenCoal pellets demonstrated similar reactivity at low temperatures. In comparison with the coal, adding hydrochar to the mix had a clear positive effect on the GreenCoals' reactivity at low conversions. Comparing the mean $R_{X=10\%}$ of the hydrochar and GreenCoals with the $R_{X=10\%}$ of coal at the respective gasification temperatures, showed that the $R_{X=10\%}$ increased with a factor of 2.1, 1.8, and 1.6 for a gasification temperature of 950°C, 1000°C, and 1050°C, respectively.

As seen in Figure 4-31 (b), $R_{X=50\%}$ increased with higher temperatures and higher hydrochar/coal ratios, which was likely due to the increased hydrochar content that was more reactive than the coal. The link between the hydrochar's fraction and $R_{X=50\%}$ was likely due to the higher reactivity of hydrochar in the GreenCoal, as was observed for the individual hydrochar- and coal pellets.

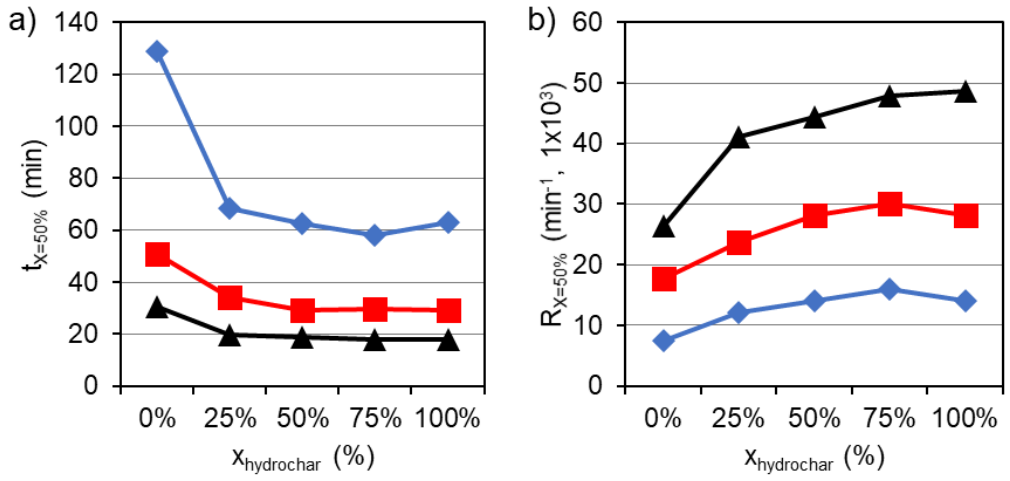

Figure 4-31: The (a) conversion time ($t_{X=50\%}$) and (b) reactivity ($R_{X=50\%}$) at X=50% as a function of the fraction hydrochar and gasification temperature: 950°C (■), 1000°C (■), and 1050°C (■)

At high conversions (X=90%), $R_{X=90\%}$ increased as the gasifying temperature increased; however, at 1050°C, the effect of the temperature was slightly different from the two lower temperatures. At 950°C and 1000°C, $R_{X=90\%}$ demonstrated a linear relationship with the hydrochar/coal ratio, which was likely due to the more reactive nature of hydrochar, while at 1050°C the hydrochar- and GreenCoals pellets (excluding the coal) demonstrated a linear trend at a higher reactivity;

therefore, the temperature and the hydrochar/coal ratio had a synergistic effect at higher temperatures.

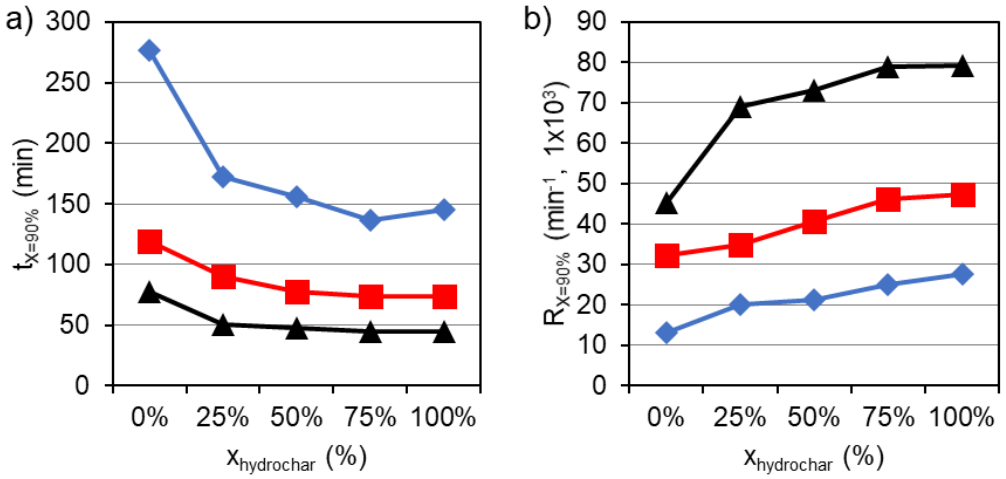

Figure 4-32: The (a) conversion time ($t_{X=90\%}$) and (b) reactivity ($R_{X=90\%}$) at X=90% as a function of the fraction hydrochar and gasification temperature: 950°C (■), 1000°C (■), and 1050°C (■)

Figure 4-30 (a), Figure 4-31 (a), and Figure 4-32 (a) showed that the difference between the maximum and minimum conversion times at an X=10%, 50%, and 90% for all the samples decreased as the gasification temperature increased, e.g. at a conversion of 50%, the difference between the coal- (maximum) and the GC 3:1 char's (minimum) conversion times at a gasification temperature of 950°C was 71.1 minutes; however, at a gasification temperature of 1050°C, the difference between the coal- (maximum) and the HC char's (minimum) conversion time was 12.6 minutes. The conversion times, $t_{X=10\%}$ and $t_{X=90\%}$, showed similar trends. The smaller difference between the conversion time at higher temperatures showed that at higher temperatures, the reactivity of the hydrochar, GreenCoals, and coal converged due to the synergetic effect associated with higher temperatures.

Analysing Figure 4-30 (a), Figure 4-31 (a), and Figure 4-32 (a), it was clear that the coal pellets demonstrated indifferent behaviour during CO_2-gasification, while the hydrochar and GreenCoal had comparable conversion times, showcasing a linear trend. Excluding the coal samples, and evaluating $t_{X=10\%}$, $t_{X=50\%}$, and $t_{X=90\%}$ at a gasification temperature of 950°C, the hydrochar and GreenCoal had a mean conversion time of 12.2 min, 63.0 min, and 152.6 min, respectively, with a standard deviation of 0.6 min, 4.4 min, and 15.1 min. At a gasification temperature of 1000°C, the corresponding mean conversion times were 5.7 min, 30.5 min, and 78.7 min with a smaller standard deviation of 0.5 min, 2.5 min, and 7.8 min. Finally, at an even higher temperature of

1050°C, the corresponding mean conversion times were 3.4 min, 18.5 min and 46.9 min with an even smaller standard deviation of 0.1 min, 0.7 min, and 2.6 min. Once again the conversion times decreased as the gasification temperature increased; however, more noteworthy was the very low standard deviations between the conversion times, which supported the suggestion the hydrochar and GreenCoals had similar CO_2-gasification behaviour at higher temperatures and in comparison with the coal, had improved reactivity.

4.6.2 Synergy

The conversion curves for the GreenCoals did not show a combination of the hydrochar- and the coal's conversion curve according to the hydrochar/coal ratio. To illustrate the latter, Figure 4-33, Figure 4-34, and Figure 4-35 show the experimental and calculated conversion curves at a gasification temperature of 950°C, 1000°C, 1050°C.

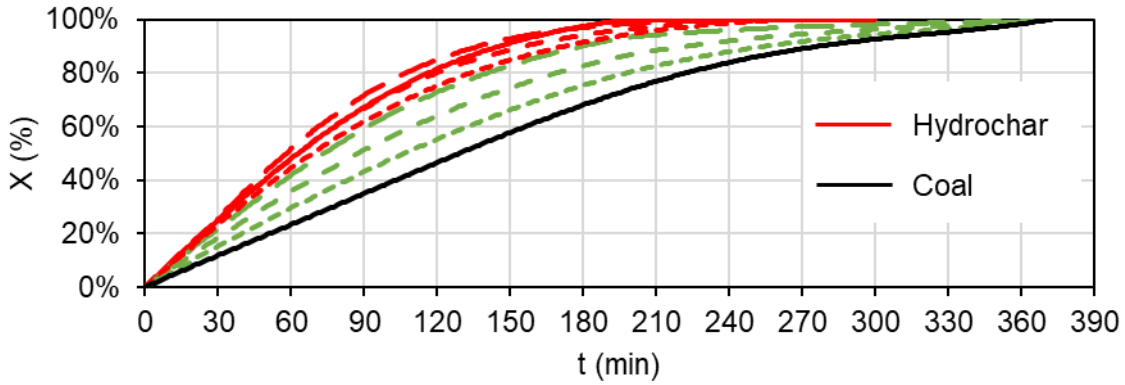

Figure 4-33: The experimental (■) and calculated (■) conversion curves of GC3:1 (—— ——), GC3:1 (— — —), GC3:1 (- - -) chars at a gasification temperature of 950°C

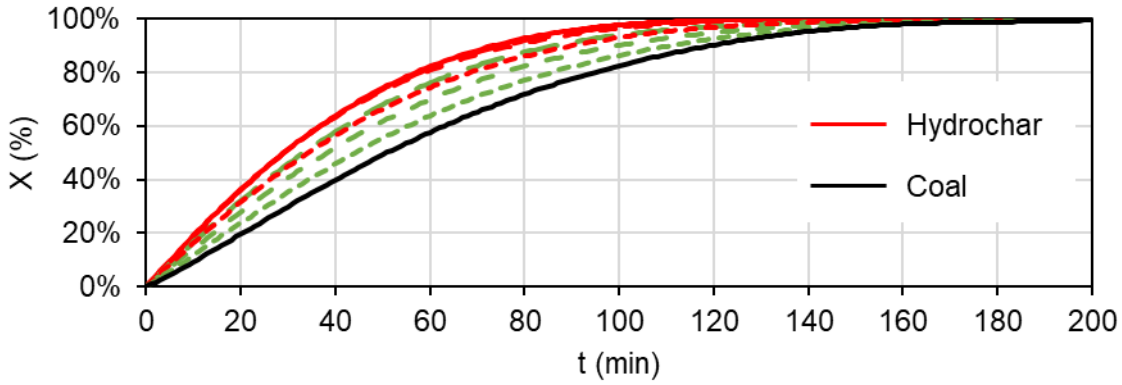

Figure 4-34: The experimental (■) and calculated (■) conversion curves of GC3:1 (—— ——), GC3:1 (— — —), GC3:1 (- - -) chars at a gasification temperature of 1000°C

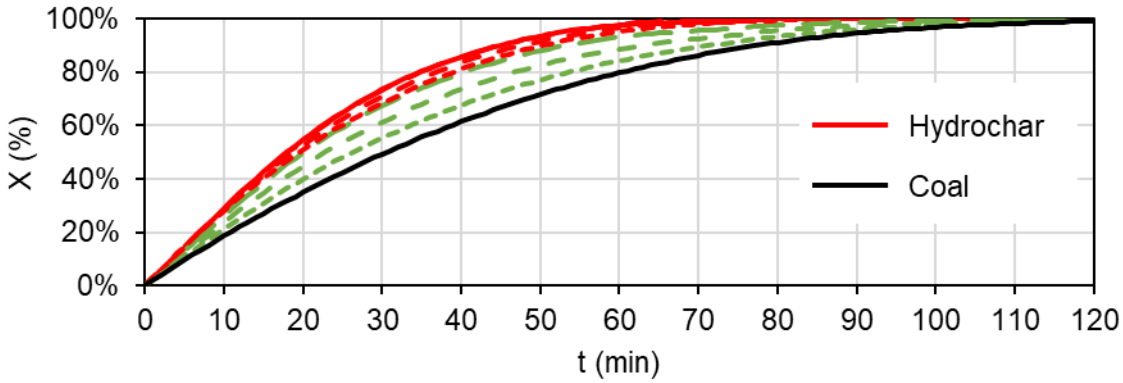

Figure 4-35: The experimental (■) and calculated (■) conversion curves of GC3:1 (—— ——), GC3:1 (— — —), GC3:1 (- - -) chars at a gasification temperature of 1050°C

The calculated and experimental curves demonstrated that the GreenCoal pellets had synergistic behaviour. Figure 4-36, Figure 4-37, and Figure 4-38 show the synergy index, calculated with (Eqn. 2-10 for X=10%, 50%, and 90%, as a function of the hydrochar's fraction, i.e. GreenCoal 1:3 (25%), GreenCoal 1:1 (50%), and GreenCoal 3:1 (75%), and the three gasification temperatures.

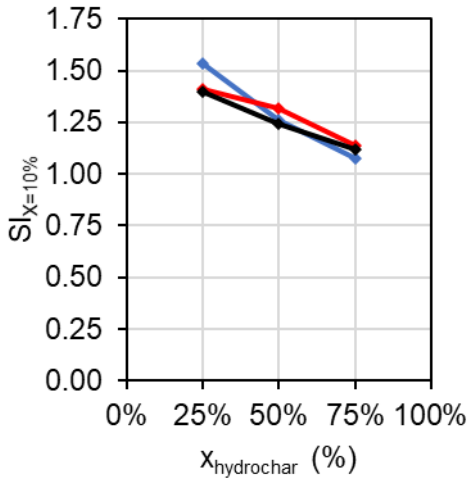

Figure 4-36: The synergy index ($SI_{X=10\%}$) as a function of hydrochar's fraction and gasification temperature: 950°C (■), 1000°C (■), and 1050°C (■)

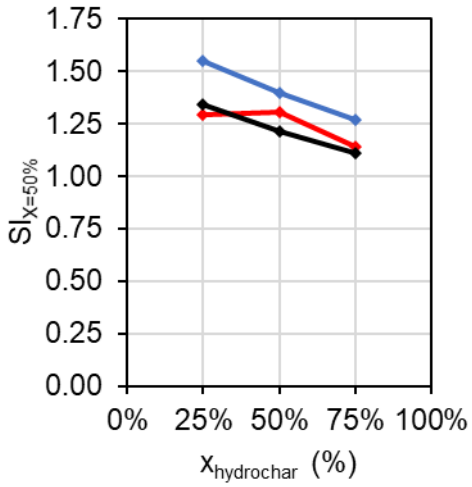

Figure 4-37: The synergy index ($SI_{X=50\%}$) as a function of hydrochar's fraction and gasification temperature: 950°C (■), 1000°C (■), and 1050°C (■)

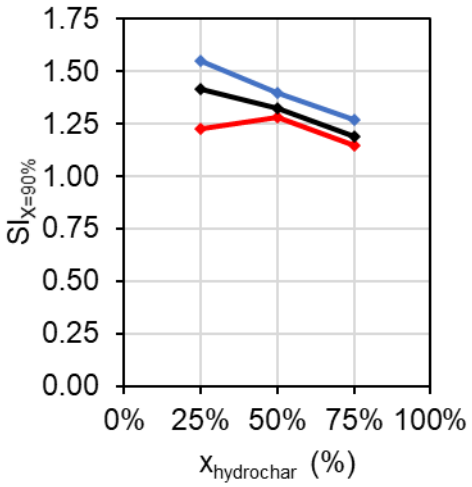

Figure 4-38: The synergy index ($SI_{X=90\%}$) as a function of hydrochar's fraction and gasification temperature: 950°C (■), 1000°C (■), and 1050°C (■)

The SI_X for all cases (X=10%, 50%, and 90%) had a value above one, indicating a synergistic effect for all the samples, throughout gasification (X=10%–90%) under the different conditions (950°C, 1000°C, and 1050°C). Overall, the general trend was a decrease in synergy for higher hydrochar/coal ratios, except for gasification at 1000°C. As seen in Figure 4-37 and Figure 4-38, synergy initially increased with higher hydrochar/coal ratios, but then decreased for a fraction of hydrochar above 50%. Previous authors linked the synergetic behaviour during CO_2 gasification to the AAEM content of the hydrochar. The main compositional elements of the hydrochar- and coal ash are reported in Table 4-13, which was used to calculate the alkali index of the pellets before pyrolysis and CO_2 gasification. The alkali index was similar to the catalytic index used by Xu *et al.* (2016).

In this study, the coal pellet had the highest alkali index, yet it had the lowest reactivity. The hydrochar produced via hydrothermal liquefaction had a very low alkali index in comparison to the coal's alkali index; therefore, producing GreenCoal pellets with higher hydrochar/coal ratio would have effectively decreased the alkali index. In most instances, the synergy of the GreenCoal pellets decreased as the hydrochar's fraction increased, showing a link with the theoretical alkali index of the GreenCoal pellets, also decreasing as the hydrochar's fraction increased.

The decreasing synergy with higher hydrochar/coal ratios was likely due to the low potassium and calcium content of the hydrochar, as well as the higher SiO_2 content. It was also previously

suggested that potassium was the main contributor to synergy, due to the catalytic effect associated with it (Jeong *et al.*, 2014; Wei *et al.*, 2019; Yuan *et al.*, 2012; Zhang *et al.*, 2016). Also, high silicon content was unfavourable since silicon had an inhibiting effect by deactivating potassium; however, the inhibiting effect of silicon on potassium was countered by the calcium. As shown by previous authors, silicon has a higher affinity towards calcium (Jeong *et al.*, 2014; Wei *et al.*, 2019; Yuan *et al.*, 2012; Zhang *et al.*, 2016).

Combining these observation made by previous authors and analysing the observed synergistic effect and the AAEM content, the high synergy of GreenCoal 1:3 was likely due to the high potassium- and calcium content associated with the sourced coal. As the coal fraction increased for the GreenCoal, the potassium and calcium content increased, contributing to the observed synergy due to the silicon's affinity towards calcium and higher potassium content. The synergy decreased with higher fractions of hydrochar due to the higher silicon content in the hydrochar, having an inhibiting effect during CO_2 gasification (Jeong *et al.*, 2014; Mafu *et al.*, 2018; Wei *et al.*, 2019).

Despite the observed behaviour for GreenCoals and the calculated values for the alkali index, it did not explain the reactivity associated with the coal and hydrochar. As stated, other factors not considered, i.e. the mineralogy, morphology, pyrolysis conditions, and porosity could have explained the observed behaviour. Therefore, the interpretation of the gasification results was limited. Furthermore, for a more accurate interpretation of the gasification reactivity as a function of the mineralogy, a more extensive mineralogy characterisation was required for the samples and chars.

Table 4-13: Compositional analysis of sugarcane bagasse-, hydrochar-, and coal ash, and calculated alkali index

	Hydrochar	Coal
Alkali index	0.32	2.86
K_2O	0.83	0.96
CaO	1.15	6.41
Na_2O	0.03	0.40
Fe_2O_3	2.79	6.78
MgO	0.13	1.58
SiO_2	78.09	48.17
Al_2O_3	12.14	30.65

CHAPTER CONCLUSION AND RECOMMENDATIONS

5.1 Introduction

This chapter presents the key outcomes with regards to the beneficiation of sugarcane bagasse to produce hydrochar via hydrothermal liquefaction for heat and power generation and includes recommendations for future work.

5.2 Conclusion

Hydrothermal liquefaction (HTL) was performed successfully and produced a hydrochar from sugarcane bagasse with improved fuel properties. Dehydration and deoxygenation reactions during HTL produced a hydrochar with favourable proximate- and elemental composition. Lower O/C and H/C atomic ratios were comparable with lignite, and the energy content of the hydrochar was similar to the sourced coal, indicating the potential to substitute or supplement coal resources. The favourable chemical composition of the hydrochar was linked to the formation of primary- and secondary hydrochar with a higher degree of aromatisation as shown by the FTIR analysis.

Producing hydrochar/coal blends was beneficial with regards to the ultimate composition, yielding lower O/C and H/C atomic ratios and approached ratios typically associated with South African coal as the hydrochar/coal ratio increased.

Upgrading sugarcane bagasse to hydrochar and producing pellets would have a positive effect on the economic value and the transportation costs due to the high mass density and improved energy density. Similar to sugarcane bagasse, hydrochar pellets demonstrated excellent strength with good resistance to external forces caused by compression and impact forces; however, upgrading sugarcane bagasse to hydrochar had an advantage over the former due to improved hydrophobicity that translated to water resistance during wetting conditions.

The compressibility of hydrochar lead to a linear relationship between the hydrochar/coal ratio and mass density. Since the HHV of the hydrochar was on par with the coal, the energy density and the hydrochar/coal fraction showed a linear relationship, adding value to the GreenCoal due to higher energy content. From this work, it was clear that hydrochar/coal blends might eliminate the need for binders and a wax layer to improve the respective strength and water resistance of

the pellets. The compression strength, impact resistance and water resistance of GreenCoal pellet were better than coal's and improved with higher hydrochar/coal ratios.

The low reactivity reflected the improved fuel properties of hydrochar during pyrolysis, combustion and CO_2-gasification, accredited to the secondary and primary hydrochar. The thermal gravimetric analysis showed that hydrochar consisted mainly out of primary hydrochar. The improved thermal stability would decrease the risk of auto-ignition and biological degradation associated with the storage of biomass. Sugarcane bagasse demonstrated rapid combustion behaviour; however, the hydrochar showcased prolonged combustion at higher temperatures, which was indicative of greater heat production.

Overall, the ignition index and the comprehensive combustion index showed that GreenCoal had the best combustion behaviour, suggesting combustion applications utilising pellets would benefit by using GreenCoal pellets. Moreover, theoretical calculations indicated that GreenCoal and hydrochar was a cleaner fuel due to the lower NO_x and SO_x emissions, as well as the lower ash burden.

The higher fixed carbon content of hydrochar, resulted in higher char yield during pyrolysis, demonstrating the benefit of upgrading sugarcane bagasse to hydrochar. The char yield was directly proportional to the CO production during CO_2-gasification; therefore, upgrading sugarcane bagasse to hydrochar would yield greater quantities of syngas. The reactivity of GreenCoal at higher conversion increased with higher hydrochar/coal ratios and demonstrated synergistic behaviour over the entire conversion profile. The synergistic behaviour during CO gasification would improve the capacity of gasifiers.

Subsequently, beneficiation of sugarcane bagasse via continuous hydrothermal liquefaction to produce GreenCoal for combustion and gasification processes showed positive results. The physicochemical properties and mineral content of hydrochar were superior to sugarcane bagasse. GreenCoal pellets showed superior properties against the pure sugarcane bagasse- and pure coal pellets, with improved mechanical strength and stability under various conditions (external forces on pellets and wet environment). Considering that most sugar mills use wet sugarcane bagasse as fuel for boilers, hydrochar and GreenCoal would be a superior fuel with greater combustion efficiency. Finally, GreenCoal favourable higher reactivity during CO_2-gasification and demonstrated synergetic behaviour.

5.3 Recommendations

This study excluded an investigation of the hydrothermal liquefaction (HTL) process parameters and what the effect of these parameters was on the hydrochar's properties. With the current installation, it would be possible to adjust the temperature, pressure and process flowrate. The latter affects the residence time, as well as the temperature. Future work should include an investigation on what effect these process parameters have on the hydrochar's physicochemical properties.

Optimising the process will be a key factor in a techno-economic evaluation to determine the prospects of commercialisation. The analysis should include the liquid phase and gas phase to fully understand the thermochemical processing and reaction mechanisms during continuous HTL.

This study investigated the effect of the hydrochar's fraction on the mechanical strength of the GreenCoal pellets and included a comparison to sugarcane bagasse, hydrochar and coal. Future work should include an evaluation of the mechanical strength and stability of GreenCoal pellets against pellets produced with binders and wax coatings.

On a commercial scale, briquetting machines produce large briquettes; therefore, future work should include an evaluation of these.

In this study, the morphology of the pellets and chars, produced via pyrolysis, were not evaluated; however, future work should include analyses to determine the morphology (i.e. total surface area and pore structures), providing insight into the kinetics and dominating reaction mechanism during pyrolysis, combustion and CO_2 gasification.

Future work should include a more comprehensive study on the mineralogy, including characterisation after charring, combustion and CO_2 gasification.

Future work should be more comprehensive concerning combustion and gasification. Concerning combustion, the majority of commercial combustion processes in South Africa are pulverised fluidised bed boilers. Two characteristics not investigated by this study were the combustion of powders at higher heating rates, which would be more representative of these applications. Subsequently, future work should include higher heating rates during combustion of powders.

Future work should include a comprehensive kinetic analysis under the different thermochemical processes.

Finally, in this study, the theoretical calculation was completed to determine the emissions of SO_x, NO_x and ash burden. Future work should include online gas analysis during thermogravimetric analysis, which would provide a higher understanding of the combustion and gasification products produced. Depending on the findings, future studies could include other work, i.e. in situ sulphur capturing via $CaCO_3$ enriched GreenCoal.

REFERENCES

Aboyade, A.O., Görgens, J.F., Carrier, M., Meyer, E.L., & Knoetze, J.H. 2013. Thermogravimetric study of the pyrolysis characteristics and kinetics of coal blends with corn and sugarcane residues. Fuel Process. Technol. Elsevier B.V. 106:310–320.

Acharjee, T.C., Coronella, C.J., & Vasquez, V.R. 2011. Effect of thermal pretreatment on equilibrium moisture content of lignocellulosic biomass. Bioresour. Technol. Elsevier Ltd. 102(7):4849–4854.

Adapa, P., Tabil, L., & Schoenau, G. 2009. Compression characteristics of selected ground agricultural biomass. Agric. Eng. Int. CIGR J. XI.

Agbor, E., Zhang, X., & Kumar, A. 2014. A review of biomass co-firing in North America. 40:930–943.

Akhtari, S., Sowlati, T., Siller-benitez, D.G., & Roeser, D. 2018. Impact of inventory management on demand fulfilment, cost and emission of forest-based biomass supply chains using simulation modelling. Biosyst. Eng. Elsevier Ltd. 178:184–199.

Al-mansour, F. & Zuwala, J. 2010. An evaluation of biomass co-firing in Europe. Biomass and Bioenergy. Elsevier Ltd. 34(5):620–629.

Arias, B., Pevida, C., Fermoso, J., Plaza, M.G., Rubiera, F., & Pis, J.J. 2008. Influence of torrefaction on the grindability and reactivity of woody biomass. Fuel Process. Technol. 89(2):169–175.

Bach, Q.V. & Skreiberg, O. 2016. Upgrading biomass fuels via wet torrefaction: A review and comparison with dry torrefaction. Renew. Sustain. Energy Rev. Elsevier. 54:665–677.

Baxter, L. 2005. Biomass-coal co-combustion: opportunity for affordable renewable energy. Fuel. 84:1295–1302.

Belkheiri, T., Andersson, S., Mattsson, C., Olausson, L., Theliander, H., & Vamling, L. 2018. Hydrothermal Liquefaction of Kraft Lignin in Subcritical Water: Influence of Phenol as Capping Agent. Energy & Fuels. American Chemical Society. 32:5923–5932.

Bergström, D., Israelsson, S., Öhman, M., Dahlqvist, S.A., Gref, R., Boman, C., & Wästerlund, I. 2008. Effects of raw material particle size distribution on the characteristics of Scots pine sawdust fuel pellets. Fuel Process. Technol. Elsevier B.V. 89(12):1324–1329.

Boeriu, C.G., Bravo, D., Gosselink, R.J.A., & Dam, J.E.G. Van. 2004. Characterisation of structure-dependent functional properties of lignin with infrared spectroscopy. Ind. Crop. Prod. 20:205–218.

Boström, D., Grimm, A., Boman, C., Björnbom, E., & Öhman, M. 2009. Influence of Kaolin and Calcite Additives on Ash Transformations in Small-Scale Combustion of Oat. Energy & Fuels. 23(23):5184–5190.

Brus, E., Marcus, O., & Nordin, A. 2005. Mechanisms of bed agglomeration during fluidized-bed combustion of biomass fuels. Energy & Fuels. 19(3):825–832.

Bunt, J.R., Neomagus, H.W.J.P., Botha, A.A., & Waanders, F.B. 2015. Reactivity study of fine discard coal agglomerates. J. Anal. Appl. Pyrolysis. Elsevier B.V. 113:723–728.

Bunt, J.R. & Waanders, F.B. 2008. Identification of the reaction zones occurring in a commercial-scale Sasol-Lurgi FBDB gasifier. Fuel. 87(10–11):1814–1823.

Camargo, L.A., Pereira, S.C., Correa, A.C., Farinas, C.S., Marconcini, J.M., & Mattoso, L.H.C. 2016. Feasibility of Manufacturing Cellulose Nanocrystals from the Solid Residues of Second-Generation Ethanol Production from Sugarcane Bagasse. Bioenergy Res. BioEnergy Research. 9(3):894–906.

Carrier, M., Hardie, A.G., Uras, Ü., Görgens, J., & Knoetze, J. 2012. Production of char from vacuum pyrolysis of South-African sugarcane bagasse and its characterization as activated carbon and biochar. J. Anal. Appl. Pyrolysis. Elsevier B.V. 96:24–32.

Carroll, J.P. & Finnan, J. 2012. Physical and chemical properties of pellets from energy crops and cereal straws. Biosyst. Eng. IAgrE. 112(2):151–159.

Castellano, J.M., Gómez, M., Fernández, M., Esteban, L.S., & Carrasco, J.E. 2015. Study on the effects of raw materials composition and pelletization conditions on the quality and properties of pellets obtained from different woody and non woody biomasses. Fuel. Elsevier Ltd. 139:629–636.

Cetin, E., Gupta, R., & Moghtaderi, B. 2005. Effect of pyrolysis pressure and heating rate on radiata pine char structure and apparent gasification reactivity. Fuel. 84(10):1328–1334.

Cha, J.S., Park, S.H., Jung, S.C., Ryu, C., Jeon, J.K., Shin, M.C., & Park, Y.K. 2016. Production and utilization of biochar: A review. J. Ind. Eng. Chem. The Korean Society of Industrial and Engineering Chemistry. 40:1–15.

Chan, Y.H., Yusup, S., Quitain, A.T., Uemura, Y., & Sasaki, M. 2014. Bio-oil production from oil palm biomass via subcritical and supercritical hydrothermal liquefaction. J. Supercrit. Fluids. Elsevier B.V. 95:407–412.

Channiwala, S.A. & Parikh, P.P. 2002. A unified correlation for estimating HHV of solid, liquid and gaseous fuels. Fuel. 81(8):1051–1063.

Chen, W.H., Ye, S.C., & Sheen, H.K. 2012. Hydrothermal carbonization of sugarcane bagasse via wet torrefaction in association with microwave heating. Bioresour. Technol. Elsevier Ltd. 118:195–203.

Chen, X., Ma, X., Peng, X., Lin, Y., & Yao, Z. 2018. Conversion of sweet potato waste to solid fuel via hydrothermal carbonization. Bioresour. Technol. Elsevier. 249(381):900–907.

Choung, M., Tung, C., Ng, J., Shiung, S., & Tran, M. 2018. Liquid biofuels production and emissions performance in gas turbines: A review. Energy Convers. Manag. Elsevier. 173:640–658.

Commandré, J.M. & Leboeuf, A. 2015. Volatile Yields and Solid Grindability After Torrefaction of Various Biomass Types. Environ. Sci. Technol. 34(4):1180–1186.

Cong, K., Han, F., Zhang, Y., & Li, Q. 2019. The investigation of co-combustion characteristics of tobacco stalk and low rank coal using a macro-TGA. Fuel. Elsevier. 237:126–132.

CSIR. 2015. Final Technical Report Intended Nationally Determined Contributions.

Davidsson, K.O., Åmand, L., Steenari, B., Elled, A., Eskilsson, D., & Leckner, B. 2008. Countermeasures against alkali-related problems during combustion of biomass in a circulating fluidized bed boiler. Chem. Eng. Sci. 63:5314–5329.

de Miranda, I. & Mothé, C.G. 2009. Characterization of sugarcane and coconut fibers by thermal analysis and FTIR. 97(2):661–665.

DEA South Africa. 2011a. White Paper on National Climate Change Response. South Africa.

DEA South Africa. 2011b. National Strategy for Sustainable Development and Action Plan.

DEA South Africa. 2015. South Africa's Intended Nationally Determined Contribution (INDC) Introduction Context: National Priorities and Circumstances.

Demirbas, A. 2001. Relationships between lignin contents and heating values of biomass. Energy Convers. Manag. 42(2):183–188.

Demirbas, A. 2003a. Relationships between lignin contents and fixed carbon contents of biomass samples. Energy Convers. Manag. 44:1481–1486.

Demirbas, A. 2003b. Sustainable cofiring of biomass with coal. 44:1465–1479.

Demirbas, A. 2004. Combustion characteristics of different biomass fuels. Prog. Energy Combust. Sci. 30(2):219–230.

Department of Energy. 2019. COP 17 Background [WWW Document]. URL http://www.energy.gov.za/cop 17/default.html.

Department of Environmental Affairs. 2016. South Africa signs Paris Agreement on Climate Change in New York [WWW Document]. URL https://www.environment.gov.za/mediarelease/southafricasignsparisagreementonclimate.

Dewangan, A., Pradhan, D., & Singh, R.K. 2016. Co-pyrolysis of sugarcane bagasse and low-density polyethylene : Influence of plastic on pyrolysis product yield. Fuel. Elsevier Ltd. 185:508–516.

Di Blasi, C. 2009. Combustion and gasification rates of lignocellulosic chars. Prog. Energy Combust. Sci. Elsevier Ltd. 35(2):121–140.

Division, I.P. 1990. Physical Testing of Fuel Briquettes. Fuel Process. Technol. 25:89–100.

DoE South Africa. 2015. Integrated Energy Plan.

DoE South Africa. 2018. Integrated Resource Plan.

Donar, Y.O., Çağlar, E., & Sinağ, A. 2016. Preparation and characterization of agricultural waste biomass based hydrochars. Fuel. 183:366–372.

Dorez, G., Ferry, L., Sonnier, R., & Taguet, A. 2014. Effect of cellulose , hemicellulose and lignin contents on pyrolysis and combustion of natural fibers. J. Anal. Appl. Pyrolysis. Elsevier B.V. 107:323–331.

Edreis, E.M.A., Luo, G., & Yao, H. 2014. Investigations of the structure and thermal kinetic analysis of sugarcane bagasse char during non-isothermal CO_2 gasification. J. Anal. Appl. Pyrolysis. Elsevier B.V. 107:107–115.

Elliott, D.C., Biller, P., Ross, A.B., Schmidt, A.J., & Jones, S.B. 2015. Hydrothermal liquefaction of biomass: Developments from batch to continuous process. Bioresour. Technol. Elsevier Ltd. 178:147–156.

Elliott, D.C., Hart, T.R., Neuenschwander, G.G., Rotness, L.J., Roesijadi, G., Zacher, A.H., & Magnuson, J.K. 2014. Hydrothermal processing of macroalgal feedstocks in continuous-flow reactors. ACS Sustain. Chem. Eng. 2(2):207–215.

Elliott, D.C., Hart, T.R., Schmidt, A.J., Neuenschwander, G.G., Rotness, L.J., Olarte, M. V, Zacher, A.H., Albrecht, K.O., Hallen, R.T., & Holladay, J.E. 2013. Process development for hydrothermal liquefaction of algae feedstocks in a continuous-flow reactor. Algal Res. Elsevier B.V. 2(4):445–454.

Fang, J.M., Fowler, P., Tomkinson, J., & Hill, C.A.S. 2002. Preparation and characterisation of methylated hemicelluloses from wheat straw. Carbohydr. Polym. 47:285–293.

Friedl, A., Padouvas, E., Rotter, H., & Varmuza, K. 2005. Prediction of heating values of biomass fuel from elemental composition. Anal. Chim. Acta. 544(1–2):191–198.

Fuertes, A.B., Sevilla, M., & Macia, J.A. 2011. Hydrothermal carbonization of biomass as a route for the sequestration of CO_2: Chemical and structural properties of the carbonized products. Biomass and Bioenergy. 35(7):3152–3159.

Gao, L., Volpe, M., Lucian, M., Fiori, L., & Goldfarb, J.L. 2019. Does hydrothermal carbonization as a biomass pretreatment reduce fuel segregation of coal-biomass blends during oxidation? Energy Convers. Manag. Elsevier. 181:93–104.

Gao, P., Zhou, Y., Meng, F., Zhang, Y., Liu, Z., Zhang, W., & Xue, G. 2016. Preparation and characterization of hydrochar from waste eucalyptus bark by hydrothermal carbonization. Energy. Elsevier Ltd. 97:238–245.

Gao, Y., Wang, X., Wang, J., Li, X., Cheng, J., Yang, H., & Chen, H. 2013. Effect of residence time on chemical and structural properties of hydrochar obtained by hydrothermal carbonization of water hyacinth. Energy. Elsevier Ltd. 58:376–383.

Gao, Y., Yu, B., Wu, K., Yuan, Q., Wang, X., & Chen, H. 2016. Physicochemical, pyrolytic, and combustion characteristics of hydrochar obtained by hydrothermal carbonization of biomass. BioResources. 11(2):4113–4133.

Garcia-maraver, A., Mata-sanchez, J., Carpio, M., & Perez-jimenez, J.A. 2017. Critical review of predictive coefficients for biomass ash deposition tendency. J. Energy Inst. Elsevier Ltd. 90(2):214–228.

Gil, M. V., Casal, D., Pevida, C., Pis, J.J., & Rubiera, F. 2010. Thermal behaviour and kinetics of coal/biomass blends during co-combustion. Bioresour. Technol. Elsevier Ltd. 101(14):5601–5608.

Gil, M. V., Oulego, P., Casal, M.D., Pevida, C., Pis, J.J., & Rubiera, F. 2010. Mechanical durability and combustion characteristics of pellets from biomass blends. Bioresour. Technol. Elsevier Ltd. 101(22):8859–8867.

Gil, M. V, García, R., Pevida, C., & Rubiera, F. 2015. Grindability and combustion behavior of coal and torrefied biomass blends. Bioresour. Technol. Elsevier Ltd. 191:205–212.

Gonçalves, A.R., Corso, D.L.S., Rocha, G.J.M., Nascimento, V.M., & Silva, V.F.N. da. 2014. Contributing to the environmental sustainability of the second generation ethanol production: Delignification of sugarcane bagasse with sodium hydroxide recycling. Ind. Crops Prod. 59:63–68.

Görling, M., Larsson, M., & Alvfors, P. 2013. Bio-methane via fast pyrolysis of biomass. Appl. Energy. Elsevier Ltd. 112:440–447.

Guizani, C., Escudero Sanz, F.J., & Salvador, S. 2013. The gasification reactivity of high-heating-rate chars in single and mixed atmospheres of H_2O and CO_2. Fuel. Elsevier Ltd. 108:812–823.

Guizani, C., Jeguirim, M., Gadiou, R., Escudero Sanz, F.J., & Salvador, S. 2016. Biomass char gasification by H_2O, CO_2 and their mixture: Evolution of chemical, textural and structural properties of the chars. Energy. Elsevier Ltd. 112:133–145.

Harun, N.Y. & Afzal, M.T. 2016. Effect of Particle Size on Mechanical Properties of Pellets Made from Biomass Blends. Procedia Eng. 148:93–99.

Haykiri-Açma, H. 2003. Combustion characteristics of different biomass materials. Energy Convers. Manag. 44(1):155–162.

He, C., Giannis, A., & Wang, J. 2013. Conversion of sewage sludge to clean solid fuel using hydrothermal carbonization : Hydrochar fuel characteristics and combustion behavior. Appl. Energy. Elsevier Ltd. 111:257–266.

Heidenreich, S., Müller, M., & Foscolo, P.U. 2016. Chapter 3 - Biomass Pretreatment. , in: Heidenreich, S., Müller, M., Foscolo, P.U. (Eds.), Advanced Biomass Gasification. Academic Press. . Academic Press, pp. 11–17.

Higman, C. & Van der Burgt, M. 2008. Gasification. Elsevier Ltd: Burlington.

Holzapfel, W.B. 1969. Effect of Pressure and Temperature on the Conductivity and Ionic Dissociation of Water up to 100 kbar and 1000°C. J. Chem. Phys. American Institute of Physics. 50(10):4424–4428.

Höök, M. & Aleklett, K. 2010. A review on coal-to-liquid fuels and its coal consumption. Int. J. energy Res. 34(August 2007):848–864.

Hu, J., Shen, D., Wu, S., Zhang, H., & Xiao, R. 2014. Effect of temperature on structure evolution in char from hydrothermal degradation of lignin. J. Anal. Appl. Pyrolysis. Elsevier B.V. 106:118–124.

Hu, X. & Gholizadeh, M. 2019. Biomass pyrolysis: A review of the process development and challenges from initial researches up to the commercialisation stage. J. Energy Chem. Elsevier B.V. and Science Press. 39(x):109–143.

Huang, Y., Finell, M., Larsson, S., Wang, X., Zhang, J., Wei, R., & Liu, L. 2017. Biofuel pellets made at low moisture content – Influence of water in the binding mechanism of densified biomass. Biomass and Bioenergy. Elsevier Ltd. 98:8–14.

Huang, Y., Yin, X., Wu, C., Wang, C., Xie, J., Zhou, Z., Ma, L., & Li, H. 2009. Effects of metal catalysts on CO_2 gasification reactivity of biomass char. Biotechnol. Adv. Elsevier Inc. 27(5):568–572.

Illovo Sugar. 2019a. Electricity Co-Generation [WWW Document]. URL https://sasa.org.za/sugar-milling-and-refining/.

Illovo Sugar. 2019b. Products Overview [WWW Document]. URL https://www.illovosugarafrica.com/Products.

Imran, M. & Khan, A.R.A. 2018. Characterization of Agricultural Waste Sugarcane Bagasse Ash at 1100 0 C with various hours. Mater. Today Proc. Elsevier Ltd. 5(2):3346–3352.

IPP Office. 2019. Introduction to the IPP procurement programme [WWW Document]. URL https://www.ipp-projects.co.za/Home/CopyrightNotice.

IPP Office. 2019. Independent Power Producers Procurement Programme (IPPPP) An Overview.

Jackson, J., Turner, A., Mark, T., & Montross, M. 2016. Densification of biomass using a pilot scale flat ring roller pellet mill. Fuel Process. Technol. Elsevier B.V. 148:43–49.

Jain, A., Balasubramanian, R., & Srinivasan, M.P. 2016. Hydrothermal conversion of biomass waste to activated carbon with high porosity: A review. Chem. Eng. J. Elsevier B.V. 283:789–805.

Jazrawi, C., Biller, P., Ross, A.B., Montoya, A., Maschmeyer, T., & Haynes, B.S. 2013. Pilot plant testing of continuous hydrothermal liquefaction of microalgae. Algal Res. Elsevier B.V. 2(3):268–277.

Jeffrey, L.S. 2005. Characterization of the coal resources of South Africa. J. South. African Inst. Min. Metall. Southern African Institute of Mining and Metallurgy. 105(2):95–102.

Jena, U. & Das, K.C. 2011. Comparative evaluation of thermochemical liquefaction and pyrolysis for bio-oil production from microalgae. Energy and Fuels. 25(11):5472–5482.

Jeong, H.J., Park, S.S., & Hwang, J. 2014. Co-gasification of coal-biomass blended char with CO_2 at temperatures of 900-1100°C. Fuel. Elsevier Ltd. 116:465–470.

Kalen, G., Thyrel, M., Xiong, S., Burvall, J., Håkan, O., Marcus, O., & Bostro, D. 2008. Slagging characteristics during combustion of corn stovers with and without kaolin and calcite. Energy & Fuels. 22:3465–3470.

Kaliyan, N. & Vance Morey, R. 2009. Factors affecting strength and durability of densified biomass products. Biomass and Bioenergy. Elsevier Ltd. 33(3):337–359.

Kaliyan, N. & Vance Morey, R. 2010. Natural binders and solid bridge type binding mechanisms in briquettes and pellets made from corn stover and switchgrass. Bioresour. Technol. Elsevier Ltd. 101(3):1082–1090.

Kambo, H.S. & Dutta, A. 2014. Strength, storage, and combustion characteristics of densified lignocellulosic biomass produced via torrefaction and hydrothermal carbonization. Appl. Energy. Elsevier Ltd. 135:182–191.

Kang, S., Li, X., Fan, J., & Chang, J. 2012. Characterization of hydrochars produced by hydrothermal carbonization of lignin, cellulose, d-xylose, and wood meal. Ind. Eng. Chem. Res. 51(26):9023–9031.

Karayıldırım, T., Sınağ, A., & Kruse, A. 2008. Char and Coke Formation as Unwanted Side Reaction of the Hydrothermal Biomass Gasification. Chem. Eng. Technol. 31(11):1561–1568.

Kastanaki, E. & Vamvuka, D. 2006. A comparative reactivity and kinetic study on the combustion of coal-biomass char blends. Fuel. 85(9):1186–1193.

Kent Hoekman, S.; Broch, A.; Robbins, C. 2011. Hydrothermal carbonization of lignocellulosic biomass. Energy and Fuels. 25:1802–1810.

Khan, M.Z., Chun, D.H., Yoo, J., Kim, S. Do, Rhim, Y.J., Choi, H.K., Lim, J., Lee, S., & Rifella, A. 2015. Evaluation of the effect of a palm acid oil coating on upgrading low rank coal. RSC Adv. Royal Society of Chemistry. 5(78):63955–63963.

Koike, N., Hosokai, S., Takagaki, A., Nishimura, S., Kikuchi, R., & Ebitani, K. 2016. Upgrading of pyrolysis bio-oil using nickel phosphide catalysts. J. Catal. Elsevier Inc. 333:115–126.

Krerkkaiwan, S., Fushimi, C., Tsutsumi, A., & Kuchonthara, P. 2013. Synergetic effect during co-pyrolysis/gasification of biomass and sub-bituminous coal. Fuel Process. Technol. Elsevier B.V. 115:11–18.

Kruse, A. 2009. Hydrothermal biomass gasification. J. Supercrit. Fluids. 47(3):391–399.

Kruse, A. & Dinjus, E. 2007. Hot compressed water as reaction medium and reactant. Properties and sythesis reactions. J. Supercrit. Fluids. 41(3):361–379.

Kruse, A., Funke, A., & Titirici, M.M. 2013. Hydrothermal conversion of biomass to fuels and energetic materials. Curr. Opin. Chem. Biol. Elsevier Ltd. 17(3):515–521.

Kumar, M., Sansaniwal, S.K., & Khatak, P. 2016. Progress in solar dryers for drying various commodities. Renew. Sustain. Energy Rev. Elsevier. 55:346–360.

Leeuw, K.A., Strydom, C.A., Bunt, J.R., & van Niekerk, D. 2016. The influence of K_2CO_3 and KCl on H_2 formation during heat treatment of an acid-treated inertinite-rich bituminous coal–char. J. Therm. Anal. Calorim. Springer Netherlands. 126(2):905–912.

Leng, L., Li, J., Wen, Z., & Zhou, W. 2018. Use of microalgae to recycle nutrients in aqueous phase derived from hydrothermal liquefaction process Mixed algae. Bioresour. Technol. Elsevier. 256:529–542.

Li, Y., Lin, H., Xiao, K., & Lasek, J. 2018. Combustion behavior of coal pellets blended with Miscanthus biochar. Energy. Elsevier Ltd. 163:180–190.

Liu, Z., Guo, Y., Balasubramanian, R., & Hoekman, S.K. 2016. Mechanical stability and combustion characteristics of hydrochar/lignite blend pellets. Fuel. Elsevier Ltd. 164:59–65.

Liu, Z., Mi, B., Jiang, Z., Fei, B., Cai, Z., & Liu, X. 2016. Improved bulk density of bamboo pellets as biomass for energy production. Renew. Energy. Elsevier Ltd. 86:1–7.

Liu, Z., Quek, A., & Balasubramanian, R. 2014. Preparation and characterization of fuel pellets from woody biomass, agro-residues and their corresponding hydrochars. Appl. Energy. Elsevier Ltd. 113:1315–1322.

Liu, Z., Quek, A., Kent Hoekman, S., & Balasubramanian, R. 2013. Production of solid biochar fuel from waste biomass by hydrothermal carbonization. Fuel. Elsevier Ltd. 103:943–949.

Liu, Z., Quek, A., Kent Hoekman, S., Srinivasan, M.P., & Balasubramanian, R. 2012. Thermogravimetric investigation of hydrochar-lignite co-combustion. Bioresour. Technol. Elsevier Ltd. 123:646–652.

Lu, J.J. & Chen, W.H. 2015. Investigation on the ignition and burnout temperatures of bamboo and sugarcane bagasse by thermogravimetric analysis. Appl. Energy. Elsevier Ltd. 160(2015):49–57.

Lucian, M., Volpe, M., Gao, L., Piro, G., Goldfarb, J.L., & Fiori, L. 2018. Impact of hydrothermal carbonization conditions on the formation of hydrochars and secondary chars from the organic fraction of municipal solid waste. Fuel. Elsevier. 233:257–268.

Ma, J., Shi, S., Jia, X., Xia, F., Ma, H., Gao, J., & Xu, J. 2019. Advances in catalytic conversion of lignocellulose to chemicals and liquid fuels. J. Energy Chem. Elsevier B.V. and Science Press. 36:74–86.

Mafu, L.D., Neomagus, H.W.J.P., Everson, R.C., Okolo, G.N., Strydom, C.A., & Bunt, J.R. 2018. The carbon dioxide gasification characteristics of biomass char samples and their effect on coal gasification reactivity during co-gasification. Bioresour. Technol. 258:70–78.

Mäkelä, M., Benavente, V., & Fullana, A. 2015. Hydrothermal carbonization of lignocellulosic biomass: Effect of process conditions on hydrochar properties. Appl. Energy. 155:576–584.

Makishima, S., Mizuno, M., Sato, N., Shinji, K., & Suzuki, M. 2009. Development of continuous flow type hydrothermal reactor for hemicellulose fraction recovery from corncob. Bioresour. Technol. Elsevier Ltd. 100(11):2842–2848.

Malmgren, A. & Riley, G. 2018. Biomass Power Generation. Earth Syst. Environ. Sci. Elsevier Inc.

Mariusz, W., Vos, M.P., Willem, D., & Brilman, F. 2018. Effect of process conditions on bio-oil obtained through continuous hydrothermal liquefaction of Scenedesmus sp. microalgae. J. Anal. Appl. Pyrolysis. 134:415–426.

Marriott, P.E., Gómez, L.D., & Mcqueen-Mason, S.J. 2016. Unlocking the potential of lignocellulosic biomass through plant science. New Phytol. 209(4):1366–1381.

Marshall, W.L. & Franck, E.U. 1983. Ion product of water substance, 0-1000°C, 1-10,000 bars new international formulation and its background. J. Phys. Chem. Ref. Data. 10(2):295–304.

Mashoko, L., Mbohwa, C., & Thomas, V.M. 2013. Life cycle inventory of electricity cogeneration from bagasse in the South African sugar industry. J. Clean. Prod. Elsevier Ltd. 39:42–49.

Miléo, P.C., Oliveira, M.F., Luz, S.M., Rocha, G.J.M., & Gonçalves, A.R. 2016. Thermal and chemical characterization of sugarcane bagasse cellulose/lignin-reinforced composites. Polym. Bull. 73(11):3163–3174.

Moretti, M.M. de S., Bocchini-Martins, D.A., Nunes, C. da C.C., Villena, M.A., Perrone, O.M., Silva, R. da, Boscolo, M., & Gomes, E. 2014. Pretreatment of sugarcane bagasse with microwaves irradiation and its effects on the structure and on enzymatic hydrolysis. Appl. Energy. Elsevier Ltd. 122:189–195.

Mostafa, M.E., Hu, S., Wang, Y., Su, S., Hu, X., & Elsayed, S.A. 2019. The significance of pelletization operating conditions: An analysis of physical and mechanical characteristics as well as energy consumption of biomass pellets. Renew. Sustain. Energy Rev. Elsevier Ltd. 105:332–348.

Mu, L., Zhao, L., Liu, L., & Yin, H. 2012. Elemental distribution and mineralogical composition of ash deposits in a large-scale wastewater incineration plant: a case study. Ind. Eng. Chem. Res. 51:8684–8694.

Mukherjee, A., Zimmerman, A.R., & Harris, W. 2011. Surface chemistry variations among a series of laboratory-produced biochars. Geoderma. Elsevier B.V. 163(3–4):247–255.

Munir, S., Daood, S.S., Nimmo, W., Cunliffe, A.M., & Gibbs, B.M. 2009. Thermal analysis and devolatilization kinetics of cotton stalk, sugar cane bagasse and shea meal under nitrogen and air atmospheres. Bioresour. Technol. Elsevier Ltd. 100(3):1413–1418.

Mureddu, M., Dessì, F., Orsini, A., Ferrara, F., & Pettinau, A. 2018. Air- and oxygen-blown characterization of coal and biomass by thermogravimetric analysis. Fuel. Elsevier. 212:626–637.

Nakason, K., Panyapinyopol, B., Kanokkantapong, V., Viriya-empikul, N., Kraithong, W., & Pavasant, P. 2018. Hydrothermal carbonization of unwanted biomass materials: Effect of process temperature and retention time on hydrochar and liquid fractionaaa. J. Energy Inst. Elsevier Ltd. 91(5):786–796.

Nielsen, N.P.K., Holm, J.K., & Felby, C. 2009. Effect of fiber orientation on compression and frictional properties of sawdust particles in fuel pellet production. Energy and Fuels. 23(6):3211–3216.

Niu, Y., Wang, Z., Zhu, Y., Zhang, X., Tan, H., & Hui, S. 2016. Experimental evaluation of additives and K_2O – SiO_2 – Al_2O_3 diagrams on high-temperature silicate melt-induced slagging during biomass combustion. FUEL. Elsevier Ltd. 179:52–59.

Ocfemia, K.S., Zhang, Y., & Funk, T. 2006. Hydrothermal processing of swine manure into oil using a continuous reactor system: Development and testing. Trans. ASABE. 49(2):533–541.

Okolo, G.N., Neomagus, H.W.J.P., Everson, R.C., Roberts, M.J., Bunt, J.R., Sakurovs, R., & Mathews, J.P. 2015. Chemical-structural properties of South African bituminous coals: Insights from wide angle XRD-carbon fraction analysis, ATR-FTIR, solid state 13C NMR, and HRTEM techniques. Fuel. Elsevier Ltd. 158:779–792.

Parshetti, G.K., Quek, A., Betha, R., & Balasubramanian, R. 2014. TGA – FTIR investigation of co-combustion characteristics of blends of hydrothermally carbonized oil palm biomass (EFB) and coal. Fuel Process. Technol. Elsevier B.V. 118:228–234.

Patel, B. & Hellgardt, K. 2015. Hydrothermal upgrading of algae paste in a continuous flow reactor. Bioresour. Technol. Elsevier Ltd. 191:460–468.

Pimchuai, A., Dutta, A., & Basu, P. 2010. Torrefaction of agriculture residue to enhance combustible properties. Energy and Fuels. 24(9):4638–4645.

Prajitno, H., Insyani, R., Park, J., Ryu, C., & Kim, J. 2016. Non-catalytic upgrading of fast pyrolysis bio-oil in supercritical ethanol and combustion behavior of the upgraded oil. Appl. Energy. Elsevier Ltd. 172:12–22.

Prapaiwatcharapan, K., Sunphorka, S., Kuchonthara, P., & Kangvansaichol, K. 2015. Single- and two-step hydrothermal liquefaction of microalgae in a semi-continuous reactor: Effect of the operating parameters. Bioresour. Technol. Elsevier Ltd. 191:426–432.

Qua, E.H., Hornsby, P.R., Sharma, H.S.S., & Lyons, G. 2011. Preparation and characterisation of cellulose nanofibres. J. Mater. Sci. 46(18):6029–6045.

Razuan, R., Finney, K.N., Chen, Q., Sharifi, V.N., & Swithenbank, J. 2011. Pelletised fuel production from palm kernel cake. Fuel Process. Technol. 92(3):609–615.

RCL Foods. 2018. Sustainable business report.

Reza, M.T., Lynam, J.G., Vasquez, V.R., & Coronella, C.J. 2012. Pelletization of biochar from hydrothermally carbonized wood. Environ. Prog. Sustain. Energy. 31(2):225–234.

Roberts, V.M., Stein, V., Reiner, T., Lemonidou, A., Li, X., & Lercher, J.A. 2011. Towards Quantitative Catalytic Lignin Depolymerization. Chem. - A Eur. J. 17(21):5939–5948.

Rocca, P.A.D., Cerrella, E.G., Bonelli, P.R., & Cukierman, A.L. 1999. Pyrolysis of hardwoods residues: on kinetics and chars characterization. Biomass and Bioenergy. 16(1):79–88.

Rocha, G.J. de M., Nascimento, V.M., Gonçalves, A.R., Silva, V.F.N., & Martín, C. 2015. Influence of mixed sugarcane bagasse samples evaluated by elemental and physical-chemical composition. Ind. Crops Prod. 64:52–58.

Roddy, D. & Manson-Whitton, C. 2012. Biomass Gasification and Pyrolysis. Earth Planet. Sci. 5:133–153.

Rodríguez-díaz, J.M., Omar, J., García, P., Ramón, L., Sánchez, B., Gurgel, M., Lins, V., & Arteaga-pérez, L.E. 2015. Comprehensive Characterization of Sugarcane Bagasse Ash for Its Use as an Adsorbent. Bioenergy Res. 8(4):1885–1895.

Román, S., Nabais, J.M. V, Laginhas, C., Ledesma, B., & González, J.F. 2012. Hydrothermal carbonization as an effective way of densifying the energy content of biomass. Fuel Process. Technol. Elsevier B.V. 103:78–83.

Sabio, E., Álvarez-Murillo, A., Román, S., & Ledesma, B. 2016. Conversion of tomato-peel waste into solid fuel by hydrothermal carbonization: Influence of the processing variables. Waste Manag. Elsevier Ltd. 47:122–132.

Sahu, S.G., Sarkar, P., Chakraborty, N., & Adak, A.K. 2010. Thermogravimetric assessment of combustion characteristics of blends of a coal with different biomass chars. Fuel Process. Technol. Elsevier B.V. 91(3):369–378.

Saidur, R., Abdelaziz, E.A., Demirbas, A., Hossain, M.S., & Mekhilef, S. 2011. A review on biomass as a fuel for boilers. Renew. Sustain. Energy Rev. Elsevier Ltd. 15(5):2262–2289.

Sansaniwal, S.K., Rosen, M.A., & Tyagi, S.K. 2017. Global challenges in the sustainable development of biomass gasification: An overview. Renew. Sustain. Energy Rev. Elsevier Ltd. 80:23–43.

SARS. 2017. SARS to collect for sugar tax (SBL) from 1 April 2018 [WWW Document]. URL https://www.sars.gov.za/Media/MediaReleases/Pages/15-December-2017---SARS-to-collect-for-sugar-tax-from-1-April-2018-.aspx.

SARS. 2018. Exercise external policy Health Promotion Levy on sugar [WWW Document]. URL https://www.sars.gov.za/AllDocs/OpsDocs/Policies/SE-SB-02 - Health Promotion Levy on Sugary Beverages - External Policy.pdf.

SASA. 2019a. South African sugar indusry to march over influx of imports [WWW Document]. URL https://sasa.org.za/south-african-sugar-industry-to-march-over-influx-of-imports/.

SASA. 2019b. Sugar Milling and Refining [WWW Document]. URL https://sasa.org.za/sugar-milling-and-refining/.

Sekar, R., Shin, H.D., & DiChristina, T.J. 2016. Direct conversion of cellulose and hemicellulose to fermentable sugars by a microbially-driven Fenton reaction. Bioresour. Technol. Elsevier Ltd. 218:1133–1139.

Sermyagina, E., Saari, J., Kaikko, J., & Vakkilainen, E. 2015. Hydrothermal carbonization of coniferous biomass: Effect of process parameters on mass and energy yields. J. Anal. Appl. Pyrolysis. Elsevier B.V. 113:551–556.

Sevilla, M. & Fuertes, A.B. 2009. The production of carbon materials by hydrothermal carbonization of cellulose. Carbon N. Y. Elsevier Ltd. 47(9):2281–2289.

Shemfe, M.B., Gu, S., & Ranganathan, P. 2015. Techno-economic performance analysis of biofuel production and miniature electric power generation from biomass fast pyrolysis and bio-oil upgrading. FUEL. Elsevier Ltd. 143:361–372.

Sheng, C., Xu, M., Zhang, J., & Xu, Y. 2000. Comparison of sulphur retention by coal ash in different types of combustors. Fuel Process. Technol. 64(1–3):1–11.

Sheng, K., Zhang, S., Liu, J., Shuang, E., Jin, C., & Xu, Z. 2019. Hydrothermal carbonization of cellulose and xylan into hydrochars and application on glucose isomerization. J. Clean. Prod. Elsevier Ltd. 237:117831.

SMRI. 2019. Moving from sugarcane mills to integrated sugarcane biorefineries [WWW Document]. URL http://www.smri.org/biorefineries.php.

Sun, Y., Gao, B., Yao, Y., Fang, J., Zhang, M., Zhou, Y., Chen, H., & Yang, L. 2014. Effects of feedstock type, production method, and pyrolysis temperature on biochar and hydrochar properties. Chem. Eng. J. Elsevier B.V. 240:574–578.

Tan, P., Zhang, C., Xia, J., Fang, Q.Y., & Chen, G. 2015. Estimation of higher heating value of coal based on proximate analysis using support vector regression. Fuel Process. Technol. Elsevier B.V. 138:298–304.

Tavasoli, A., Barati, M., & Karimi, A. 2015. Conversion of sugarcane bagasse to gaseous and liquid fuels in near-critical water media using K_2O promoted Cu/γ-Al_2O_3-MgO nanocatalysts. Biomass and Bioenergy. Elsevier Ltd. 80:63–72.

Teixeira, S.R., Souza, E. De, Tadeu, G., Santos, D.A., & Miguel, G. 2008. Sugarcane bagasse ash as a potential quartz replacement in red ceramic. J. Am. Ceram. Soc. 91(6):1883–1887.

Theerarattananoon, K., Xu, F., Wilson, J., Ballard, R., Mckinney, L., Staggenborg, S., Vadlani, P., Pei, Z.J., & Wang, D. 2011. Physical properties of pellets made from sorghum stalk, corn stover, wheat straw, and big bluestem. Ind. Crops Prod. 33(2):325–332.

Titirici, M., Antonietti, M., & Baccile, N. 2008. Hydrothermal carbon from biomass: a comparison of the local structure from poly- to monosaccharides and pentoses/hexoses. Green Chemisry. 10(11):1204–1212.

Tongaat Hulett Sugar. 2019. Renewable Energy [WWW Document]. URL http://www.huletts.co.za/prod/renewable_energy.asp.

UCL. 2019. Sugar Production [WWW Document]. URL https://www.ucl.co.za/business-units/manufacturing-sugar.html.

Ul, N., Baroutian, S., & Sarmah, A.K. 2018. Physicochemical , structural and combustion characterization of food waste hydrochar obtained by hydrothermal carbonization. Bioresour. Technol. Elsevier. 266(June):357–363.

UN. 2015. Paris Agreement.

UN. 2019. The Paris Agreement and NDCs [WWW Document]. URL https://unfccc.int/process-and-meetings/the-paris-agreement/nationally-determined-contributions-ndcs.

Vamvuka, D., Tsamourgeli, V., Galetakis, M., & Galetakis, M. 2014. Study on Catalytic Combustion of Biomass Mixtures with Poor Coals. Combust. Sci. Technol. 186(1):68–82.

Van Krevelen, D.W. 1950. Graphical-statistical method for the study of structure and reaction processes of coal. Fuel. 29:269–284.

Varma, A.K. & Mondal, P. 2016. Pyrolysis of sugarcane bagasse in semi batch reactor: Effects of process parameters on product yields and characterization of products. Ind. Crops Prod. Elsevier B.V. 95:704–717.

Vassilev, S. V, Vassileva, C.G., & Vassilev, V.S. 2015. Advantages and disadvantages of composition and properties of biomass in comparison with coal : An overview. FUEL. Elsevier Ltd. 158:330–350.

Visser, H., Thopil, G.A., & Brent, A. 2019. Life cycle cost profitability of biomass power plants in South Africa within the international context. Renew. Energy. Elsevier Ltd. 139(September 2018):9–21.

Volpe, M. & Fiori, L. 2017. From olive waste to solid biofuel through hydrothermal carbonisation: The role of temperature and solid load on secondary char formation and hydrochar energy properties. J. Anal. Appl. Pyrolysis. Elsevier B.V. 124:63–72.

Volpe, M., Wüst, D., Merzari, F., Lucian, M., Andreottola, G., Kruse, A., & Fiori, L. 2018. One stage olive mill waste streams valorisation via hydrothermal carbonisation. Waste Manag. Elsevier Ltd. 80:224–234.

Waanders, F.B., Marx, S., & Bunt, J.R. 2018. Production of a carbonaceous feedstock material from a waste carbon source.

Wang, G., Zhang, J., Hou, X., Shao, J., & Geng, W. 2015. Study on CO_2 gasification properties and kinetics of biomass chars and anthracite char. Bioresour. Technol. Elsevier Ltd. 177:66–73.

Wang, G., Zhang, J., Shao, J., Liu, Z., Zhang, G., Xu, T., Guo, J., Wang, H., Xu, R., & Lin, H. 2016. Thermal behavior and kinetic analysis of co-combustion of waste biomass/low rank coal blends. Energy Convers. Manag. Elsevier Ltd. 124:414–426.

Wang, L., Barta-rajnai, E., Skreiberg, Ø., Khalil, R., Czégény, Z., Jakab, E., Barta, Z., & Grønli, M. 2018. Effect of torrefaction on physiochemical characteristics and grindability of stem wood , stump and bark. Appl. Energy. Elsevier Ltd. 227:137–148.

Wang, Q., Han, K., Qi, J., Zhang, J., Li, H., & Lu, C. 2018. Investigation of potassium transformation characteristics and the in fl uence of additives during biochar briquette combustion. Fuel. Elsevier. 222:407–415.

Wang, Q., Wang, G., Zhang, J., Lee, J.Y., Wang, H., & Wang, C. 2018. Combustion behaviors and kinetics analysis of coal, biomass and plastic. Thermochim. Acta. Elsevier. 669:140–148.

Wang, Q., Zhao, W., Liu, H., Jia, C., & Xu, H. 2012. Reactivity and kinetic analysis of biomass during combustion. Energy Procedia. 17:869–875.

Wei, J., Gong, Y., Guo, Q., Chen, X., Ding, L., & Yu, G. 2019. A mechanism investigation of synergy behaviour variations during blended char co-gasification of biomass and different rank coals. Renew. Energy. Elsevier Ltd. 131:597–605.

Wei, J., Guo, Q., Ding, L., Yoshikawa, K., & Yu, G. 2017. Synergy mechanism analysis of petroleum coke and municipal solid waste (MSW)-derived hydrochar co-gasification. Appl. Energy. Elsevier. 206:1354–1363.

Wei, J., Guo, Q., Gong, Y., Ding, L., & Yu, G. 2017. Synergistic effect on co-gasification reactivity of biomass-petroleum coke blended char. Bioresour. Technol. Elsevier Ltd. 234:33–39.

Wei, J., Guo, Q., He, Q., Ding, L., Yoshikawa, K., & Yu, G. 2017a. Co-gasification of bituminous coal and hydrochar derived from municipal solid waste: Reactivity and synergy. Bioresour. Technol.

Wei, J., Guo, Q., He, Q., Ding, L., Yoshikawa, K., & Yu, G. 2017b. Co-gasification of bituminous coal and hydrochar derived from municipal solid waste: Reactivity and synergy. Bioresour. Technol. Elsevier Ltd. 239:482–489.

Xiao, L.P., Shi, Z.J., Xu, F., & Sun, R.C. 2012. Hydrothermal carbonization of lignocellulosic biomass. Bioresour. Technol. Elsevier Ltd. 118:619–623.

Xu, C., Liao, B., Pang, S., Nazari, L., Mahmood, N., Tushar, M., Dutta, A., & Ray, M. 2018. 1.19 Biomass Energy. , in: Comprehensive Energy Systems. . pp. 770–794.

Xu, R., Zhang, J., Wang, G., Zuo, H., Zhang, P., & Shao, J. 2016. Gasification behaviors and kinetic study on biomass chars in CO 2 condition. Chem. Eng. Res. Des. Institution of Chemical Engineers. 107:34–42.

Xue, J., Chellappa, T., Ceylan, S., & Goldfarb, J.L. 2018. Enhancing biomass + coal co-firing scenarios via biomass torrefaction and carbonization: Case study of avocado pit biomass and Illinois No . 6 coal. Renew. Energy. Elsevier Ltd. 122:152–162.

Yang, W., Wang, H., Zhang, M., Zhu, J., Zhou, J., & Wu, S. 2016. Fuel properties and combustion kinetics of hydrochar prepared by hydrothermal carbonization of bamboo. Bioresour. Technol. Elsevier Ltd. 205:199–204.

Yuan, S., Dai, Z., Zhou, Z., Chen, X., Yu, G., & Wang, F. 2012. Rapid co-pyrolysis of rice straw and a bituminous coal in a high-frequency furnace and gasification of the residual char. Bioresour. Technol. Elsevier Ltd. 109:188–197.

Zawiślak, K., Sobczak, P., Kraszkiewicz, A., Niedziółka, I., Parafiniuk, S., Kuna-Broniowska, I., Tanaś, W., Żukiewicz-Sobczak, W., & Obidziński, S.I. 2019. The use of lignocellulosic waste in the production of pellets for energy purposes. Renew. Energy. Elsevier Ltd.

Zhang, B., Heidari, M., Regmi, B., Salaudeen, S., & Arku, P. 2018. Hydrothermal Carbonization of Fruit Wastes: A Promising Technique for Generating Hydrochar. Energies. 11:1–14.

Zhang, L., Xu, S., Zhao, W., & Liu, S. 2007. Co-pyrolysis of biomass and coal in a free fall reactor. Fuel. 86(3):353–359.

Zhang, M. & Yang, H. 2012. Hydrophobic precipitation of carbonaceous spheres from fructose by a hydrothermal process. Carbon N. Y. Elsevier Ltd. 50(6):2155–2161.

Zhang, Y., Zheng, Y., Yang, M., & Song, Y. 2016. Effect of fuel origin on synergy during co-gasification of biomass and coal in CO_2. Bioresour. Technol. Elsevier Ltd. 200:789–794.

Zhao, C., Jiang, E., & Chen, A. 2017. Volatile production from pyrolysis of cellulose, hemicellulose and lignin. J. Energy Inst. Elsevier Ltd. 90(6):902–913.

Zhou, C., Liu, G., Cheng, S., Fang, T., & Lam, P.K.S. 2014. Thermochemical and trace element behavior of coal gangue, agricultural biomass and their blends during co-combustion. Bioresour. Technol. Elsevier Ltd. 166:243–251.

Zhu, G., Yang, L., Gao, Y., Xu, J., Chen, H., Zhu, Y., Wang, Y., Liao, C., Lu, C., & Zhu, C. 2019. Characterization and pelletization of cotton stalk hydrochar from HTC and combustion kinetics of hydrochar pellets by TGA. Fuel. Elsevier. 244:479–491.

ANNEXURES

Appendix A – Raw data

Appendix A presents the raw data of the various analysis not completed by an external laboratory. Section A.1. presents the data for the proximate analysis, the higher heating value,

A.1. Proximate analysis and analysis of the heating value

Table A-1 shows the results for the proximate analysis and the higher heating value obtained for the sugarcane bagasse, hydrochar, GreenCoals and coal samples. The mean, standard deviation, standard error, confidence level and experimental error were calculated and were reported.

Table A-1: Proximate composition for sugarcane bagasse,- hydrochar-, GreenCoal-(GC3:1, GC1:1 and GC1:3) and coal samples

Sample	Inherent moisture (%)	VM (%)	FC (%)	ASH (%)	HHV (MJ/kg)
Sugarcane bagasse					
Sample 1	6.3	69.5	13.3	10.9	15.9
Sample 2	6.3	69.7	13.1	10.9	15.8
Sample 3	6.3	69.9	12.8	11.0	15.7
Sample 4	-	-	-	-	15.7
Sample 5	-	-	-	-	15.8
Average	6.3	69.7	13.1	10.9	15.8
Standard deviation	0.0	0.2	0.2	0.0	0.1
Standard error	0.0	0.2	0.2	0.0	0.0
t-critical value	4.303	4.303	4.303	4.303	2.776
Confidence level	0.1	0.7	0.8	0.1	0.1
Experimental error (%)	1.3	0.9	5.8	1.0	0.7
Hydrochar					
Sample 1	5.5	44.5	44.0	6.0	27.3
Sample 2	5.1	44.8	44.1	5.9	27.2
Sample 3	4.8	45.2	44.0	5.9	27.3
Sample 4	-	-	-	-	27.3
Sample 5	-	-	-	-	27.3

Table A-1: Proximate composition for sugarcane bagasse,- hydrochar-, GreenCoal-(GC3:1, GC1:1 and GC1:3) and coal samples

Sample	Inherent moisture (%)	VM (%)	FC (%)	ASH (%)	HHV (MJ/kg)
Average	5.1	44.9	44.1	6.0	27.3
Standard deviation	0.4	0.4	0.1	0.0	0.0
Standard error	0.3	0.3	0.1	0.0	0.0
t-critical value	4.303	4.303	4.303	4.303	2.776
Confidence level	1.1	1.2	0.3	0.1	0.0
Experimental error (%)	21.9	2.6	0.6	2.4	0.2
GreenCoal 3:1					
Sample 1	4.2	42.0	46.7	7.2	27.2
Sample 2	4.1	41.6	46.7	7.5	27.2
Sample 3	4.0	42.1	46.9	7.1	27.3
Sample 4	-	-	-	-	27.2
Sample 5	-	-	-	-	27.3
Average	4.1	41.9	46.7	7.3	27.2
Standard deviation	0.1	0.2	0.1	0.3	0.1
Standard error	0.1	0.2	0.1	0.2	0.0
t-critical value	4.303	4.303	4.303	4.303	2.776
Confidence level	0.3	0.7	0.4	0.8	0.1
Experimental error (%)	7.3	1.7	0.8	10.8	0.3
GreenCoal 1:1					
Sample 1	2.6	34.8	53.7	8.8	27.1
Sample 2	2.5	34.7	53.6	9.1	27.1
Sample 3	2.7	34.5	53.6	9.3	27.1
Sample 4	-	-	-	-	27.1
Sample 5	-	-	-	-	27.1
Average	2.6	34.7	53.6	9.1	27.1
Standard deviation	0.1	0.2	0.1	0.2	0.0
Standard error	0.0	0.1	0.0	0.2	0.0
t-critical value	4.303	4.303	4.303	4.303	2.776
Confidence level	0.2	0.5	0.2	0.7	0.0
Experimental error (%)	8.2	1.5	0.3	7.2	0.0
GreenCoal 1:3					
Sample 1	1.4	30.1	57.1	11.4	27.0
Sample 2	1.4	30.4	56.9	11.4	27.0
Sample 3	1.4	30.5	57.1	11.0	27.0
Sample 4	-	-	-	-	27.0

Table A-1: Proximate composition for sugarcane bagasse,- hydrochar-, GreenCoal-(GC3:1, GC1:1 and GC1:3) and coal samples

Sample	Inherent moisture (%)	VM (%)	FC (%)	ASH (%)	HHV (MJ/kg)
Sample 5	-	-	-	-	27.0
Average	1.4	30.3	57.0	11.3	27.0
Standard deviation	0.0	0.2	0.1	0.2	0.0
Standard error	0.0	0.1	0.1	0.1	0.0
t-critical value	4.303	4.303	4.303	4.303	2.776
Confidence level	0.1	0.6	0.4	0.6	0.0
Experimental error (%)	7.9	2.1	0.6	5.7	0.1
		Coal			
Sample 1	0.5	24.9	60.6	14.0	27.1
Sample 2	0.3	25.2	60.5	14.0	26.9
Sample 3	0.3	25.2	60.7	13.9	26.8
Sample 4	-	-	-	-	26.7
Sample 5	-	-	-	-	26.6
Average	0.3	25.1	60.6	14.0	26.8
Standard deviation	0.1	0.1	0.1	0.1	0.2
Standard error	0.1	0.1	0.1	0.1	0.1
t-critical value	4.303	4.303	4.303	4.303	2.776
Confidence level	0.3	0.4	0.2	0.2	0.2
Experimental error (%)	92.1	1.4	0.4	1.7	0.8

A.2. Fibre analysis

Table A-2 shows the neutral detergent fibre (NDF), acid detergent fibre (ADF) and acid detergent liquids (ADL) for the sugarcane bagasse and hydrochar samples.

Table A-2: Fibre analysis

Sample	Sugarcane bagasse	Hydrochar
NDF	72.8	35.2
ADF	37.6	26.2
ADL	7.7	23.8

A.3. EDS analysis of hydrochar

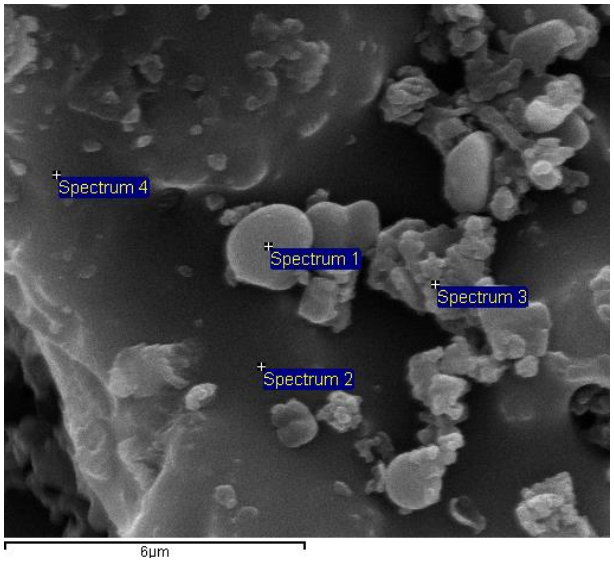

Figure A-1: EDS measurement of hydrochar surface

Table A-3: Surface composition of hydrochar according to EDS analysis

Spectrum	C	O	Al	Si	Total	O/C
1	74.08	24.91	0.4	0.6	100	0.25
2	78.07	19.86	0.8	1.3	100	0.19
3	71.04	25.23	1.2	2.5	100	0.27
4	82.35	14.56	1.0	2.1	100	0.13

A.4. Pellet properties

Table A-4 shows the results for the mass, diameter and height of the sugarcane bagasse, hydrochar, GreenCoals and coal pellets, used to calculate the respective mass density.

Table A-4: Diameter, height, volume and mass density of sugarcane bagasse-, hydrochar-, GreenCoal- (GC3:1, GC1:1 and GC1:3), and coal pellets

Sample	Mass (g)	Height (mm)	Diameter (mm)	Volume ($1x10^6$, m^3)	Density (kg/m^3)
Sugarcane bagasse					
Sample 1	1.65	9.20	13.06	1.23	1338.8
Sample 2	1.66	9.22	13.04	1.23	1348.3

Table A-4: Diameter, height, volume and mass density of sugarcane bagasse-, hydrochar-, GreenCoal- (GC3:1, GC1:1 and GC1:3), and coal pellets

Sample	Mass (g)	Height (mm)	Diameter (mm)	Volume ($1x10^6$, m^3)	Density (kg/m^3)
Sample 3	1.70	9.48	13.06	1.27	1339.7
Sample 4	1.67	9.22	13.04	1.23	1353.4
Sample 5	1.71	9.48	13.06	1.27	1343.1
Average					1344.7
Standard deviation					6.2
Standard error					2.8
t-critical value					2.776
Confidence level					7.6
Experimental error (%)					0.6
Hydrochar					
Sample 1	1.50	9.04	13.14	1.23	1224.5
Sample 2	1.53	9.22	13.20	1.26	1215.4
Sample 3	1.57	9.46	13.14	1.28	1221.3
Sample 4	1.61	9.68	13.16	1.32	1219.7
Sample 5	1.61	9.74	13.14	1.32	1221.8
Average					1220.5
Standard deviation					3.4
Standard error					1.5
t-critical value					2.776
Confidence level					4.2
Experimental error (%)					0.3
GreenCoal 3:1					
Sample 1	1.49	9.12	13.18	1.24	1199.5
Sample 2	1.50	9.12	13.22	1.25	1195.7
Sample 3	1.58	9.66	13.16	1.31	1205.0
Sample 4	1.68	10.20	13.18	1.39	1206.7
Sample 5	1.49	9.18	13.16	1.25	1197.0
Average					1200.8
Standard deviation					4.8
Standard error					2.2
t-critical value					2.776
Confidence level					56.0
Experimental error (%)					0.5
GreenCoal 1:1					
Sample 1	1.53	9.45	13.22	1.30	1178.3

Table A-4: Diameter, height, volume and mass density of sugarcane bagasse-, hydrochar-, GreenCoal- (GC3:1, GC1:1 and GC1:3), and coal pellets

Sample	Mass (g)	Height (mm)	Diameter (mm)	Volume ($1x10^6$, m^3)	Density (kg/m^3)
Sample 2	1.57	9.72	13.24	1.34	1176.2
Sample 3	1.40	8.68	13.22	1.19	1172.7
Sample 4	1.41	8.70	13.22	1.19	1176.7
Sample 5	1.84	11.38	13.22	1.56	1176.4
Average					1176.1
Standard deviation					2.1
Standard error					0.9
t-critical value					2.776
Confidence level					2.6
Experimental error (%)					0.2
GreenCoal 1:3					
Sample 1	1.87	11.78	13.30	1.64	1142.9
Sample 2	1.48	9.30	13.30	1.29	1148.4
Sample 3	1.95	12.22	13.30	1.70	1148.8
Sample 4	1.92	11.92	13.30	1.66	1158.2
Sample 5	1.88	11.70	13.30	1.63	1154.6
Average					1170.0
Standard deviation					4.4
Standard error					2.0
t-critical value					2.776
Confidence level					5.5
Experimental error (%)					0.5
Coal					
Sample 1	1.54	9.46	13.28	1.31	1174.1
Sample 2	1.52	9.42	13.26	1.30	1167.4
Sample 3	1.94	12.06	13.28	1.67	1163.8
Sample 4	2.05	12.62	13.28	1.75	1170.8
Sample 5	1.47	9.08	13.26	1.25	1173.7
Average					1150.6
Standard deviation					5.9
Standard error					2.7
t-critical value					2.776
Confidence level					7.4
Experimental error (%)					0.6

Table A-5 shows the compression strength, durability and impact resistance index of the sugarcane bagasse, hydrochar, GreenCoals and coal pellets.

Table A-5: Compression strength, durability and impact resistance index of sugarcane bagasse-, hydrochar-, GreenCoal- (GC3:1, GC1:1 and GC1:3), and coal pellets

	Compression Strength (N)	Durability ($m_{retained}$, %)			Impact resistance index (IRI)		
Sample	Force (N)	$m_{initial}$ (g)	m_{final} (g)	retained (%)	Drop	Pieces	IRI
Sugarcane bagasse							
Sample 1	578.0	1.78	1.78	100.0	4	1	
Sample 2	614.0	1.71	1.71	100.0	4	1	
Sample 3	580.0	1.70	1.70	100.0	4	1	
Sample 4	771.0	1.72	1.72	100.0	4	1	
Sample 5	689.0	1.78	1.78	99.9	4	1	
Average	646.4			100.0	4	1	400
Standard deviation				0.0			
Standard error				0.0			
t-critical value				2.776			
Confidence level				0.0			
Experimental error (%)				0.0			
Hydrochar							
Sample 1	187.0	1.62	1.61	99.1	4	1	
Sample 2	243.0	1.60	1.59	99.4	4	1	
Sample 3	179.0	1.58	1.58	99.7	4	1	
Sample 4	154.0	1.44	1.44	99.9	4	1	
Sample 5	110.0	1.44	1.43	99.0	4	1	
Average	174.6			99.4	4	1	400
Standard deviation				0.4			
Standard error				0.2			
t-critical value				2.776			
Confidence level				0.5			
Experimental error (%)				0.5			
GreenCoal 3:1							
Sample 1	149.0	1.53	1.51	98.6	4	1	
Sample 2	150.0	1.53	1.52	99.4	4	1	
Sample 3	154.0	1.43	1.43	99.8	4	1	

Table A-5: Compression strength, durability and impact resistance index of sugarcane bagasse-, hydrochar-, GreenCoal- (GC3:1, GC1:1 and GC1:3), and coal pellets

	Compression Strength (N)	Durability ($m_{retained}$, %)			Impact resistance index (IRI)		
Sample	Force (N)	$m_{initial}$ (g)	m_{final} (g)	retained (%)	Drop	Pieces	IRI
Sample 4	141.0	1.37	1.37	99.8	4	1	
Sample 5	131.0	1.30	1.29	98.6	4	1	
Average	145.0			99.2	4	1	400
Standard deviation				0.6			
Standard error				0.3			
t-critical value				2.776			
Confidence level				0.8			
Experimental error (%)				0.8			
GreenCoal 1:1							
Sample 1	49.0	1.48	0.79	53.2	3	2	
Sample 2	55.0	1.63	1.04	63.6	4	2	
Sample 3	73.0	1.56	0.90	57.6	4	2	
Sample 4	72.0	1.58	1.12	71.0	4	1	
Sample 5	46.0	1.47	1.09	73.8	4	2	
Average	59.0			63.8	3.8	1.8	211.1
Standard deviation				8.7			
Standard error				3.9			
t-critical value				2.776			
Confidence level				10.8			
Experimental error (%)				16.9			
GreenCoal 1:3							
Sample 1	52.0	1.61	0.61	38.1	2	3	
Sample 2	34.0	1.53	0.56	36.3	2	3	
Sample 3	41.0	1.55	0.75	48.3	2	2	
Sample 4	34.0	1.50	0.90	59.9	3	2	
Sample 5	51.0	1.50	0.72	47.8	3	2	
Average	42.4			46.1	2.4	2.4	100
Standard deviation				9.5			
Standard error				4.2			
t-critical value				2.776			
Confidence level				11.8			

Table A-5: Compression strength, durability and impact resistance index of sugarcane bagasse-, hydrochar-, GreenCoal- (GC3:1, GC1:1 and GC1:3), and coal pellets

	Compression Strength (N)	Durability ($m_{retained}$, %)			Impact resistance index (IRI)		
Sample	Force (N)	$m_{initial}$ (g)	m_{final} (g)	retained (%)	Drop	Pieces	IRI
Experimental error (%)				25.5			
			Coal				
Sample 1	40.0	1.53	0.82	53.4	3	3	
Sample 2	28.0	1.50	0.68	45.4	2	3	
Sample 3	36.0	1.60	1.07	66.7	2	2	
Sample 4	24.0	1.64	0.86	52.2	2	2	
Sample 5	25.0	1.70	0.86	51.0	2	2	
Average	30.6			53.7	2.2	2.4	91.7
Standard deviation				7.9			
Standard error				3.5			
t-critical value				2.776			
Confidence level				9.8			
Experimental error (%)				18.2			

Table A-6 shows the EMC and the water-resistance of the sugarcane bagasse, hydrochar, GreenCoals and coal pellets.

Table A-6: Hydrophobicity: equilibrium moisture content (EMC) and water resistance capacity (WRC) of sugarcane bagasse-, hydrochar-, GreenCoal- (GC3:1, GC1:1 and GC1:3), and coal pellets

	EMC (%)			WRC (%)		
Sample	$m_{initial}$ (g)	m_{final} (g)	EMC (%)	$m_{initial}$ (g)	m_{final} (g)	WRC (%)
Sample 1	1.78	1.60	10.2	1.63	-	Disintegrated
Sample 2	1.70	1.53	10.0	1.61	-	Disintegrated
Sample 3	1.64	1.48	10.1	1.58	-	Disintegrated
Sample 4	1.68	1.51	10.0	1.66	-	Disintegrated
Sample 5	1.54	1.38	10.1	1.70	-	Disintegrated
Average			10.1			-
Standard deviation			0.1			-
Standard error			0.0			-

Table A-6: Hydrophobicity: equilibrium moisture content (EMC) and water resistance capacity (WRC) of sugarcane bagasse-, hydrochar-, GreenCoal- (GC3:1, GC1:1 and GC1:3), and coal pellets

Sample	EMC (%)			WRC (%)		
	$m_{initial}$ (g)	m_{final} (g)	EMC (%)	$m_{initial}$ (g)	m_{final} (g)	WRC (%)
t-critical value			2.776			-
Confidence level			0.1			-
Experimental error (%)			1.0			-
Sample 1	1.62	1.50	7.0	1.45	1.47	1.2
Sample 2	1.56	1.45	7.1	1.42	1.43	0.8
Sample 3	1.44	1.34	7.2	1.40	1.41	0.8
Sample 4	1.55	1.43	7.2	1.49	1.50	1.0
Sample 5	1.45	1.35	7.2	1.52	1.54	1.0
Average			7.2			1.0
Standard deviation			0.1			0.2
Standard error			0.0			0.1
t-critical value			2.776			2.776
Confidence level			0.1			0.2
Experimental error (%)			1.5			20.0
Sample 1	1.49	1.39	6.6	1.47	1.51	2.7
Sample 2	1.61	1.51	6.3	1.49	1.53	2.6
Sample 3	1.63	1.53	6.0	1.45	1.49	2.4
Sample 4	1.59	1.50	6.1	1.41	1.45	2.6
Sample 5	1.36	1.28	6.0	1.44	1.47	2.3
Average			6.2			2.5
Standard deviation			0.2			0.1
Standard error			0.1			0.1
t-critical value			2.776			2.776
Confidence level			0.3			0.2
Experimental error (%)			4.6			7.1
Sample 1	1.64	1.56	4.9	1.44	1.48	3.1
Sample 2	1.62	1.54	4.7	1.44	1.48	3.2
Sample 3	1.63	1.55	4.7	1.38	1.42	3.1
Sample 4	1.60	1.53	4.7	1.45	1.49	2.9
Sample 5	1.50	1.43	4.7	1.45	1.49	2.5
Average			4.8			2.9
Standard deviation			0.1			0.3
Standard error			0.0			0.1
t-critical value			2.776			2.776

Table A-6: Hydrophobicity: equilibrium moisture content (EMC) and water resistance capacity (WRC) of sugarcane bagasse-, hydrochar-, GreenCoal- (GC3:1, GC1:1 and GC1:3), and coal pellets

Sample	EMC (%)			WRC (%)		
	$m_{initial}$ (g)	m_{final} (g)	EMC (%)	$m_{initial}$ (g)	m_{final} (g)	WRC (%)
Confidence level			0.1			0.3
Experimental error (%)			1.8			11.5
Sample 1	1.64	1.60	2.8	1.73	1.79	3.6
Sample 2	1.55	1.50	2.9	1.55	1.61	3.5
Sample 3	1.60	1.56	2.8	1.42	1.47	3.1
Sample 4	1.67	1.62	2.9	1.54	1.58	3.0
Sample 5	1.72	1.67	2.8	1.59	1.63	2.5
Average			2.8			3.1
Standard deviation			0.1			0.5
Standard error			0.0			0.2
t-critical value			2.776			2.776
Confidence level			0.1			0.6
Experimental error (%)			2.3			18.2
Sample 1	1.54	1.50	2.2	1.5	-	Disintegrated
Sample 2	1.55	1.53	1.8	1.5	-	Disintegrated
Sample 3	1.54	1.50	2.1	1.3	-	Disintegrated
Sample 4	1.46	1.43	2.1	1.5	-	Disintegrated
Sample 5	1.43	1.40	2.2	1.6	-	Disintegrated
Average			2.1			-
Standard deviation			0.2			-
Standard error			0.1			-
t-critical value			2.776			-
Confidence level			0.2			-
Experimental error (%)			10.4			-

A.5. Pyrolysis

This section contains all the TG-DTG curves used to interpret the behaviour during pyrolysis.

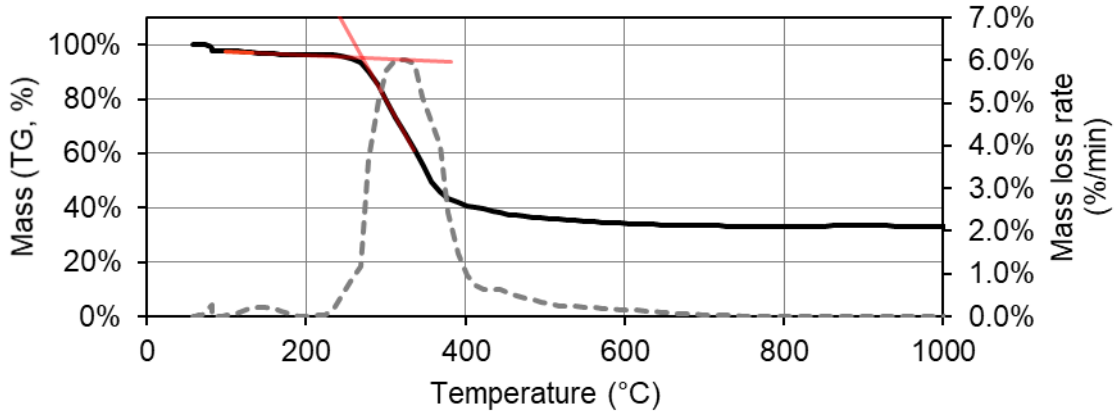

Figure A-2: The mass loss and mass loss rate of sugarcane bagasse during pyrolysis at a heating rate of 10 °C/min

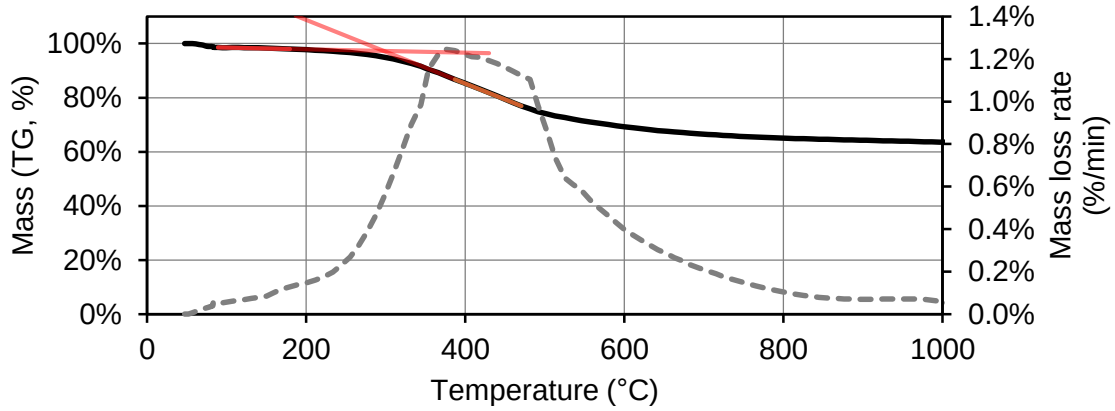

Figure A-3: The mass loss and mass loss rate of hydrochar during pyrolysis at a heating rate of 10 °C/min

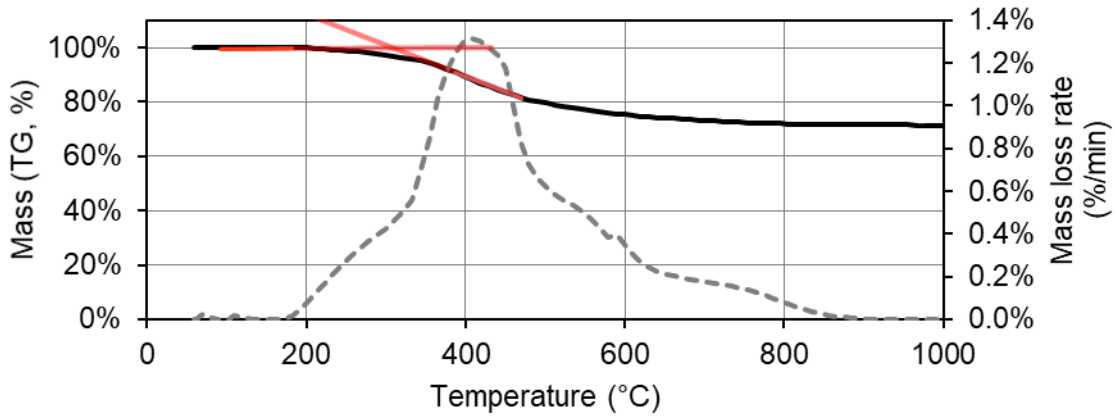

Figure A-4: The mass loss and mass loss rate of GreenCoal 3:1 during pyrolysis at a heating rate of 10 °C/min

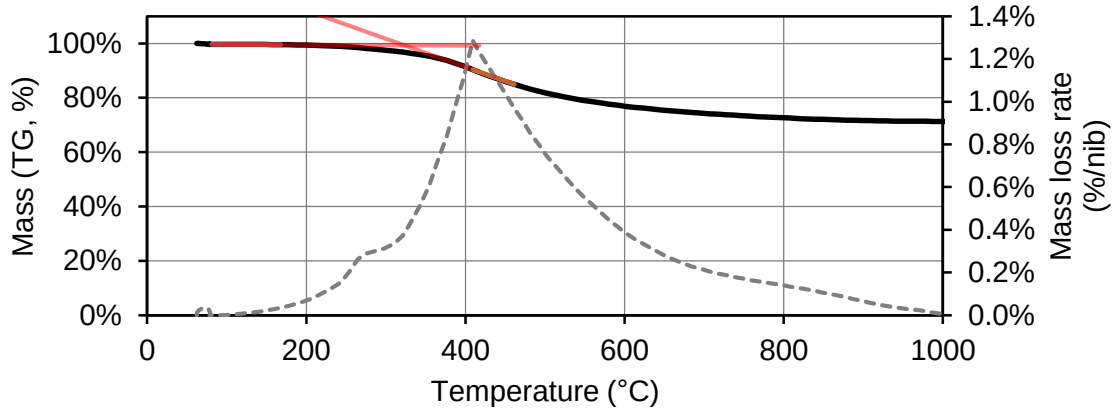

Figure A-5: The mass loss and mass loss rate of GreenCoal 1:1 during pyrolysis at a heating rate of 10 °C/min

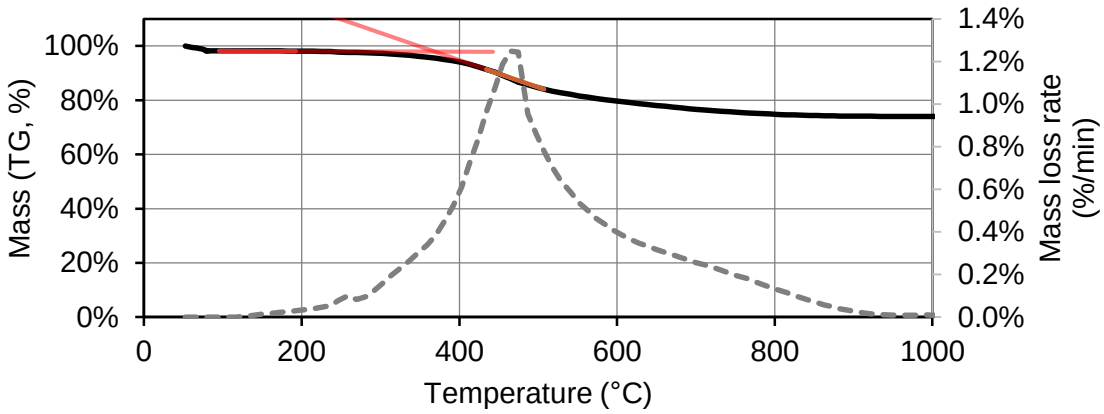

Figure A-6: The mass loss and mass loss rate of GreenCoal 1:3 during pyrolysis at a heating rate of 10 °C/min

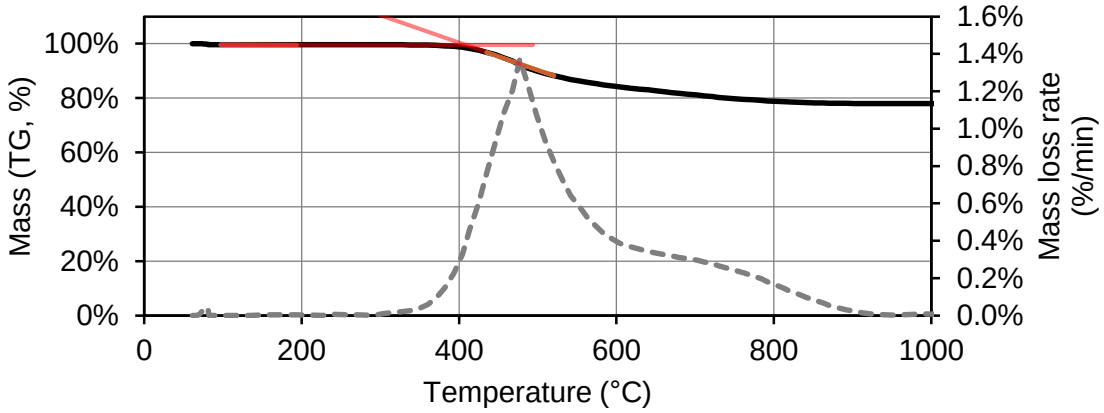

Figure A-7: The mass loss and mass loss rate of coal during pyrolysis at a heating rate of 10 °C/min

A.6. Combustion

This section contains all the TG-DTG curves used to interpret combustion behaviour.

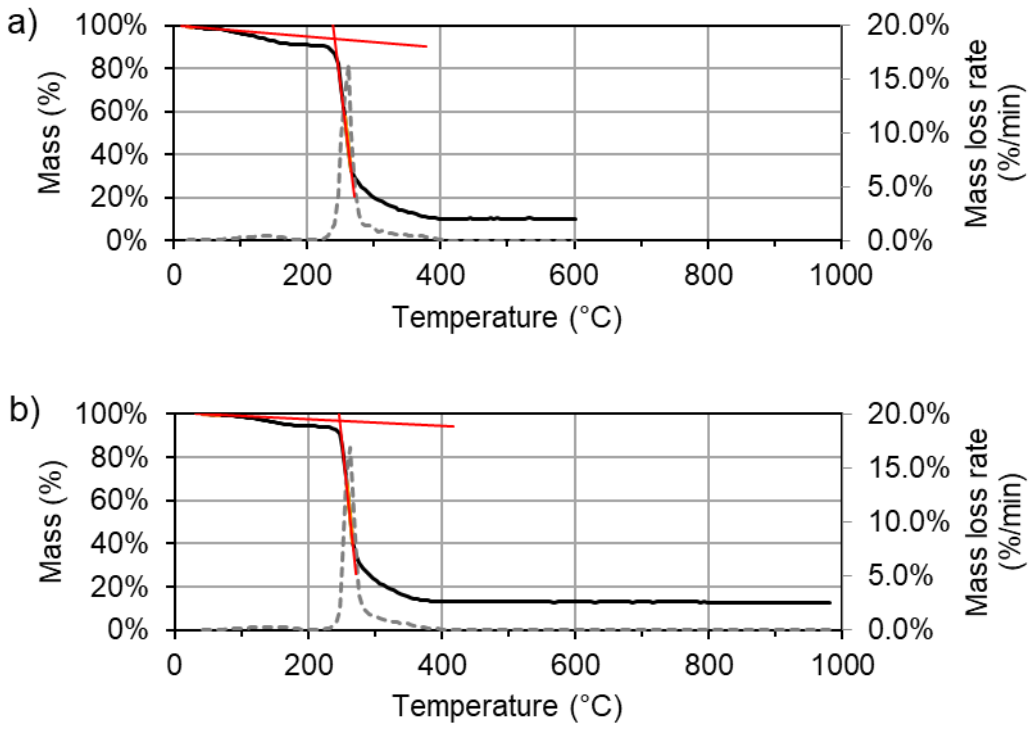

Figure A-8: The mass loss and mass loss rate of sugarcane bagasse at 5 °C/min: (a) run 1 and (b) run 2

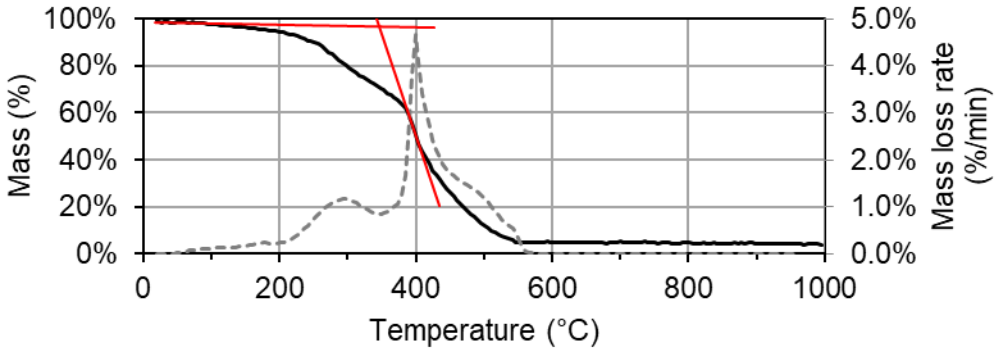

Figure A-9: The mass loss and rate of mass loss of hydrochar at 5 °C/min

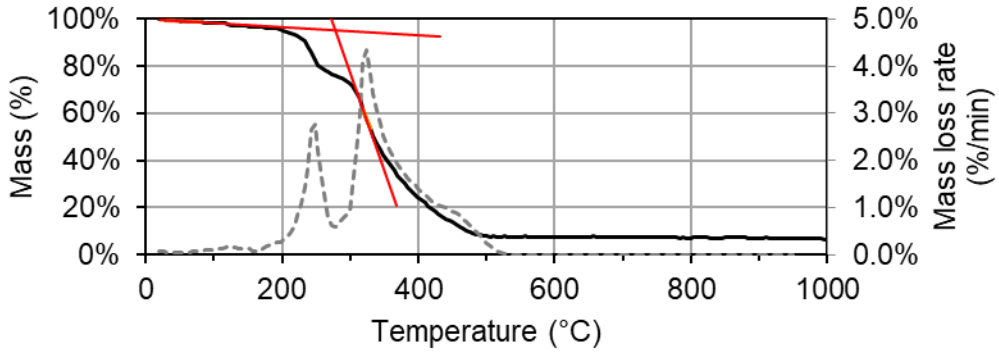

Figure A-10: The mass loss and rate of mass loss of GreenCoal 3:1 at 5 °C/min

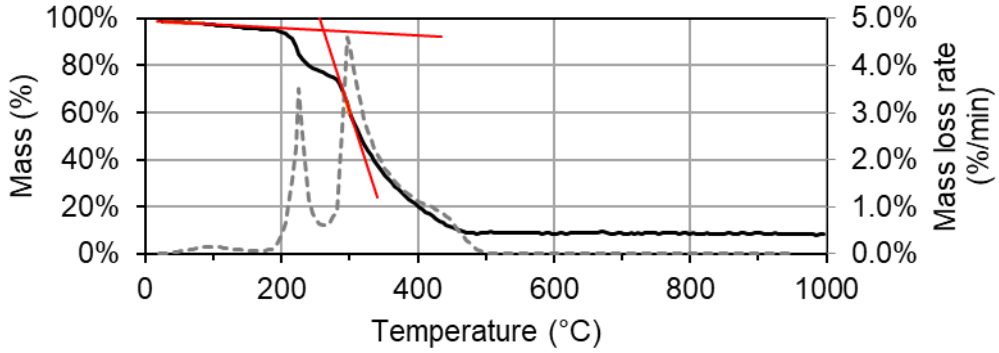

Figure A-11: The mass loss and rate of mass loss of GreenCoal 1:1 at 5 °C/min

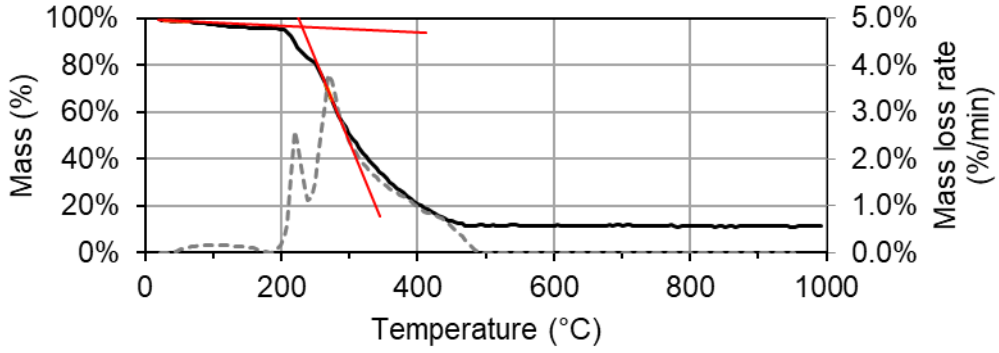

Figure A-12: The mass loss and rate of mass loss of GreenCoal 1:3 at 5 °C/min

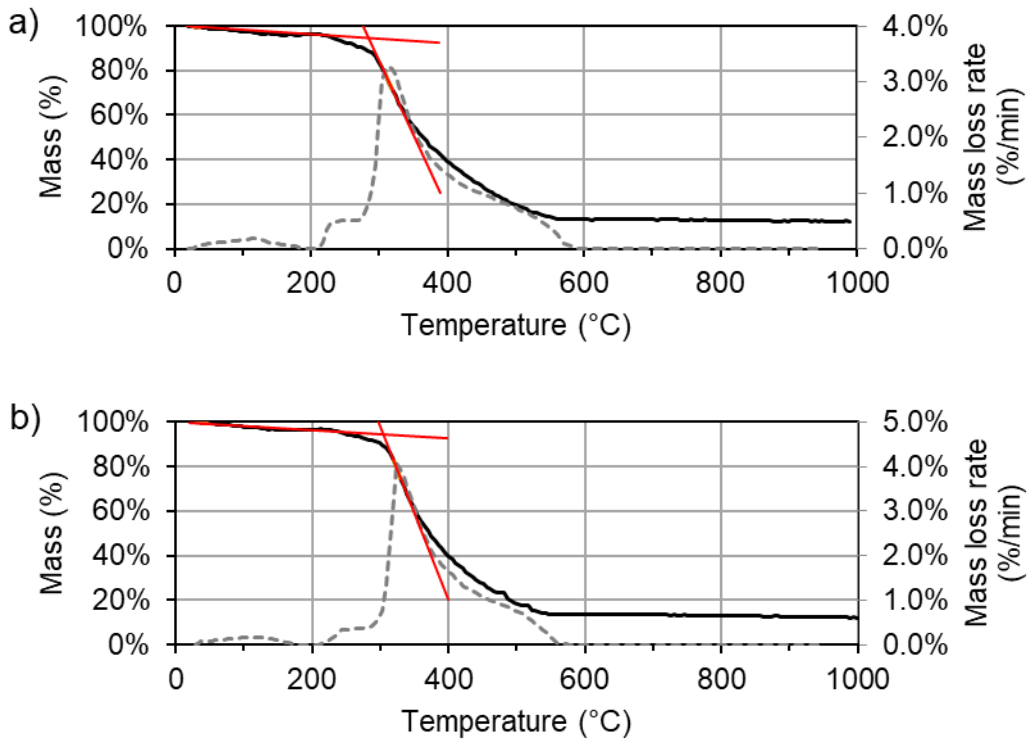

Figure A-13: The mass loss and rate of mass loss of coal at 5 °C/min: (a) run 1 and (b) run 2

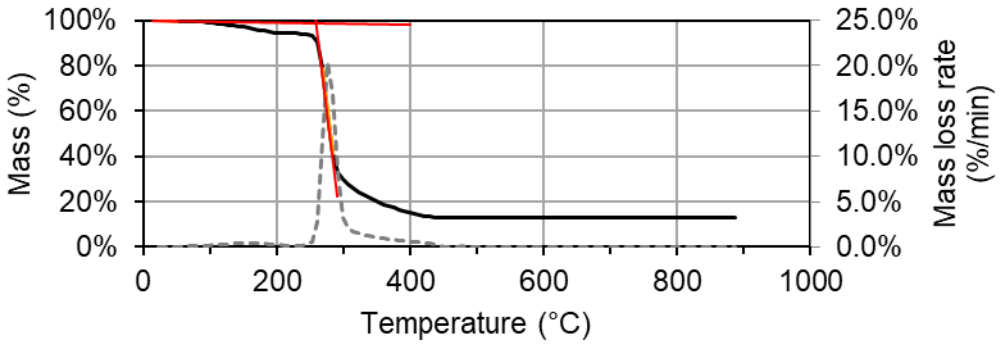

Figure A-14: The mass loss and rate of mass loss of sugarcane bagasse at 7.5 °C/min: (a) run 1 and (b) run 2

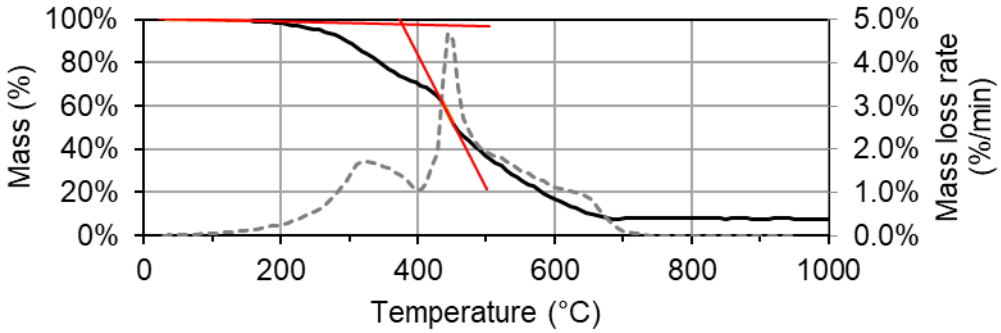

Figure A-15: The mass loss and rate of mass loss of hydrochar at 7.5 °C/min: (a) run 1 and (b) run 2

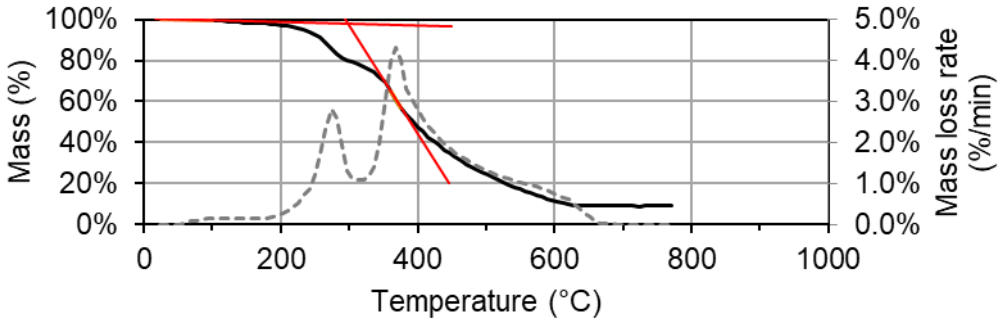

Figure A-16: The mass loss and rate of mass loss of GreenCoal 3:1 at 7.5 °C/min

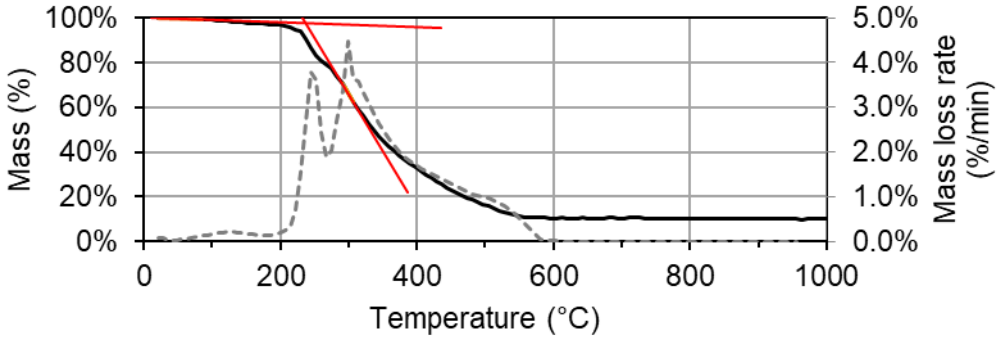

Figure A-17: The mass loss and rate of mass loss of GreenCoal 1:1 at 7.5 °C/min

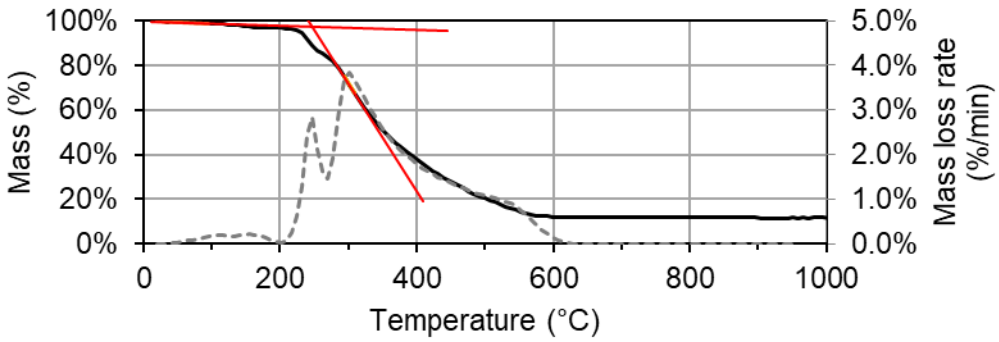

Figure A-18: The mass loss and rate of mass loss of GreenCoal 1:3 at 7.5 °C/min

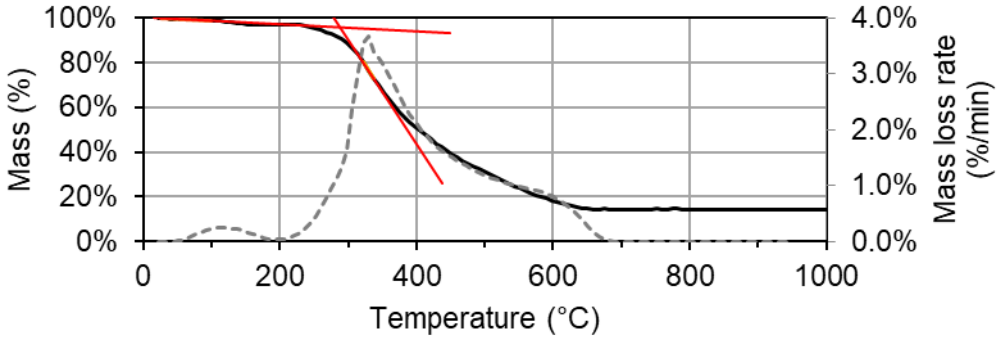

Figure A-19: The mass loss and rate of mass loss of Coal at 7.5 °C/min

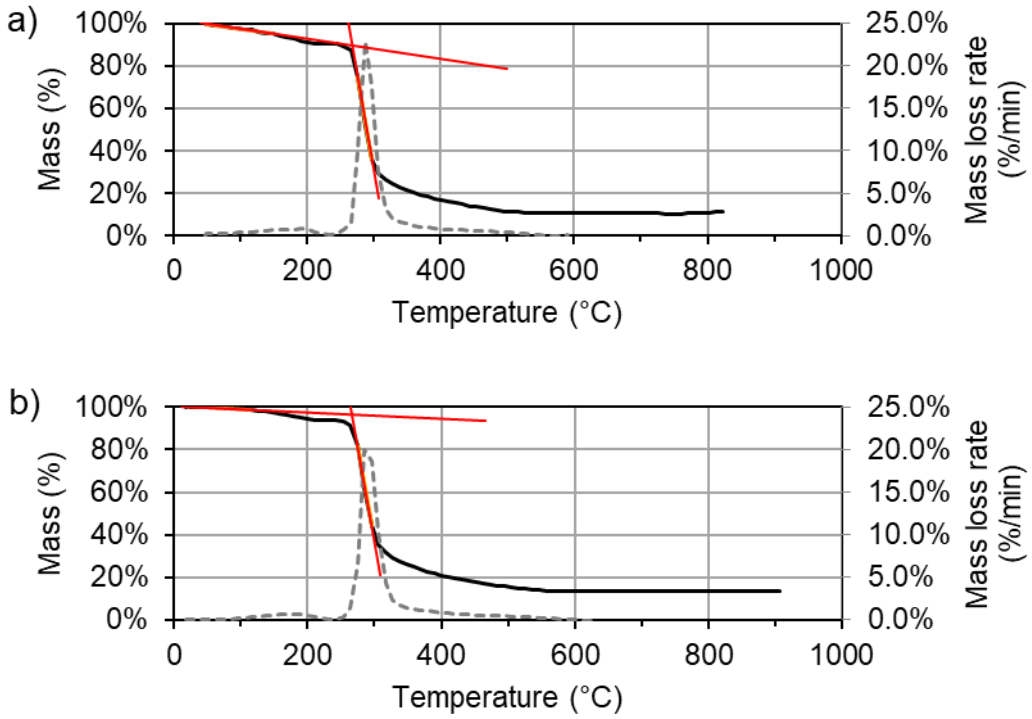

Figure A-20: The mass loss and rate of mass loss of sugarcane bagasse at 10 °C/min: (a) run 1 and (b) run 2

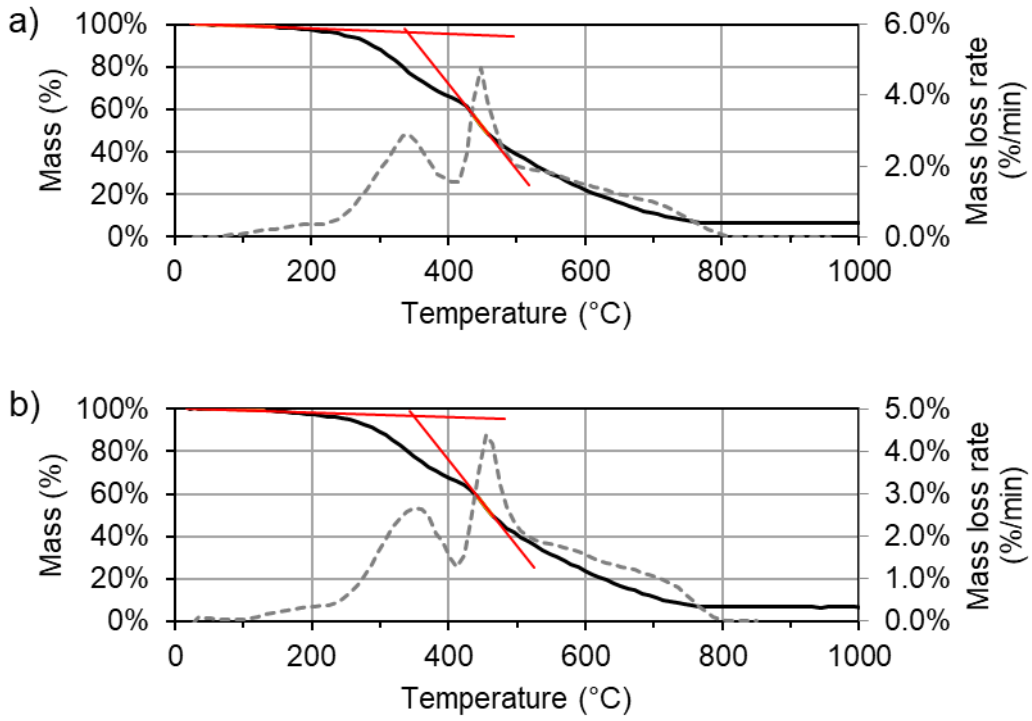

Figure A-21: The mass loss and rate of mass loss of hydrochar at 10 °C/min: (a) run 1 and (b) run 2

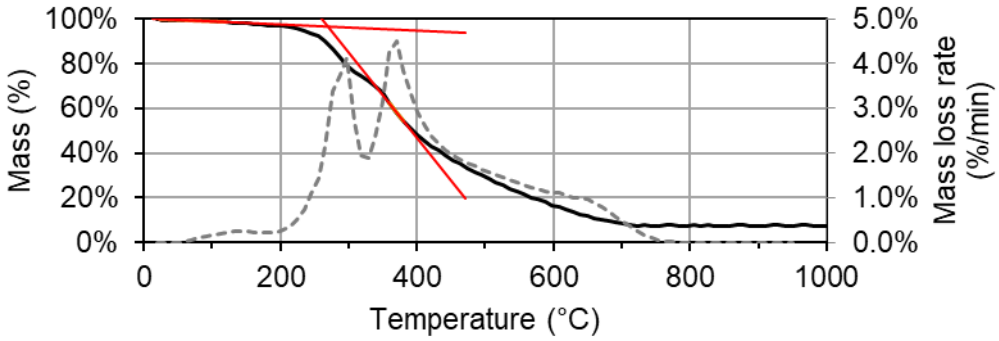

Figure A-22: The mass loss and rate of mass loss of GreenCoal 3:1 at 10 °C/min

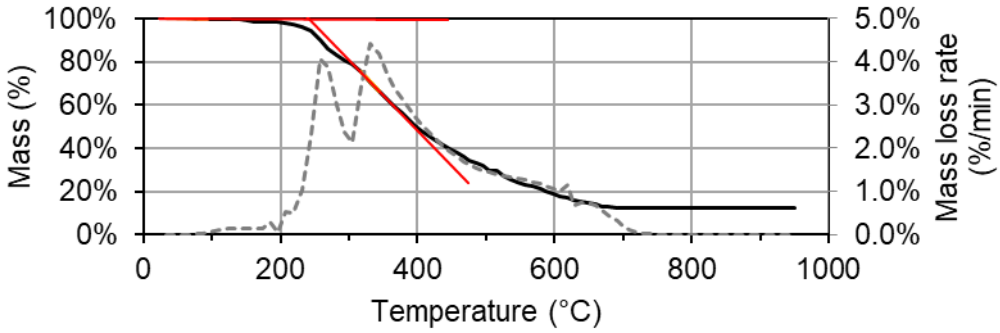

Figure A-23: The mass loss and rate of mass loss of GreenCoal 1:1 at 10 °C/min: (a) run 1 and (b) run 2

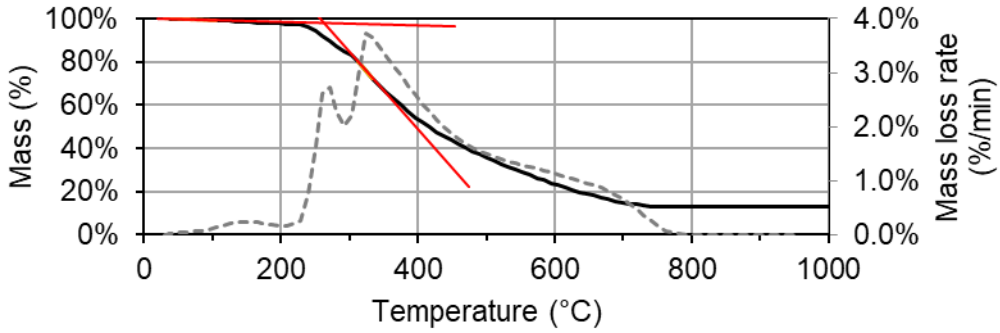

Figure A-24: The mass loss and rate of mass loss of GreenCoal 1:3 at 10 °C/min: (a) run 1 and (b) run 2

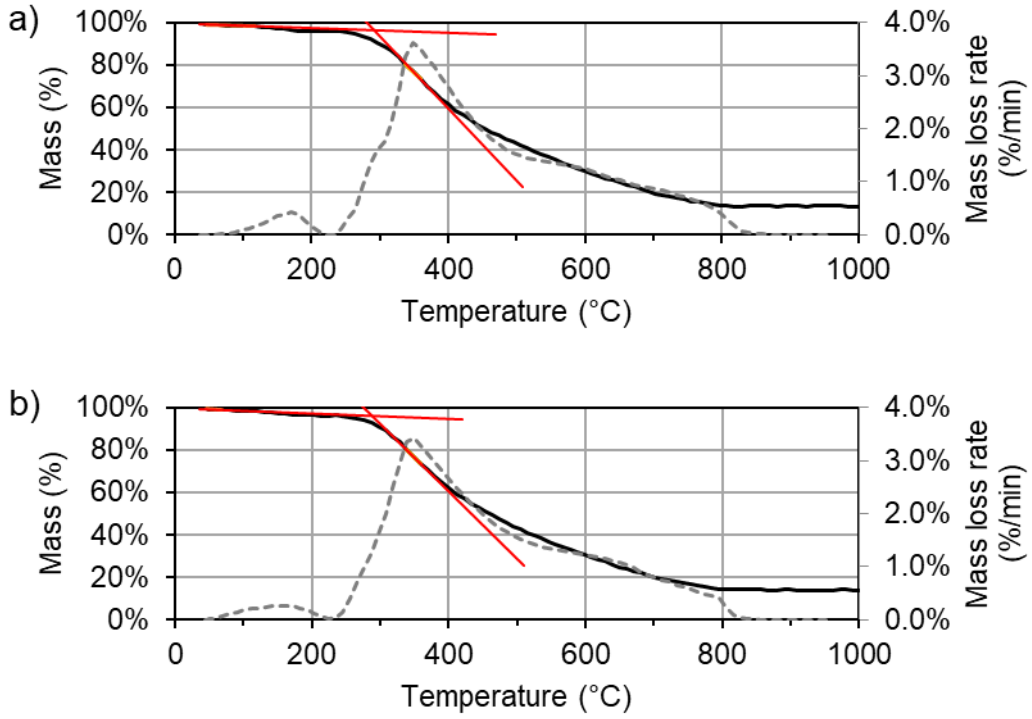

Figure A-25: The mass loss and rate of mass loss of coal at 10 °C/min: (a) run 1 and (b) run 2

A.7. CO_2 gasification

Table A-7 reports the conversion times ($t_{X=10\%}$, $t_{X=50\%, tX=90\%}$) and the reactivity ($R_{X=10\%}$, $R_{X=50\%,}$ $R_{X=90\%}$) for the Sugarcane bagasse, hydrochar, GreenCoals and coal pellets at three isothermal temperatures (950°C, 1000°C, and 1050°C).

Table A-7: Conversion times and reactivities for CO_2 gasification of charred samples at 950°C, 1000°C, and 1050°C

Sample	$t_{X=10\%}$ (min)	$R_{X=10\%}$ (min^{-1}) ($1x10^3$)	$t_{X=50\%}$ (min)	$R_{X=50\%}$ (min^{-1}) ($1x10^3$)	$t_{X=90\%}$ (min)	$R_{X=90\%}$ (min^{-1}) ($1x10^3$)
T=950°C						
Sugarcane bagasse	2.3	47.4	14.5	50.4	47.9	42.6
Hydrochar	11.4	9.5	62.8	14.0	145.5	27.6
GreenCoal 3:1	12.3	9.6	57.9	15.9	137.0	25.0
GreenCoal 1:1	11.9	9.4	63.9	13.1	174.3	15.2
GreenCoal 1:3	12.6	8.8	68.6	12.2	172.1	20.2
Coal	25.1	4.3	129.0	7.6	276.8	13.0
T=1000°C						
Sugarcane bagasse	1.1	104.1	6.9	107.9	24.1	77.7
Hydrochar	5.1	21.4	29.1	28.2	73.4	47.5
GreenCoal 3:1	6.2	19.0	29.6	30.1	73.7	46.1
GreenCoal 1:1	5.3	20.9	29.2	28.1	77.6	40.5
GreenCoal 1:3	6.0	18.2	34.2	23.7	90.1	34.9
Coal	10.6	11.1	50.9	17.7	119.2	32.4
T=1050°C						
Sugarcane bagasse	0.7	115.6	4.8	157.9	16.7	123.8
Hydrochar	3.6	32.0	17.9	48.7	44.9	79.3
GreenCoal 3:1	3.4	32.6	18.0	48.0	44.8	78.9
GreenCoal 1:1	3.1	36.1	17.0	48.7	45.0	67.8
GreenCoal 1:3	3.3	32.7	19.5	41.1	50.3	69.2
Coal	5.2	20.8	30.5	26.4	77.3	45.4

Appendix B – Confidence interval and experimental error

Appendix B contains the methodology that was used to determine the confidence interval and experimental error for all experiments or analysis completed internally. It was assumed that the results followed a normal distribution with a 95% confidence interval. The sample mean was calculated with:

$$\bar{x}=\frac{1}{N}\sum_{i=1}^{N} x_i, \qquad \text{Eqn. B-1}$$

where x_i is the individual observation/measurement of a sample and N the number of samples. The standard deviation of the samples was calculated with

$$s=\sqrt{\frac{\sum(x_i-\bar{x})^2}{N-1}}. \qquad \text{Eqn. B-2}$$

The standard error (SE) is defined with

$$SE=\frac{s}{\sqrt{N}}. \qquad \text{Eqn. B-3}$$

The t-critical value was determined at a 95% confidence level by using a t-critical value table. The t-critical value is dependent on the Degrees of Freedom (df, df = N-1), which is related to the sample group size. As an example, a sample group with five samples has Degrees of Freedom of four and a t-critical value of 2.776 for a 95% confidence level (see Table B-1).

Table B-1: Critical value for a 95% t-interval

Degrees of Freedom	95%
1	12.706
2	4.303
3	3.182
4	2.776
5	2.571

The two-sided confidence interval was calculated with

confidence interval= $\bar{x}\pm(SE\times t)$. (Eqn. B-4)

using the standard error and t-critical value. Last, of all, the experimental error can be calculated with

$$\text{Experimental error } (\%) = \frac{\text{confidence interval}}{\bar{x}} \times 100\%. \quad \text{(Eqn. B-5)}$$

Appendix C - Coal combustion mass balance and pollutant emissions

A coal combustion mass balance was used as a basis for all samples. The mass balances completed and presented here was based on notes from a Graduate Diploma in Engineering course (Coal combustion) at Wits University (Anon. 1995).

C.1. The air required for combustion and composition of flue gas

The mass balance was completed to calculate the theoretical flue gas mole quantities, the volume of the flue gas and the total mole of flue gas produced. For these calculations, a 100 kg (daf) coal was used as a basis, and it was assumed that combustion would take place in 20% excess air.

The mass of air required for the combustion of carbon, hydrogen, and sulphur can be calculated by using the ultimate composition on a dry-ash-free basis as below:

$$m_{O_2,1}(kg) = x_{C,daf} \times 100 \text{ kg daf sample} \times \frac{32}{12}, \quad \text{Eqn. C-1}$$

$$m_{O_2,2}(kg) = x_{H,daf} \times 100 \text{ kg daf sample} \times \frac{16}{2}, \quad \text{Eqn. C-2}$$

$$m_{O_2,3}(kg) = x_{S,daf} \times 100 \text{ kg daf sample} \times \frac{32}{32}, \quad \text{Eqn. C-3}$$

The mass oxygen (O_2) in the daf coal is calculated with:

$$m_{O_2,4}(kg) = (x_{H,daf} \times 100 \text{ kg daf sample}) \quad \text{Eqn. C-4}$$

The total mass oxygen required to combust 100 kg daf coal is then calculated with:

$$m_{O_2,total}(kg)=m_{O_2,1}+m_{O_2,2}+m_{O_2,3}-m_{O_2,4} \quad \text{Eqn. C-5}$$

The mass oxygen (O_2) in the daf coal is calculated with:

$$m_{air,daf}\left(\frac{\text{kg air}}{\text{kg daf sample}}\right)=\frac{m_{O_2,total}(\text{kg } O_2)}{100 \text{ kg daf sample}}\times\frac{100 \text{ kg air}}{23 \text{ kg } O_2} \quad \text{Eqn. C-6}$$

The total mass air required to combust 100 kg daf coal is then calculated with:

$$m_{air}\left(\frac{\text{kg air}}{\text{kg coal}}\right)=\frac{m_{daf}\text{ (kg daf sample)}}{100 \text{ kg sample}}, \quad \text{Eqn. C-7}$$

where m_{daf} is calculate with

$$m_{daf}\text{ (kg daf sample)}=100\times(1-x_{IM}-x_{ash}), \quad \text{Eqn. C-8}$$

and x_{IM} and x_{ash} are the mass fractions of the inherent moisture- and ash content according to the proximate composition. The stoichiometric molar quantity of air required for combustion can be calculated by using the ultimate composition on a dry-ash-free basis. The mole air required to combust carbon, hydrogen, and sulphur (reported on daf basis) can be calculated with:

$$n_{O_2,1}(kmole)=x_{C,daf}\times 100 \text{ kg daf sample}\times\frac{1}{12kg/mole}, \quad \text{Eqn. C-9}$$

$$n_{O_2,2}(kmole)=x_{H,daf}\times 100 \text{ kg daf sample}\times\frac{1}{4kg/mole}, \quad \text{Eqn. C-10}$$

$$n_{O_2,3}(kmole)=x_{S,daf}\times 100 \text{ kg daf sample}\times\frac{1}{32kg/mole}, \quad \text{Eqn. C-11}$$

The mole oxygen (O_2) in the daf coal is calculated with:

$$n_{O_2,4}(kmole)=\frac{x_{O_2,daf}(\text{kg } O_2/\text{kg daf sample})\times 100 \text{ kg daf sample}}{32}. \quad \text{Eqn. C-12}$$

The total mole oxygen required to combust 100 kg daf coal is then calculated with:

$$n_{O_2,total}(kmole)=n_{O_2,1}+n_{O_2,2}+n_{O_2,3}-n_{O_2,4}. \quad \text{Eqn. C-13}$$

The volume of air required to combust 100 kg daf coal at standard conditions is calculated with:

$$V_{air}\ (m^3\ @\ STP)= n_{O_2,total}\times\frac{22.4m^3}{kmole}\times\frac{100m^3\ air}{21m^3\ O_2}. \quad \text{Eqn. C-14}$$

The composition of the flue gas when the sample is combusted in 20% excess air, can be calculated by using the information above. For these calculations, it is important to realise that for ideal gases, the mole fraction and volume fraction of the individual gas species in the flue gas will be the same. Therefore, by using the mole quantities determine above, the mole quantities of CO_2, H_2O and SO_2 are determined with:

$$n_{CO_2}(kmole)=n_{O_2}(kmole), \quad \text{Eqn. C-15}$$

$$n_{H_2O}(kmole)=2\times n_{O_2}(kmole), \quad \text{Eqn. C-16}$$

$$n_{SO_2}(kmole)=n_{O_2}(kmole), \quad \text{Eqn. C-17}$$

Since combustion takes place in 20% excess air, implying that O_2 is at 20% excess, the mole amount of O_2 in the flue gas is calculated as:

$$n_{O_2,flue\ gas}(kmole)=0.2\times n_{O_2,\ total}(kmole). \quad \text{Eqn. C-18}$$

The amount of N_2 in the flue gas is calculated as the sum of the nitrogen in the coal and the nitrogen (N_2) in the air. The nitrogen in the 100 kg dry-ash-free sample is calculated as:

$$n_{N_2,\ daf\ sample}(kmole)=\frac{x_{N_2,\ daf\ sample}\times 100kg\ daf\ sample}{28\ kg/kmole}. \quad \text{Eqn. C-19}$$

The nitrogen in the air is calculated with:

$$n_{N_2,\,air}(\text{kmole}) = 1.2 \times n_{O_2,\,total}(\text{kmole}) \times \frac{79 \text{ mole } N_2}{21 \text{ mole } O_2}. \qquad \text{Eqn. C-20}$$

Subsequently, the total mole N_2 in the flue gas is calculated with:

$$n_{N_2,\text{flue gas}}(\text{kmole}) = n_{N_2,\,\text{daf sample}}(\text{kmole}) + n_{N_2,\,air}(\text{kmole}). \qquad \text{Eqn. C-21}$$

The total mole flue gas produced is then calculated as follow:

$$n_{\text{total, flue gas}}(\text{kmole}) = n_{CO_2} + n_{H_2O} + n_{SO_2} + n_{O_2,\text{flue gas}} + n_{N_2,\text{flue gas}}. \qquad \text{Eqn. C-22}$$

C.2. Ash burden

The ash burden is the fly ash produced without collection. Assuming a basis of 100 kg sample, the ash burden at any temperature is estimated with:

$$\text{dust burden } \left(\frac{\text{kg ash}}{\text{kg coal}}\right) = x_{\text{ash, ad}} \times 100\text{kg} \left(\frac{\text{kg ash}}{\text{kg sample}}\right) \times \frac{100\text{kg sample}}{m_{daf}} \times \frac{100 \text{ kg daf sample}}{n_{\text{total, flue gas}}} \times \frac{\text{kmole gas}}{22.4\text{m}^3} \times \frac{273(\text{K})}{\text{T}}. \qquad \text{Eqn. C-23}$$

C.3. SOx and NOx

For bituminous coals, 90% of the sulphur will be converted to SO_2. The quantity SO_2 in the flue gas for the different samples are calculated by assuming that 90% of sulphur for all samples will be converted to SO_2. Subsequently, the sulphur in the flue gas (ppm) is calculated with:

$$S\ (\text{ppm}) = \frac{x_{S,daf} \times 100\text{kg daf sample}}{32\text{kg/kmole}} \times 0.9 \times 10^6. \qquad \text{Eqn. C-24}$$

Next, it is assumed that 25% of N in the sample is converted to oxides of nitrogen (NOx). Using a basis of 100 kg sample, the amount oxides of nitrogen produced (ppm) will be:

$$N\ (\text{ppm}) = \frac{x_{N,\,\text{daf sample}} \times 100\text{kg}}{14\text{kg/kmole}} \times \frac{1}{n_{\text{total, flue gas}}} \times 0.25 \times 10^6. \qquad \text{Eqn. C-25}$$